Hierarchical 1-3D titania Hyper-Branched Nanorods (HBNs) thin films for photocatalytic CO$_2$ utilisation applications

Gavrielides Stelios

SUBMITTED FOR THE DEGREE OF DOCTOR OF PHILOSOPHY

HERIOT-WATT UNIVERSITY

SCHOOL OF ENGINEERING AND PHYSICAL SCIENCES,

INSTITUTE OF MECHANICAL, PROCESS AND ENERGY ENGINEERING

RESEARCH CENTRE FOR CARBON SOLUTIONS (RCCS).

June 2022

Abstract

Despite our efforts, the concentration of CO_2 in the atmosphere is constantly rising at an alarming rate. It is of paramount importance to develop technologies that will expedite the reduction of the rate that CO_2 is released into the atmosphere. CO_2 utilisation technologies consider CO_2 as a valuable carbon building block in a circular carbon economy approach, where the released CO_2 is captured, and utilised to produce valuable chemicals. One of these technologies is the photocatalytic utilisation of CO_2 for the production of solar fuels and value added chemicals, which has the added advantage of utilising light with mild reaction conditions. However, photocatalysis is limited to the absorbed light energy and CO_2 is a very stable molecule which requires a large amount of energy for its conversion. Therefore, designing highly efficient materials as photocatalysts becomes a very important task.

The current thesis is concerned with the growth of titania 1-3D hierarchical hyperbranched nanorods (HBNs) on fluorine-doped tin oxide (FTO) conductive glass as thin films to be used as photocatalysts for CO_2 reduction reactions. This thesis is focused on investigating the capabilities and photocatalytic behaviour of the titania HBNs material. The HBNs were found to have improved light harvesting when compared to Degussa P25 TiO_2 (48.2 to 28.6 μmol m^{-2} s^{-1}), attributed to their 1-3D morphology. P25 is a blend of mainly anatase and traces of rutile phase TiO_2, commonly used as a benchmark for photocatalytic applications. P25 was supported on FTO glass and its performance was compared with that of FTO supported HBNs. This thesis is presented as a collection of published bodies of work, where the HBNs are characterised, modified and tested in photocatalytic reactions. In more detail, two reactions are presented, firstly the CO_2 photoreduction to produce solar fuels such as CH_4 and CO. The HBNs were found to have superior conversion rates (up to 8.7 μmol g_{cat}^{-1} h^{-1}) compared to P25 (6.9 μmol g_{cat}^{-1} h^{-1}) but, more importantly, offer the ability to shift the selectivity of the reaction product from CO to CH_4, utilising a facile phase altering treatment. Additionally, the HBNs were loaded with CuO and RuO_2 and their performance was investigated and compared. CuO has shown the ability to improve the optical properties of the material, while RuO_2 exhibited improved charge separation and suppressed the recombination rate, which led to further improvement in the photocatalytic performance. The second reaction is the CO_2 cycloaddition

to epoxides, for the photogeneration of cyclic carbonates, which are primarily used as electrolytes in Li-ion batteries amongst others. In the current thesis it is demonstrated that a photocatalytic approach is possible for this reaction. Additionally, RuO_2-HBNs are shown to be the best performing photocatalyst in terms of conversion. The main appeal of the photocatalytic approach is the significantly milder reaction conditions (below 55 °C and 200 kPa) when compared to the conditions currently being used in the industry (100-200 °C and 5-10 MPa).

This thesis is dedicated to my family.

Acknowledgments

Prof. Mercedes, I couldn't have asked for a better supervisor. My time in RCCS was both pleasant and eye-opening. I truly appreciate and admire the way you have allowed the freedom of scientific curiosity and exploration throughout this PhD project yet always managed to keep me on track and focused on the end goal. You were always there when I needed guidance and I have learned so much from you and from the way you handled every problem or concern these four years. Lastly, I thank you for all the conferences that I was able to attend and the experiences I had.

Dr. Jeannie, you have not only been a great mentor to me, but more importantly a very good friend. I have learned something from you every day in the lab, and we travelled all over the UK to many conferences together. Your contribution to this PhD project is immense you were always my first stop for any concern, and I value your opinion greatly. Also, you opened your house so many times and have been an incredible host. I am very grateful to you and your family, Euan and Dr. Eugene. I am happy to know that I have made good friends throughout my time in this PhD project.

Dr. Warren, you were a truly valuable member to the utilisation group. I will always remember our inspiring discussions in the office, both research related and not. Additionally, this PhD project has greatly utilised your prototype CO_2 photoreduction rig and has benefited from the automated result analysis you created. I am grateful for both your contribution and your friendship.

Doug, you have helped me set up an entire reaction rig and maintain another and a custom glove box. You were the go-to person for any technical difficulty I faced in the lab. Moreover, I thank you for your input on designing the numerous custom pieces required to complete this research. I am grateful for all the work you have done, but also for our little, short breaks and nice talks we shared almost daily.

I would also like to thank my family for their support and patience for all these years I have been away from them. My entire academic journey lasted for 10 years, and I have been abroad and away for too long. However, you were there every step of the way and for that I am grateful. Also, this Thesis is dedicated to my family.

Research Thesis Submission

Please note this form should be bound into the submitted thesis.

Name*:	Stelios Gavrielides		
School:	EPS		
Version: *(i.e. First, Resubmission, Final)*	Final	Degree Sought:	PhD

Declaration

In accordance with the appropriate regulations I hereby submit my thesis and I declare that:

1. The thesis embodies the results of my own work and has been composed by myself
2. Where appropriate, I have made acknowledgement of the work of others
3. The thesis is the correct version for submission and is the same version as any electronic versions submitted*.
4. My thesis for the award referred to, deposited in the Heriot-Watt University Library, should be made available for loan or photocopying and be available via the Institutional Repository, subject to such conditions as the Librarian may require
5. I understand that as a student of the University I am required to abide by the Regulations of the University and to conform to its discipline.
6. I confirm that the thesis has been verified against plagiarism via an approved plagiarism detection application e.g. Turnitin.

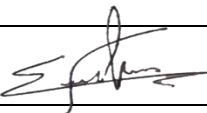## ONLY for submissions including published works

Please note you are only required to complete the Inclusion of Published Works Form (page 2) if your thesis contains published works)

7. Where the thesis contains published outputs under Regulation 6 (9.1.2) or Regulation 43 (9) these are accompanied by a critical review which accurately describes my contribution to the research and, for multi-author outputs, a signed declaration indicating the contribution of each author (complete)
8. Inclusion of published outputs under Regulation 6 (9.1.2) or Regulation 43 (9) shall not constitute plagiarism.

* *Please note that it is the responsibility of the candidate to ensure that the correct version of the thesis is submitted.*

Signature of Candidate*:		Date:	09/06/2022

Submission

Submitted By *(name in capitals):*	STELIOS GAVRIELIDES
Signature of Individual Submitting:	
Date Submitted:	09/06/2022

For Completion in the Student Service Centre (SSC)
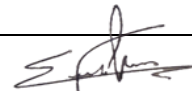
Limited Access	Requested	Yes		No		Approved	Yes		No	
E-thesis Submitted **(mandatory for final theses)**										
Received in the SSC by *(name in capitals):*						Date:				

Inclusion of Published Works

<u>**Declaration**</u>

This thesis contains one or more multi-author published works. In accordance with Regulation 6 (9.1.2) I hereby declare that the contributions of each author to these publications is as follows:

Citation details	G. Stelios, J. Z. Y. Tan, and M. M. Maroto-Valer, "Hierarchical hyper-branched titania nanorods with tuneable selectivity for CO2 photoreduction," *RSC Adv.* vol. 11, no. 51, pp. 32022-32029, 2021
Author 1	Conceptualisation, methodology, data curation, writing the original draft
Author 2	Conceptualisation, methodology, writing- review & editing, supervision.
Author 3	Supervision.
Signature:	
Date:	09/06/2022

Citation details	M. Ávila-López, G. Stelios, X. Luo, A.O. Ezra, J.Z.Y. Tan, E. L. Hipólito, L.M.T.Martínez, M.M.Maroto-Valer, "Comparative study of CO2 photoreduction using different conformations of CuO photocatalyst: Powder, coating on mesh and thin film," *Journal of CO2 Utilization,* vol. 50, p. 101588, 2021
Author 1-2	Methodology, Data curation, Writing- Original draft preparation.
Author 3	Investigation, Data curation, Software, Validation.
Author 4	Methodology
Author 5	Conceptualization, Methodology, Writing- Reviewing and Editing.
Author 6-8	Supervision.
Signature:	
Date:	09/06/2022

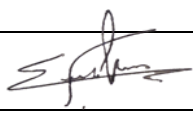| Citation details	S. Gavrielides, J. Z. Y. Tan, E. S. Fernandez, and M. M. Maroto-Valer, "Photo-generation of cyclic carbonates using hyper-branched Ru–TiO2," *Faraday Discuss.,* vol. 215, no. 0, pp. 407-421, 2019
Author 1	Conceptualisation, methodology, data curation, writing the original draft.
Author 2	Conceptualisation, methodology, writing- review & editing, supervision.

Author 3-4	Supervision.
Signature:	
Date:	09/06/2022

Table of Contents

PhD research output

This is a summary of the research output of this PhD project.

Publications

1) S. Gavrielides, J. Z. Y. Tan, E. Sanchez Fernandez and M. M. Maroto-Valer *Photo-generation of cyclic carbonates using hyper-branched Ru–TiO$_2$, Faraday Discuss., 2019,215, 407-421,* DOI: 10.1039/C8FD00181B.

2) M. Alejandro Ávila-López, S. Gavrielides, XiaoJiao Luo, Abah Ezra Ojoajogwu, Jeannie Z. Y. Tan, E. Luévano-Hipólito, Leticia M. Torres-Martínez, M. Mercedes Maroto-Valer *Comparative Study of CO2 Photoreduction Using Different Conformations of CuO Photocatalyst: Powder, Coating on Mesh and Thin Film Journal of CO2 Utilization, vol. 50, p. 101588,* DOI: 10.1016/j.jcou.2021.101588

3) S. Gavrielides, J. Z. Y. Tan, and M. M. Maroto-Valer, "Hierarchical hyper-branched titania nanorods with tuneable selectivity for CO2 photoreduction," RSC Adv., 10.1039/D1RA05414G vol. 11, no. 51, pp. 32022-32029, 2021, DOI: 10.1039/D1RA05414G.

4) J. Z. Y. Tan, S. Gavrielides, H. R. Xu, W. A. Thompson, and M. M. Maroto-Valer, "Alkali modified P25 with enhanced CO2 adsorption for CO2 photoreduction," RSC Adv., 10.1039/D0RA05010E vol. 10, no. 47, pp. 27989-27994, 2020, DOI: 10.1039/D0RA05010E.

5) J. Z. Y. Tan, S. Gavrielides, M. Belekoukia, W. A. Thompson, Leila Negahdar, Fang Xia, M. Mercedes Maroto-Valer and   Andrew M. Beale, *"Synthesis of TiO$_{2-x}$/W$_{18}$O$_{49}$ hollow double-shell and core–shell microspheres for CO$_2$ photoreduction under visible light,"* Chem. Commun., 10.1039/D0CC04036C vol. 56, no. 81, pp. 12150-12153, 2020, DOI: 10.1039/D0CC04036C.

6) R. Abe *et al.*, "*Beyond artificial photosynthesis: general discussion*," *Faraday Discuss.,* 10.1039/C9FD90022E vol. 215, no. 0, pp. 422-438, 2019, DOI: 10.1039/C9FD90022E.

7) J. Tan, S. Gavrielides, X. Luo, W. Thompson, and M. Maroto-Valer, "Development of photocatalysts and system optimization for CO2 photoreduction," in Nanostructured Photocatalysts 2020, pp. 39-73. DOI: 10.1016/B978-0-12-817836-2.00003-X

Conference oral presentations

1) S. Gavrielides, Jeannie Z. Y. Tan, Eva Sanchez Fernandez and M. Mercedes Maroto-Valer, Photo-generation of cyclic carbonates using hyper-branched Ru–TiO$_2$, Artificial Photosynthesis: Faraday Discussion, March 2019, Cambridge, United Kingdom.

2) S. Gavrielides, Jeannie Z. Y. Tan, Eva Sanchez Fernandez and M. Mercedes Maroto-Valer, Hyper-branched Ru–TiO$_2$ nanorods for the photogeneration of cyclic carbonates, 17th International Conference on Carbon Dioxide Utilization - ICCDU 2019 June 2019 Aachen, Germany.

3) S. Gavrielides, J. Z. Y. Tan, and M. M. Maroto-Valer*, Tuneable selectivity for CO$_2$ photoreduction using hierarchical Hyper-Branched Nanorods* 18th International Conference on Carbon Dioxide Utilization, June 2021, KAIST Daejeon, South Korea.

4) S. Gavrielides, J. Z. Y. Tan, and M. M. Maroto-Valer, Tuneable selectivity for CO$_2$ photoreduction using hierarchical Hyper-Branched Nanorods HBNs, Annual CRITICAT conference, March 2021, St-Andrews University, United Kingdom.

5) S. Gavrielides, J. Z. Y. Tan Eva Sanchez Fernandez and M. Mercedes Maroto-Valer, Photocatalytic generation of cyclic-carbonates using Hyper-branched Ru-TiO$_2$ Nanorods, Annual CRITICAT conference, March 2019, Heriot-Watt University, United Kingdom.

Conference poster presentations

1) S. Gavrielides, J. Z. Y. Tan, and M. M. Maroto-Valer, Hyper-branched nanorods for CO$_2$ utilisation applications, Annual CRITICAT conference, March 2020, St-Andrews University, United Kingdom.

2) S. Gavrielides, J. Z. Y. Tan Eva Sanchez Fernandez and M. Mercedes Maroto-Valer, Photocatalytic CO$_2$ cycloaddition to epoxides using hyper-branched nanorods, 7th UK Solar Fuels Symposium, March 2019, University of Cambridge, United Kingdom.

Chapter 1

Introduction

1.1 Energy sector overview

The increasing concentration of anthropogenic CO_2 and other greenhouse gases (GHG) in the atmosphere is a great concern due to their detrimental effects on our climate. Annual global CO_2 emissions show that in the year of 2000 the CO_2 emitted was 25.12 billion metric tonnes while the latest pre-pandemic data of 2019 show a significant increase to 36.44 billion metric tonnes. The energy demand is constantly rising due to the increasing population and our high energy-demanding lifestyles. The global energy sector and industry remain heavily reliant on fossil fuels despite the efforts made towards more sustainable energy sources.[1] It is important to note, for a comprehensive understanding of the issue, that the largest contribution of CO_2 emissions comes from power generation, electricity and heat production derived from fossil fuels. On the other hand, relatively mature technologies such as hydrothermal, wind, solar energy amongst others provide alternative ways of tapping into large energy reserves without the harmful side effects to the environment, enabling a more sustainable future. The challenge remains, to develop new technologies that are both economically viable and environmentally sustainable, in a relatively short timeframe.
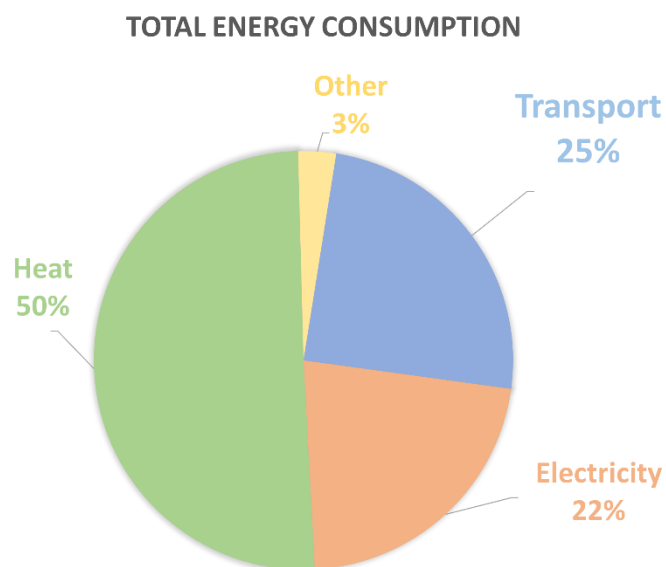
Figure 1.1 - Scottish energy sector breakdown for 2019 [2]

In Scotland, heat energy has the highest demand of approximately 50% of the entire energy sector, followed by transport energy at 25% and electrical energy at 22% (Figure 1.1). Heat and transport energy which account for 75% of the entire energy requirements according to government reports for 2019[2] remain heavily fossil fuel based sources, while noteworthy advances have been achieved for renewable electrical energy sources.[3] The more challenging energy sources for heat and transport need to be addressed as they account for a significantly larger percentage of the total energy requirement. As can be seen in Figure 1.2, out of 23.8% total renewable energy sources, only 3.2 % and 1.3 % are heat and transport energy sources respectively, while 19.4 % accounts for the renewable electricity sources. Unfortunately, the idea of complete electrification of the heat and transport energy sources is practically very unlikely as it would require unrealistic multiplication of the current renewable electricity infrastructure as well as solving very challenging electricity storage and transport issues. It is therefore paramount that researchers focus their attention on renewable heat and transport energy.
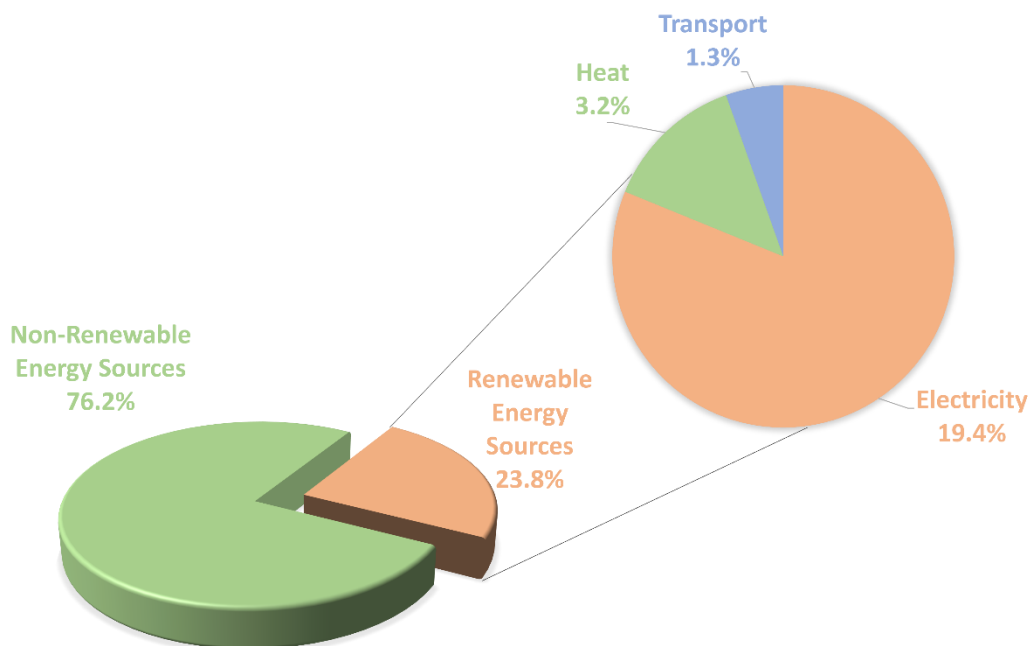
Figure 1.2 - Renewable energy breakdown of Scottish energy sector in 2019 [3]

1.2   Carbon Capture Utilisation and Storage technology

Carbon Capture Utilisation and Storage (CCUS) aims to capture CO_2 primarily from high emitting sources or hubs, utilise the captured CO_2 as feedstock in industrial processes producing valuable chemicals or fuels, and storing the remaining (not utilised) CO_2 under

impermeable rock formation or large reservoirs underground. There are numerous sources of anthropogenic CO_2, either large scale sources such as power generation industry, steel and cement industries, or medium scale sources related to commercial and industrial buildings as well as small scale sources like the transportation sector. The largest contributor is considered to be the fossil-fuel combustion process mainly related to power generation and oil refining processes. According to literature reports, the coal boiler fossil fuel power production process is responsible for 59.69% of the total CO_2 anthropogenic emissions globally, followed by cement, iron and steel production at 6.97%.[4-6]

The UK government has adopted emission targets in line with the Paris agreement which would require a 63 % reduction of carbon emissions from the year 2019 to 2035, in order to achieve the net zero target, set for the year of 2050. Some of the headline actions set by the UK government as (mid-way) targets for the year 2030, include plans regarding offshore wind, electric vehicles, emissions reductions in manufacturing and refining sectors, tree planting, peatland restoration, nuclear power and CCUS as outlined in the Climate Change Committee (CCC) report of 2021.[6] In more detail the target set for CCUS, was developing infrastructure capable of capturing and storing 10 $MtCO_2$ annually, across four industrial clusters. However, under the review of CCC it is suggested that the target should be revised to 22 $MtCO_2$ across at least 5 industrial clusters to be in line with the 2050 net zero target, under the legally binding commitment of Climate Change Act (2008).[6] CCUS has the potential to suppress CO_2 concentration in our existing industrial and power generation infrastructures, thus providing a path towards the decarbonisation of the industrial and energy sector. Additionally, suggestions of CCC include that all Energy from Waste (EfW) plants are retrofitted with CCUS from the late 2020s, as well as introducing policy for new plants to be constructed with CCUS or be CCUS ready.[7]

The UK government has also committed to reducing carbon concentration while maintaining a rising economic sector with their "Clean Growth Strategy" program. In October 2017, the government has made a commitment in using CCUS approach and low carbon technologies to decarbonise the industry sector which falls in agreement with the "European Green Deal communication" program to achieve the global climate goals. The goal of the UK government is to demonstrate international leadership in CCUS with global partner collaborations investing up to £100 million in CCUS and work closely with the industry sector to deploy CCUS at scale in the UK.[8]

Despite all the plans and targets that were mentioned above, to this date no CCUS unit is operational in the UK to the best of the authors knowledge. This raises concerns regarding the genuine intentions of the UK government to achieve the targets that were set. CO_2 utilisation can be part of CCUS but can also be applied as a standalone technology. The lack of any operational CCUS units to date, might suggest the need to focus our efforts on technologies of smaller scale but easily applicable, such as CO_2 utilisation techniques. CO_2 Utilisation is discussed in more detail in the following section.

1.3 CO_2 utilisation

CO_2 utilisation attempts to shift the current perspective towards CO_2, where CO_2 will be considered as a valuable feedstock and source of carbon, rather than an environmentally harmful waste chemical. The utilisation approach has the potential to utilise approximately 500 million metric tonnes (out of 35-36 billion metric tonnes) per year globally and can be divided into five sections as shown in Figure 1.3.

The five utilisation divisions are briefly discussed below. Mineralisation is the reaction of CO_2 with minerals to form carbonates, which are most commonly applied in cement and steel industries with a large potential of CO_2 sequestration.

Enhanced Oil Recovery (EOR) is by far the largest CO_2 utilisation technology, where CO_2 is injected into oil reservoirs is used to enhance the oil extraction. It is important to note that EOR does not chemically convert CO_2 and is used to extract fossil fuels, consequently releasing more CO_2 in the atmosphere.

The biological conversion of CO_2 follows the photosynthetic route where algae directly absorb CO_2 from the atmosphere and produce biofuel. Various industries are utilising CO_2 directly, commonly used in carbonation of beverages, food preservatives and as a refrigerant.[9]

Lastly, the chemical conversion of CO_2 approach can produce important chemicals such as urea, formic acid, organic carbonates, cyclic carbonates and polycarbonates amongst others. These chemicals have important applications in the industry, for example urea has significant applications mainly as a fertiliser amongst others and formic acid is primarily used as preservative in livestock feed. Carbonates are used by the cement industry and cyclic carbonates (CCs) are implemented as electrolytes

in lithium-ion battery technology. Additionally, CO_2 can be chemically converted to produce hydrocarbons used as fuels, mainly methane (CH_4) and carbon monoxide (CO).

The current thesis is concerned with the photocatalytic conversion of CO_2 and more specifically with the photocatalytic reduction of CO_2 to produce CO and CH_4, as well as CO_2 photocatalytic conversion to CCs. Photocatalysis is an attractive approach as it has the potential to produce valuable chemicals and solar fuels utilising solar irradiation as the energy input resulting in mild reaction conditions (55 °C and 200 kPa as opposed to 100-200 °C and 5-10 MPa). Photocatalysis is discussed further in the following section 1.4.
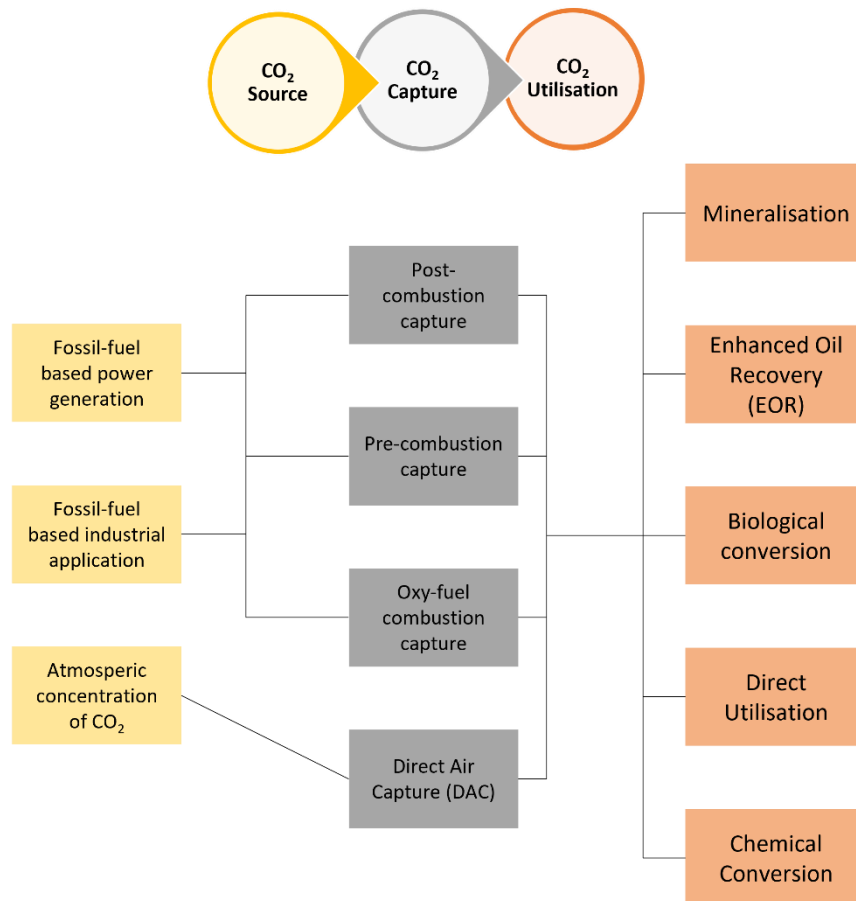
Figure 1.3 - CO_2 Source Capture and Utilisation processes.[9]

1.4   Underlying principles of photochemistry

1.4.1   Light absorption

Axiomatically, absorption of light must precede for photochemistry processes to occur and this known as the first law of photochemistry. When there is interaction of electromagnetic irradiation with a material three different things might occur. The light can be transmitted through the material, or reflected off of its surface, and light can also be absorbed by the material.[10] If we assume the incident light intensity to be I_0, then the transmitted, reflected and absorbed light intensities would be I_T, I_R, and I_A respectively.[11] Experimental observations have shown that:

$$I_R + I_T < I_0 \tag{1.1}$$

This is attributed to the absorbed light. It can then be derived that:

$$I_0 = I_R + I_T + I_A \tag{1.2}$$

Given Eq.1.2, dimensionless coefficients can be implemented with values from 0-1 that refer to (T) transmittance, (R) reflectance and (A) absorbance. These coefficients can be defined as follows, i.e for (R) reflectance, the ratio of the Reflected light (I_R) to the overall incident light (I_O).

$$I_R = RI_O \tag{1.3a}$$

$$I_T = TI_0 \tag{1.3b}$$

$$I_A = AI_0 \tag{1.3c}$$

Light absorption is essentially a transfer of energy from an electromagnetic field to a molecule, or more specifically the transfer of photon energy into the energy of electronic excitation (see section 1.4.3). Given the conservation of energy, we can derive the conclusion that:

$$R + T + A = 1 \tag{1.4}$$

1.4.2   Electromagnetic radiation

Electromagnetic radiation consists of electromagnetic waves. An electromagnetic wave consists of an electric and magnetic field travelling through space at right angles to each other and there is a wide spectrum of electromagnetic waves with varying wavelengths

from 10^8 m down to 10^{-16} m. There is an inverse relationship of wavelength to frequency as shown in Eq.1.5:

$$c = \lambda v \qquad (1.5)$$

Where c is a constant and represents the speed of light ($\sim 3 \times 10^8$ m/s), λ is the wavelength (m) and v is the frequency (Hz). Higher frequency waves have more energy as described by the Planck-Einstein relation Eq.1.6.

$$E = hv \qquad (1.6)$$

Where E = energy (J) and h is Planck`s constant (6.626×10^{-34} J s).[11] Consequently, longer wavelengths possess lower energy as electromagnetic waves. For photochemistry applications typically infrared (IR), visible (VIS) and ultraviolet (UV) radiation are commonly used. Longer wavelengths like far-infrared tend to cause vibrational excitation to molecules which results in heat, and shorter wavelengths like X-rays cause ionization of atoms.

Electromagnetic radiation has the ability to be absorbed or reflected, which is a property of waves. However, in certain situations electromagnetic radiation was found to behave as particles with properties of matter. The quantum theory of light suggests that light travels in bundles of waves (quanta), and each of these bundles, behaves as a particle, a photon. Each photon contains a packet of energy which is accurately calculated with the Planck-Einstein relation mentioned above. Photons have been found to have mass upon interaction with matter, (particle behaviour), this is explained with the relativity equation (Eq.1.7).[12]

$$E = mc^2 \qquad (1.7)$$

Also, light has been proven to interfere, diffract and reflect which are all characteristics of waves. This wave and particle behaviour of light is often called the duality of light and it was first introduced with the discovery of the photoelectric effect. The photoelectric effect describes the observation that when electromagnetic irradiation with certain energy (hv) or higher, collides with a material surface, electrons are emitted. For each material the energy threshold in which electrons are released is different. This behaviour suggests that light comes in discrete amounts of energy rather than waves.[13] This discovery explained the quantized nature of light and introduced the concept of photons. Additionally, it was observed that when the incident electromagnetic irradiation was of higher energy than the energy threshold required for the specific material, the

excess energy was converted into kinetic energy of the photoexcited electron. Therefore, increasing the irradiation frequency resulted in higher kinetic energies of the same amount of photoexcited electrons. When the irradiation energy (frequency) was kept constant, but a higher amount of light of that same energy (wavelength) was shown on the material, a higher number of electrons were released. This discovery was awarded with a Nobel prize for Prof. A. Einstein and it marked the beginning of quantum physics.

1.4.3   *Energy levels, Excitation and Relaxation processes*

As the second law of photochemistry states, one molecule can absorb one photon. The energy of the photon absorbed is transferred into the electron which is then excited from the ground state to a higher energy level. This is referred to as excitation. S_0 refers to the ground state while S_1, S_2 etc refers to higher excited singlet states where $E_{S0} < E_{S1} < E_{S2}$.[11] A singlet state is defined as the electronic state that has no unpaired electrons, meaning that its electrons possess opposite spins, or more accurately, intrinsic angular momentum, and their net angular momentum equals zero.[14] The main difference of a triplet to a singlet state is that in a singlet state the electrons are of opposite spin while in a triplet state the electrons possess a similar spin direction and their net angular momentum value is 1. A singlet, doublet and triplet state have 0, 1 and 2 unpaired electrons respectively.

Each atom has excitation states with discrete energy levels that electrons can be excited to. The incident photon has to have a certain frequency which matches the absorption spectrum of the irradiated atom in order for the photon to be absorbed and excite the electron. If the $E_{photon} \geq E_{S1}$ then the incident photon can be absorbed, and the electron is excited to the S_1 excited state. The excited electron will then attempt to return to its equilibrium state the ground state S_0.[10] This process can happen very rapidly via non-radiative relaxation called internal conversion (10^{-12} sec), or via radiative relaxation by emitting a photon of less energy compared to the absorbed energy due to internal collisions.[15] These processes are shown in detail in the Jablonski diagram in Figure 1.4.[15] The main process of radiative relaxation is called fluorescence and is a fast process (10^{-9} to 10^{-7} seconds). The internal collisions that occur moving through the vibrational levels will reduce the fluorescence intensity, such processes are often called quenching effects. Another radiative relaxation process that the electron can follow to relax back to S_0 is phosphorescence which involves two steps.[10]   First step is the

intersystem crossing of the electron from the S_1 (singlet) excitation level to the first triplet excitation level T_1 which is slightly lower in energy and only then it emits a photon to release back to the ground state S_0 similarly to fluorescence process. This process takes longer to occur, 10^{-3} to 10^{-2} seconds. This causes the material to continue emitting light, shortly after there are not incident photons to be absorbed. These are the basic processes that an excited electron can return to its ground state.[15]

Each electronic excitation level has several vibrational levels that are responsible for the internal conversion energy mentioned earlier. An excitation of an electron from S_0 to S_1 can happen from any vibrational level of the ground state, with different probability to one another as shown in Figure 1.4.[16]   Similarly, the photoexcited electron can be excited to any vibrational level of the S_1 electronic energy level. However, immediately after the absorption of a photon, there are several processes that might occur, the most common being the relaxation to the lowest vibrational energy level of the S_1 excited state (internal conversion). The excess vibrational energy is dissipated into heat which is transferred to neighbouring molecules though collisions.
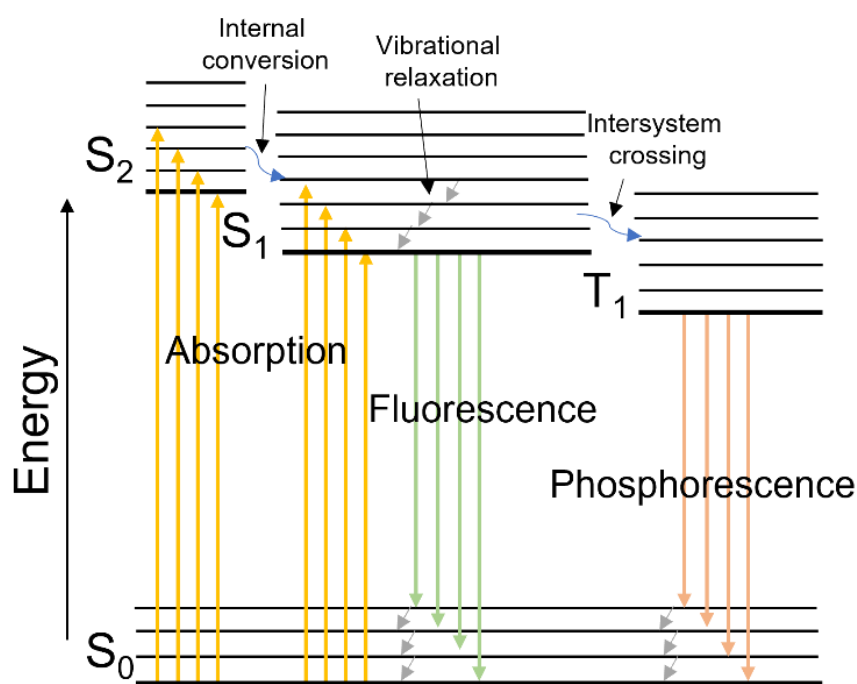
Figure 1.4 Schematic representation of excitation and relaxation processes (Jablonski Diagram). [16]

1.4.4 Photocatalysis

A photocatalytic reaction can be defined as the chemical reaction induced by the absorption of electromagnetic radiation of a material which remains chemically unchanged after the reaction. Therefore, the term photocatalysis, refers to a group of photocatalytic reactions where the primary reaction is initiated by the absorbance of photons from electromagnetic irradiation. The material exhibits a catalytic behaviour without any changes to its chemical compositions and structure and is therefore referred to as a photocatalyst.[17]

As discussed in the previous section 1.4.3, when light is absorbed by a semiconductive material, electrons are excited from the valence band to the conduction band. These excitons (excited particles) are referred to as photogenerated electron-hole pairs. At that moment the conduction and valence band possess reduction and oxidation potential respectively. The recombination of these photogenerated excitons via the processes mentioned in section 1.4.3, be it radiative (photoluminescence) or non-radiative (internal conversion), is something that works against the quantum efficiency of a photocatalyst and is desired to be reduced when designing a material for photocatalysis application.[18] Recombination of photoexcited charge carriers mainly occurs in the bulk of the catalyst and typically the process takes 10-100 nanoseconds, however, it can be prolonged if the charge carrier species are separated. The recombination effect can also be reduced by introducing electron trap sites such as defects or by incorporating suitable metal nanoparticles to act as scavengers which could provide a better chance for the charge carriers to migrate to the surface of the photocatalyst and be utilised to drive chemical reaction.[19]

1.4.5 CO$_2$ Photoreduction

One promising CO_2 utilisation technology is CO_2 photoreduction which has received a lot of attention from the academic community.[20] It is a particularly attractive reaction due to its potential to produce solar fuels and chemicals such as CH_4 and CO using light as the sole energy input and H_2O as an electron donor.[21] As mentioned in section 1.1, developing ways of producing renewable heat sources is paramount for a sustainable future. CO_2 photoreduction could provide a pathway towards that goal. While CO_2 photoreduction has been studied for the last four decades, research for a detailed understanding of the CO_2 photoreduction mechanism is still ongoing. The process involves complex sequential multi-electron processes occurring at varying timescales

from fs to s, which makes investigation a challenging task. However significant advancements have been made which provide an understanding of the underlining mechanisms. In general, when light is absorbed by the photocatalyst, an electron is excited from the occupied valence band (VB) to the empty conduction band (CB), generating an e^-/h^+ pair. Subsequently, the photoexcited charges migrate to the surface of the photocatalyst to reduction and oxidation sites respectively. The adsorbed CO_2 and H_2O molecules on the surface of the photocatalyst are reduced and oxidized respectively via electron exchange with the photoexcited semiconductor surface.

When the CO_2 molecule is adsorbed on the surface of the semiconductor, the molecule is activated due to the bend (CO_2*) that is introduced to its otherwise linear structure.[22] The CO_2* is capable for charge transfer from the material leading to a partially charged $CO_2^{-\delta}$ (activated) which is thermodynamically favourable for electron injection into the CO_2 molecule.[23] The discussed mechanism is illustrated in Figure 1.5.[24] Fourier transform infrared spectroscopy (FT-IR) studies have shown the presence of carboxylated groups such as CO_2* and has been able to identify the increase under illumination conditions.[24-26] Oxygen vacancies have been shown to be able to adsorb the CO_2 molecule and liberating the CO by Scanning Tunnelling Microscopy (STM) studies, which could explain the CO production observed in the reaction.[18, 27, 28]
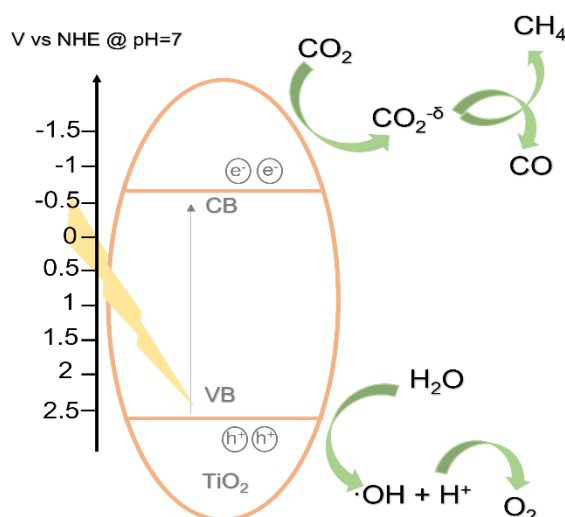
Figure 1.5 – CO_2 photoreduction mechanism diagram [23, 24]

Reduction is only possible when the potential of the photoexcited e^- is more negative than the reduction potential and similarly the oxidation occurs when the h^+ has

a more positive potential than the oxidation potential. It is therefore important that the VB and CB of the semiconductor used as a photocatalyst, are positioned at a thermodynamically beneficial position in relation to the redox potentials of the reaction.[19] The electrochemical potentials for CO_2 reduction and H_2O oxidation are shown in Table 1.1 with reference to normal hydrogen electrode (NHE) at pH 7 in aqueous solution, $25°C$, and 1 atm gas pressure. CO_2 is a stable non-polar molecule due to its double carbon oxygen bonds with high energy requirements for bond cleavage to affect its conversion (C=O, bond enthalpy $\Delta H° \approx 805$ kJ.mol^{-1}). The conversion of CO_2 to solar fuels is a series of uphill or non-spontaneous reactions. For example, to convert CO_2 to CO the Gibbs energy value is $\Delta G°= +257$ kJ.mol^{-1} while for CH_4 the Gibbs energy is $\Delta G°= +818$ kJ.mol^{-1}.[29] This high energy requirement is translated to low conversion rates which is one of the main challenges of CO_2 photoreduction. Additionally, the most widely used photocatalyst (TiO_2) suffers from deactivation which then requires a re-calcination step to re-activate the photocatalyst. Given the high energy requirements, in addition to the reaction limitation of light as the only energy input source, highly efficient photocatalyst design becomes a highly important task. Designing an efficient photocatalyst material is the aim of the current thesis, as is discussed in section (1.6).

Table 1.1 – Electrochemical (Nernst) potentials for CO_2 reduction and H_2O oxidation reactions with reference to normal hydrogen electrode (NHE) at pH 7 in aqueous solution, $25°C$, and 1 atm gas pressure [30, 31].

	Reactions	$E°$ (V) vs. NHE at pH 7
1	$2H_2O + 4h^+ \rightarrow O_2 + 4H^+$	+0.82
2	$CO_2 + e^- \rightarrow CO^-_2$	-1.9
3	$CO_2 + H^+ + 2e^- \rightarrow HCO^-_2$	-0.49
4	$CO_2 + 2H^+ + 2e^- \rightarrow CO + H_2O$	-0.51
5	$2H^+ + 2e^- \rightarrow H_2$	-0.41
6	$CO_2 + 8H^+ + 8e^- \rightarrow CH_4 + 2H_2O$	-0.24

1.4.6   Photo-generation of cyclic carbonates

The production of cyclic carbonates (CCs) by the coupling of CO_2 and epoxides is a mature CO_2 utilisation industrial application and it has been commercially available more than six decades.[32]   CCs are valuable monomers, polymers and fine chemical intermediates.   They also have applications in pharmaceuticals but arguably their most important role in the industry is their use as electrolytes in Li-ion batteries.   Li-ion batteries are widely used in our modern lifestyle and their demand is constantly rising. More importantly, with the emerging electric vehicle market, the projected future demands for Li-ion batteries are dramatically increasing.   The global market demand for 2020 was estimated at 215 GWh. The predicted demand one decade later reaches up to 1,515 GWh for the year 2030.[33]

Currently, in commercial production of CCs, homogeneous catalysts are being used, such as quaternary ammonium[34] or phosphonium halides.   Although these homogeneous catalysts are cost-effective, they require harsh reaction conditions.[35] More specifically, the reaction conditions were reported to be at 100-200 °C, and 5-10 MPa.[36]   Furthermore, since these catalysts are corrosive, the reactor materials for the particular reaction tend to be expensive.   For these reasons, the generation of cyclic carbonates has received a lot of attention in the literature.[37-39]   Recently, new methods have been proposed for the synthesis of CCs.[37, 40-42]   Many researchers used other homogeneous catalysts, for example (salen)Cr(III) complexes[43], (salen)Co(III),[44] (salen)Mn(III),[45] and supramolecular metal complexes.[46]   However, they have been reported to exhibit low catalyst stability and air sensitivity.[42, 47, 48]   More importantly, homogeneous catalysts require extensive recovery and purification steps which creates a slow and expensive reaction process.

To mitigate the above issues mentioned regarding the homogeneous catalysts, researchers have focused on heterogeneous catalysts for the synthesis of CCs. Heterogeneous catalysts can offer an easier and cheaper separation step and convenient handling. Researchers have reported Zn-ZIF-67 Metal Organic Frameworks (MOFs)[49] Fe(III)[50] and bimetallic complexes[47] to catalyse the cycloaddition of the CO_2 molecule to the open ring of epoxides at the C-O bond for the generation of cyclic carbonates.[51] Co-catalysts are often used to facilitate the epoxide activation and ring opening. This is achieved with a nucleophilic attack to the oxygen atom bond. Most commonly used co-catalysts are DMAP (4-Dimethylaminopyridine)[36, 52] and TBAB (tetrabutylammonium bromide)[53, 54]. The activated CO_2 can then attach to the opened

ring forming a cyclic carbonate molecule.[55] Recently, Prajapati et al. revealed the first photocatalytic generation of CCs using cobalt pthalocyanine grafted on TiO_2. An impressive 94.2% conversion was reported after 24 h of irradiation at 25 °C and 1 atm. The reaction was monitored by thin layer chromatography (TLC). After the completion of the reaction, the solvent was removed using the rotary evaporator and the crude product was purified by column chromatography. The conversion and selectivity of the products were determined using GC-FID.[56] It is important to note the dramatic decrease in both temperature and pressure when comparing the photocatalytic route to the previously mentioned existing industrial reaction. The photocatalytic approach has shown to have the potential to be an environmentally friendly approach, with a significant cost reduction in terms of energy expenditure, yet promising results.

1.5   Titania photocatalyst

As a photocatalyst, TiO_2 has become one of the most popular materials for energy and environmental applications such as solar fuels, photovoltaics and environmental pollutants degradation.[57] The increase of scientific interest around TiO_2 was fuelled by the publication of Fujishima and Honda on the electrochemical photolysis of H_2O under UV irradiation back in 1972. Another important milestone was the invention of commercially viable dye-sensitized solar cells (DSSCs) devices by Gratzel and O`Regan, in 1991, where replacing bulk TiO_2 with TiO_2 nanoparticles a few nanometres in size, allowed for high enough efficiency (light-to-energy 7.1 - 7.9 %) for commercially viable device.[58] Since then, TiO_2 nanostructures have been widely investigated by material engineers and scientists.

Due to the high energy requirements for CO_2 conversion associated with the double carbon-oxygen bonds and linear formation, the photocatalyst material is required to perform well in maximising light harvesting, have a negative enough conduction band potential to effectively reduce CO_2, and selectivity towards the target products of the reaction (see Table 1.1). TiO_2 and titania based photocatalysts are widely researched in photocatalytic applications for CO_2 utilisation reactions. The main advantages of TiO_2 are its chemical and thermal stability, low cost, good photoactivity with high charge transfer potential and an effective redox potential for CO_2 reduction. On the other hand, its photoactivity is limited to the UV light range which is attributed to its wide band gap energy of 3.2 eV and 3 eV for the anatase and rutile crystal structure respectively. The

3.2 eV band gap energy corresponds to a wavelength of 375nm which falls into the UV light spectrum, which limits the solar light absorbance to 5 % of the entire solar spectrum.

There is a broad range of modifications that can be implemented to alter the optical and electronic properties of TiO_2 to modify its behaviour to the desired effect. The incorporation of foreign elements as dopants in the crystal lattice, or the construction of heterojunctions using other oxides or noble metal particles have been widely applied to achieve better performance. In this thesis, the use of titania hyper-branched nanorods (HBNs) thin film is presented and proposed as a photocatalytic material for CO_2 utilisation applications. The HBNs have a 1-3D hierarchical nanostructure composed of 1D nanorods (lower dimension building blocks) growing in all directions. Their morphology allows for improved light harvesting and enhanced charge mobility.[56] During the last decades there is an increasing number of scientific studies concerned with the investigation of more complex morphological alterations as a way to further improve the photocatalyst performance in terms of light absorbance and conversion yields.[29] These are discussed in detail in the following Chapter 2, which is dedicated to various modifications techniques and morphological alterations that researchers have implemented to affect the photocatalytic behaviour.

1.6   Research aim and objectives

As was discussed earlier in previous section 1.4.5 and 1.5, designing an efficient photocatalyst for CO_2 utilisation applications is an important and challenging task. An efficient photocatalyst must have primarily enhanced light absorption, favourable electrochemical potential (reaction specific), high charge transfer and mobility and product selectivity. The aim of the current thesis is the fabrication of a novel photocatalyst material for CO_2 utilisation reactions, particularly, CO_2 photoreduction and photocatalytic CO_2 cycloaddition to epoxides. The titania HBNs have been developed as part of this process. To effectively achieve this goal, four main areas of focus were pursued. These main areas of focus are outlined as the objectives listed below followed by a brief description:

   1) Enhance the electronic properties of the titania HBNs photocatalyst.

To affect the electronic properties of the photocatalyst material several properties were considered. These include thermodynamically favourable electrochemical potentials,

photoexcited charge recombination rate and charge mobility & migration. This objective was addressed in the research presented in Chapters 4 and 5 of this Thesis.

2) *Improve the optical properties of the titania HBNs photocatalyst.*

The optical properties of a photocatalyst are essential for efficient photocatalytic behaviour. Attention was directed mainly to light harvesting capability and wavelength absorption range. This objective was addressed in the research presented in Chapters 4 and 6 of this Thesis.

3) *Introduce tuneability and control.*

Tuneability and control refers to modification techniques which could offer an element of control over the performance of the photocatalyst. These modifications could affect selectivity, conversion rates, light wavelength absorption range, recombination rate etc. This objective was addressed in the research presented in Chapter 4.

4) *Consider ease of use & ease of fabrication.*

Lastly, ease of use and fabrication would include ease of use in both liquid and gaseous systems without the need for complex separation/purification techniques and use of simple fabrication techniques without many or difficult steps. This objective was addressed in the research presented in Chapter 6 of this research.

1.7   Thesis structure

Designing efficient purpose-build photocatalyst material involves careful consideration of the requirements of the reaction and reaction conditions the photocatalyst is designed for, as well as applying appropriate modification techniques to affect the optical and electronic properties of the fabricated photocatalyst. Chapter 2 is concerned with the modifications that can be used to affect the optical and electronic properties of the photocatalytic material. Namely, these include morphological alterations, thin-film immobilisation techniques, elemental doping, heterostructure formation and fabrication techniques such as hydrothermal and solvothermal. A detailed analysis of modification and fabrication techniques as well as relevant studies from the available literature are presented. Moving on in Chapter 3 the process of developing the hierarchical 1-3D titania

HBNs morphology synthesis recipe is described. Additionally, a review of the analytical techniques that were used in the current thesis is included.

The experimental part of this thesis is presented as published articles in the following chapters (Chapters 4-6). Each publication is preceded by 4 and followed by 1 additional section. The 4 preceding sections are listed below.

1) *Aim and objectives*
2) *Highlights and key findings*
3) *Research impact*
4) *Personal development*

After these 4 sections the published article is presented. Following the publication there is 1 more following section as listed below.

5) *Further research (Not published work)*

The aim and objectives section describes what the study was trying to achieve (aim) and how the study was structured (objectives). Highlights and key findings is a summary of the important outcomes of the study. The Research impact section discusses the study and its value into context within the field of photocatalytic CO_2 utilisation. Additionally, Personal development is discussed as a result of the study. Lastly, the further research section which comes after the publication describes any work that has been done after the article was published and presents complimentary research work. At the end of each chapter there is a reference section.

References

[1]   S. E. Statistics. "Total final energy consumption by sector." https://scotland.shinyapps.io/Energy/_w_430b244f/?Section=WholeSystem&Chart=EnConsumption (accessed 20/12, 2021).

[2]   S. E. Statistcs. "Share of renewable energy in gross final consumption." https://scotland.shinyapps.io/Energy/_w_430b244f/?Section=WholeSystem&Chart=RenEnTgt (accessed 20/12, 2021).

[3]   R. Chauvy, N. Meunier, D. Thomas, and G. De Weireld, "Selecting emerging CO_2 utilization products for short- to mid-term deployment," *Applied Energy,* vol. 236, pp. 662-680, 2019/02/15/ 2019, doi: https://doi.org/10.1016/j.apenergy.2018.11.096.

[4]   I. Ghiat and T. Al-Ansari, "A review of carbon capture and utilisation as a CO_2 abatement opportunity within the EWF nexus," *Journal of CO_2 Utilization,* vol. 45, p. 101432, 2021/03/01/ 2021, doi: https://doi.org/10.1016/j.jcou.2020.101432.

[5]   J. Gale *et al.*, "Sources of CO_2," *Carbon dioxide capture and storage, Cambridge University Press, UK,* p. 94, 2005.

[6]   C. C. Committe, "2021 Progress Report to Parliament," 2021. [Online]. Available: www.theccc.org.uk/publications

[7]   E. a. I. S. Department for Buisiness. "Clean Growth Strategy: executive summary." https://www.gov.uk/government/publications/clean-growth-strategy/clean-growth-strategy-executive-summary (accessed 10/10/2021.

[8]   R. Chauvy and G. De Weireld, "CO2 Utilization Technologies in Europe: A Short Review," *Energy Technology,* vol. 8, no. 12, p. 2000627, 2020, doi: https://doi.org/10.1002/ente.202000627.

[9]   T. A. Egerton, "UV-absorption—the primary process in photocatalysis and some practical consequences," *Molecules,* vol. 19, no. 11, pp. 18192-18214, 2014.

[10]   A. V. Emeline, V. N. Kuznetsov, V. K. Ryabchuk, and N. Serpone, "Chapter 1 - Heterogeneous Photocatalysis: Basic Approaches and Terminology," in *New and Future Developments in Catalysis*, S. L. Suib Ed. Amsterdam: Elsevier, 2013, pp. 1-47.

[11]   J. M. Coxon and B. Halton, *Organic photochemistry*. Cambridge University Press, 1987.

[12]   Q.-R. Zhang, "Intensity dependence of the photoelectric effect induced by a circularly polarized laser beam," *Phys. Lett. A,* vol. 216, no. 1, pp. 125-128, 1996/06/17/ 1996, doi: https://doi.org/10.1016/0375-9601(96)00259-9.

[13]   M. Klessinger and J. Michl, *Excited states and photochemistry of organic molecules*. VCH publishers, 1995.

[14]   N. J. Turro, *Modern molecular photochemistry*. University science books, 1991.

[15]   H. H. Jaffé and A. L. Miller, "The fates of electronic excitation energy," *J. Chem. Educ.,* vol. 43, no. 9, p. 469, 1966.

[16]   B. Ohtani, "Principle of photocatalysis and design of active photocatalysts," *New and Future Developments in Catalysis,* pp. 121-144, 2013.

[17]   Y. Nosaka, M. Nishikawa, and A. Y. Nosaka, "Spectroscopic investigation of the mechanism of photocatalysis," *Molecules,* vol. 19, no. 11, pp. 18248-18267, 2014.

[18]   F. Fresno *et al.*, "Mechanistic View of the Main Current Issues in Photocatalytic CO_2 Reduction," *The Journal of Physical Chemistry Letters,* vol. 9, no. 24, pp. 7192-7204, 2018/12/20 2018, doi: 10.1021/acs.jpclett.8b02336.

[19]   K. Li, C. Teng, S. Wang, and Q. Min, "Recent Advances in TiO2-Based Heterojunctions for Photocatalytic CO2 Reduction With Water Oxidation: A Review," (in English), *Frontiers in Chemistry,* Review vol. 9, no. 88, 2021-April-15 2021, doi: 10.3389/fchem.2021.637501.

[20]   M. Tahir and N. S. Amin, "Recycling of carbon dioxide to renewable fuels by photocatalysis: Prospects and challenges," *Renewable and Sustainable Energy Reviews,* vol. 25, pp. 560-579, 2013/09/01/ 2013, doi: 10.1016/j.rser.2013.05.027.

[21]   A. Víctor, S. González, F. Illas, and J. L. Fierro, "Evidence for spontaneous CO_2 activation on cobalt surfaces," *Chem. Phys. Lett.,* vol. 454, no. 4-6, pp. 262-268, 2008.

[22]   J. Baltrusaitis, J. Schuttlefield, E. Zeitler, and V. H. Grassian, "Carbon dioxide adsorption on oxide nanoparticle surfaces," *Chem. Eng. J.,* vol. 170, no. 2-3, pp. 471-481, 2011.

[23]   B. S. Kwak and M. Kang, "Evaluation of Photoreduction Performance of CO_2 to CH_4 with H_2O Over Alkaline-Earth-Metal-Based Peroskite Nanoparticles," *Journal of Nanoscience and Nanotechnology,* vol. 17, no. 10, pp. 7351-7357, // 2017, doi: 10.1166/jnn.2017.14794.

[24]   L. Mino, G. Spoto, and A. M. Ferrari, "CO_2 capture by TiO_2 anatase surfaces: a combined DFT and FTIR study," *The Journal of Physical Chemistry C,* vol. 118, no. 43, pp. 25016-25026, 2014.

[25]   G. Busca and V. Lorenzelli, "Infrared spectroscopic identification of species arising from reactive adsorption of carbon oxides on metal oxide surfaces," *Materials Chemistry,* vol. 7, no. 1, pp. 89-126, 1982.

[26]   M. A. Henderson, "Evidence for bicarbonate formation on vacuum annealed TiO_2 (110) resulting from a precursor-mediated interaction between CO_2 and H_2O," *Surf. Sci.,* vol. 400, no. 1-3, pp. 203-219, 1998.

[27]   F. Calaza *et al.*, "Carbon dioxide activation and reaction induced by electron transfer at an oxide–metal interface," *Angew. Chem. Int. Ed.,* vol. 54, no. 42, pp. 12484-12487, 2015.

[28]   D. Acharya, N. Camillone III, and P. Sutter, "CO_2 adsorption, diffusion, and electron-induced chemistry on rutile TiO_2 (110): a low-temperature scanning tunneling microscopy study," *The Journal of Physical Chemistry C,* vol. 115, no. 24, pp. 12095-12105, 2011.

[29]   O. Ola and M. M. Maroto-Valer, "Review of material design and reactor engineering on TiO2 photocatalysis for CO2 reduction," *Journal of Photochemistry and Photobiology C: Photochemistry Reviews,* vol. 24, no. Supplement C, pp. 16-42, 2015/09/01/ 2015, doi: 10.1016/j.jphotochemrev.2015.06.001.

[30]   Y. Yang, S. Ajmal, X. Zheng, and L. Zhang, "Efficient nanomaterials for harvesting clean fuels from electrochemical and photoelectrochemical CO_2 reduction," *Sustainable Energy & Fuels,* 10.1039/C7SE00371D vol. 2, no. 3, pp. 510-537, 2018, doi: 10.1039/C7SE00371D.

[31]   E. Alper and O. Y. Orhan, "CO_2 utilization: Developments in conversion processes," *Petroleum,* vol. 3, no. 1, pp. 109-126, 2017.

[32]   Statista. "Estimated market demand for lithium-ion batteries used in electric vehicles in 2019 with a forecast for 2020 through 2030." https://www.statista.com/statistics/309570/lithium-ion-battery-market-in-electric-vehicles/ (accessed 20/12, 2021).

[33] L. Wang, P. Li, X. Jin, J. Zhang, H. He, and S. Zhang, "Mechanism of fixation of CO2 in the presence of hydroxyl-functionalized quaternary ammonium salts," *Journal of CO2 Utilization,* vol. 10, pp. 113-119, 2015.

[34] J. A. Castro-Osma, M. North, and X. Wu, "Development of a Halide-Free Aluminium-Based Catalyst for the Synthesis of Cyclic Carbonates from Epoxides and Carbon Dioxide," *Chemistry–A European Journal,* vol. 20, no. 46, pp. 15005-15008, 2014.

[35] I. Korosteleva, N. Markova, N. Kolesnichenko, N. Ezhova, S. Khadzhiev, and N. Trukhmanova, "Catalytic synthesis of propylene carbonate from propylene oxide and carbon dioxide in the presence of rhodium complexes modified with organophosphorus ligands and chitosan," *Petroleum Chemistry,* vol. 53, no. 6, pp. 412-417, 2013.

[36] R. L. Paddock, Y. Hiyama, J. M. McKay, and S. T. Nguyen, "Co (III) porphyrin/DMAP: an efficient catalyst system for the synthesis of cyclic carbonates from CO_2 and epoxides," *Tetrahedron Lett.,* vol. 45, no. 9, pp. 2023-2026, 2004.

[37] A. Decortes, A. M. Castilla, and A. W. Kleij, "Salen-complex-mediated formation of cyclic carbonates by cycloaddition of CO_2 to epoxides," *Angew. Chem. Int. Ed.,* vol. 49, no. 51, pp. 9822-9837, 2010.

[38] M. North and R. Pasquale, "Mechanism of cyclic carbonate synthesis from epoxides and CO_2," *Angew. Chem. Int. Ed.,* vol. 48, no. 16, pp. 2946-2948, 2009.

[39] H. Kawanami and Y. Ikushima, "Chemical fixation of carbon dioxide to styrene carbonate under supercritical conditions with DMF in the absence of any additional catalysts," *Chemical Communications,* no. 21, pp. 2089-2090, 2000.

[40] H. S. Kim, J. J. Kim, B. G. Lee, O. S. Jung, H. G. Jang, and S. O. Kang, "Isolation of a pyridinium alkoxy ion bridged dimeric zinc complex for the coupling reactions of CO_2 and epoxides," *Angewandte Chemie International Edition,* vol. 39, no. 22, pp. 4096-4098, 2000.

[41] M. North and R. Pasquale, "Mechanism of cyclic carbonate synthesis from epoxides and CO_2," *Angewandte Chemie,* vol. 121, no. 16, pp. 2990-2992, 2009.

[42] R. L. Paddock and S. T. Nguyen, "Chemical CO2 fixation: Cr (III) salen complexes as highly efficient catalysts for the coupling of CO_2 and epoxides," *J. Am. Chem. Soc.,* vol. 123, no. 46, pp. 11498-11499, 2001.

[43] X.-B. Lu *et al.*, "Asymmetric Catalysis with CO_2: Direct Synthesis of Optically Active Propylene Carbonate from Racemic Epoxides," *J. Am. Chem. Soc.,* vol. 126, no. 12, pp. 3732-3733, 2004/03/01 2004, doi: 10.1021/ja049734s.

[44] F. Jutz, J.-D. Grunwaldt, and A. Baiker, "Mn(III)(salen)-catalyzed synthesis of cyclic organic carbonates from propylene and styrene oxide in "supercritical" CO_2," *Journal of Molecular Catalysis A: Chemical,* vol. 279, no. 1, pp. 94-103, 2008/01/02/ 2008, doi: https://doi.org/10.1016/j.molcata.2007.10.010.

[45] J. Peng, H.-J. Yang, Y. Geng, Z. Wei, L. Wang, and C.-Y. Guo, "Novel, recyclable supramolecular metal complexes for the synthesis of cyclic carbonates from epoxides and CO_2 under solvent-free conditions," *Journal of CO2 Utilization,* vol. 17, pp. 243-255, 2017/01/01/ 2017, doi: https://doi.org/10.1016/j.jcou.2016.10.013.

[46] J. W. Comerford, I. D. Ingram, M. North, and X. Wu, "Sustainable metal-based catalysts for the synthesis of cyclic carbonates containing five-membered rings," *Green Chemistry,* vol. 17, no. 4, pp. 1966-1987, 2015.

[47]   S. Gavrielides, J. Z. Y. Tan, E. Sanchez Fernandez, and M. Maroto-Valer, "Photo–generation of Cyclic Carbonates Using Hyper–branched Ru–TiO_2," *Faraday Discussions,* 10.1039/C8FD00181B 2019, doi: 10.1039/C8FD00181B.

[48]   A. Zanon, S. Chaemchuen, B. Mousavi, and F. Verpoort, "1 Zn-doped ZIF-67 as catalyst for the CO2 fixation into cyclic carbonates," *Journal of CO_2 Utilization,* vol. 20, pp. 282-291, 2017.

[49]   A. Buonerba *et al.*, "Novel iron(iii) catalyst for the efficient and selective coupling of carbon dioxide and epoxides to form cyclic carbonates," *Catalysis Science & Technology,* 10.1039/C4CY01187B vol. 5, no. 1, pp. 118-123, 2015, doi: 10.1039/C4CY01187B.

[50]   J. Peng, H.-J. Yang, N. Song, and C.-Y. Guo, "An effective Ni/Zn catalyst system for the chemical fixation of carbon dioxide with epoxides," *Journal of CO_2 Utilization,* vol. 9, pp. 16-22, 2015/03/01/ 2015, doi: https://doi.org/10.1016/j.jcou.2014.11.002.

[51]   V. Butera and H. Detz, "Cyclic Carbonate Formation from Epoxides and CO_2 Catalyzed by Sustainable Alkali Halide–Glycol Complexes: A DFT Study to Elucidate Reaction Mechanism and Catalytic Activity," *ACS Omega,* vol. 5, no. 29, pp. 18064-18072, 2020/07/28 2020, doi: 10.1021/acsomega.0c01572.

[52]   R. L. Paddock and S. T. Nguyen, "Chiral (salen)Coiii catalyst for the synthesis of cyclic carbonates," *Chem. Commun.,* 10.1039/B401543F no. 14, pp. 1622-1623, 2004, doi: 10.1039/B401543F.

[53]   P. K. Prajapati, A. Kumar, and S. L. Jain, "First Photocatalytic Synthesis of Cyclic Carbonates from CO_2 and Epoxides Using CoPc/TiO_2 Hybrid under Mild Conditions," *ACS Sustain. Chem. Eng.,* vol. 6, no. 6, pp. 7799-7809, 2018/06/04 2018, doi: 10.1021/acssuschemeng.8b00755.

[54]   G. Zhai *et al.*, "Light-Promoted CO_2 Conversion from Epoxides to Cyclic Carbonates at Ambient Conditions over a Bi-Based Metal–Organic Framework," *ACS Catalysis,* vol. 11, no. 4, pp. 1988-1994, 2021/02/19 2021, doi: 10.1021/acscatal.0c05145.

[55]   V. B. Saptal and B. M. Bhanage, "Current advances in heterogeneous catalysts for the synthesis of cyclic carbonates from carbon dioxide," *Curr. Opin. Green Sustain. Chem.,* vol. 3, pp. 1-10, 2017/02/01/ 2017, doi: https://doi.org/10.1016/j.cogsc.2016.10.006.

[56]   L. Sang, Y. Zhao, and C. Burda, "TiO_2 Nanoparticles as Functional Building Blocks," *Chem. Rev.,* vol. 114, no. 19, pp. 9283-9318, 2014/10/08 2014, doi: 10.1021/cr400629p.

[57]   B. O'regan and M. Grätzel, "A low-cost, high-efficiency solar cell based on dye-sensitized colloidal TiO_2 films," *nature,* vol. 353, no. 6346, pp. 737-740, 1991.

[58]   G. Stelios, J. Z. Y. Tan, and M. M. Maroto-Valer, "Hierarchical hyper-branched titania nanorods with tuneable selectivity for CO_2 photoreduction," *RSC Adv.,* 10.1039/D1RA05414G vol. 11, no. 51, pp. 32022-32029, 2021, doi: 10.1039/D1RA05414G.

Chapter 2

Material design and morphology

The current thesis is concerned with the fabrication of purpose-built photocatalyst material for CO_2 utilisation reactions. There is a plethora of material fabrication and modification techniques available in the literature. This chapter reviews the fabrication and modification techniques that were effectively used for the photocatalysts produced as product of the research presented in this thesis. The aim of this chapter is to provide insight and context for the techniques applied for the fabrication of the hyper-branched nanorods (HBNs) thin films as photocatalyst for CO_2 utilisation reactions.

2.1 Material design

In pursuit of designing highly efficient photocatalyst materials, there is a wide range of material fabrication techniques and modifications that can be applied. These modifications will affect the properties of the materials, and therefore, influence their photocatalytic behaviour. Consequently, it is important to understand the possible effects of each modification approach in order to design advanced materials that are purposely fabricated to perform specific tasks.[1] Fabrication and modification techniques can affect both optical and electronic properties, for example light absorption, band gap narrowing, light harvesting, redox potential and charge transfer, charge separation etc. Some of these fabrication techniques and modifications that are relevant to the current thesis are discussed in the following sections. Initially, the effects of morphological alterations are discussed in section 2.1.1. Photocatalyst immobilisation is discussed next as a method of altering the photocatalytic behaviour of materials in section 2.1.2. In the following photocatalyst modification section the effect of elemental doping (section 2.2.1) and heterojunction formation (section 2.2.2) are analysed. Lastly, a section regarding the synthesis of photocatalyst using hydrothermal and solvothermal treatment is discussed (section 2.3). The discussion in this chapter involves relevant studies drawn from the literature.

2.1.1 Morphology

One of the most impactful properties of a material is its morphology and morphological features, as they can alter the behaviour of a photocatalyst material in numerous ways.

This is partly because morphology encapsulates various properties, such as particle size, shape, architecture, texture and porosity. Advanced material design studies heavily rely on morphological alterations to create highly efficient purpose-built task specific materials.[1, 2] There is a plethora of various morphological architectures available in the literature, from simple spherical nanoparticles (NPs), nanorods[3], to dendritic nanowires[4], and more complex architectures, such as hollow double shell and core-shell materials[5] each exhibiting individualised behaviour. The primary role of a functional photocatalyst semiconductor material is to efficiently harvest light in order to stimulate the production of photoexcited charges for the subsequent photocatalytic reactions.

3D hierarchical nanostructured TiO_2 photocatalysts have been widely reported exhibiting enhanced light absorption through multiple reflections as a result of their morphological features. Particularly 1-3D nanostructures have been reported as more appealing than nanoparticle spheres (also referred to as 0D NPs or quantum dots) as they effectively scatter light, and therefore, enhance the overall light absorption of the photocatalyst.[6] However, while morphology can increase the amount of light absorbed, it is unable to widen the wavelength absorption range of the material. The limited wavelength absorption range is one of the main disadvantages of TiO_2 because it absorbs light only in the UV range due to its wide band gap. To overcome this shortcoming of TiO_2, researchers have implemented other techniques, such as elemental doping (section 2.2.1) to extend the wavelength range of TiO_2 into visible light.

Another important property of an effective photocatalyst is the ability to transfer the photogenerated charge to the surface of the material where any photocatalytic reaction would take place. Therefore, introducing internal electric fields (IEF) can induce charge separation to avoid the recombination of the photoexcited charges and promoting charge mobility become desired attributes for a photocatalytic material. 1D nanostructure building blocks have shown to have enhanced charge mobility, and thus, reducing charge recombination.[7] 3D hierarchical nanostructures are built up using lower dimensional building blocks like spheres, sheets, wires, rods, tubes, etc. The resulting 3D hierarchical structures retain the benefits of their lower dimensional components, whilst they benefit from the advantages of the 3D structure in a synergistic manner.[6] For example, a hyper-branched superstructure that consists of 1D nanorods, retains the improved charge mobility associated with the 1D components yet benefit from the improved light harvesting associated with the superstructure as discussed above. Relevant studies with hierarchical structures are reviewed in the next paragraph.

23

Nguyen-Phan et al. designed a 3D sea-urchin like TiO_2 doped with ruthenium, which was composed of 1D nanorods, to stimulate the visible-light driven H_2 production. The fabricated 3D sea-urchin like TiO_2 exhibited improved light absorption and charge separation while the ruthenium doping allowed the photocatalytic reaction to take place under visible light by introducing defect impurity levels, such as oxygen vacancies. It was found that the optimally doped $Ru-TiO_2$ sea urchin material produced 15 times more H_2 when compared to the undoped TiO_2 under visible light.[6] Wang et al. fabricated microspheres composed of 2D anatase TiO_2 nano-sheets for dye-sensitized solar cells. The material was reported to exhibit enhanced light scattering and enlarged surface area compared to P25. Also, the 2D nanosheet lower-dimension components of the microspheres superstructures exposed the high surface energy facet [001], and it was able to outperform P25 TiO_2 by producing 36% higher current density (11 mA/cm^2 for P25 TiO_2 as opposed to 15 mA/cm^2 for as-prepared 2D nanosheets TiO_2 spheres).[8] Kong et al. achieved a similar morphological structure composed of rutile nanoneedles decorated with TiO_2 nanoparticles (NPs) as the support for a quantum-dot-sensitised solar cells (QDSSCs). The material demonstrated enhanced light harvesting efficiency due to internal light scattering and charge collection as a result of reduced recombination rate and was able produce 20% higher current density.[9] Fang et al. demonstrated that the microspheres composed of 2D nanosheets, due to their large surface area for dye loading in addition to the light scattering properties, provide higher current density and have enhanced incident photon-to-current conversion efficiency for DSSCs.[10]

As mentioned earlier (section 2.1.1), porosity is another important and impactful morphological feature. Porosity typically enhances surface area and shortens the distance the photo-excited charge that is required to reach to the surface of the photocatalyst and therefore inhibits bulk recombination and enhances conversion rates. It should be mentioned at this point that the work presented for CO_2 photoreduction refers to a gaseous system which could benefit from porosity as mentioned above. However, in aqueous systems porosity might cause some hinderance due to bubble trapping which could block the reactants from reaching the photocatalytic sites. Zhang and Yu fabricated hierarchical porous titania (HPT) spheres. Mesoporous frameworks were aggregated to form meso- and macro-porous hierarchical structure and was reported to have 50% higher photocatalytic activity when compared to non-porous P25 in the reaction of photodegrading n-pentane in air.[11] Apart from the enhanced conversion rates due to reduced recombination, porosity has also been used as a trapping site for CO_2 molecules.

Crake et al. fabricated composites of titanate or titania with metal-organic frameworks (MOFs) as photocatalysts for CO_2 photoreduction.[12] The MOFs were grown on both titanate and anatase phase titania nanowires. Anatase phase was found to perform better than the titanate counterpart in CO_2 photoreduction. The porous MOFs were used as CO_2 trapping sites bringing CO_2 molecules close to the surface of the titania nanowires. Particular attention was given to the morphology of the composites, as it was hypothesized that maximum contact of the MOFs to the titania nanowires can impact charge transfer and provide a synergistic effect between the two materials. This study confirmed that morphology had a positive effect on charge separation and that the composites benefited from interfacial charge transfer across the heterojunction.

2.1.2   Thin-film immobilisation

The most common form for heterogeneous photocatalyst is powder form. However, many researchers have fabricated or coated their photocatalyst material on substrates such as thin-films. Common substrates used as supports for thin-film deposition are conductive glasses such as fluorine doped tin oxide (FTO) glass, silicon wafer, alumina beads or porous structures (e.g., alumina substrates).[13-15] Thin films offer a certain set of advantages over their powder counterparts, including the former often offer short diffusion distances of photoexcited charges to the surface and short spatial separation of reducing and oxidising sites compared to the latter one.[14] Additionally, thin films offer high surface to volume ratio due to their 2D layout and can inhibit severe agglomeration. Moreover, for liquid-based reactions, separation from the reaction solution is significantly easier and could potentially offer noteworthy economic benefits for industrial exploitation.[13] Studies with immobilised photocatalysts are reviewed in the following paragraph.

Yasumori et al. fabricated a TiO_2 thin film supported on porous alumina by spin-coating a TiO_2 sol on the alumina substrate.[14] A platinum electrode was sputter-coated on the porous substrate to be used for hydrogen generation from ethanol aqueous solution under UV irradiation. The synthesized thin film demonstrated improved photocatalytic activity when compared to its powder counterpart, platinised fine TiO_2 particles. Its increased photocatalytic activity was attributed to the shortened diffusion distances of the photoexcited charge carriers from the surface and the separation of the redox reaction sites. Lei et al. supported small amounts of titania on a porous alumina substrate and demonstrated similar photocatalytic conversion as Degussa P25 with lower TiO_2 content,

while maintaining the benefit of easy separation from the aqueous solution.[16] The enhanced photocatalytic activity was attributed to the dispersion of the active phase of TiO_2 on the porous alumina substrate which offered a higher surface area compared to powder P25. Wu et al. fabricated arrays of anatase cactus-like branched TiO_2 (CBT), vertically aligned supported on FTO glass.[15] Thin films have demonstrated an impressive power conversion efficiency of 6.43% for DSSCs application. The CBTs are composed of nanowires and nanosheets and their impressive performance was attributed to the increased light scattering and harvesting ability attributed to their hierarchical morphology and increased surface area of the synthesised thin films. Thin films offer their own set of unique advantages and provide alternative options for presenting a photocatalyst material to the reaction.

2.2   Photocatalyst modification

2.2.1   Elemental doping

As mentioned previously (section 2.1.1), the greatest disadvantage of TiO_2 as a photocatalytic material is its limited visible light wavelengths absorption, as it absorbs mostly in the UV light range which accounts for roughly 5% of solar irradiation. Morphological alterations can increase the amount of light harvested, but it does not extend the absorption range of a material into the visible range. To overcome this drawback, doping TiO_2 with foreign atoms can induce band gap modifications to the semiconductor that would allow for light absorption in longer wavelengths compared to UV (>400 nm). Additionally, doping allows for manipulation of the optical and electrical properties of the semiconductor. More specifically, doping can modify valence and conduction band and promote photoexcited charge carriers excitation and separation.[17] For this reason, doping is one of the most widely applied modification on TiO_2 for CO_2 photoreduction.[18]

The insertion of foreign atoms can either occur within the crystal lattice, commonly referred to as interstitial doping, or by substitution of a metal atom from the semiconductor crystal lattice, referred to as substitutional doping (Figure 2.1).[19] The intrinsic properties of the foreign atom will determine the dominant charge carrier within the doped semiconductor, resulting as positive (p-type) or negative (n-type) semiconductor. A p-type semiconductor can be seen as having mobile holes in its valence band, which tend to stack towards the edge of the valence band over time. An n-type

semiconductor material has an abundance of electrons in its conduction band that tend to accumulate at the edge of the conduction band. This phenomenon is due to vibrational relaxation as explained in section 1.4.3 (see Figure 1.4). The incorporation of dopants, either substitutional or interstitial, in the titania lattice, is able to modify the band gap by creating electron trap energy levels. Before any modification, the energy required for an electron to be excited into the conduction band follows Eq.(2.1). After doping, shallow energy levels could be introduced that can function as traps and hinder the recombination rate, consequently increasing the photocatalytic activity of the semiconductor. These trap energy levels could be stacked below the conduction band or above the valence band. After the introduction of shallow energy levels the energy requirement for an electron to be excited follows Eq.(2.2). However, dopants could also act as recombination centres which would considerably reduce the photocatalytic activity.[19] This generally occurs when deep energy levels are created within the band gap where there is an approximately equal probability for electrons and holes to reach the deep energy level. The recombination probability is higher in the bulk of the crystal lattice. This explains why 2D or 1D structures show great potential for advanced photocatalyst materials.

$$E_g \leq hv \tag{2.1}$$

$$(E_g - E_t) \leq hv \tag{2.2}$$

$E_t : Edge\ of\ the\ electron\ trap\ band\ (J)$

$E_g : band\ gap\ energy\ (J)$

$h : Plank`s\ constant\ (J \cdot s)$
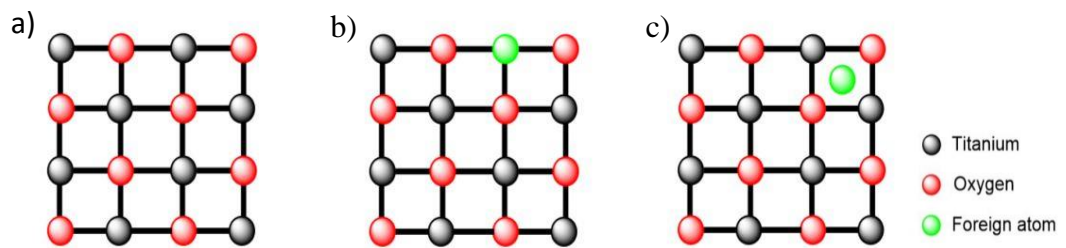
$v : frequency\ (Hz)$

Figure 2.1 – Graphical representation of various types of crystal lattice of a) un-doped, b) substitutional, and c) Interstitial doped TiO_2.[19]

Elemental doping can be implemented using metal or non-metal elements. Hou et al. demonstrated the synthesis of anatase TiO_2 nanotube arrays (TNAs) with nanotube/nanoworms by submerging amorphous TNAs in hot ammonia solution for 8 h.[20] Additionally, the resulted material was doped with N atoms that produced an isolated localised state of N 2p band at 0.75 eV above the valence band. It was also reported that the N doping introduced oxygen vacancies (Ti^{3+} sites) on the surface of the crystal lattice that formed localised donor states located at 0.75 – 1.18 eV below the conduction band. The resulting N doped TNAs hierarchical anatase structures benefited from large surface area, higher electrical conductivity and the reduced band gap increased their visible light absorption leading to significantly improved photocatalytic performance. Other researchers have reported similar findings with N-doped titania.[21, 22] Indium (In) doped 0D nanoparticles were synthesized using a facile controlled sol-gel method by Tahir and Amin.[23] It was reported that the presence of In inhibited the growth of crystal growth and produced anatase phase mesoporous nanoparticles. After Brunauer-Emmett-Teller (BET) characterisation it was found that In doping increased the surface area, and the band gap was enlarged with increasing In loading under UV-vis analysis. At 20% of In loading, the band gap was shifted from 3.1 (without In loading) to 3.7 eV, which allows for a UV active semiconductor with reduced recombination rate of the photoexcited charges. Under CO_2 photoreduction, the In-doped TiO_2 0D nanostructures at their optimum loading (10%) produced 7.9 times more CH_4 than bare TiO_2 and has shown a remarkable increase in photocatalytic activity under UV light irradiation. The increased activity was attributed to the interfacial charge transfer which caused effective charge separation. Sood et al. synthesized Fe-doped TiO_2 nanoparticles for the photodegradation of the toxic pollutant paranitrophenol.[24] It was determined that the Fe (III) ions substituted Ti^{4+} ions into the crystal lattice. Fe^{3+} ions possessed a similar ionic radius to Ti^{4+} ions (0.69 to 0.745Å). Maximum surface area was found on the sample with 0.05 mol% of Fe. The recombination rate was reduced when the sample was doped up to 0.075 mol% of Fe, while samples with higher loading, such as 0.1 mol% Fe, showed increased recombination which suggested that Fe ions acted as recombination sites. The best performing sample (0.05 mol % Fe ions) achieved a 92% degradation of the target pollutant in 5 h under visible light irradiation (400 to 520 nm), which was much more efficient compared to the undoped TiO_2 (*i.e.*, 42% degradation in 5 h).

2.2.2 Heterojunction formation

Forming heterojunctions is a widely employed modification technique as it can offer significant advantages to the synthesized material. Heterojunctions could effectively improve charge carrier separation, as well as widen the absorption range of the material. The most common approaches to induce heterojunction formation are semiconductor coupling, and noble metal incorporation. When a suitable semiconductor material is chosen, according to the desired effect (band positioning), heterojunctions can be greatly beneficial to the photocatalytic behaviour of TiO_2, which suffers from limited light absorption range and fast recombination rate. In a coupled semiconductor material both semiconductors could be excited by irradiation, producing electron-hole pairs. The movement of those charges strongly depends on the relative positioning of the valence band (VB) and conduction band (CB) of the two semiconductor materials.[19] For example, when the CB and VB of semiconductor A is lower than the CB and VB of semiconductor B respectively, then the photoexcited electrons will flow towards the CB of semiconductor A while the holes will flow towards the VB of semiconductor B. This essentially creates a highly effective charge separation mechanism, in which there is high concentration of electrons in semiconductor A and high concentration of holes in semiconductor B as shown in Figure 2.2a. If the CB and VB of the coupled semiconductors are positioned as shown in Figure 2.2b, both photoexcited charges, electrons and holes, are accumulated on semiconductor A.[18]

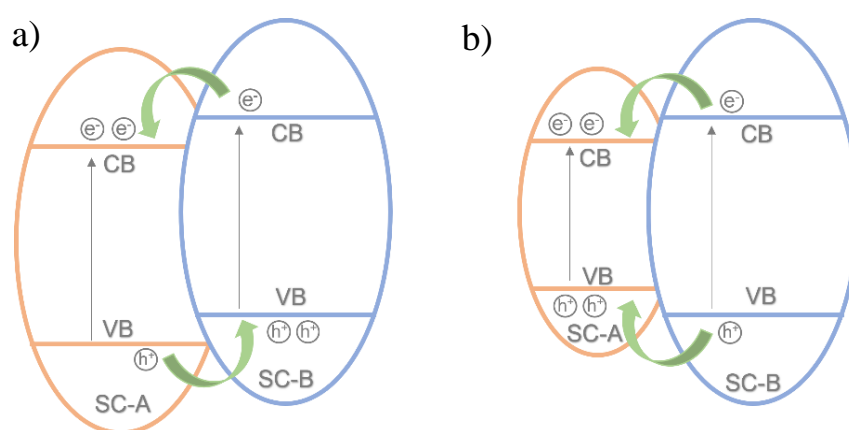Figure 2.2 – Schematic diagram of the two main types of semiconductor coupling.[19]

Yuan et al. fabricated a multi-laminated ZnO/TiO_2 heterojunction thin film on conductive substrates using a layer-by-layer (LBL) self-assembly method.[25] This synthesis technique allowed for improved surface contact between the p-type ZnO and n-type TiO_2 that was used as the working electrode in a 3-electrode photoelectrochemical

cell (PEC). The photocurrent density measured during a light on-light off experiment has shown that the ZnO/TiO_2 thin film has managed to produce 5 times more current density when compared to an LBL thin film of TiO_2 with similar thickness. The remarkably improved photoactivity was attributed to the improved separation efficiency of the well-connected heterojunction. The ZnO/TiO_2 heterojunction has been reported by other researchers.[26-28] Guo and Yin fabricated $SrTiO_3/TiO_2$ heterostructures nanosheets using a facile hydrothermal approach to be used in DSSCs. The synthesized heterostructures have been reported to provide high surface area and porosity which improved dye loading. The beneficial positioning of the CB and VB of the materials allow for efficient charge separation, as was confirmed by photoluminescence (PL) and incident photon-to-electron conversion efficiency (IPCE) measurements. The material exhibited reduced recombination rate and longer electron lifetime compared to each individual photocatalyst. Five variations of Sr/Ti molar ratio were synthesized and the optimal ratio was found to be Sr/Ti: 2/4 producing 12.55 mA/cm^{-2} as opposed to 9.17 mA/cm^{-2} for TiO_2. Higher concentrations of Sr resulted in reduced surface area, and therefore, significantly reduced current density. Other researchers reported $SrTiO_3/TiO_2$ heterojunctions with similar observations concerning reduced recombination and effective charge separation.[29-31]

The addition of non-chemically bonded noble metals to semiconductors has also been widely applied in the field of photocatalysis as an effective semiconductor modification technique. The incorporation of metal NPs on TiO_2 surface can act as electron traps, effectively separating electron-hole pairs, increasing the life span of photoexcited charges leading to potentially higher photocatalytic conversion (Figure 3a). When the metal and semiconductor come in contact, the fermi levels will reach equilibrium by the diffusion of electrons from the semiconductor to the metal.[32] This diffusion current creates an upward band bend of the semiconductor which essentially creates a potential barrier known as Schottky barrier (Figure 2.3a). The Schottky barrier acts as an electron trap preventing the electrons from the metal to transfer back into the semiconductor.[18, 19] However, high concentration of metallic islands on the semiconductor surface, or increased particle size can yield negative impact to the photo-reactivity as a result of reduced illumination of the semiconductor surface, also known as shading effects.[19, 33] Noble metal deposition has also been reported to increase visible light activation through the surface plasmon resonance (SPR) effect (Figure 2.3b). Essentially, collective oscillations of energised electrons are able to transfer to the

conduction band of the semiconductor by visible light activation. Krejcikova et al. prepared Ag enriched TiO_2 with various loading concentrations using a sol-gel approach. The material was tested for CO_2 photoreduction and increased yield of methane was observed with higher loading of Ag under 254 nm irradiation. The synthesized materials were compared with commercial Degussa P25 and synthesized TiO_2 without the addition of Ag. The highest performance of methane yield was observed in the sample with the highest Ag loading (*i.e.*, 5.2 wt%), under 254 nm irradiation. The increased performance was assigned to the Schottky barrier formed at the metal-semiconductor interface, creating a charge separation effect (electron trap) and increasing photocatalytic activity of TiO_2.[34] Fang et al. synthesized mesoporous plasmonic Au-TiO_2 nanocomposites via co-polymer assisted sol-gel method.[35] The nanocomposites were characterized and Au nanoparticles of the range of 10-14 nm were found embedded in the mesoporous TiO_2 matrix. Remarkable visible light activity was observed for H_2 evolution from photocatalytic water reduction using ascorbic acid as the electron donor. The improved performance was attributed to three main reasons. The weak visible light absorption due to defect and impurity states induced by the co-polymer synthesis. The plasmon-excitation of Au nanoparticles which enhances the weak visible light absorptions through strong localised electric field. Lastly, to sufficiently high energy plasmon-excited electrons that could transfer to the conduction band of TiO_2 and reduce H_2. Liu et al. deposited plasmonic Ag nanoparticles on TiO_2 nano-wire films (NWFs) using a hydrothermal route and microwave assisted chemical reduction route.[36] The material was used for CO_2 photoreduction in aqueous phase. The Ag nanoparticles were well
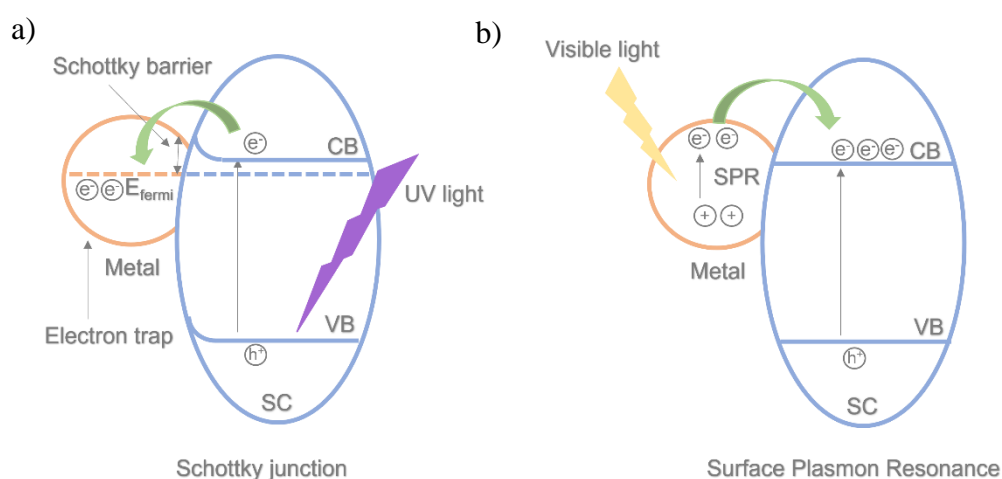

Figure 2.3 - Schematic representation of a) Schottky junction working as an electron trap, b) Surface Plasmon Resonance induced by visible light absorption.[19]

dispersed on the mixed phase anatase/rutile NWFs and under UV-Vis examination it was found that Ag loading significantly improved the light absorption of the NWFs at the 413 nm wavelength, due to SPR absorption of Ag nanoparticles. The methanol yield was increased with higher concentration of Ag loading up to 0.6 mM concentration while further increase to 0.7mM produced the similar methanol yield (8.3 μmol.cm^{-2}). The Ag/TiO$_2$ nanocomposites produced 10 times more methanol than pure TiO$_2$ NWFs and the improved performance was attributed to enhanced charge transfer and visible light harvesting of the plasmonic Ag nanoparticles.

2.3 Synthesis of photocatalysts

2.3.1 *Hydrothermal and solvothermal methods*

Hydrothermal and solvothermal methods are used to synthetise materials in a sealed and heated aqueous (hydrothermal) solution or organic solvent solution (solvothermal) at temperatures ranging from 100 – 1000 °C and pressures from 1 – 100 MPa. Typically, these methods require a strong and sealed container that can withstand high pressures like an autoclave vessel (Figure 2.4). The main difference of hydrothermal and solvothermal methods compared to other solid state material preparation methods (*e.g.*, sintering process) lies in the reactivity of the reactants, since the method promotes their reaction in solution under high temperature and pressure; whereas solid state methods rely on diffusion of raw materials at the interface.[37] In most cases of material synthesis, hydrothermal or solvothermal approaches do not exceed 200 °C, especially when volatile solvents are being used, which offers an alternative milder synthetic method to solid state reactions which typically require higher temperatures.

Generally, hydrothermal and solvothermal methods are very effective and widely used to synthesise nanostructured materials. It can be used to efficiently and relatively easy fabricate a wide variety of morphologies such as nanoparticles, nanospheres, -wires, -rods, -tubes, -sheets and so on. However, it is not only used for the fabrication of simple nanomaterials, but more complex morphological nanocomposites with great control over their shape and size.[38] Additionally, hydrothermal and solvothermal method can process almost all advanced materials, metals, oxides, silicates, sulfides, titanates, carbon, zeolites, ceramics, thin-films, membranes and more. It is therefore apparent why it has been an effective tool for advanced material synthesis.[38]

In short, the main advantages of hydrothermal and solvothermal methods are that the applied heat and pressure of the system can induce solubility of most materials. Moreover, solvothermal method significantly enhances the chemical activity of the reactants. Hydrothermal and solvothermal methods also allows for material synthesis not possible with solid state synthesis techniques, such as intermediate state or metastable phases, allowing exploration of novel materials not easily achieved otherwise.[37] Last but not least, it is the simplified yet precise control over size and shape as well as homogeneity and crystallinity of the resulting material. Easily adjusted external parameters, such as temperature and reaction time as well as internal parameters, such as solvents, precursors, polarity, density, structure-directing agents, templating etc.[37]

However, hydrothermal and solvothermal methods have certain disadvantages. The main disadvantage from a material synthesis standpoint would be the fact that hydrothermal and solvothermal methods are essentially a black box process, which means it is impossible to observe the reaction process while its happening.[38] Some practical considerations are also important, such as the need for specialised equipment, like autoclaves. Additionally, safety considerations are very important, as high pressures are developed during the synthesis and the autoclaves are typically heavy thick-walled stainless-steel containers, and therefore, careful consideration and risk assessment are paramount.
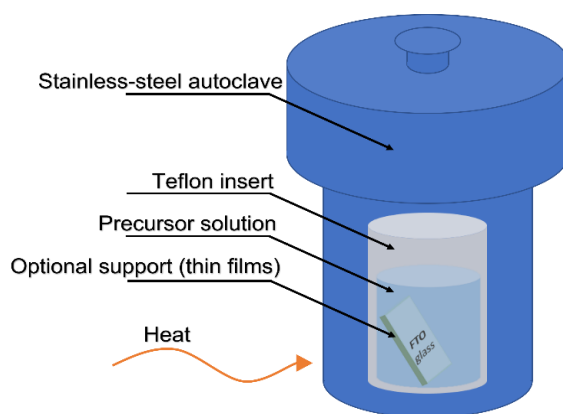
Figure 2.4 - Schematic representation of an autoclave vessel and its components

2.4   Conclusion

In summary, this chapter discussed material design techniques for purpose-build photocatalysts. Emphasis was given to morphology, photocatalyst immobilisation and photocatalyst modification techniques, specifically elemental doping and heterojunction formation. Lastly, the hydrothermal and solvothermal fabrication method was reviewed.

The topics discussed in this chapter are applied to the photocatalysts presented in the following experimental chapters (Chapter 4,5,6). Each chapter is concerned with one published article produced in the current Ph.D project.

References

[1]   L. Sang, Y. Zhao, and C. Burda, "TiO$_2$ Nanoparticles as Functional Building
        Blocks," *Chem. Rev.,* vol. 114, no. 19, pp. 9283-9318, 2014/10/08 2014, doi:
        10.1021/cr400629p.

[2]   T. R. Gordon *et al.*, "Nonaqueous Synthesis of TiO$_2$ Nanocrystals Using TiF$_4$ to
        Engineer Morphology, Oxygen Vacancy Concentration, and Photocatalytic
        Activity," *J. Am. Chem. Soc.,* vol. 134, no. 15, pp. 6751-6761, 2012/04/18 2012,
        doi: 10.1021/ja300823a.

[3]   J. Z. Y. Tan, Y. Fernández, D. Liu, M. Maroto-Valer, J. Bian, and X. Zhang,
        "Photoreduction of CO$_2$ using copper-decorated TiO2 nanorod films with
        localized surface plasmon behavior," *Chem. Phys. Lett.,* vol. 531, pp. 149-154,
        2012/04/02/ 2012, doi: https://doi.org/10.1016/j.cplett.2012.02.016.

[4]   J. Z. Yie Tan, J. Zeng, D. Kong, J. Bian, and X. Zhang, "Growth of crystallized
        titania from the cores of amorphous tetrabutyl titanate@PVDF nanowires," *J.
        Mater. Chem.,* vol. 22, no. 35, pp. 18603-18608, 2012 2012, doi:
        10.1039/C2JM33691J.

[5]   J. Z. Y. Tan *et al.*, "Synthesis of TiO$_2$−x/W$_{18}$O$_{49}$ hollow double-shell and core–
        shell microspheres for CO$_2$ photoreduction under visible light," *Chem.
        Commun.,* 10.1039/D0CC04036C vol. 56, no. 81, pp. 12150-12153, 2020, doi:
        10.1039/D0CC04036C.

[6]   T.-D. Nguyen-Phan *et al.*, "Three-dimensional ruthenium-doped TiO$_2$ sea
        urchins for enhanced visible-light-responsive H2 production," *Phys. Chem.
        Chem. Phys.,* 10.1039/C6CP00472E vol. 18, no. 23, pp. 15972-15979, 2016,
        doi: 10.1039/C6CP00472E.

[7]   Y. Ma, X. Wang, Y. Jia, X. Chen, H. Han, and C. Li, "Titanium Dioxide-Based
        Nanomaterials for Photocatalytic Fuel Generations," *Chem. Rev.,* vol. 114, no.
        19, pp. 9987-10043, 2014/10/08 2014, doi: 10.1021/cr500008u.

[8]   Y. Wang, W. Yang, and W. Shi, "Preparation and Characterization of Anatase
        TiO2 Nanosheets-Based Microspheres for Dye-Sensitized Solar Cells," *Ind.
        Eng. Chem. Res.,* vol. 50, no. 21, pp. 11982-11987, 2011/11/02 2011, doi:
        10.1021/ie2016202.

[9]   E.-H. Kong, Y.-J. Chang, Y.-C. Park, Y.-H. Yoon, H.-J. Park, and H. M. Jang,
        "Sea urchin TiO$_2$–nanoparticle hybrid composite photoelectrodes for
        CdS/CdSe/ZnS quantum-dot-sensitized solar cells," *Phys. Chem. Chem. Phys.,*
        10.1039/C2CP24106D vol. 14, no. 13, pp. 4620-4625, 2012, doi:
        10.1039/C2CP24106D.

[10]   F. Xu, X. Zhang, Y. Wu, D. Wu, Z. Gao, and K. Jiang, "Facile synthesis of TiO$_2$
        hierarchical microspheres assembled by ultrathin nanosheets for dye-sensitized
        solar cells," *J. Alloys Compd.,* vol. 574, pp. 227-232, 2013/10/15/ 2013, doi:
        https://doi.org/10.1016/j.jallcom.2013.04.119.

[11]   L. Zhang and J. C. Yu, "A sonochemical approach to hierarchical porous titania
        spheres with enhanced photocatalytic activity," *Chem. Commun.,*
        10.1039/B306013F no. 16, pp. 2078-2079, 2003, doi: 10.1039/B306013F.

[12]   A. Crake, K. C. Christoforidis, A. Gregg, B. Moss, A. Kafizas, and C. Petit,
        "The Effect of Materials Architecture in TiO$_2$/MOF Composites on CO$_2$
        Photoreduction and Charge Transfer," *Small,* vol. 15, no. 11, p. 1805473, 2019,
        doi: https://doi.org/10.1002/smll.201805473.

[13]   S.-H. Lee *et al.*, "Synthesis of TiO2 photocatalyst thin film by solvothermal
        method with a small amount of water and its photocatalytic performance,"

Journal of Photochemistry and Photobiology A: Chemistry, vol. 146, no. 1, pp. 121-128, 2001/12/13/ 2001, doi: https://doi.org/10.1016/S1010-6030(01)00553-6.

[14]   A. Yasumori, K. Ishizu, S. Hayashi, and K. Okada, "Preparation of a TiO_2 based multiple layer thin film photocatalyst," *J. Mater. Chem.,* 10.1039/A803265C vol. 8, no. 11, pp. 2521-2524, 1998, doi: 10.1039/A803265C.

[15]   W.-Q. Wu, H.-S. Rao, H.-L. Feng, X.-D. Guo, C.-Y. Su, and D.-B. Kuang, "Morphology-controlled cactus-like branched anatase TiO_2 arrays with high light-harvesting efficiency for dye-sensitized solar cells," *J. Power Sources,* vol. 260, pp. 6-11, 2014/08/15/ 2014, doi: https://doi.org/10.1016/j.jpowsour.2014.02.107.

[16]   L. Lei, H. P. Chu, X. Hu, and P.-L. Yue, "Preparation of Heterogeneous Photocatalyst (TiO_2/Alumina) by Metallo-Organic Chemical Vapor Deposition," *Industrial & Engineering Chemistry Research,* vol. 38, no. 9, pp. 3381-3385, 1999/09/01 1999, doi: 10.1021/ie980677j.

[17]   M. A. Ávila-López *et al.*, "Comparative study of CO_2 photoreduction using different conformations of CuO photocatalyst: Powder, coating on mesh and thin film," *Journal of CO2 Utilization,* vol. 50, p. 101588, 2021/08/01/ 2021, doi: https://doi.org/10.1016/j.jcou.2021.101588.

[18]   M. Humayun, F. Raziq, A. Khan, and W. Luo, "Modification strategies of TiO_2 for potential applications in photocatalysis: a critical review," *Green Chemistry Letters and Reviews,* vol. 11, no. 2, pp. 86-102, 2018/04/03 2018, doi: 10.1080/17518253.2018.1440324.

[19]   O. Ola and M. M. Maroto-Valer, "Review of material design and reactor engineering on TiO2 photocatalysis for CO_2 reduction," *Journal of Photochemistry and Photobiology C: Photochemistry Reviews,* vol. 24, no. Supplement C, pp. 16-42, 2015/09/01/ 2015, doi: 10.1016/j.jphotochemrev.2015.06.001.

[20]   X. Hou *et al.*, "Preparation of nitrogen-doped anatase TiO_2 nanoworm/nanotube hierarchical structures and its photocatalytic effect," *Solid State Sciences,* vol. 29, pp. 27-33, 2014/03/01/ 2014, doi: https://doi.org/10.1016/j.solidstatesciences.2014.01.007.

[21]   C. Burda, Y. Lou, X. Chen, A. C. S. Samia, J. Stout, and J. L. Gole, "Enhanced Nitrogen Doping in TiO2 Nanoparticles," *Nano Lett.,* vol. 3, no. 8, pp. 1049-1051, 2003/08/01 2003, doi: 10.1021/nl034332o.

[22]   C.-J. Li and G.-R. Xu, "Influence of ammonia on the morphologies and enhanced photocatalytic activity of TiO_2 micro/nanospheres," *Appl. Surf. Sci.,* vol. 257, no. 11, pp. 4951-4955, 2011/03/15/ 2011, doi: https://doi.org/10.1016/j.apsusc.2011.01.002.

[23]   B. Tahir, M. Tahir, and N. S. Amin, "Gold–indium modified TiO_2 nanocatalysts for photocatalytic CO_2 reduction with H_2 as reductant in a monolith photoreactor," *Appl. Surf. Sci.,* vol. 338, pp. 1-14, 2015/05/30/ 2015, doi: 10.1016/j.apsusc.2015.02.126.

[24]   S. Sood, A. Umar, S. K. Mehta, and S. K. Kansal, "Highly effective Fe-doped TiO2 nanoparticles photocatalysts for visible-light driven photocatalytic degradation of toxic organic compounds," *J. Colloid Interface Sci.,* vol. 450, pp. 213-223, 2015/07/15/ 2015, doi: https://doi.org/10.1016/j.jcis.2015.03.018.

[25]   S. Yuan, J. Mu, R. Mao, Y. Li, Q. Zhang, and H. Wang, "All-Nanoparticle Self-assembly ZnO/TiO₂ Heterojunction Thin Films with Remarkably Enhanced Photoelectrochemical Activity," *ACS Applied Materials & Interfaces,* vol. 6, no. 8, pp. 5719-5725, 2014/04/23 2014, doi: 10.1021/am500314n.

[26]   K. Pan et al., "Facile Fabrication of Hierarchical TiO_2 Nanobelt/ZnO Nanorod Heterogeneous Nanostructure: An Efficient Photoanode for Water Splitting," *ACS Applied Materials & Interfaces,* vol. 5, no. 17, pp. 8314-8320, 2013/09/11 2013, doi: 10.1021/am402154k.

[27]   F.-X. Xiao, "Construction of Highly Ordered $ZnO–TiO_2$ Nanotube Arrays (ZnO/TNTs) Heterostructure for Photocatalytic Application," *ACS Applied Materials & Interfaces,* vol. 4, no. 12, pp. 7055-7063, 2012/12/26 2012, doi: 10.1021/am302462d.

[28]   R. Zha, R. Nadimicherla, and X. Guo, "Ultraviolet photocatalytic degradation of methyl orange by nanostructured TiO_2/ZnO heterojunctions," *Journal of Materials Chemistry A,* 10.1039/C5TA00764J vol. 3, no. 12, pp. 6565-6574, 2015, doi: 10.1039/C5TA00764J.

[29]   F. Zhu, C. Li, M. N. Ha, Z. Liu, Q. Guo, and Z. Zhao, "Molten-salt synthesis of $Cu–SrTiO_3/TiO_2$ nanotube heterostructures for photocatalytic water splitting," *Journal of Materials Science,* vol. 51, no. 9, pp. 4639-4649, 2016/05/01 2016, doi: 10.1007/s10853-016-9779-9.

[30]   J. Zhang, J. H. Bang, C. Tang, and P. V. Kamat, "Tailored $TiO_2−SrTiO_3$ Heterostructure Nanotube Arrays for Improved Photoelectrochemical Performance," *ACS Nano,* vol. 4, no. 1, pp. 387-395, 2010/01/26 2010, doi: 10.1021/nn901087c.

[31]   T. Yu, W.-l. Hu, L. Jia, X. Tan, J. Huang, and X. Huang, "Enhanced Photoelectrochemical Performance of Coaxial-Nanocoupled Strontium-Rich $SrTiO_3/TiO_2$ {001} Nanotube Arrays," *Industrial & Engineering Chemistry Research,* vol. 54, no. 33, pp. 8193-8200, 2015/08/26 2015, doi: 10.1021/acs.iecr.5b01903.

[32]   A. L. Linsebigler, G. Lu, and J. T. Yates, "Photocatalysis on TiO_2 Surfaces: Principles, Mechanisms, and Selected Results," *Chem. Rev.,* vol. 95, no. 3, pp. 735-758, 1995/05/01 1995, doi: 10.1021/cr00035a013.

[33]   M. Schiavello, *Heterogeneous photocatalysis*. Wiley, 1997.

[34]   S. Krejčíková et al., "Preparation and characterization of Ag-doped crystalline titania for photocatalysis applications," *Applied Catalysis B: Environmental,* vol. 111-112, pp. 119-125, 2012/01/12/ 2012, doi: https://doi.org/10.1016/j.apcatb.2011.09.024.

[35]   J. Fang et al., "Mesoporous plasmonic $Au–TiO_2$ nanocomposites for efficient visible-light-driven photocatalytic water reduction," *Int. J. Hydrogen Energy,* vol. 37, no. 23, pp. 17853-17861, 2012/12/01/ 2012, doi: https://doi.org/10.1016/j.ijhydene.2012.09.023.

[36]   E. Liu et al., "Photoconversion of CO_2 to methanol over plasmonic Ag/TiO_2 nano-wire films enhanced by overlapped visible-light-harvesting nanostructures," *Ceram. Int.,* vol. 41, no. 1, Part B, pp. 1049-1057, 2015/01/01/ 2015, doi: https://doi.org/10.1016/j.ceramint.2014.09.027.

[37]   S. H. Feng and G. H. Li, "Chapter 4 - Hydrothermal and Solvothermal Syntheses," in *Modern Inorganic Synthetic Chemistry (Second Edition)*, R. Xu and Y. Xu Eds. Amsterdam: Elsevier, 2017, pp. 73-104.

[38]   N. Asim, S. Ahmadi, M. A. Alghoul, F. Y. Hammadi, K. Saeedfar, and K. Sopian, "Research and Development Aspects on Chemical Preparation Techniques of Photoanodes for Dye Sensitized Solar Cells," *International Journal of Photoenergy,* vol. 2014, p. 518156, 2014/01/12 2014, doi: 10.1155/2014/518156.

Chapter 3

Methods and analytical techniques

3.1   Introduction

In the present chapter, the experimental work and screening process that was conducted to develop the 1-3D hierarchical titania HBN thin films is presented. The resulting material of this work served as the base titania HBNs with no further modifications unless otherwise specified (sections 3.1 - 3.2). It was used as a photocatalyst in the following chapters of this thesis. After the experimental work that was conducted to develop the HBNs synthesis protocol, a review of the analytical techniques that were used to characterise the HBNs as part of the work presented in the following chapters are discussed (sections 3.3 - 3.12).

3.2   Recipe development and screening process

3.2.1   Materials & preliminary work

Fluorine-doped tin oxide (FTO) glass TEC-15 was purchased from Ossila (dimensions 2.5 cm x 2.5 cm, roughness of 12.5 nm, FTO layer thickness of 200 nm, 83.5% transmission and resistivity of 12-14 $\Omega.cm^{-1}$). FTO glass TEC-8 was also purchased from Ossila (dimensions 2.5 cm x 2.5 cm, roughness of 34.8 nm, FTO layer thickness of 600 nm, 76.4% transmission and resistivity of 6-9 $\Omega.cm^{-1}$). Potassium titanium oxide oxalate dihydrate (PTO, ≥98.0%), diethylene glycol (DEG, 99.0%). Isopropanol (IPA, 99.5%), acetone (>95.0%) and ethanol (99.0%) were procured from Fisher Scientific. All chemicals were used without any further purification. All aqueous solutions were prepared using Milli-Q ultrapure type 1 water (18.2 M$\Omega.cm$) collected from a Millipore system.

The FTO glass was cleaned prior to use with a solution of H_2O, IPA, and Acetone in a ratio of 1:1:1, for 1 h in the sonicator and air dried at 75 °C for 30 mins.

Synthesis of 1:7 TiO₂ thin film recipe

The TiO_2 thin-film was fabricated using the hydrothermal approach. Certain molar concentration of PTO *(0.05M, 0.03M, 0.01M)* was dissolved in a mixture of H_2O and DEG with a ratio of 1 : 7 respectively. After 1h of vigorous stirring the mixture is transferred into the 100ml Teflon-lined autoclave along with a piece of FTO glass resting against the Teflon-liner`s walls with the conductive face down. The autoclave is then tightened and transferred into the oven at 180 °C for 9 h. After completing the reaction time, the autoclave was allowed to cool down to room temperature. The TiO_2 thin film was rinsed several times with Milli-Q Type 1 water and ethanol, and then calcined at atmospheric conditions at 550 °C for 1 h.

Synthesis of 1:1.5:1.5 TiO₂ thin film recipe

The TiO_2 thin-film was fabricated using the hydrothermal approach. Certain molar percentage of PTO *(0.05M, 0.03M, 0.01M)* was dissolved in H_2O, IPA and DEG in a ratio of 1 : 1,5 : 1,5 respectively. After 1h of vigorous stirring the mixture is transferred into the 100ml Teflon-lined autoclave along with a piece of FTO glass resting against the Teflon-liner`s walls with the conductive face down. The autoclave is then tightened and transferred into the oven at 180 °C for 9 h. After completing the reaction time, the autoclave was allowed to cool down to room temperature. The TiO_2 thin film was rinsed several times with Milli-Q Type 1 water and ethanol, and then calcined at atmospheric conditions at 550 °C for 1 h.

Synthesis of finalised hyper-branched nanorods (HBNs) TiO₂ thin-film recipe

HBNs were fabricated using a hydrothermal approach. PTO was dissolved in a mixture of H_2O and DEG with a ratio of 1:7. The concentration of PTO was 0.05 M. After 30 minutes of vigorous stirring, the precursor solution was transferred to a 100 mL Teflon-lined autoclave along with the FTO glass. The FTO glass was positioned resting against the Teflon-liner walls with the conductive side facing down at approximately 60°. The hydrothermal synthesis was carried out at 180 °C for 9 h. After completing the reaction time, the autoclave was allowed to cool down to room temperature. The TiO_2 nanorods were rinsed several times with milli-Q

Type 1 water and ethanol, and then calcined at atmospheric conditions at 550 °C for 1 h.

3.2.2 *Screening process for the development of hyper-branched TiO₂ nanorods*

Initially, two recipes were investigated in parallel (referred to as 1 : 7 and 1 : 1.5 : 1.5). For each recipe, three different molar concentrations of titania precursor (PTO) were synthesized in an attempt to identify the required molar concentration for the desired morphology. The three different molar concentrations used are 0.05 M, 0.03 M and 0.01 M. Additionally, the initial experiments were conducted on stock-FTO glass, which was available in the laboratory, created by a previous PhD student. However, since this was a limited source and limited information regarding specifications were available, FTO glass was outsourced. TEC-8 FTO glass was ordered from Ossila, of the highest available conductivity (resistivity 6-9 $\Omega.cm^{-1}$), with an FTO thickness of 600nm, roughness of 34.8nm and 76.4% transmission. The best performing recipe samples were reproduced using TEC-8 FTO glass and compared to the stock FTO samples, however the results were significantly altered. This sparked an investigation for the FTO specifications, mainly resistivity and roughness of the FTO glass. Therefore, more FTO glasses were ordered from Ossila, TEC-15, of the lowest roughness, 12.5 nm, FTO thickness of 200nm, 83.5% transmission and resistivity of 12-14 $\Omega.cm^{-1}$ therefore, significantly reduced conductivity compared to the TEC-8 FTO glass.

The samples produced are code-named using the FTO-type glass used, followed by recipe name and molar concentration of precursor solution.

Using the stock FTO glass, the 1 : 7 precursor formula was investigated in producing TiO₂ thin layer FTO nanostructures with varied concentrations of PTO precursor at 0.01 M, 0.03 M and 0.05 M. At the lowest concentration of 0.01 M, under SEM investigation there were no nanorods formed. Instead, the nucleation sites were visible forming a seeding layer on the surface of the FTO glass Figure 3.1d. The band gap was measured with Kubelka Munk function to be 3.7 eV. The band gap measurements depend on the FTO surface (FTO coating band gap 3.7 eV) and the grown thin-film. At 0.03 M concentration, there were nanowire hyper-branched structures forming, visible under SEM. Interestingly nucleation sites were also spotted on the grown nanowires leading in the formation of a complex network of nanowires. The band gap that was measured at 3.4 eV (narrowed compared to previously measured 3.7 eV) which indicates the presence of

titania on the FTO layer Figure 3.1c. The 0.05 M concentration produced a structure resembling the desired dendritic hyper-branched nanorod morphology with a band gap of 3.4 eV Figure 3.1a.

Using stock FTO glass, The precursor solution recipe 1 : 1.5 : 1.5 was investigated with a PTO concentration of 0.05 M and produced a dense hyper-branched nanowire structure with a band gap of 3.4 eV Figure 3.1b. Similar to the stock FTO 1:7 0.03 M sample, nucleation sites were observed on the grown nanowires resulting in a dense and complex network of nanowires. These nanowire structures did not resemble the dendritic hyper-branched morphology as well as the stock FTO 1:7 0.05 M sample. The 0.03 M concentration of the 1 : 1.5 : 1.5 recipe have produced thin nanowires and the 0.01 M did not produce any visible nanostructures hence they were excluded from further investigation.

During the investigation mentioned earlier regarding the various types of FTO glass further experiments where conducted.

While using the TEC-8 glass, at 0.05 M concentration, the 1 : 1.5 : 1.5 formula produced thick nanopillars with a cross-shaped cross-section Figure 3.1f instead of the nanowires that were observed with the stock glass. While the 0.05 M 1:7 formula, produced a spider-web over-layer on top of the hyper-branched nanorods Figure 3.1e. These significant
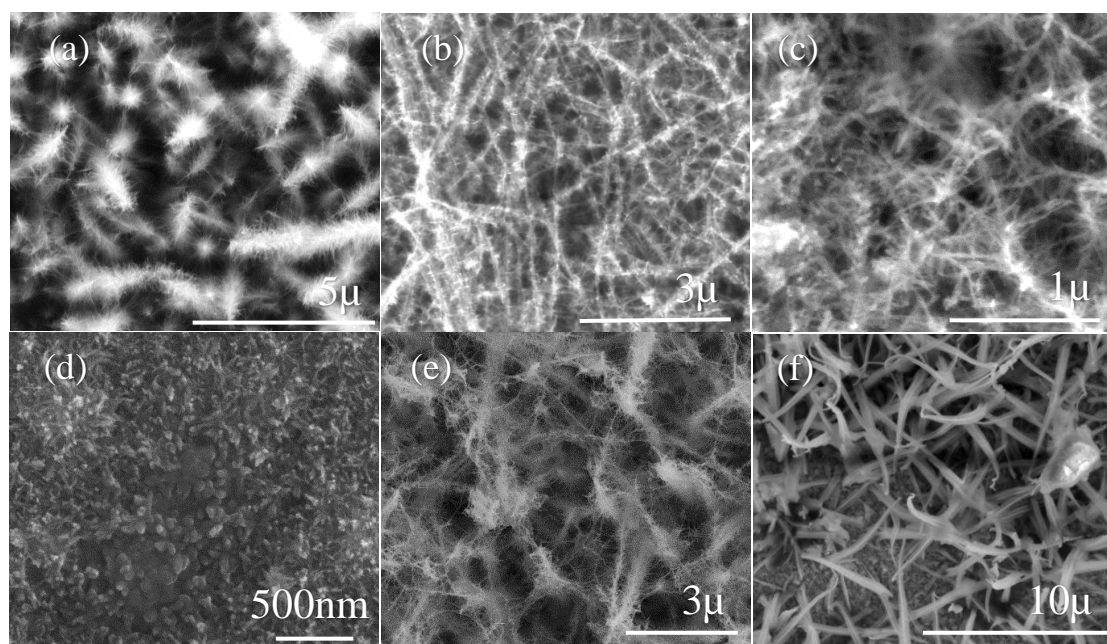

Figure 3.1 - SEM micrographs of samples with different concentrations, precursor formula and different FTO glass (a) stock FTO 1:7 0.05M (b) stock FTO 1:1,5:1,5 0.05M (c) stock FTO 1:7 0.03M (d) stock FTO 1:7 0.01M (e) TEC-8 FTO 1:7 0.05M (f) TEC-8 FTO 1:15:15 0.05M

differences are attributed to the higher conductivity and lower roughness of the substrate compared to the stock FTO glass.

A comparison study was conducted with all three FTO glasses, stock FTO, TEC-8 and TEC 15 which showed that the TEC-15 produced HBNs without eliminating the overgrown layer. All three glasses produced nanostructures, however their structure differs dramatically, with the TEC-8 producing fine hyper-branched nanowires, and TEC-15 producing the dendritic hyper-branched nanorods while the stock FTO produced HBNs with significant overlayer and fine nanowires as shown in Figure 3.2. From these experiments the best performing recipe was 1:7 at 0.05 M using TEC-15. However, the overlayer issues continued to exist, and further investigation was required.
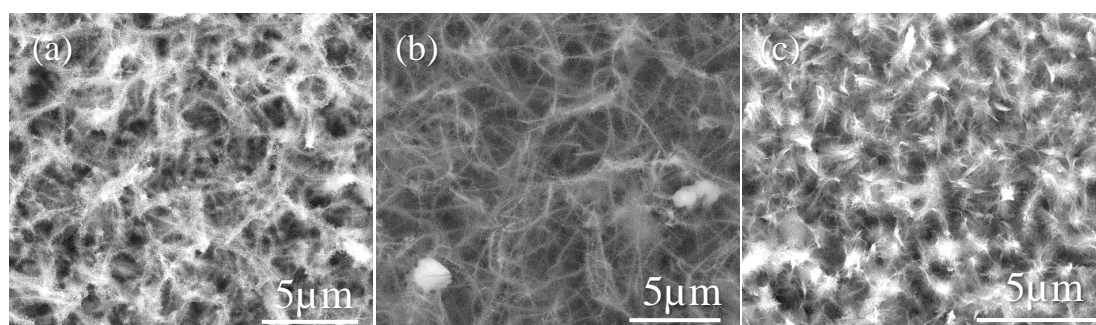

Figure 3.2 - (a) stock FTO 1:7 0.05 M, (b) TEC-8 FTO 1:7 0.05 M, (c) TEC-15 FTO

In an attempt to expand the understanding of the effects of concentration and help decrease the overlayer on the surface of the HBNs, the precursor solution level within the Teflon liner was investigated.

For all the previously mentioned samples, the FTO glass was fully covered with the precursor liquid in the teflon holder (25 ml of precursor solution), however after reducing the coverage of the FTO glass, the solution to FTO surface area ratio is altered, thus altering the relative concentration as shown in Figure 3.3. The results that were obtained after the solution level reduction are shown in Figure 3.4. It is hypothesised that reducing the solution level increases the relative concentration of the precursor to the specific FTO surface area ratio, which produced slightly more overlayer when compared to the previous experiments. Therefore, for future experiments the solution was kept at 100% level fully covering the FTO glass.
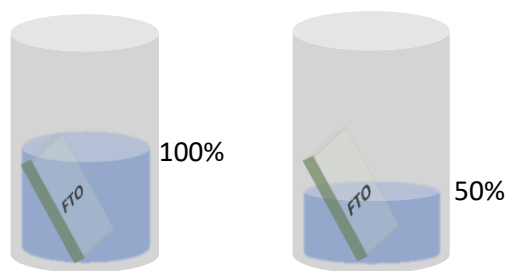
Figure 3.3 - FTO surface area to precursor solution ratio
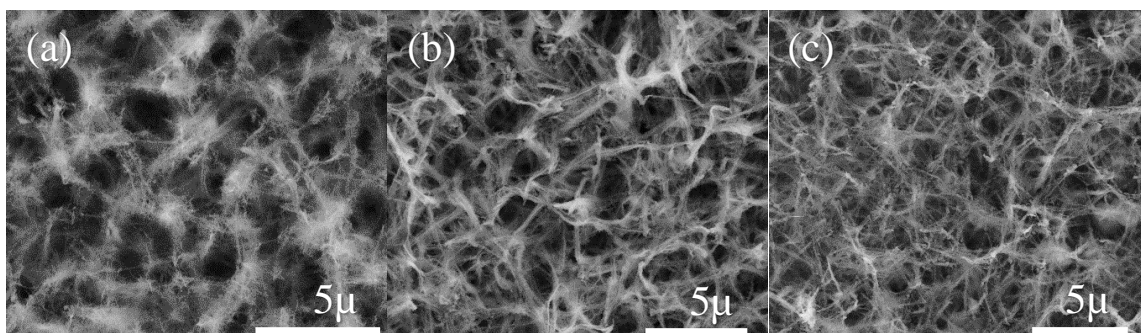
Figure 3.4 - (a) stock FTO 1:7 0.05 M, 50% full, (b) TEC-8 FTO 1:7 0.05 M 50% full, (c) TEC-15 FTO 1:7 0.05 M 50% full

The ramp up rate of the calcination temperature effects were also investigated using these samples. As previously mentioned, the calcination temperature was set to 550 °C for 9 h. The ramping rate for the previous results was set to 10 °C min^{-1}. Another experiment was conducted with the ramping set at 1 °C min^{-1} to investigate the effects of the ramping rate. It was shown that the slow ramping rate preserves the structure and the nano-hairs of the nanorods are intact Figure 3.5. As an attempt to reduce the overlayer on the samples, the ramping rate was kept at 10 °C min^{-1}.

Figure 3.5 - Ramp up calcination rate comparison (a) TEC-8 0.04 M 1:7 10°C/min (b) TEC-8 0.04 M 1:7 1°C/min

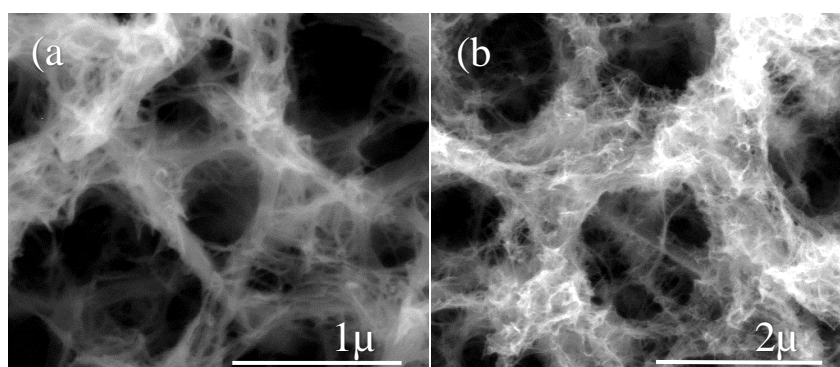The overgrown layer on top of the hyper-branched nanorods was still an unresolved issue. It was at first hypothesized to be attributed to the higher concentration of precursor in the solution during the hydrothermal reaction, or to the greater conductivity of the FTO glass. However, over time and since many of the samples were reproduced many times during the above experiments, it was observed that while keeping concentration and FTO glass constant in identical conditions the results were inconsistent in terms of the overgrown layer. While the concentration can impact the structure and potentially contribute to an overgrown layer, it was hypothesized that the reaction might be starting the moment the precursor solution is mixed together, before it is placed in the oven. It is possible that the nucleation starts without any heat or pressure applied. Therefore, the time elapsed between the moment of mixing the chemicals until the time it is placed in the oven was now monitored and investigated. It was observed that in the "30 minutes" samples the resulted nanorods were free of any overgrown layer as shown below. For the best performing sample, TEC-15 FTO glass was used at 100 % full coverage of the glass with precursor solution of 0.05 M concentration in the oven at 180 °C for 9 h. This sample consistently exhibited fully developed HBNs without any traces of an overlayer Figure 3.6.
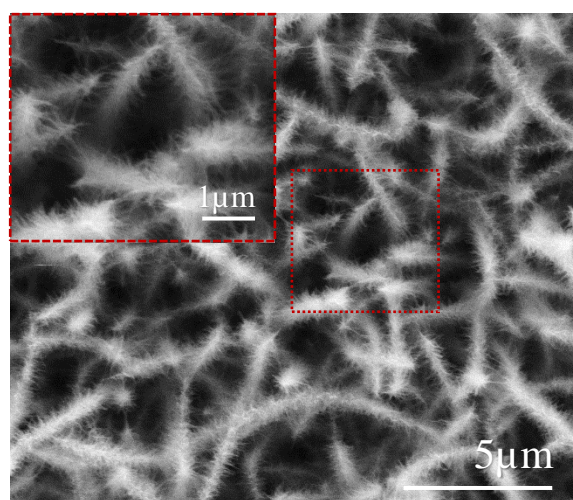

Figure 3.6 - 30-minute TEC-15, 1:7, 0.05 M,
100% coverage at 180°C for 9 hours

The angle experiment was set to investigate the effect of the angle that the FTO glass rests within the Teflon holder while in the oven. In order have accurate angle positioning, a holder was designed using Autodesk Fusion 360 and produced out of Teflon material

using a laser cutter machine Figure 3.7. The holders were used to stabilize the glass inside the Teflon holder at the specific angle. Three different holders were made for 60, 45 and 30 degrees. The resulting samples showed that the higher angles produce a denser population of nanorods, while there is no effect on the nanostructure Figure 3.8.
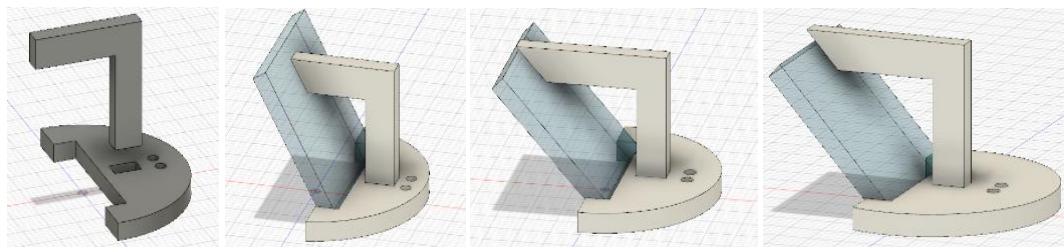
Figure 3.7 - Initial design and holder for 60, 45, and 30 degrees respectively
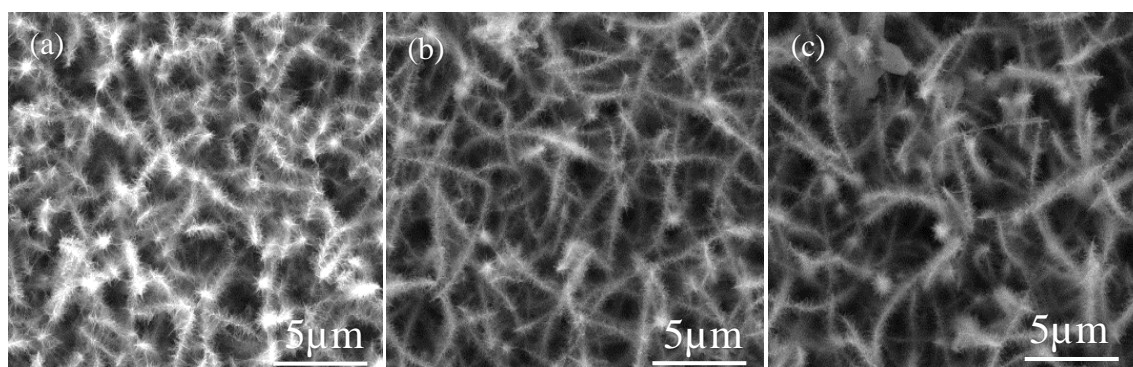
Figure 3.8 - (a) sample with the 60 degree FTO glass holder, (b) 45 degree FTO glass holder, (c) 30 degree FTO glass holder

A synthesis mechanism study was performed to gather more information on the process of the formation of these Hyper-branched nanorods. One of the disadvantages of hydrothermal synthesis, is that it is impossible to observe *in situ* the synthesis of the material as opposed to other synthesis methods. Five autoclaves were prepared at the same time using the optimised synthesis parameters which were TEC-15 FTO glass at 100 % full coverage of the glass of 0.05M concentration precursor liquid in the oven at 180 °C. One autoclave was pulled out of the oven at 30 minutes, 1 h, 3 h, 6 h, 9 h respectively. The samples were washed with H_2O and ethanol multiple times and calcined at 550 °C for 1 h. The first two samples of 30 minutes and 1 hour have shown no sign of grown nanostructures on the FTO layer so they were excluded from the figure. The samples 3 h 6 h and 9 h demonstrate the nucleation and growth of the nanorods on the FTO layer and can be seen on Figure 3.9. The 9 h sample (Figure 3.9a,d) shows the fully

grown hyper branched nanorods. In the high magnification image it can be observed that no nucleation sites are shown and the branches are fully developed. Regarding the 6 h sample (Figure 3.9b,e), the main shafts of the nanorods seem to be fully grown however, the majority of the branches are still under-developed and the nucleation sites are clearly seen in the high magnification image *Figure 3.9e*. Some branches are shown to be developed at 6 h. The 3 h sample (Figure 3.9c,f) shows the development process of the bases of the nanorod shafts, while no branches developed. This synthesis mechanism study leads to the conclusion that the synthesis of the hyper-branched nanorods follows a pattern where the nucleation and growth of the nanorods shafts forms first, and as the nanorods are fully developed, and only then the nucleation sites around the main nanorod shaft start growing the branches until they reach a point of a fully developed hyper-branched nanorod. The finalised recipe produced an overlayer-free dendritic hierarchical 1-3D hyper-branched nanorods thin film which was used as a base for the titania HBNs photocatalysts developed as part of the research conducted in the following chapters. The as-prepared photocatalysts were characterised and analysed in detail in the following chapters, the most important analytical techniques that were used are discussed below. The HBNs, due to the fact that they are grown and not deposited on FTO glass, but also due to their complex 1-3D morphology were unable to be characterised to acquire a quantifiable surface area. BET measurements could not occur due to the HBNs being
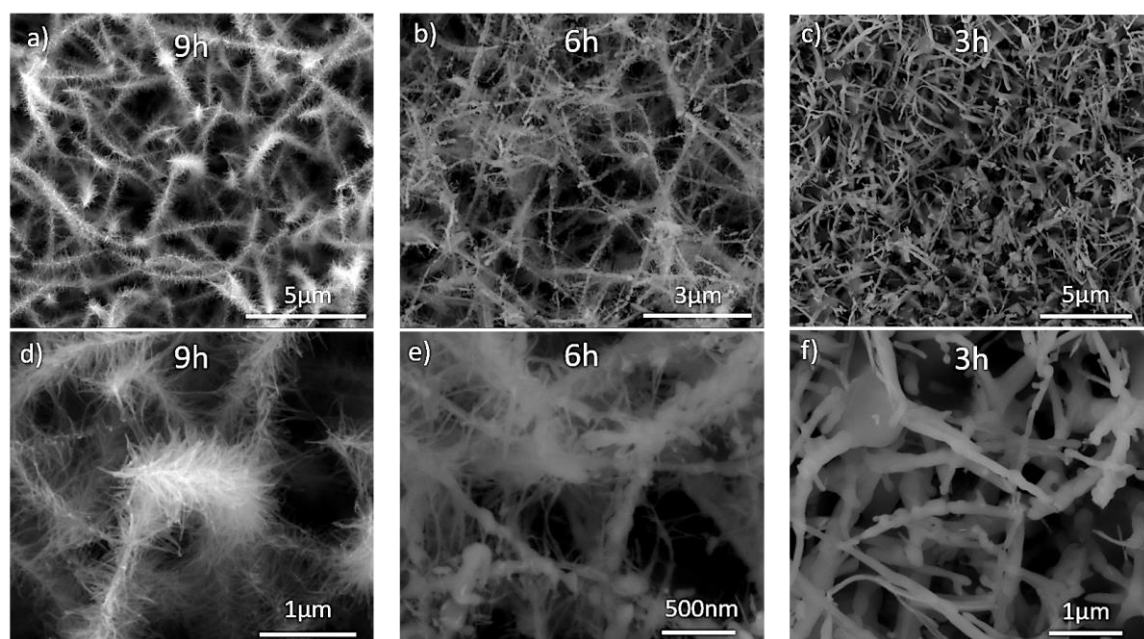
Figure 3.9 – Synthesis Mechanism study for the synthesis of TiO_2 hyper-branched nanorods. Low magnification SEM micrographs on top and high magnification on the bottom row for the samples 9 h,6 h, and 3 h respectively.

attached to the FTO glass slide and scraping the HBNs off the glass slide was shown under TEM microscopy that will produce heavily entangled agglomerated clusters that would compromise the surface area. Ellipsometry measurements were then attempted where due to the low reflectance of the surface and surface roughness created by the 1-3D morphology, no signal was produced. Further investigation on Surface acoustic waves measurements required the HBNs to be supported on other substrates which was interfering with the synthesis protocol of the HBNs and therefore a quantified surface area measurement was not achieved. The following sections present the main analytical techniques that were used to characterise the HBNs.

3.3   X-ray diffraction (XRD) analysis

XRD is a characterisation technique that allows the identification of crystalline materials and unit cell dimensions. It was developed after the observation that crystalline materials act as three-dimensional diffraction gratings for X-ray wavelengths due to their similar size of atomic scale spacing in a crystal lattice.

XRD makes use of the Bragg`s law. The Bragg`s law is the observation that when two monochromatic X-ray beams are incident on the crystal lattice, at a certain angle θ, constructive interference occurs, only when the extra distance covered by the X-ray is equal to the wavelength of the X-ray.[1] This constructive interference is referred to as diffracted ray. The additional distance covered is the interplanar distance d of atoms and can be calculated using geometric equations. The diffracted ray which occurs when conditions satisfy Bragg`s Law ($n\lambda = 2d \sin\theta$), sends a signal through the detector which allows for further analysis. The principle described above can be seen in Figure 3.10. Bragg`s law correlates the incident ray angle with the d spacing (interplanar distance) of the crystal lattice. The sample is exposed to X-rays in a range of 2θ angles which then produce all the possible diffraction directions. The d spacing is then calculated and the mineral is identified through standard reference databases, since each mineral has its own set of unique d-spacings in the lattice[2].

Through XRD we can determine the average interplanar spacing between layers or rows of atoms. Determine the phase and orientation as well as the lattice parameters *(a,b and c)*, grain or particle size of the substance.[3] In the current research XRD was used to identify the phase of the photocatalyst and as an indicator of the degree of crystallinity of the photocatalyst. However, since the particular (hyperbranched nanorod) HBN morphology allows for X-ray penetration to the FTO glass support which produced overpowering signals, XRD was unable to consistently produce tangible results and was

used as a complimentary method along with more sensitive techniques like Raman and XPS.
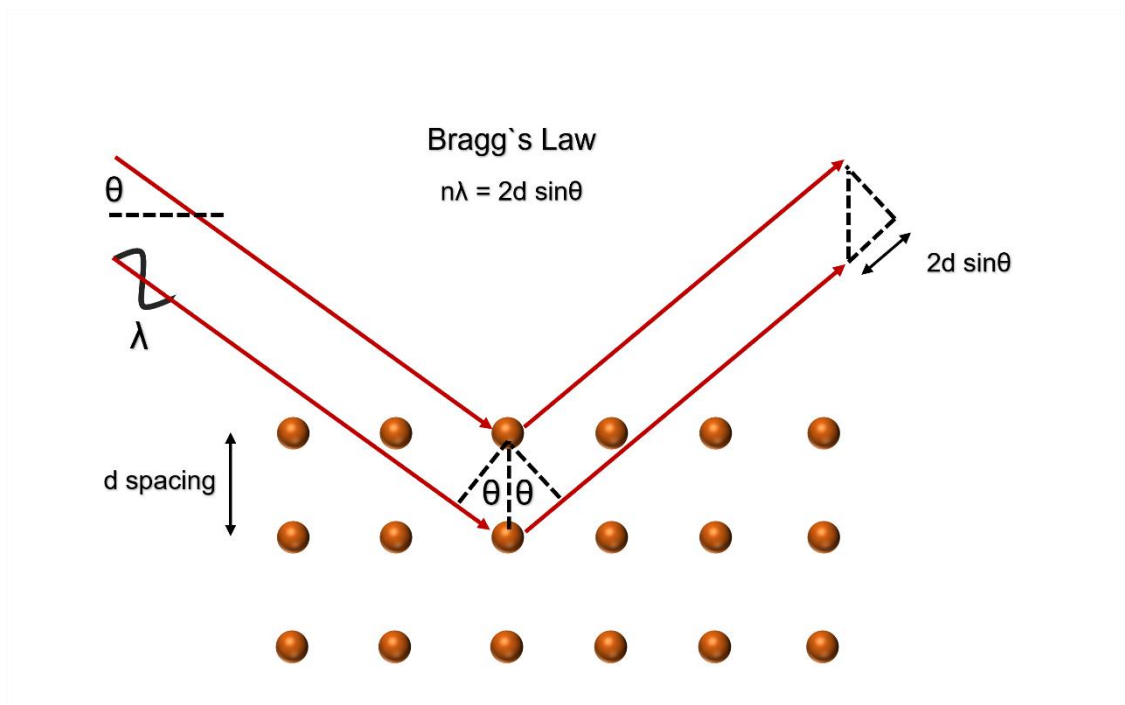
Figure 3.10 - Bragg`s Law diagram indicating the correlation of interplanar spacing with the diffracted ray.[1]

3.4 UV-Vis spectroscopy

Radiation of ultraviolet and visible range interacts with semiconductor material exciting electrons from ground state to higher energy states by absorbing certain wavelengths of the radiation. This takes place only upon collision of irradiation of certain wavelengths with the semiconductor, which have sufficient energy to excite electrons to a higher state. This allows for monitoring the behaviour of the examined matter under irradiation of a range of wavelengths and draw information regarding its electronic structure.[4] Additionally, this allows for identifying the range of wavelengths in which the sample matter absorbs the most (λ_{max}) of the incident irradiation. This information could be used to increase the materials reactivity when exposed to the appropriate wavelengths of irradiation for application purposes where photoexcitation is important or, which wavelengths should be avoided when photodegradation is a problem. The UV range falls between 190-380nm, where the visible range in the range of 380 – 750 nm.

UV-Vis spectroscopy utilises the Beer-Lambert Law, which is a relationship between the attenuation of light through the examined matter or substance. Beer-Lambert Law is shown below (Eq.3.1).

$$A = \varepsilon c l \tag{3.1}$$

Where A, ε, c and l, correspond to the absorbance, molar absorption coefficient [$M^{-1}cm^{-1}$], molar concentration [M] and optical path length [cm] respectively. Transmittance and Absorbance is discussed since absorbance appears in the Beer-Lambert law and it is calculated using transmittance measurements. Transmittance (T) is defined as the ratio of the transmitted intensity I over the incident intensity I_0 and takes values from 0 to 1 (Eq.3.2). However, transmittance is often expressed as a percentage (T%) (Eq.3.3). The absorbance of the examined sample is found to be a logarithmic relationship to the transmittance as shown in Eq.3.4.

$$T = \frac{I}{I_0} \tag{3.2}$$

$$T(\%) = 100\frac{I}{I_0} \tag{3.3}$$

$$A = -\log_{10} T \tag{3.4}$$

Molar absorption coefficient (ε) is a sample dependant property that measures how strong of an absorber is the sample to a specific wavelength of radiation. The molar concentration is the moles of the sample dissolved in the solution, and the length corresponds to the length that the beam travels through the sample before reaching the detector.[5]

A typical UV-Vis set up consists of the light source, typically use D2 and Tungsten lamp, the light passes through a monochromator, a prism, isolating wavelengths of light, then through a beam splitter. The two beams pass through the reference sample and examined sample respectively, to the detector where the signal is processed and shown on the monitor as shown in Figure 3.11.[6]

Kubelka Munk function is a model that allows the estimation of the band gap energy using the UV-Vis measurements. The diffuse reflectance R_∞ is given by Eq.3.5 where s is the scattering coefficient and k is the absorption coefficient of the sample. Eq.3.5 is then solved for k/s producing the K-M function (Eq.3.6).[7]

50

$$R_\infty = 1 + \frac{k}{s} \sqrt{\frac{k}{s}\left(2 + \frac{k}{s}\right)} \qquad (3.5)$$

$$F(R) = \frac{k}{s} = \frac{(1-R_\infty)^2}{2R_\infty} \qquad (3.6)$$

In this research UV-Vis is an important characterisation technique as it allows for measurements of light absorption wavelengths, band gap energy calculations using the Kubelka Munk function but also to identify changes occurred with loading foreign materials on the TiO_2 HBN photocatalyst.
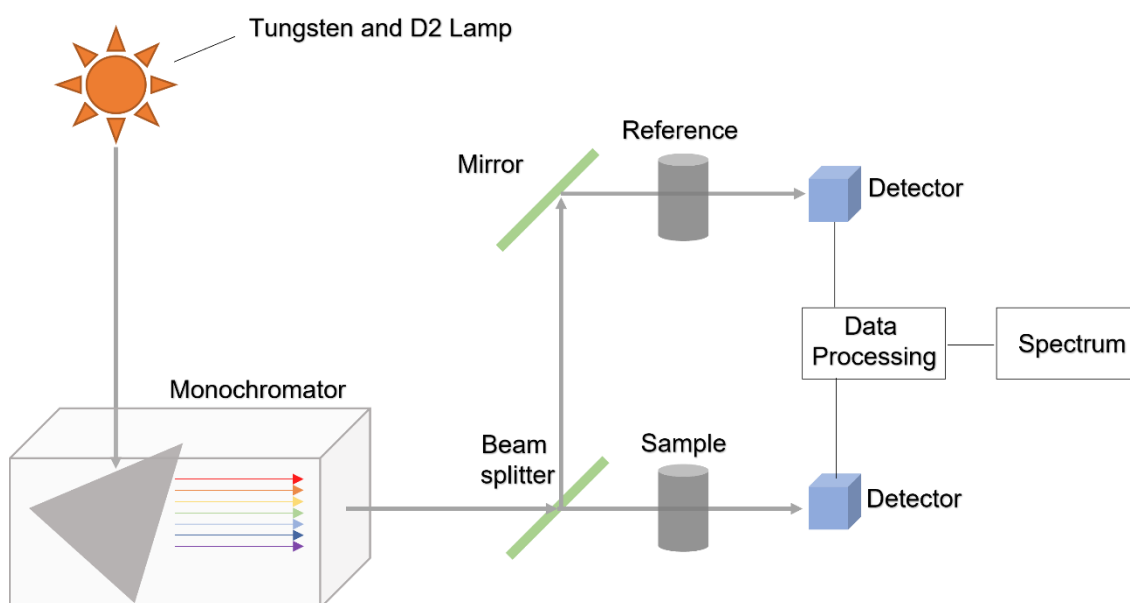
Figure 3.11 – Typical UV-Vis spectroscopy configuration and internal components.[6]

3.5 Infrared Spectroscopy

Most molecules have the ability to absorb radiation in the infrared region of the electromagnetic spectrum. The infrared spectrum includes wavelengths from the edge of the visible light spectrum, 700 nm, up to 1 mm. When a molecule absorbs infrared radiation (IR), it is converted into molecular vibrations to the bonds of the molecule. The vibrational energy levels change from ground to excited state, and the vibrational gap is what is used to determine the absorption peaks frequency. The degree of freedom of the molecule is determined from the number of absorption peaks. With IR spectroscopy a molecular fingerprint can be acquired to identify molecules. The IR spectra are usually plotted as absorbance vs wavenumber. The wavenumbers most commonly examined are

from 4000 to 400 cm^{-1}. A wavelength can be converted to wavenumber using the following equation (Eq.3.7) [8].

$$k = \frac{2\pi}{\lambda}$$ (3.7)

Fourier-transformed infrared spectroscopy (FT-IR) is often used because it allows for more accurate results, due to increased signal to noise ratio, but is also faster. FT-IR differs from the conventional IR because all IR wavelengths are examined at the same time which makes FT-IR faster than conventional IR. The signals acquired from this method are then Fourier-transformed to produce the accustomed IR plot.[9]

A common FT-IR consists of a IR source, interferometer, a sample compartment and a detector, a beam splitter, and one fixed and one moving mirror as in the configuration shown in Figure 3.12.[8] In this thesis, FT-IR was used to identify organic substances such as products and by products in the reaction solution for the cyclic carbonates experiments.
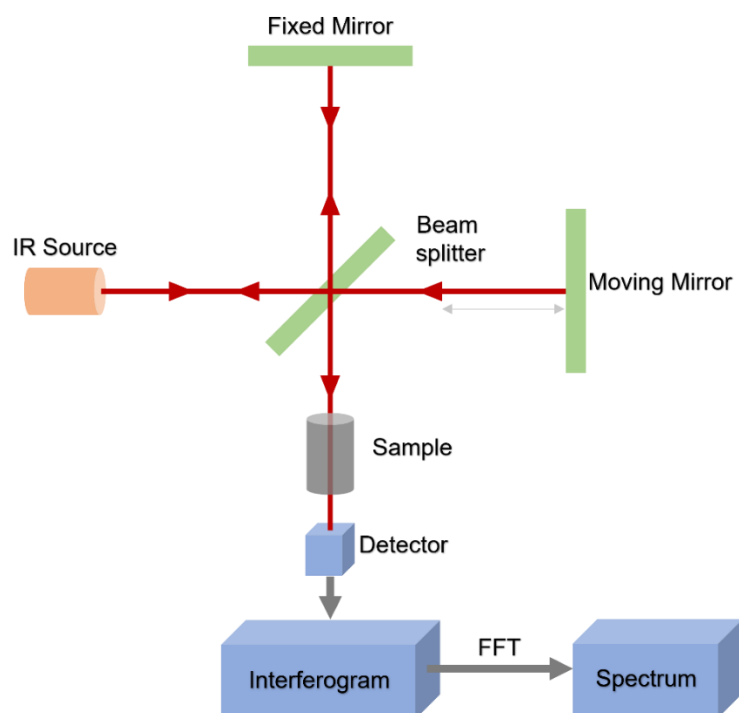

Figure 3.12 – FT-IR spectroscopy configuration and internal components.[8]

3.6   Raman spectroscopy

When light interacts with materials different processes can occur. Light can be absorbed by the material or reflected. It can also be transmitted through the material, or it can be scattered off. The wavelength of the incident light as well as the material plays a crucial role to this phenomenon. When a material scatters off light, the wavelength of the light is typically unchanged, in other words the energy of the incident light is equal to the energy of the scattered light and therefore elastic scattering occurs. This is known as Rayleigh scattering. However, a fraction of the scattered light has slightly altered energy level which is attributed to inelastic scattering, where the photon loses energy donating to the internal energy of the matter. This process is referred to as Raman scattering as shown in Figure 3.13.[10] This phenomenon is attributed to the interaction between the oscillation of light and molecular vibration.[11]

Due to the frequency modulation which is specific to molecular vibrations and phonon in crystals, it is possible to analyse the composition of crystal lattice using Raman spectroscopy since it produces a fingerprint signal specific to the crystal lattice. For Raman spectroscopy, monochromatic laser in the visible, near infrared or near ultraviolet is used. The shift in the energy from the Raman scattered signals gives information about the vibrational modes of the sample. Raman spectra are plotted as Raman intensity vs Raman shift measured in (cm^{-1}). Raman shift is basically wavenumber and can be calculated using the Eq.3.7. From intensity, information on the concentration of the specific substance can be acquired, while from the width of the peak, crystallinity of the material can be determined. Peak shifts are common also and express stress within the crystal lattice.[12, 13]

Raman has been very helpful for this thesis due to its localised sensitivity where the laser beam is focused, which can overcome the issues that occurred with the XRD characterisation. Therefore, the HBN morphology was no longer an obstacle in identifying the composition, crystallinity, and phase of the photocatalyst.
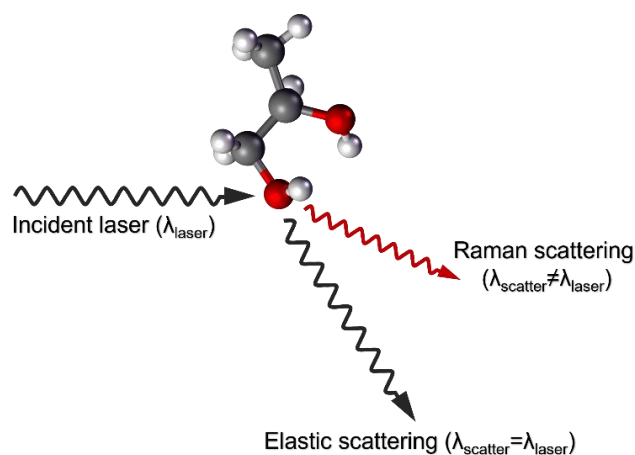
Figure 3.13 – Elastic and inelastic scattering mechanics upon incident irradiation.[10]

3.7   Scanning electron microscopy (SEM)

Scanning electron microscopy is an imaging technique that produces an image of the material making use of a beam of electrons rather than light. The surface of the sample is scanned and the intensity along with the beam-atom interaction depth and position of the beam provides information capable of producing an image. Electrons are used rather than light in an optical microscope, the reason being that the electrons have much shorter wavelengths and therefore allow for a much greater resolution image. These microscopes are capable of producing images at resolutions of 1 nm. Typically, the samples are observed in high vacuum conditions, however alternatives exists such as low vacuum or wet conditions[14]. The generic configuration of SEM is shown in Figure 3.14.[15]

Some SEM machines are equipped with back scattered electron microscopes which are signals from higher depths into the sample. This is useful in analytical techniques when trying to identify different elements inside a material such as doped elements, because the intensity of the back scattered beam is strongly related to the atomic number of the element[16-18].

Due to the importance of nanoscale morphology in the current research for the HBN photocatalyst, SEM imaging was extremely important to achieve the desired morphology results and optimise the synthesis method. Additionally, any foreign material introduced to the HBN photocatalyst could be observed using SEM. However, some foreign materials were too small to be observed even with SEM magnification, therefore Transmission electron microscopy (TEM) was incorporated for further analysis.
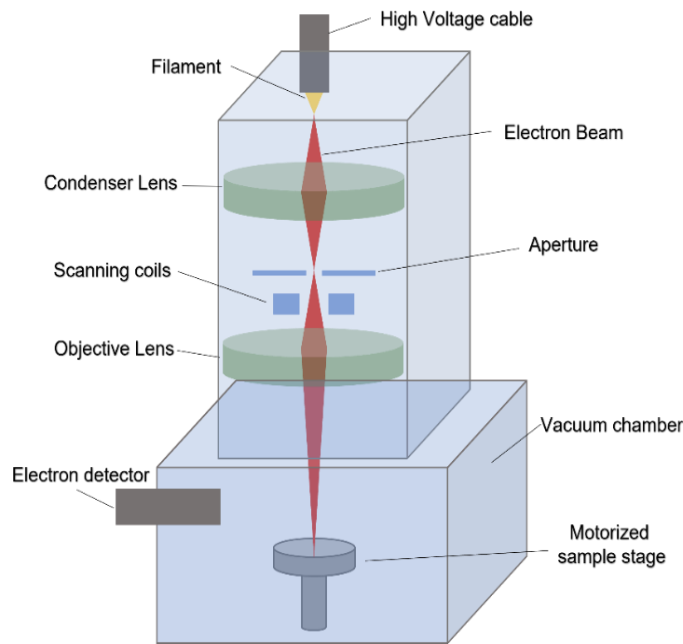
Figure 3.14 – SEM microscope configuration with basic components.[15]

3.8   Transmission electron microscopy (TEM)

Similarly, to SEM, TEM uses a beam of electrons to produce an image of the sample material instead of light. However, TEM has the potential to produce the highest possible resolution image, up to atomic level, due to the use of electrons which offer a very small wavelength, but also the way matter is presented to the microscope and magnification process. The sample is presented as a thin film suspended on a grid. The limitation in terms of sample preparation is that the thin film must be below 100 nm in thickness because the electrons travel through the material in order to reach the detector placed underneath the sample grid. This way the alterations of the electron beam reaching the detector are producing the image of the sample which is magnified.[19] This technique allows for a closer inspection due to the electron beam passing through the entire sample which can provide information that the SEM (surface examination of the sample) cannot provide. For example elemental composition is more accurate on TEM examination since the intensity of the signal can be correlated to the atomic number of the element. This instruments usually have a vertical configuration where the electron source is on top where the beam of electrons is accelerated and passes through a condenser lens, straight through the suspended sample grid, and through a set of lenses that magnify and project the beam on a fluorescent screen placed at the bottom of the instrument.[20, 21] The configuration of a TEM microscope is shown in Figure 3.15.[22]

TEM had a significant contribution to the current research which allowed for clear observation of the foreign elements added to the HBNs in the form of nanospheres, but also, identifying elements using elemental composition (EDX). Additionally, TEM provided accurate measurements of d-spacing in the lattice to identify whether the foreign metals were loaded or doped into the crystal lattice.
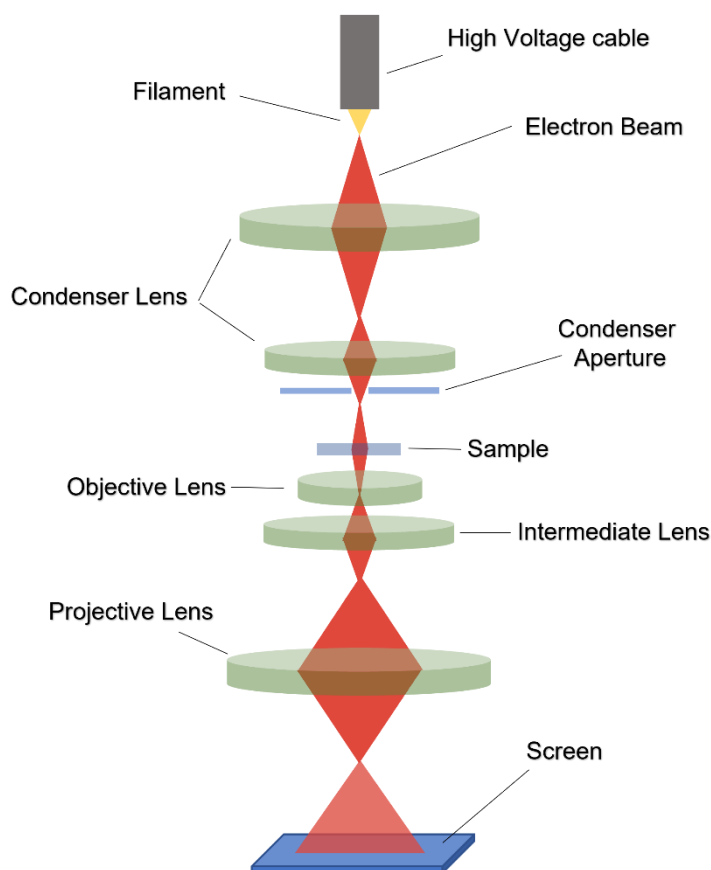
Figure 3.15 – TEM microscope configuration and internal components.[22]

3.9   Nuclear magnetic resonance spectroscopy (NMR)

NMR is an analytical technique that is most commonly use to definitively identify organic compounds. It is considered one of the most accurate analytical techniques to identify complex molecules and it is a standard procedure of modern organic chemistry. The most common NMR types are proton and carbon 13 NMR but can be applied to any nuclei that contains an odd number of protons or neutrons which posses a spin (or more accurately, intrinsic angular momentum). These atoms have a certain spin which acts as a magnet, creating a magnetic field around it. NMR is the technique where an external magnetic field is applied to the sample forcing the orientation of the nuclei to α-spin state, which is the lower energy state. Then radiation is applied, hence the name spectroscopy, which will bring the nuclei in the state of resonance, the β- spin state, which is the higher energy

56

state. When the external energy source is removed, radiation, the nuclei returns to the α-spin state producing a radio wave signal which is then used to produce the NMR spectrum.[23] The concept described above is illustrated in Figure 3.16 along with a typical NMR configuration and internal components.[24] The NMR spectra is a highly detailed technique that not only provides definitive signals for functional groups but also provides distinguishable signals for identical functional groups when they are in varying chemical environments, to the point where the molecule can be fully described from information acquired only by a successful NMR spectrum. Highly purified and relatively large amounts of products are required for a successful NMR characterisation. However, it is a non-destructive analytical technique.[25, 26]

In the current research, NMR was the identification method for the molecular structure of reaction products of the cyclic carbonates reaction to confirm the FT-IR observations.
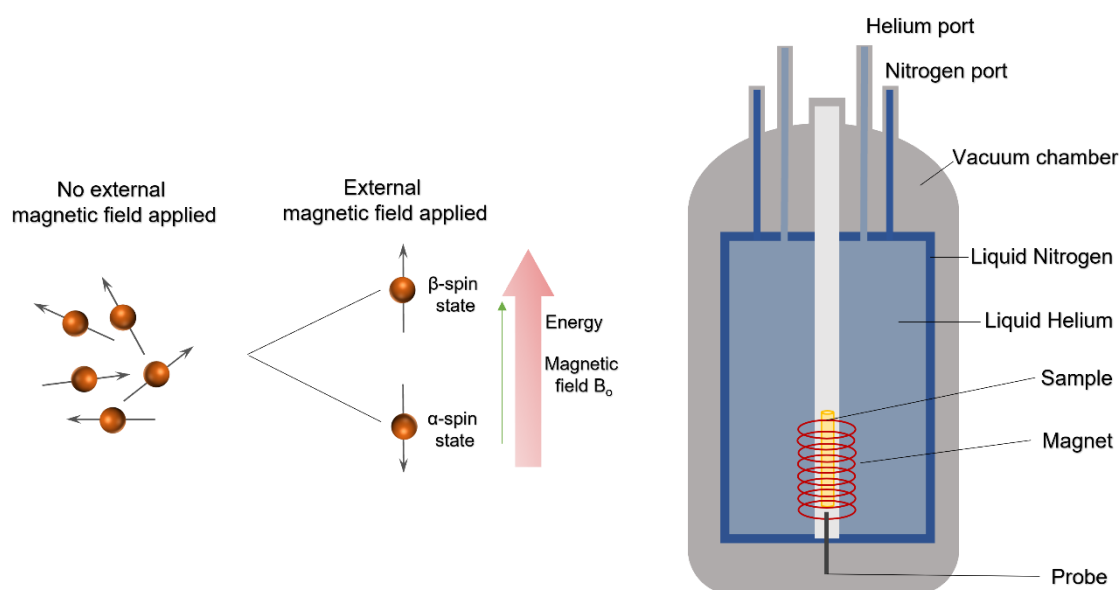
Figure 3.16 – NMR principles and internal components configuration. [24]

3.10   X-ray photoelectron spectroscopy (XPS)

XPS is based on the photoelectric effect. The photoelectric effect describes the observation that when electromagnetic irradiation with certain energy (hv) collides with a material, electrons are emitted from the atom. For each material the energy threshold in which electrons are released is different. More importantly it explained the quantized nature of light and introduced the concept of photons. Additionally, it was observed that

when the incident electromagnetic irradiation was of higher energy than the energy threshold required for the specific material, the excess energy was converted into kinetic energy of the photoexcited electron. It is based in this effect that the XPS characterisation works. XPS is an accurate and useful surface analytical technique. The surface atoms are not surrounded by other atoms on all sides as atoms found in the bulk which makes them more reactive, and these are the atoms XPS is analysing. The sample is irradiated with monochromatic X-rays, usually Al Kα, which emit electrons from the surface of the sample.[27] The kinetic energy of the emitted electrons is measured and from the kinetic energy signals the element but also its chemical state and the orbital it was emitted from can be determined as shown in Figure 3.17.[28] Different elements give different kinetic energy signals which are characteristic to the individual elements. From the kinetic energy of the electron, the binding energy is determined from which the chemical state of the sample can be acquired because each chemical state alters the binding energy.[27, 29]

XPS was incorporated as an identification of the elements contained in each sample, but also provided information about the oxidation states of these elements.
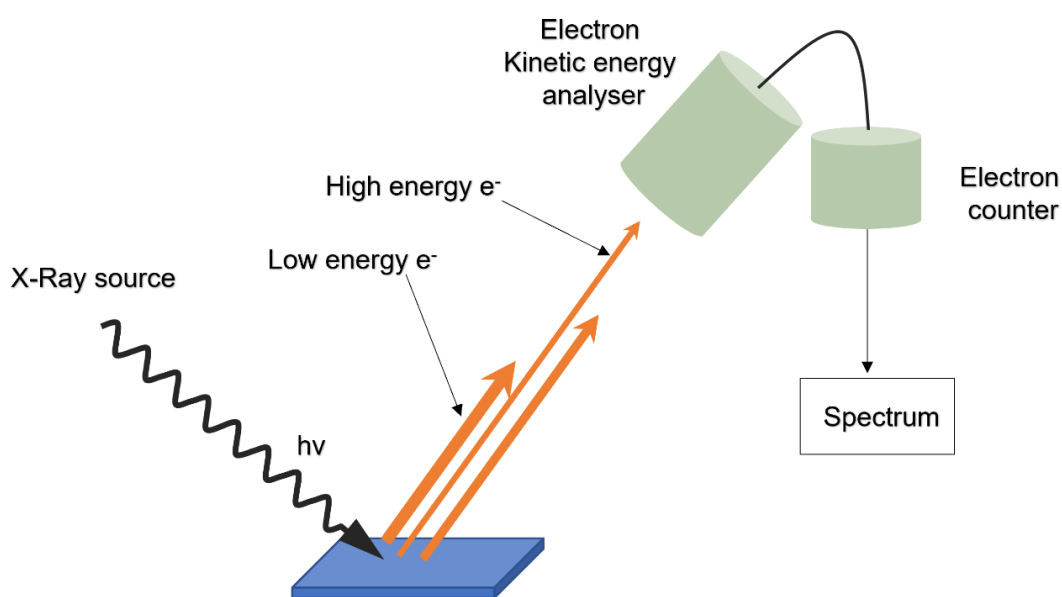

Figure 3.17 – Schematic representation of the emitted electrons upon X-ray irradiation and XPS device.[28]

3.11   Chronoamperometry (CA)

Chronoamperometry (CA) is an electrochemical technique frequently used to monitor the resulting current when the working electrode is subjected to a stepped voltage. CA is often

used to monitor the kinetics of chemical reactions, diffusion processes, adsorption of products and generally provides insight on the electrochemical response of the working electrode through the response waveform. The resulting current (due to the potential step) is plotted as a function of time and the potential step can be a single or a double potential step which provides is used to investigate the reversibility of a reaction. This experiment requires the use of an electrochemical workstation (potentiostat) to apply the potential step or steps and monitor the current response at the working electrode.[30]

The three-electrode configuration system is commonly used for this experiment where a reference electrode (RE), a counter electrode (CE), and the working electrode (WE) are submerged in an electrolyte solution as shown in Figure 3.18. The external voltage is applied (using potentiostat) between the RE and the WE. The CE should be placed close to the WE in order to minimise ohmic losses, yet it must not interfere with the reactions taking place at the WE. The 3-electrode system provides a better control and more accurate measurement of the potential and current going through the system as opposed to a 2-electrode system.

In the current research, an Autolab (AUT84966) electrochemical workstation was used with 0.1M NaOH as an electrolyte, the reference electrode was made of Ag/AgCl and CE was made of Pt. The working electrode was the examined sample coated on FTO glass as thin-film with an area of 1x1 cm^2. Chronoamperometry was used to measure the photocurrent response of the examined sample by 60 s on-off cycles of irradiation. The resulting photocurrent response was plotted against time.
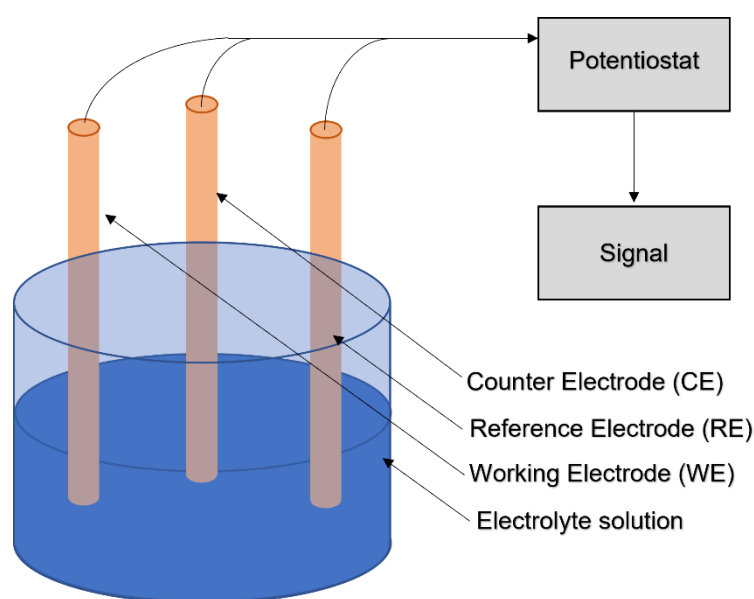

Figure 3.18 – Schematic diagram of the three-electrode system configuration.[30]

3.12 Gas chromatography (GC)

Gas chromatography allows for the separation, identification and quantification of compounds within a gaseous or liquid sample. Generally, A GC consists of a sample injector port (for gaseous and liquid samples), a column (thin tube), a column oven, and a detector or multiple detectors. The vapourised sample passes through the column with the help of a carrier gas (inert). Depending on the compounds of the sample they pass through the column at different rates and upon exiting the column the detectors can provide information (regarding identification and quantification) through signals. Commonly GCs are fitted with flame ionisation detectors (FID) and thermal conductivity detectors. Each detector can identify different group of compounds, or has a different sensitivity to certain compounds, depending on their physical and chemical properties. FID detectors can identify hydrocarbons with good sensitivity such as CH_4, as well as CO after a methanation step, while a TCD detector will identify CO_2, O_2, H_2 and N_2 with good sensitivity.[31]

Gas chromatography was used in the current research to analyse the products of CO_2 photoreduction reaction. The GC was connected to a prototype continuous flow reactor setup, developed by Dr. Warren Thompson, which included a CO_2 mass flow controller and a temperature-controlled saturator providing vapourised H_2O. The CO_2 flow rate was set to 0.35 mL min^{-1}, to maintain a steady atmospheric pressure throughout the experiments. The reactants then passed through the irradiated custom made photoreactor leading to the GC for product analysis. A continuous flow reactor was favoured over a batch reactor as it allows for a uniform temperature and improved mixing that inhibit the formation of gradients withing the photoreactor. In addition, in-line analysis is possible with continuous flow reactors which provides better insight of the reaction process. The photoreactor was designed to increase the ratio of reagent gas volume to illuminated photocatalyst and provide uniform light distribution, with direct illumination above the quartz glass window of the photoreactor. The entire system was kept at 40 °C with the help of a hotplate under the photoreactor and heated lines, to prevent condensation, and a water trap was used to protect the GC from humidity related damage. A detailed description of the photoreduction rig can be found in section 4.8.

References

[1]   P. P. Ewald, *Fifty Years of X-Ray Diffraction: Dedicated to the International Union of Crystallography on the Occasion of the Commemoration Meeting in Munich July 1962*. Springer Science & Business Media, 2012.

[2]   W. H. Bragg, "The Nature of γ and X-Rays," *Nature,* vol. 77, no. 1995, pp. 270-271, 1908/01/01 1908, doi: 10.1038/077270a0.

[3]   W. Barlow, "Probable Nature of the Internal Symmetry of Crystals," *Nature,* vol. 29, no. 738, pp. 186-188, 1883/12/01 1883, doi: 10.1038/029186a0.

[4]   D. A. Skoog, F. J. Holler, and S. R. Crouch, "Principles of Instrumental Analysis . Belmont, CA: Thomson Brooks/Cole," *ISBN 9780495012016,* pp. 169-173, 2007.

[5]   A. Metha, "Limitations and Deviations of Beer-Lambert Law," *PharmaXChange. info,* 2012.

[6]   F. S. Rocha, A. J. Gomes, C. N. Lunardi, S. Kaliaguine, and G. S. Patience, "Experimental methods in chemical engineering: Ultraviolet visible spectroscopy—UV-Vis," *The Canadian Journal of Chemical Engineering,* https://doi.org/10.1002/cjce.23344 vol. 96, no. 12, pp. 2512-2517, 2018/12/01 2018, doi: https://doi.org/10.1002/cjce.23344.

[7]   A. K. R. Choudhury, *Principles of colour and appearance measurement: Visual measurement of colour, colour comparison and management*. Woodhead Publishing, 2014.

[8]   P. R. Griffiths and J. A. De Haseth, *Fourier transform infrared spectrometry*. John Wiley & Sons, 2007.

[9]   V. Saptari, *Fourier transform spectroscopy instrumentation engineering*. SPIE press, 2004.

[10]   Y. C. Cho and S. I. Ahn, "Fabricating a Raman spectrometer using an optical pickup unit and pulsed power," *Sci. Rep.,* vol. 10, no. 1, p. 11692, 2020/07/16 2020, doi: 10.1038/s41598-020-68650-7.

[11]   P. Graves and D. Gardiner, "Practical raman spectroscopy," *Springer,* 1989.

[12]   C. V. Raman and K. S. Krishnan, "The Negative Absorption of Radiation," *Nature,* vol. 122, no. 3062, pp. 12-13, 1928/07/01 1928, doi: 10.1038/122012b0.

[13]   R. L. McCreery, *Raman spectroscopy for chemical analysis*. John Wiley & Sons, 2005.

[14]   D. Stokes, *Principles and practice of variable pressure/environmental scanning electron microscopy (VP-ESEM)*. John Wiley & Sons, 2008.

[15]   C. Suryanarayana, "Microstructure: An Introduction," 2017, pp. 105-123.

[16]   D. McMullan, "Scanning electron microscopy 1928–1965," *Scanning,* vol. 17, no. 3, pp. 175-185, 1995.

[17]   C. Oatley, D. McMullan, and K. Smith, *The development of the scanning electron microscope*. Elsevier: Amsterdam, Netherlands, 1985.

[18]   K. Smith and C. Oatley, "The scanning electron microscope and its fields of application," *British Journal of Applied Physics,* vol. 6, no. 11, p. 391, 1955.

[19]   A. V. Crewe, M. Isaacson, and D. Johnson, "A simple scanning electron microscope," *Review of Scientific Instruments,* vol. 40, no. 2, pp. 241-246, 1969.

[20]   A. V. Crewe, J. Wall, and J. Langmore, "Visibility of Single Atoms," *Science,* vol. 168, no. 3937, pp. 1338-1340, 1970, doi: 10.1126/science.168.3937.1338.

[21]   D. B. Murphy, *Fundamentals of light microscopy and electronic imaging*. John Wiley & Sons, 2002.

[22]   N. Marturi, "Vision and visual servoing for nanomanipulation and nanocharacterization in scanning electron microscope," 11/19 2013.

[23]   Q. Teng, *Structural biology: practical NMR applications*. Springer Science & Business Media, 2012.

[24]   C. B. Crawford and B. Quinn, "10 - Microplastic identification techniques," in *Microplastic Pollutants*, C. B. Crawford and B. Quinn Eds.: Elsevier, 2017, pp. 219-267.

[25]   C. Gorter and L. Broer, "Negative result of an attempt to observe nuclear magnetic resonance in solids," *Physica,* vol. 9, no. 6, pp. 591-596, 1942.

[26]   I. Rabi, "The Discovery of NMR."

[27]   M. P. Seah and W. Dench, "Quantitative electron spectroscopy of surfaces: A standard data base for electron inelastic mean free paths in solids," *Surface and interface analysis,* vol. 1, no. 1, pp. 2-11, 1979.

[28]   H. Seyama, M. Soma, and B. K. G. Theng, "Chapter 2.5 - X-Ray Photoelectron Spectroscopy," in *Developments in Clay Science*, vol. 5, F. Bergaya and G. Lagaly Eds.: Elsevier, 2013, pp. 161-176.

[29]   K. M. Siegbahn, "Nobel Lecture. Nobel Media AB 2019," *Nobel Lecture. NobelPrize.org. Nobel Media AB 2019. Fri. 6 Dec 2019. https://www.nobelprize.org/prizes/physics/1981/siegbahn/lecture/,* Fri. 6 Dec 2019 2019. [Online]. Available: https://www.nobelprize.org/prizes/physics/1981/siegbahn/lecture/.

[30]   J.-S. Yu and Z.-X. Zhang, "Double potential-step chronoamperometry and chronocoulometry at an ultramicrodisk electrode: Theory and experiment1," *J. Electroanal. Chem.,* vol. 439, pp. 73–80, 12/10 1997, doi: 10.1016/S0022-0728(97)00258-1.

[31]   J. Hong, W. Zhang, J. Ren, and R. Xu, "Photocatalytic reduction of CO2: a brief review on product analysis and systematic methods," *Analytical Methods,* 10.1039/C2AY26270C vol. 5, no. 5, pp. 1086-1097, 2013, doi: 10.1039/C2AY26270C.

Chapter 4

Hierarchical hyper-branched titania nanorods with tuneable selectivity for CO_2 photoreduction
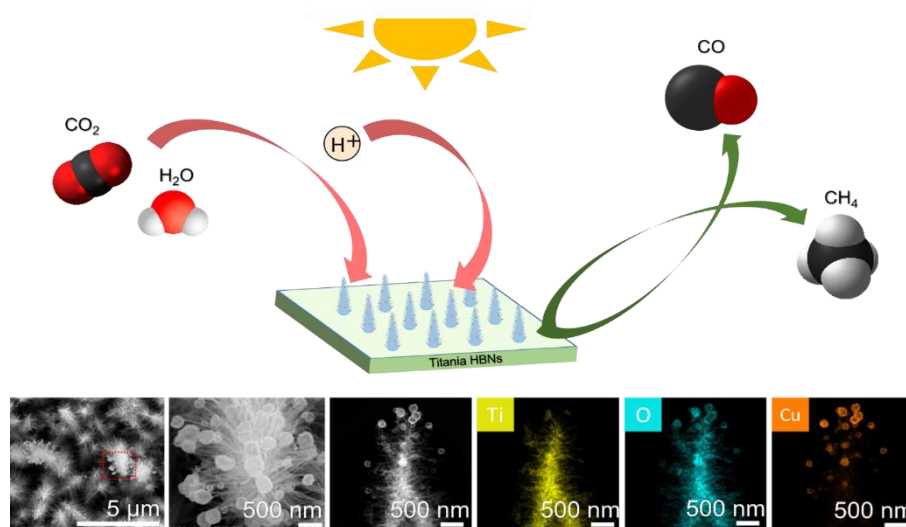
4.1   Aim and objectives

The chapter presents a published study on the fabrication of hierarchical hyper-branched nanostructured titania material (HBNs) as a photocatalyst for CO_2 photoreduction.[1] The nanostructures were grown on Fluorine-doped Tin Oxide (FTO) glass slides as thin films with a hyper-branched morphology designed to enhance light harvesting. The HBNs optical properties and light absorption were examined and evaluated by UV-Vis spectroscopy and spectroradiometry. Additionally, morphological and chemical composition was investigated by conducting SEM, HR-TEM, EDX, XRD, Raman, SAED and XPS studies. The aim of this work was to investigate the potential of fabricating a high performing photocatalyst in terms of conversion with easily tuneable selectivity for CO_2 photoreduction. Therefore, the HBNs were subjected to a facile protonation treatment which has shown successful selectivity shifts, while maintaining high conversion rates.[1] During this facile treatment, potassium ions are replaced with hydrogen ions and the subsequent re-calcination step forces a re-organisation takes place

which successfully shifts the titania phase. A photocatalyst which allows for tuneable selectivity provides a higher level of control to the products of the reaction and becomes more appealing for industrial applications. To further investigate the potential of the HBNs material, RuO_2-HBNs and CuO-HBNs compounds were fabricated. The literature benchmark Degussa P25 (TiO_2) was used to evaluate the HBNs performance in CO_2 photoreduction. The CO_2 photoreduction was performed in a custom-made flow photoreactor to accommodate FTO glass slide samples in a CO_2 and H_2O vapour atmosphere under constant irradiation of visible light (300-600 nm, 150 mW cm^{-2}). The product analysis was performed using the in-line gas chromatographer (GC).

The objectives of this work are:

- Develop a facile treatment for the HBNs to facilitate the desired selectivity shift for the CO_2 photoreduction products, from CO to CH_4.

- Preservation of the hyper-branched morphology of the HBNs nanostructures and consequently their highly efficient light harvesting capabilities throughout the facile treatment for selectivity shifts mentioned above.

- Investigate the potential charge separation enhancement and CO_2 photoreduction performance of the fabricated compound RuO_2-HBNs.

- Investigate the potential light absorption enhancement and CO_2 photoreduction performance of the fabricated CuO-HBNs compound.

4.2 Highlights and key findings

4.2.1 Hierarchical morphology and its light absorption performance

The HBNs were grown on FTO glass slides during a hydrothermal treatment, which revealed numerous dendritic microstructures of (3-5 μm) decorated with a plethora of nanobranches growing at all direction. The HBNs were then subjected to a facile protonation treatment as mentioned earlier to facilitate the desired selectivity shift. Therefore, two samples were analysed, HBNs BP, which stands for HBNs *before protonation*, and HBNs AP, which stands for HBNs *after protonation*. The HBNs BP have shown a 3.7 eV band gap while the HBNs AP exhibited a reduced band gap of 3.4 eV. The band gap for Degussa P25 (used as a benchmark) is known to be at 3.2 eV. Further discussion on what caused the band gap narrowing follows on section 3.2.2. Under the spectroradiometry examination performed, the benchmark P25 demonstrated a photon flux of 28.6 μmol m^{-2} s^{-1}. In comparison, the photon flux was measured at 39.8

and 48.2 $\mu mol\ m^{-2}\ s^{-1}$ for HBNs BP and HBNs AP, respectively. Despite the significantly narrower band gap of P25, and therefore wider wavelength light absorption range, both HBNs structures have shown the ability to absorb a significantly higher amount of light which is attributed to the light harvesting capabilities of the hyper-branched morphology of the HBNs. The improved performance of HBNs AP when compared to that of the HBNs BP is attributed to the added benefit of the band gap narrowing that was observed under UV-Vis. Essentially, the HBNs AP has a reduced band gap, while maintaining the hyper-branched morphology which increases its light absorption capabilities.

4.2.2 Phase altering treatment – product selectivity shift

The HBNs are composed mainly of potassium titanates, and the anatase phase of TiO_2. The HBNs BP has shown an estimated 7:1 potassium titanates to anatase phase ratio. With the incorporation of the facile protonation treatment, a phase shift was observed where the ratio of potassium titanates to anatase was shifted to 1:10. Therefore the HBNs AP have a dominant anatase phase. These observations were acquired from peak intensity comparisons of Raman spectra. Further investigation has shown that during the treatment an ionic exchange takes place and the potassium titanates become protonated titanates. During the subsequent calcination, a re-organisation takes place where the anatase phase emerges leaving pores in the structure of the HBNs. More information on the experiments conducted to derive to this hypothesis can be found in section 3.9. This phase-altering protonation treatment affects light absorption, as discussed in the previous section, but more importantly has significantly affected the CO_2 photoreduction product selectivity. The selectivity of the HBNs BP towards CO was 91% and 9% for CH_4, while the HBNs AP dramatically shifted to 33% towards CO and 67% for CH_4, while maintaining very good conversion rates in relation to P25. P25 demonstrated a selectivity of 44% towards CO and 56% towards CH_4. The HBNs where able to outperform P25 in both selectivity and conversion rates with the incorporation of the protonation treatment (Table 1).

4.2.3 Performance of RuO₂-HBNs and CuO-HBNs in CO₂ photoreduction

The HBNs AP have been the best performing photocatalyst material in the initial comparison between HBNs BP, HBNs AP and P25 in terms of overall CO_2 conversion and light absorption as described above. Therefore, HBNs AP was used to fabricate the RuO_2-HBNs and CuO-HBNs samples. For the RuO_2-HBNs sample, Ru^{4+} particles were

found decorating the HBNs microstructures when examined under HR-TEM, EDX and XPS analysis. The material exhibited a slightly reduced photon flux of 45 μmol m^{-2} s^{-1} as opposed to 48.2 μmol m^{-2} s^{-1} for the HBNs AP which explains the slight conversion penalty observed. However, the RuO$_2$-HBNs have shown a further increase in CH$_4$ selectivity, up to 74 % compared to 67 % for the HBNs AP which was attributed to the effective photoexcited charge separation and suppressed recombination rate. The CuO-HBNs synthesis revealed an interesting morphology where CuO particles (100-300 nm) were found decorating the tips of the nano-branches of the HBNs. The CuO-HBNs have demonstrated increased optical performance with a photon flux of 54.2 μmol m^{-2} s^{-1}, yet a selectivity profile similar to P25 and a modest CO$_2$ conversion. The CuO particles are likely acting as recombination centers prohibiting the reaction flow.

4.3   Research impact

The current study presents a novel nanostructured photocatalyst material with the ability to alter its selectivity of the reaction products of CO$_2$ photoreduction utilising a simple protonation treatment. Such material has not been reported in the literature before, to the best of the author`s knowledge. The HBNs have demonstrated superior performance in terms of light absorption, conversion and selectivity when compared to the benchmark P25. Furthermore, with the compound RuO$_2$-HBNs material a further CH$_4$ selectivity boost was achieved while the CuO-HBNs material exhibited improved optical performance. Overall, the study presents a photocatalyst with simple and uniquely tuneable selectivity control over the products of CO$_2$ photoreduction which was absent from the existing literature.

4.4   Personal development

Most of the skills required for characterisation, synthesis and reaction were acquired from previous work (refer to Chapter 5 & 6). However, the body of work reported in this chapter was conducted under strict time frames and had to be scheduled extremely carefully due to constraints resulting from the global pandemic restrictions of COVID-19. Significant scheduling and planning was required to ensure that the time-frames were met by accounting for unexpected delays such as Covid-19 lock-down or outsourced characterisations delays. One example would be when the XPS instrument from Harwell facility required a service (part replacement) and the required spare part shipping was

significantly delayed, due to reasons related to Covid-19. The samples have also been tested in another XPS facility, at St-Andrews University in order to keep the research progressing on schedule, accounting for unexpected delays. The delayed results from Harwell XPS facility were used as a confirmation of the initial analysis. Such contingency plans had to be made all throughout the entire research planning. Furthermore, ensuring adequate chemical supply and sufficient lab-time (restricted access due to university policy regarding Covid-19) was another consideration. For example, a plan was made identifying all consumables and chemicals that might have been required in the future research and their quantities. All these consumables and chemicals were pre-ordered creating a safety stock. Careful consideration of possible outcomes and anticipation of the next step, in regard to research, was required to overcome these challenges and was certainly a valuable lesson for future project planning.

Publication 1

Title: Hierarchical Hyper-branched Titania Nanorods with Tuneable Selectivity for CO$_2$ Photoreduction.

Authors: Gavrielides Stelios, Jeannie Z.Y. Tan and M. Mercedes Maroto-Valer

Status: Published

Supplementary information for Publication 1 can be found in Appendix: A

Abstract

Utilising captured CO_2 and converting it into solar fuels can be extremely beneficial in reducing the constantly rising CO_2 concentration in the atmosphere while simultaneously addressing energy crisis issues. Hence, many researchers have focused their work on the CO_2 photoreduction reaction for the last 4 decades. Herein, the titania hyper-branched nanorods (HBNs) thin films, with a novel hierarchical dendritic morphology, revealed enhanced CO_2 photoreduction performance. The HBNs exhibited enhanced photogenerated charge production (66%), in comparison with P25 (39%), due to the unique hyper-branched morphology. Furthermore, the proposed HBNs thin films exhibited high degree of control over the product selectivity, by undergoing a facile phase-altering treatment. The selectivity was shifted from 91% towards CO, to 67% towards CH_4. Additionally, the HBNs samples showed the potential to surpass the conversion rates of the benchmark P25 TiO_2 in both CO and CH_4 production. To further enhance the selectivity and overall performance of the HBNs, RuO_2 was incorporated into the synthesis, which enhanced the CH_4 selectivity from 67% to 74%; whereas the incorporation of CuO revealed a selectivity profile comparative to P25.

4.5 Introduction

CO_2 photoreduction is one of the promising carbon neutral energy sources, which has the potential to produce solar fuels, such as CH_4 and CO, by using water as an electron donor and light as the input of energy.[2, 3] However, CO_2 photoreduction is a thermodynamically unfavourable process, which requires large energy input to stimulate the occurrence of the reduction reaction.[4] The main challenge for CO_2 photoreduction is the limited light energy absorbance in addition to the high stability of the CO_2 molecule, and thus high energy input is required for this conversion (1498 kJ mol^{-1}).[5] Consequently, the fabrication of highly efficient photocatalysts becomes a very important task.

TiO_2 is the most extensively used photocatalyst for photocatalysis as well as CO_2 photoreduction, accounting for roughly 40% of the publications on CO_2 photoreduction.[6-12] The main advantages of TiO_2 are its chemical and thermal stability, high charge transfer potential, abundance, non-toxicity and cost.[13-15] TiO_2 has a relatively wide band gap, which allows for an effective redox potential for CO_2 photoreduction, but at the same time limits the range of electromagnetic radiation

wavelengths that it can absorb. Hence, the wide band gap and the consequent wavelength absorption limitation is considered the main challenge for TiO_2.[13, 16] Foreign element doping, semiconductor coupling, and photosensitisation are amongst the most popular methods implemented to expand the light absorbance and improve the photocatalytic performance of TiO_2.[17] Despite the fact that morphological alterations wouldn't widen the range of wavelengths that can be absorbed by the photocatalyst, morphology still is an important parameter and it has the potential to improve the amount of light absorbed, increase the surface area and thereby expose more active sites.

The morphological alterations of 3D hierarchical TiO_2 nanostructures have received considerable attention as they were found to enhance the photocatalytic performance.[18] This was attributed to the synergistic benefits of their complex structure, which is composed from basic nanoscale building blocks that preserve their unique individual properties (*i.e.*, 0D spheres, 1D nanorods, 2D sheets, *etc.*). Such 3D hierarchical structures, which consists of 1D building blocks that are combined to form 3D super-structures, have been reported to enhance light harvesting due to light scattering effects, increase surface area and improved charge transport.[19-23]

The effects of morphological design for CO_2 photoreduction is demonstrated herein using hierarchical 1-3D TiO_2 Hyper-Branched Nanorod (HBNs) grown on Fluorine-Tin Oxide (FTO) conductive glass. The unique morphology of the HBNs microstructures revealed a significant increase of light absorption due to increased number of exposed active sites and light scattering effects. Hence, the fabricated HBNs showed high photocatalytic performance in CH_4 and CO production under visible light irradiation. Interestingly, the fabricated HBNs demonstrated the ability to shift and increase the product selectivity through a facile protonation treatment. The best performing sample has demonstrated an internal quantum efficiency of $\Phi_{CH4} = 0.3\%$.

4.6 Experimental procedure

Materials & Synthesis

Potassium titanium oxide oxalate dihydrate (PTO, ≥98.0%), diethylene glycol (DEG, 99.0%), bis(cyclopentadienyl)ruthenium ((C_5H_5)$_2$Ru, 98.0%), Copper (II) acetate (Aldrich, 98%), *n*-hexane (C_6H_{14}, 95.0%). Isopropanol (IPA, 99.5%), acetone (>95.0%) and ethanol (99.0%) were procured from Fisher Scientific. All chemicals were used without any further purification. All aqueous solutions were prepared using milli-Q

ultrapure type 1 water (18.2 MΩ.cm) collected from a Millipore system. Fluorine-doped tin oxide (FTO) TEC-15 glass was purchased from Ossila (2.5 cm x 2.5 cm, roughness of 12.5 nm, FTO layer thickness of 200 nm, 83.5% transmission and resistivity of 12-14 Ω cm^{-1}). Degussa P25 TiO_2 was purchased from Sigma Aldrich.

Before the use of the FTO glass slides, they were cleaned using a solution of H_2O, IPA, and Acetone in a ratio of 1:1:1. The glass was submerged into the solution and sonicated for 1 h. The glass was then dried at 75 °C for 30 mins.

Titania hyper-branched nanorods (HBNs BP) were fabricated using a hydrothermal approach. Similar synthesis has been performed in our previous studies.[24] Potassium titanate oxide oxalate dihydrate (PTO) was dissolved in a mixture of H_2O and DEG in a 1:7 ratio. The concentration of PTO was 0.05 M. The precursor solution was stirred for 30 minutes before it was transferred to a 100 mL Teflon-lined autoclave along with the FTO glass. The FTO glass was resting against the Teflon-liner walls with the conductive side facing down at approximately 60°. The hydrothermal synthesis was carried out at 180 °C for 9 h. The autoclave was allowed to cool down to room temperature and the titania HBNs were rinsed several times altering between Milli-Q (18 mΩ) water and ethanol. The rinsed samples were then calcined at atmospheric conditions at 550 °C for 1 h. This sample will be depicted as **HBNs BP** which stands for "before protonation".

Hyper-branched nanorods (HBNs) protonation treatment was performed after the calcination of the previous step. The as-prepared Titania HBNs BP were allowed to naturally cool down to room temperature and were then submerged in ethanolic HCl (0.04M) for 3 h and aqueous HCl (0.02M) for another 3 h, with mild agitation. The HCl solution was replaced with fresh HCl solution every 1 h. Following this procedure, the as-prepared thin-films were rinsed with both ethanol and DI water several times and were submerged in ethanol for another 1 h in mild agitation. They were then dried in the oven at 70 °C overnight before another calcination at atmospheric conditions at 400 °C for 2 h. Samples that had undergone this protonation treatment will be depicted as **HBNs AP**.

Synthesis of RuO_2 loaded HBN (RuO_2-HBNs) was synthesized under dry nitrogen atmosphere, in a custom-made glove box. Bis(cyclopentadienyl)ruthenium $(C_5H_5)_2Ru$, was dissolved in n-hexane (C_6H_{14}) to achieve a molar concentration of 0.005M and stirred vigorously at atmospheric temperature for 1.5 h until a clear solution was obtained. The HBNs AP loaded glass-slide was then placed into the teflon liner resting against its walls at 60 ° as described before, with the coated surface facing down. The ruthenium precursor

liquid was added to the Teflon-liner to cover the entire FTO glass surface (25 ml). The Teflon liner was then transferred into the autoclave and was placed in the oven at 180 °C for 30 h. The Ru-TiO$_2$ FTO glass was then rinsed with n-hexane and calcined to 400 °C for 10 h with a ramp rate of 10 °C min^{-1}.

Synthesis of CuO loaded TiO$_2$ (CuO-HBNs) Copper (II) acetate was dissolved in 50 mL of ethanol at a concentration of 0.005 M. The solution was stirred for 30 minutes. Then 2 mL of NaOH was added drop-wise and stirred for another 60 min, obtaining the final solution that was used to fabricate the CuO-HBNs thin film. The Cu precursor solution was transferred to a 100 mL Teflon-lined autoclave along with the HBNs AP loaded FTO glass. The glass was positioned resting against the Teflon-liner walls with the coated side facing down at approximately 60°. The solvothermal treatment was carried out at 150 °C for 5 h. The autoclave was allowed to cool down to room temperature, and the CuO-HBNs slides were rinsed with ethanol and then calcined to 400 °C for 10 h with a ramp rate of 10 °C min^{-1}.

4.7 Characterization

Crystallinity and phase identification of the synthesized products were conducted using powder X–ray diffraction XRD (Bruker D8 Advanced Diffractormeter) equipped with Cu Kα radiation (λ= 1.5418 Å) and compared with the ICDD–JCPDS powder diffraction file database. The morphological features of the synthesized samples were examined by a field emission scanning electron microscope (FE-SEM, FEI Quanta 200 F). Further investigation on the morphology at higher magnification and the element composition of the samples was carried out using a high-resolution transmission electron microscope (HR-TEM, FEI Titan Themis 200) equipped with an energy dispersive X-ray spectroscope (EDX) detector operated at 200 kV. The sample for HR-TEM analysis was prepared by gently removing the coating off the FTO glass surface. And then, the powder obtained was suspended in ethanol shaken vigorously for 5 minutes until a cloudy solution was achieved, then a few drops of the solution were placed on a carbon-coated nickel TEM grid and was left to dry in atmospheric conditions. Crystallinity and phase identification of the synthesized products were performed using Raman, which were recorded using a Renishaw *inVia* Raman Microscope with 785 nm excitation source. The diffuse reflectance was measured using a Perkin Elmer Lambda 950 UV-vis equipped with an integrating sphere (150 mm) and the band gap energy was estimated using the Kubelka Munk function. X-ray photoelectron spectroscopy (XPS) was performed on

Scienta 300 XPS machine incorporating with a rotating Al Kα X-ray source operating at 13 kV x 333 mA (4.33 kW). Electron analysis was performed using a 300 cm radius hemispherical analyser and lens system. The electron counting system consist of a multichannel plate, phosphorescent screen and CCD camera. All multichannel detection counting is done using proprietary Scienta software. The elements present were determined via a wide energy range survey scan (200 mW step, 20 ms dwell time, 150 eV pass energy and summed over 3 scans). The high-resolution scans were performed at a similar pass energy (150 eV), but a step size of 20 mV. A dwell time of 533 ms was used and accumulated over 3 scans. The instrument operated at a base pressure of 1 x 10^{-9} mbar; the energy scale is calibrated using the Au 4f, Ag 3d and Cu 2p emission lines, where the half width of the Au $4f_7$ emission line is approximately 1.0 eV. All data analysis and peak fitting were performed using the CaseXPS software. The photon flux was measured by using the spectroradiometer (Apogee-200 from Apogee Instruments), at a set distance of 20 cm from the light source (OmniCure S2000) that was used in the CO_2 photoreduction reaction. The blank measurement was performed using a blank FTO glass. The quantum efficiency measurement of CO and CH_4 were calculated using equations (4.1) and (4.2) accounting for the electrons needed for the conversion of each compound, respectively. The average production value was used for the internal quantum efficiency measurement of each product.

$$\Phi_{CH4}(\%) = \frac{8 \; x \; CH_4 yield}{photons \; absorbed} x \; 100 \tag{4.1}$$

$$\Phi_{CO}(\%) = \frac{2 \; x \; CO \; yield}{photons \; absorbed} x \; 100 \tag{4.2}$$

4.8 CO_2 Photoreduction

The CO_2 photoreduction were performed using the experimental set-up as described in previous work.[25] Briefly, the FTO glass samples were inserted into the cut-out slot of the photoreactor as shown on Figure 4.1. Before each photocatalytic test, a purge and equilibration regime was followed, where the system was placed under vacuum (-100 kPa) and then the vacuum was released with CO_2 (99.995%) until it reached 100 kPa of pressure. The pressure was then released through the injection port of the gas chromatograph (GC, Agilent, Model 7890B series). This process was repeated three times and on the final repetition the system was left with a CO_2 flow rate of 0.35 mL min^{-1} passing through a temperature-controlled saturator for at least 16 h (overnight) to allow the system to equilibrate. Relative humidity (±1.8% RH) was measured using an inline

73

Sensirion SHT75 humidity sensor embedded (MG Chemicals 832HD) nested into a Swagelok 1/4" T-piece. Relative humidity is expressed as a percentage of the water vapor relative to the temperature of the air and therefore it's the percentage of the actual water vapor compared with the total amount of water vapor that can exist in the air at the current temperature. The temperature of the photoreactor (40 °C) was controlled using a hot plate and the surface of the photocatalyst measured using a Radley's pyrometer (±2.0 °C). The temperature was chosen as the lowest temperature that would allow the H_2O to remain in gaseous form. An OmniCure S2000 light source (300-600 nm wavelength) was placed 30 mm above the surface of the investigated sample. Irradiance (150 mW cm^{-2}) at the end of the fiber optic light guide was measured before each experiment using an OmniCure R2000 radiometer (±5%). An inline GC with a Hayesep Q column (1.5 m), 1/16 inch OD, 1 mm OD), Molecular Sieve 13X (1.2 m), 1/16-inch OD, 1 mm ID), thermal conductivity detector (TCD), nickel catalyzed methanizer, and flame ionization detector (FID) was used to analyze the output of the photoreactor every four min. The GC was calibrated using 1000 ppm calibration gas (H_2, CO, O_2 and CH_4 in Ar balance). It was then further diluted with Ar (99.995%) using mass flow controllers to 17.04, 4.62 and 1 ppm using the FID detector for CH_4 and CO, respectively, and 69.49, 34.72 and 17.04 ppm using the TCD detector for H_2 and O_2.
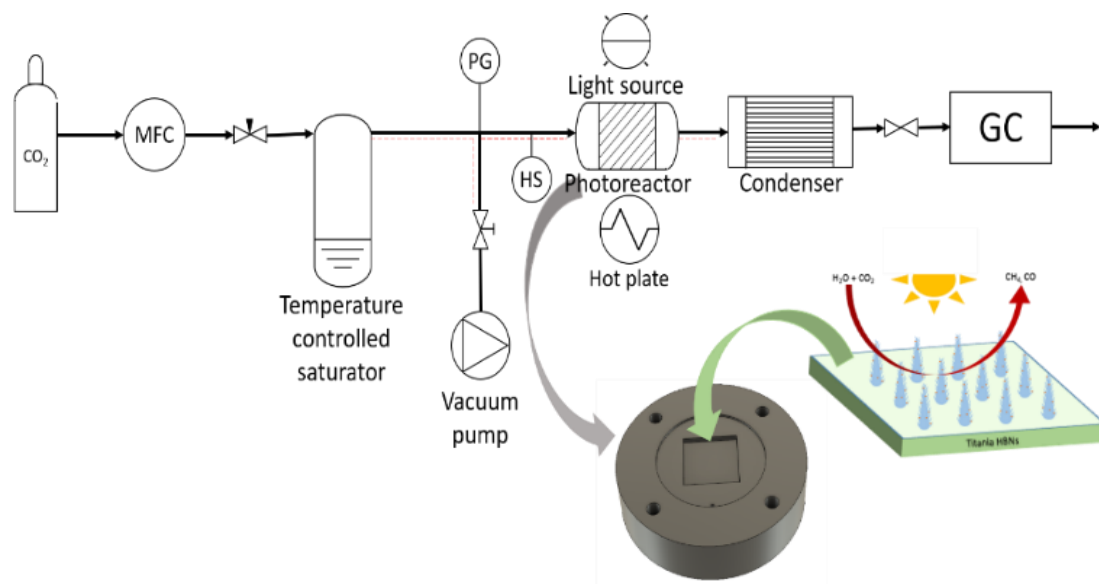

Figure 4.1 – Photoreduction rig set-up diagram including 3D rendering of the custom photoreactor and thin film HBN photocatalyst. (Not to scale)

Control experiments were carried using all the fabricated samples to investigate the genuine production of carbonaceous products from CO_2.

1. CO_2 was replaced with N_2;

2. Light source was turned off.

Other experimenting parameters were unchanged.

4.9 Results and discussion

The titania HBNs were fabricated using a facile hydrothermal treatment on conductive FTO glass slides. The XRD pattern of HBNs BP evidenced the presence of anatase and $K_2Ti_4O_9$ (Figure 4.2a). After the protonation treatment, $K_2Ti_4O_9$ was removed, leaving only anatase phase within the sample HBNs AP. Due to the weak signal in XRD, Raman spectroscopy was utilised to investigate the crystallinity and crystal phase of the samples (Figure 4.2b). Raman signal responds to spatial order, associated with crystalline structures, with a sharp peak and narrow bands, whereas amorphous solids and their lack of spatial order in the crystal lattice translates to broad peak signals.[26] The as-prepared HBNs BP sample exhibited mainly potassium titanate features shown at 188, 279, 441 and 652 cm^{-1}.[27] Meanwhile, a weak signal of the anatase phase feature was observed at 143, 395, 517, and 638 cm^{-1} associated with the E_g, B_{1g}, A_{1g}, and E_g vibrations, respectively.[24] Potassium titanate was the dominant phase and the relative ratio of potassium titanate to anatase was estimated at 7:1.

The HBNs BP was treated with a facile protonation treatment forming HBNs AP. As a result, a phase shift was observed, in which the anatase phase (*i.e.,* 143, 395, 517, and 638 cm^{-1}, Figure 4.2) was shown the dominant phase. The relative ratio of potassium titanate to anatase was reduced to 1:10. Additionally, traces of rutile phase were spotted at 442 and 631 cm^{-1}, attributing to the use of HCl acid.[27] Degussa P25, which is used as the benchmark sample in this study was also characterised as shown in Figure 4.2. Degussa P25 was suspended in water and deposited on an FTO glass.

The as-prepared HBNs samples showed homogeneous and full coverage of coating on the surface of the FTO glass (Figure 4.3a-c). A dendritic microstructure (3-5 μm in height) was revealed, decorated with numerous nano-branches growing along the dendrites. The growth orientation was generally upwards with a chaotic directionality of the nano-branches. The width and length of the nano-branches were ~5-20 and 50–350 nm, respectively (Figure 4.3d-g).[24, 28, 29]
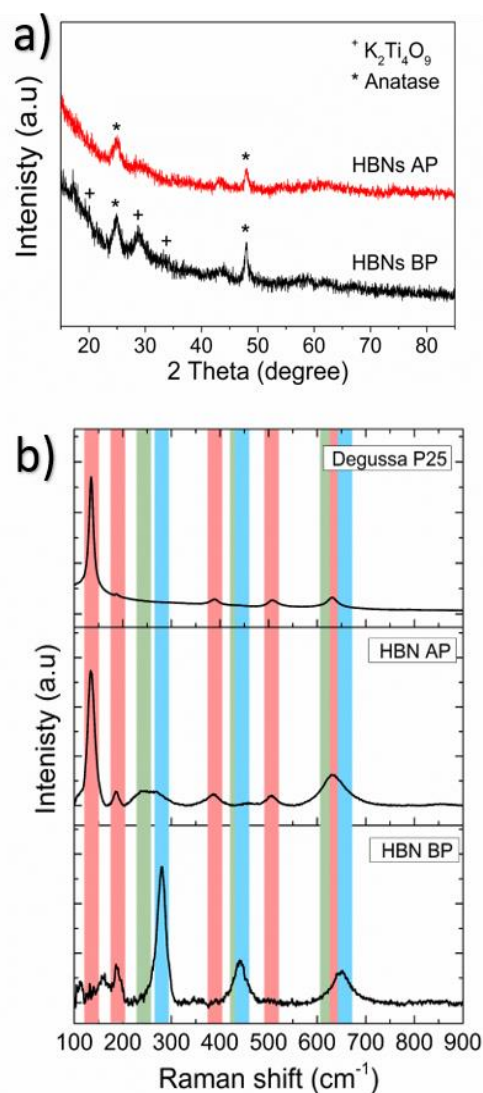
Figure 4.2 – X-ray diffraction pattern for the as prepared HBNs BP and HBNs AP (a), Raman spectra of the fabricated samples with potassium titanates (blue), anatase (red) and rutile (green) components (b).

After the protonation treatment, no significant changes were observed in the morphology of the HBNs structure (Figure 4.3g) and the thin film remained intact. Prior to the subsequent calcination, the titanate phase of the thin film remained as the dominant phase (Figure B.1) and exhibited a polycrystalline structure under SAED examination (Figure 4.4a). After the calcination, the polycrystalline titanate phase was significantly reduced and a highly crystallised c-axis elongated anatase phase emerged (Figure 4.4b). As a result of protonation treatment and calcination processes, the formation of pores was observed on the nano-branches and dendrites (Figure 4.4c, d). Hence, the mechanism of protonation was proposed. During the protonation treatment, ionic exchange reaction took place, in which potassium titanate converted to protonated-titanate. Then, the

subsequent calcination treatment resulted the protonated titanate to re-organise into anatase phase of TiO_2 as observed in the Raman spectra (Figure A.1) and the re-organisation created the observed porosity (Figure 4.4d).[27, 30]
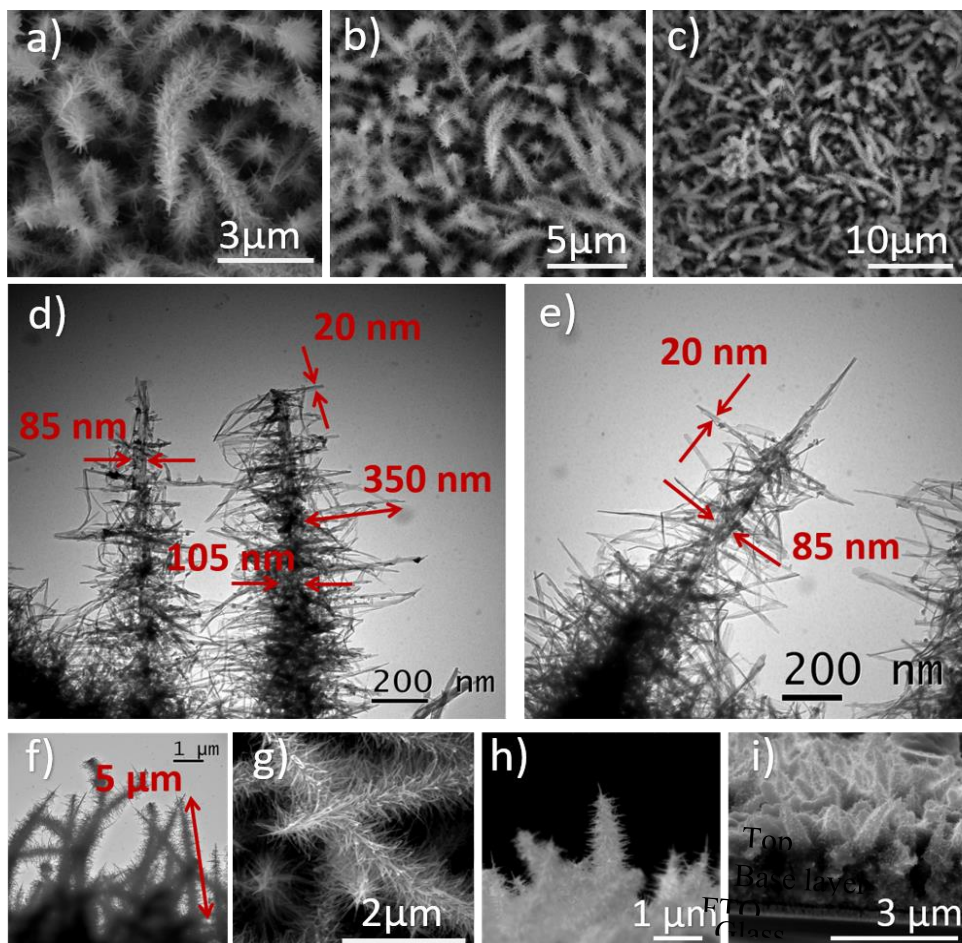

Figure 4.3 - Different magnification of the same area of the HBNs BP sample under SEM (a-c) and TEM (d-f), The top view (g) and cross-section (h and i) of HBNs AP sample.
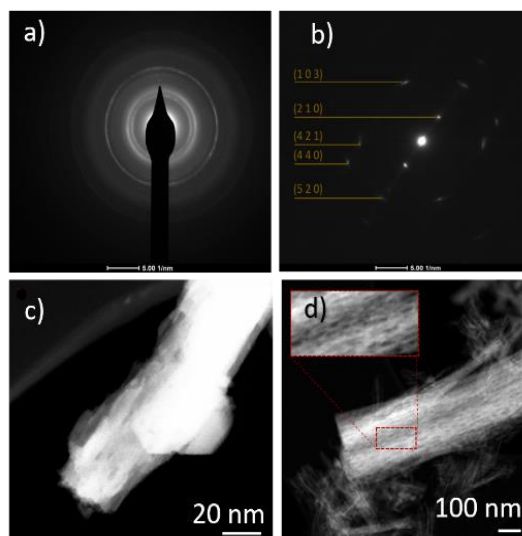

Figure 4.4 - SAED pattern and TEM imaging of HBNs BP (a and c, respectively) and HBNs AP (b and d,

The optical properties of the HBNs were analysed using UV-vis and spectroradiometry. The HBNs BP sample showed higher reflectance compared to the HBN AP, indicating the latter possessed higher optical properties than the former (Figure 4.5). Moreover, the cut-off wavelength of the HBNs AP was longer than HBNs BP, implying a band gap narrowing after the protonation treatment. The band gap of the HBNs BP was estimated at 3.7 eV; whereas after protonation treatment, the band gap was reduced to 3.4 eV. This was attributed to the shift from titanates to anatase phase. The photon-flux of HBNs AP increased from 39.8 (*i.e.,* HBNs BP sample) to 48.2 μmol m^{-2} s^{-1} under irradiation of visible light in the range of 300 – 600 nm. The increase of photon-flux could be explained by the band gap narrowing as shown in the UV-vis results. Meanwhile, the benchmark P25 showed a photon-flux of 28.6 μmol m^{-2} s^{-1}. Hence, the effective photon flux for the photocatalytic reaction obtained from the HBNs BP, HBNs AP and P25 samples were 54, 66 and 39%, respectively. As expected, the amount of light absorbed by the HBNs microstructures was significantly higher than P25 due to the large surface area of the HBNs even though P25 possessed a narrower band gap.
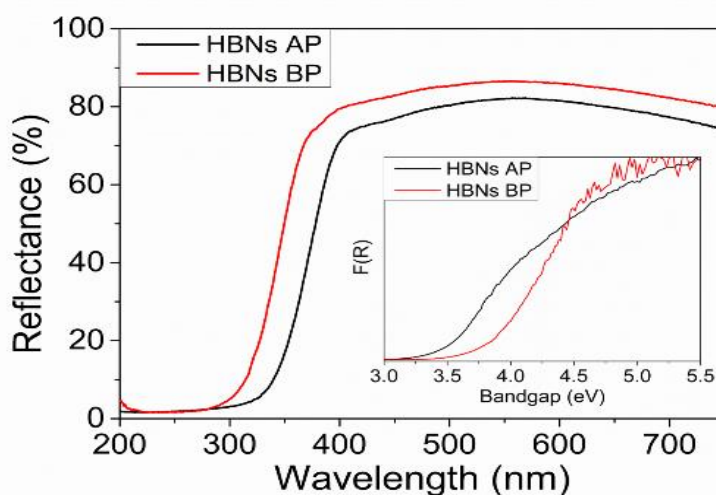
Figure 4.5 - Diffuse reflectance spectra with a Kubelka-Munk inset for band gap calculation.

The CO$_2$ photoreduction reaction was performed using a custom-made reactor designed for the FTO glass and was connected and analysed using GC (Figure 4.1).[25, 31, 32] The HBNs BP exhibited a cumulative conversion of CO at 7.9 μmol g$_{cat}^{-1}$ h^{-1}). On the other hand, it exhibited a very low selectivity towards CH$_4$ (9%) and produced only 0.4 μmol g$_{cat}^{-1}$ h^{-1} of CH$_4$ in contrast to 6.9 μmol g$_{cat}^{-1}$ h^{-1} for P25. Although the overall conversion of HBNs BP was the lowest among the samples, the superior selectivity towards CO resulted the highest production of CO. HBNs AP displayed a selectivity shift towards CH$_4$ (67%), producing the highest cumulative conversion of CH$_4$

(8.7 µmol $g_{cat}^{-1} h^{-1}$, Table 4.1) surpassing both the P25 and HBNs BP sample. Therefore, the HBNs had shown great flexibility in adjusting the product selectivity by treating the sample using a facile protonation step. It is worth noting that the HBNs AP with dominating anatase phase had shown significantly higher photocatalytic activity compared to the titanate rich HBNs BP. This was attributed to the higher charge transfer potential associated with the anatase phase of TiO_2 as well as the porosity formed which provides easy access to the surface of the material.[33] To the best of the authors knowledge, the utilisation of a simple protonation step to alter the selectivity of the HBN material for CO_2 photoreduction has not been reported in the literature

To further investigate the potential of the already modified selectivity and performance of the as-prepared photocatalyst, the HBNs microstructures were loaded with RuO_2 and CuO, respectively and the photoreduction results are shown in Table 4.1. The best performing HBNs AP sample (*i.e.*, in terms of cumulative overall conversion), was employed for the synthesis of the RuO_2-HBNs and CuO-HBNs samples. HBNs AP, RuO_2-HBNs and CuO-HBNs were examined under Raman and revealed very similar peaks of predominantly anatase, weak signals of potassium titanate and traces of rutile. However, no Ru or Cu related peaks could be identified (Figure A.2). This could be attributed to the low concentration of the RuO_2 and CuO as well as highly dispersed clusters of these foreign elements.[24, 34] The microstructure of RuO_2-HBNs and CuO-HBNs did not show significant changes after the loading of RuO_2 and CuO.

The CuO-HBNs samples revealed some dangling nanoparticles (50-150 nm) attached to the tips of the nano-branches of the HBNs (Figure 4.6a, b). These particles

Table 4.2 – Results of CO_2 photoreduction for HBNs BP, HBNs AP Degussa P25, RuO_2-HBNs and CuO-HBNs. Unprocessed GC data is available in Figure A.4. Selectivity calculations take into consideration only CH_4 and CO production values.

Sample name	CH_4 selectivity (%)	CH_4 cum. conversion (µmol $g_{cat}^{-1} h^{-1}$)	CO selectivity (%)	CO cum. conversion (µmol $g_{cat}^{-1} h^{-1}$)
HBNs BP	9	0.4	91	7.9
HBNs AP	67	8.7	33	4.3
P25 TiO_2	56	6.9	44	5.1
RuO_2-HBNs	74	5.2	26	1.8
CuO-HBNs	53	2.5	47	2.2

were evidenced as Cu nanoparticles under the elemental analysis of HR-TEM (Figure 4.6c, f). Upon closer inspection of RuO_2-HBNs under HR-TEM, some nanoparticles (50-60 nm) were found loaded on the HBNs structures (Figure 4.6g-i). Elemental analysis was performed to identify the elemental composition of the observed nanoparticles on the sample. Ru element was spotted and identified on the HBNs while Ti and O were identified as the dominant elements of the HBN structure (Figure 4.6i-l).

Further insight regarding elemental composition was acquired utilising XPS. The XPS results showed that the loaded Cu and Ru was 3 and 1 at%, respectively. The Ru $3d_{5/2}$ peak was found at 280.7 eV, which is associated to Ru^{4+}, evidencing the presence of RuO_2 nano-particles on the RuO_2-HBNs sample (Figure 4.7b).[35, 36] Regarding the CuO-HBNs sample, the Cu $2p_{3/2}$ peak emerged at 932.9 eV and was attributed to Cu^{2+}, which led to the conclusion that the observed dangling particles were CuO nanoparticles (Figure 4.7c). The Ti 2p with 5.7 eV of spacing between Ti $2p_{1/2}$ and $2p_{2/3}$ evidenced the presence of TiO_2. The Ti 2p, O1s as well as the adventitious carbon C1s peaks were found in all samples as expected under X-ray photoelectron spectroscopy.[37] A weak signal of K 2p was observed even after the protonation treatment on the survey scan for both samples, (Figure A.3) showing some amount of potassium was still present in the sample as it was also confirmed by the Raman investigation.[38]

The optical properties were examined using UV-Vis and spectroradiometer measurements. The RuO_2-HBNs exhibited a very similar reflectance to the HBN-AP, possibly because of the very low concentration of RuO_2 on the sample. However, CuO-HBNs has shown increased light absorption in the 350 – 800 nm range (Figure 4.5). The band gap energy of was estimated at 3.4 eV for all the samples as can be seen in the inset
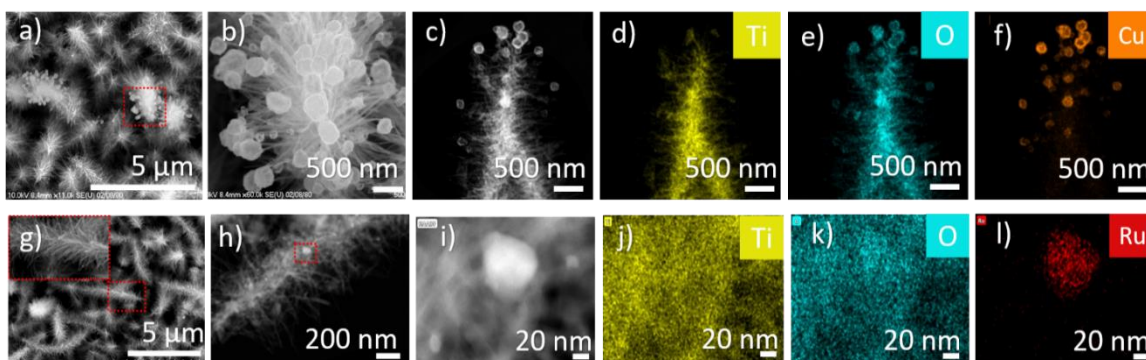

Figure 4.6 – Microscopy morphology investigation and elemental mapping EDX. a,b) SEM imaging for CuO-HBNs, c,d,e,f) EDX analysis for CuO-HBNs. g) SEM imaging with zoomed inset for RuO_2-HBNs, h) TEM imaging for RuO_2-HBNs, i,j,k,l) EDX analysis for RuO_2-HBNs.

of Figure 4.5. The spectroradiometer measurements have shown the RuO_2-HBNs to have slightly reduced photon flux 45 μmol m^{-2} s^{-1} when compared to the HBNs AP 48.2 μmol m^{-2} s^{-1}. However, the CuO-HBNs exhibited increased photon flux at 54.2 μmol m^{-2} s^{-1}. The results acquired from the GC for RuO_2-HBNs and CuO-HBNs are shown in Table 4.1. The RuO_2-HBNs sample has shown further increase on the CH_4 selectivity to 74% compared to HBNs AP sample (67%). However, a reduction in conversion yield was observed in RuO_2-HBNs (*i.e.*, from 8.7 μmol g_{cat}^{-1} h^{-1} to 5.2 μmol g_{cat}^{-1} h^{-1} in HBNs AP). This was attributed to the reduced photon flux observed under the spectroradiometer measurements when compared with HBNs AP. The improved product selectivity towards CH_4 as exhibited in RuO_2-HBNs was attributed to the effective charge separation, and suppressed electron-hole recombination, allowing more photogenerated electrons to participate in CO_2 photoreduction reaction, consequently amplifying the multi-electron conversion of CH_4 as opposed to the 2-electron conversion of CO.[39-42]

An altered selectivity profile was observed with the incorporation of CuO for CuO-HBNs where CH_4 selectivity was decreased compared to HBNs AP. The incorporation of CuO have been reported to improve optical performance and to have the potential to facilitate charge migration.[43] Despite the improved optical performance observed, the CuO-HBNs exhibited a modest overall conversion even though the loading composition was higher than RuO_2-HBNs. This was attributed to the CuO functioning as a recombination centre thereby prohibiting the reaction flow most likely due to the agglomerated relatively large ~300 nm CuO particles observed in Figure 4.6a-c, f. Researchers have previously reported CuO loading acting as a recombination centre resulting in reduced conversion rates.[17, 34, 44, 45] It has also been reported that excessive CuO loading could result in masking the illuminated TiO_2 surface therefore reducing conversion rates.[16,35] Control experiments were conducted as described in the
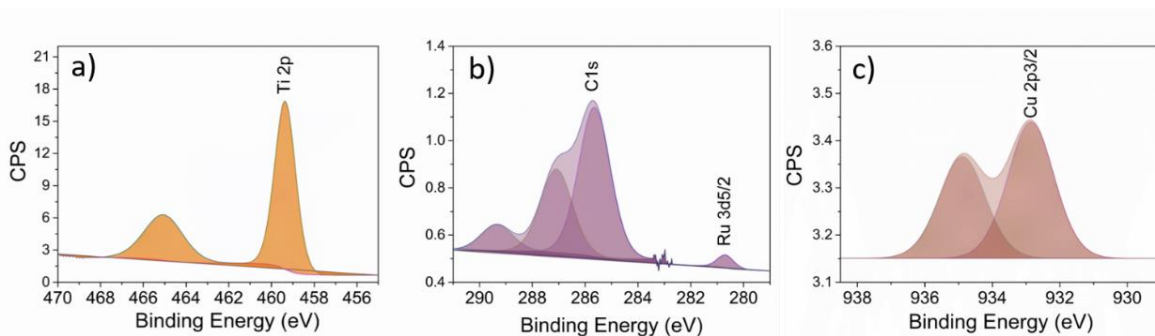

Figure 4.7 - XPS analysis, magnification of the peaks a) Ti 2p of HBNs AP, b) Ru 3d$_{5/2}$ of RuO_2-HBNs and c) Cu 2p$_{3/2}$ *of* CuO-HBNs samples.

experimental procedure section and no or only trace amount of products was observed on the GC.

4.10 Conclusions

A facile protonation treatment has demonstrated the ability to tune the product selectivity of CO_2 photoreduction under 300-600 nm of light irradiation. The hierarchical 1-3D nanostructured HBNs had significantly improved the optical properties of TiO_2, in which the HBNs possessed 66% of photon flux while P25 only showed 39% under 300-600 nm of irradiation. The proposed protonation treatment was able to manipulate the product selectivity of the as-prepared HBNs from 91% towards CO to 67% towards CH_4. As a result, as-prepared HBNs exhibited the highest production of CO, whereas the HBNs AP had the highest production of CH_4. Additionally, the overall conversion of HBNs AP was the highest amongst other samples and achieved an overall quantum efficiency of 0.3%. The RuO_2 loaded HBNs AP managed to further increase the CH_4 selectivity to 74%. CuO loaded HBNs showed drastic increased in light absorption with comparative selectivity performance as P25. Overall, the titania HBN thin films have shown to be a high performing and highly versatile nanostructured material with great flexibility in terms of selectivity for CO_2 photoreduction.

4.11 Further research (not published work)

To further investigate the fabricated photocatalysts electrical response to light, an experiment was conducted using an Autolab electrochemical workstation with a 3 electrode system. For detailed information on how the experiment was conducted refer to section 3.11. During this experiment a series of light on, light off experiments were performed and the materials response to light was recorded, measuring the photocurrent produced in relation to time (Figure 4.8). The RuO_2 HBNs shows the highest photocurrent values when irradiated, which is in agreement with the photoreduction results where the highest CH_4 selectivity was achieved. This could be attributed to the higher density of photoexcited charges which could promote the multi-electron conversion of CO_2 to CH_4. HBNs AP have produced a higher current than HBNs BP which can be expected given the narrowed band gap and improved charge transport associated with the anatase phase, while CuO-HBNs exhibited a modest photocurrent, despite its high light absorption properties. This is attributed to the CuO clusters forming recombination centres for the photoexcited charges. Lastly P25 has shown a poor performance when compared to the HBNs which is largely attributed to their morphology and light harvesting capabilities.
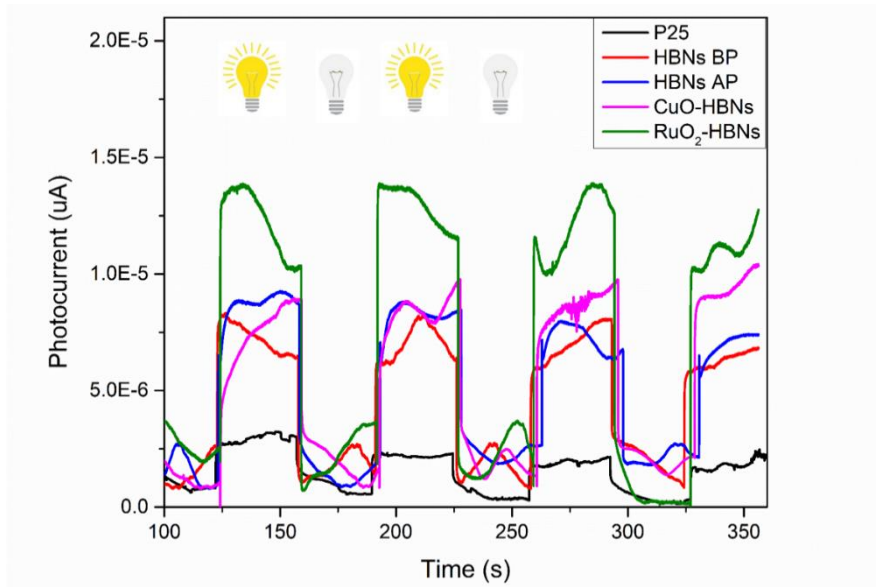

Figure 4.8 – Chronoamperometry measurements for the fabricated samples using the autolab electrochemical workstation in a 3-electrode system in a series of light on/off experiments.

References

[1]   G. Stelios, J. Z. Y. Tan, and M. M. Maroto-Valer, "Hierarchical hyper-branched titania nanorods with tuneable selectivity for CO_2 photoreduction," *RSC Adv.,* 10.1039/D1RA05414G vol. 11, no. 51, pp. 32022-32029, 2021, doi: 10.1039/D1RA05414G.

[2]   X. Chang, T. Wang, and J. Gong, "CO_2 photo-reduction: insights into CO_2 activation and reaction on surfaces of photocatalysts," *Energy Environ. Sci.,* 10.1039/C6EE00383D vol. 9, no. 7, pp. 2177-2196, 2016, doi: 10.1039/C6EE00383D.

[3]   L. Liu, C. Zhao, J. Xu, and Y. Li, "Integrated CO_2 capture and photocatalytic conversion by a hybrid adsorbent/photocatalyst material," *Appl. Catal., B,* vol. 179, pp. 489-499, 2015/12/01/ 2015, doi: https://doi.org/10.1016/j.apcatb.2015.06.006.

[4]   F. E. Osterloh, "Photocatalysis versus Photosynthesis: A Sensitivity Analysis of Devices for Solar Energy Conversion and Chemical Transformations," *ACS Energy Lett.,* vol. 2, no. 2, pp. 445-453, 2017/02/10 2017, doi: 10.1021/acsenergylett.6b00665.

[5]   W. A. Thompson, E. Sanchez Fernandez, and M. M. Maroto-Valer, "Review and Analysis of CO_2 Photoreduction Kinetics," *ACS Sustain. Chem. Eng.,* vol. 8, no. 12, pp. 4677-4692, 2020/03/30 2020, doi: 10.1021/acssuschemeng.9b06170.

[6]   R. Shankar *et al.*, "Porous boron nitride for combined CO_2 capture and photoreduction," *J. Mater. Chem.,* 10.1039/C9TA02793A vol. 7, no. 41, pp. 23931-23940, 2019, doi: 10.1039/C9TA02793A.

[7]   T. W. Woolerton, S. Sheard, E. Reisner, E. Pierce, S. W. Ragsdale, and F. A. Armstrong, "Efficient and Clean Photoreduction of CO_2 to CO by Enzyme-Modified TiO_2 Nanoparticles Using Visible Light," *J. Am. Chem. Soc.,* vol. 132, no. 7, pp. 2132-2133, 2010/02/24 2010, doi: 10.1021/ja910091z.

[8]   J. Núñez, V. A. de la Peña O'Shea, P. Jana, J. M. Coronado, and D. P. Serrano, "Effect of copper on the performance of ZnO and $ZnO1−xNx$ oxides as CO_2 photoreduction catalysts," *Catal. Today,* vol. 209, pp. 21-27, 2013/06/15/ 2013, doi: https://doi.org/10.1016/j.cattod.2012.12.022.

[9]   C. Wang, R. L. Thompson, P. Ohodnicki, J. Baltrus, and C. Matranga, "Size-dependent photocatalytic reduction of CO_2 with PbS quantum dot sensitized TiO2 heterostructured photocatalysts," *J. Mater. Chem.,* 10.1039/C1JM12367J vol. 21, no. 35, pp. 13452-13457, 2011, doi: 10.1039/C1JM12367J.

[10]   "Art Leaf Database - CO_2 Valorization by Artificial Photosynthesis. ." Art Leaf Database - CO_2 Valorization by Artificial Photosynthesis. . http://www.artleafs.eu (accessed (2021), (2021)).

[11]   S. N. Habisreutinger, L. Schmidt-Mende, and J. K. Stolarczyk, "Photocatalytic Reduction of CO_2 on TiO_2 and Other Semiconductors," *Angew. Chem. Int. Ed.,* vol. 52, no. 29, pp. 7372-7408, 2013, doi: https://doi.org/10.1002/anie.201207199.

[12]   J. Z. Y. Tan, Y. Fernández, D. Liu, M. Maroto-Valer, J. Bian, and X. Zhang, "Photoreduction of CO_2 using copper-decorated TiO_2 nanorod films with localized surface plasmon behavior," *Chem. Phys. Lett.,* vol. 531, pp. 149-154, 2012/04/02/ 2012, doi: https://doi.org/10.1016/j.cplett.2012.02.016.

[13]   J. Schneider *et al.*, "Understanding TiO_2 Photocatalysis: Mechanisms and Materials," *Chem. Rev.,* vol. 114, no. 19, pp. 9919-9986, 2014/10/08 2014, doi: 10.1021/cr5001892.

[14]   H. J. Yun, H. Lee, J. B. Joo, N. D. Kim, M. Y. Kang, and J. Yi, "Facile preparation of high performance visible light sensitive photo-catalysts," *Appl. Catal., B,* Article vol. 94, no. 3-4, pp. 241-247, 2010, doi: 10.1016/j.apcatb.2009.11.014.

[15]   Q. Zhang, Y. Li, E. A. Ackerman, M. Gajdardziska-Josifovska, and H. Li, "Visible light responsive iodine-doped TiO2 for photocatalytic reduction of CO_2 to fuels," *Appl. Catal., A,* vol. 400, no. 1, pp. 195-202, 2011/06/30/ 2011, doi: https://doi.org/10.1016/j.apcata.2011.04.032.

[16]   J. Z. Y. Tan, S. Gavrielides, X. Luo, W. A. Thompson, and M. M. Maroto-Valer, "3 - Development of photocatalysts and system optimization for CO_2 photoreduction," in *Nanostructured Photocatalysts*, R. Boukherroub, S. B. Ogale, and N. Robertson Eds.: Elsevier, 2020, pp. 39-73.

[17]   K. Song, J. Zhou, J. Bao, and Y. Feng, "Photocatalytic Activity of (Copper, Nitrogen)-Codoped Titanium Dioxide Nanoparticles," *J. Am. Ceram. Soc.,* vol. 91, no. 4, pp. 1369-1371, 2008, doi: https://doi.org/10.1111/j.1551-2916.2008.02291.x.

[18]   T.-V. Nguyen, J. C. S. Wu, and C.-H. Chiou, "Photoreduction of CO_2 over Ruthenium dye-sensitized TiO_2-based catalysts under concentrated natural sunlight," *Catal. Commun.,* vol. 9, no. 10, pp. 2073-2076, 2008/06/10/ 2008, doi: 10.1016/j.catcom.2008.04.004.

[19]   Y. Wang, W. Yang, and W. Shi, "Preparation and Characterization of Anatase TiO2 Nanosheets-Based Microspheres for Dye-Sensitized Solar Cells," *Ind. Eng. Chem. Res.,* vol. 50, no. 21, pp. 11982-11987, 2011/11/02 2011, doi: 10.1021/ie2016202.

[20]   F. Xu, X. Zhang, Y. Wu, D. Wu, Z. Gao, and K. Jiang, "Facile synthesis of TiO_2 hierarchical microspheres assembled by ultrathin nanosheets for dye-sensitized solar cells," *J. Alloys Compd.,* vol. 574, pp. 227-232, 2013/10/15/ 2013, doi: https://doi.org/10.1016/j.jallcom.2013.04.119.

[21]   E. Hosono, S. Fujihara, H. Imai, I. Honma, I. Masaki, and H. Zhou, "One-Step Synthesis of Nano–Micro Chestnut TiO_2 with Rutile Nanopins on the Microanatase Octahedron," *ACS Nano,* vol. 1, no. 4, pp. 273-278, 2007/11/30 2007, doi: 10.1021/nn700136n.

[22]   J. Lin *et al.*, "3D Hierarchical Rutile TiO_2 and Metal-free Organic Sensitizer Producing Dye-sensitized Solar Cells 8.6% Conversion Efficiency," *Sci. Rep.,* vol. 4, no. 1, p. 5769, 2014/08/29 2014, doi: 10.1038/srep05769.

[23]   E.-H. Kong, Y.-J. Chang, Y.-C. Park, Y.-H. Yoon, H.-J. Park, and H. M. Jang, "Sea urchin TiO_2–nanoparticle hybrid composite photoelectrodes for CdS/CdSe/ZnS quantum-dot-sensitized solar cells," *Phys. Chem. Chem. Phys.,* 10.1039/C2CP24106D vol. 14, no. 13, pp. 4620-4625, 2012, doi: 10.1039/C2CP24106D.

[24]   S. Gavrielides, J. Z. Y. Tan, E. S. Fernandez, and M. M. Maroto-Valer, "Photo-generation of cyclic carbonates using hyper-branched Ru–TiO_2," *Faraday Discuss.,* 10.1039/C8FD00181B vol. 215, no. 0, pp. 407-421, 2019, doi: 10.1039/C8FD00181B.

[25]   W. A. Thompson *et al.*, "Systematic study of TiO_2/ZnO mixed metal oxides for CO_2 photoreduction," *RSC Adv.,* 10.1039/C9RA03435H vol. 9, no. 38, pp. 21660-21666, 2019, doi: 10.1039/C9RA03435H.

[26]   T. David, "Why Are the Raman Spectra of Crystalline and Amorphous Solids Different?," *Spectroscopy,* vol. 32, no. 3, pp. 26–33, 2017. [Online]. Available: https://www.spectroscopyonline.com/view/why-are-raman-spectra-crystalline-and-amorphous-solids-different.

[27] H. C. X-Y Liu, "A Raman study of Titanate Nanotubes," *S. Afr. J. Chem.,* vol. 58, pp. 110 - 115, 2005.

[28] W.-Q. Wu, H.-S. Rao, H.-L. Feng, X.-D. Guo, C.-Y. Su, and D.-B. Kuang, "Morphology-controlled cactus-like branched anatase TiO_2 arrays with high light-harvesting efficiency for dye-sensitized solar cells," *J. Power Sources,* vol. 260, pp. 6-11, 2014/08/15/ 2014, doi: https://doi.org/10.1016/j.jpowsour.2014.02.107.

[29] W.-Q. Wu and L. Wang, "A 3D hybrid nanowire/microcuboid optoelectronic electrode for maximised light harvesting in perovskite solar cells," *J. Mater. Chem.,* 10.1039/C8TA09806A vol. 7, no. 3, pp. 932-939, 2019, doi: 10.1039/C8TA09806A.

[30] T. Butburee *et al.*, "2D Porous TiO_2 Single-Crystalline Nanostructure Demonstrating High Photo-Electrochemical Water Splitting Performance," *Adv. Mater.,* vol. 30, no. 21, p. 1705666, 2018, doi: https://doi.org/10.1002/adma.201705666.

[31] J. Z. Y. Tan, S. Gavrielides, H. R. Xu, W. A. Thompson, and M. M. Maroto-Valer, "Alkali modified P25 with enhanced CO_2 adsorption for CO_2 photoreduction," *RSC Adv.,* 10.1039/D0RA05010E vol. 10, no. 47, pp. 27989-27994, 2020, doi: 10.1039/D0RA05010E.

[32] W. Thompson, E. Sanchez Fernandez, and M. Maroto-Valer, "Probability Langmuir-Hinshelwood based CO_2 photoreduction kinetic models," p. 123356, 11/01 2019, doi: 10.1016/j.cej.2019.123356.

[33] T. Luttrell, S. Halpegamage, J. Tao, A. Kramer, E. Sutter, and M. Batzill, "Why is anatase a better photocatalyst than rutile? - Model studies on epitaxial TiO_2 films," *Sci. Rep.,* vol. 4, p. 4043, 2014/02/10/ 2014. [Online]. Available: http://dx.doi.org/10.1038/srep04043.

[34] Y. Li, W.-N. Wang, Z. Zhan, M.-H. Woo, C.-Y. Wu, and P. Biswas, "Photocatalytic reduction of CO2 with H2O on mesoporous silica supported Cu/TiO_2 catalysts," *Appl. Catal., B,* vol. 100, no. 1, pp. 386-392, 2010/10/11/ 2010, doi: https://doi.org/10.1016/j.apcatb.2010.08.015.

[35] X. Wei *et al.*, "A Bowknot-like RuO_2 quantum dots@V_2O_5 cathode with largely improved electrochemical performance," *Phys. Chem. Chem. Phys.,* 10.1039/C4CP02762K vol. 16, no. 35, pp. 18680-18685, 2014, doi: 10.1039/C4CP02762K.

[36] S. Kaliaguine, "Application of surface science techniques in the field of zeolitic materials," in *Studies in Surface Science and Catalysis*, vol. 102, H. Chon, S. I. Woo, and S. E. Park Eds.: Elsevier, 1996, pp. 191-230.

[37] M. Descostes, F. Mercier, C. Beaucaire, P. Zuddas, and P. Trocellier, "Nature and distribution of chemical species on oxidized pyrite surface: Complementarity of XPS and nuclear microprobe analysis," *Nucl. Instrum. Meth. B,* vol. 181, no. 1, pp. 603-609, 2001/07/01/ 2001, doi: https://doi.org/10.1016/S0168-583X(01)00627-9.

[38] Q. Wang, Z. Guo, and J. S. Chung, "Formation and structural characterization of potassium titanates and the potassium ion exchange property," *Mater. Res. Bull.,* vol. 44, no. 10, pp. 1973-1977, 2009.

[39] R. Vinoth *et al.*, "Ruthenium based metallopolymer grafted reduced graphene oxide as a new hybrid solar light harvester in polymer solar cells," *Sci. Rep.,* vol. 7, no. 1, p. 43133, 2017/02/22 2017, doi: 10.1038/srep43133.

[40] C. N. Fleming, K. A. Maxwell, J. M. DeSimone, T. J. Meyer, and J. M. Papanikolas, "Ultrafast Excited-State Energy Migration Dynamics in an Efficient Light-Harvesting Antenna Polymer Based on Ru(II) and Os(II)

Polypyridyl Complexes," *J. Am. Chem. Soc.,* vol. 123, no. 42, pp. 10336-10347, 2001/10/01 2001, doi: 10.1021/ja016304i.

[41]   C. A. Kent, B. P. Mehl, L. Ma, J. M. Papanikolas, T. J. Meyer, and W. Lin, "Energy Transfer Dynamics in Metal−Organic Frameworks," *J. Am. Chem. Soc.,* vol. 132, no. 37, pp. 12767-12769, 2010/09/22 2010, doi: 10.1021/ja102804s.

[42]   T.-D. Nguyen-Phan *et al.*, "Three-dimensional ruthenium-doped TiO_2 sea urchins for enhanced visible-light-responsive H2 production," *Phys. Chem. Chem. Phys.,* 10.1039/C6CP00472E vol. 18, no. 23, pp. 15972-15979, 2016, doi: 10.1039/C6CP00472E.

[43]   M. A. Ávila-López *et al.*, "Comparative study of CO_2 photoreduction using different conformations of CuO photocatalyst: Powder, coating on mesh and thin film," *Journal of CO2 Utilization,* vol. 50, p. 101588, 2021/08/01/ 2021, doi: https://doi.org/10.1016/j.jcou.2021.101588.

[44]   I. H. Tseng, W.-C. Chang, and J. C. S. Wu, "Photoreduction of CO_2 using sol–gel derived titania and titania-supported copper catalysts," *Appl. Catal., B,* vol. 37, no. 1, pp. 37-48, 2002/04/08/ 2002, doi: https://doi.org/10.1016/S0926-3373(01)00322-8.

[45]   B. Xin, P. Wang, D. Ding, J. Liu, Z. Ren, and H. Fu, "Effect of surface species on Cu-TiO2 photocatalytic activity," *Appl. Surf. Sci.,* vol. 254, no. 9, pp. 2569-2574, 2008/02/28/ 2008, doi: https://doi.org/10.1016/j.apsusc.2007.09.002.

Chapter 5

Comparative study of CO₂ photoreduction using different conformations of CuO photocatalyst
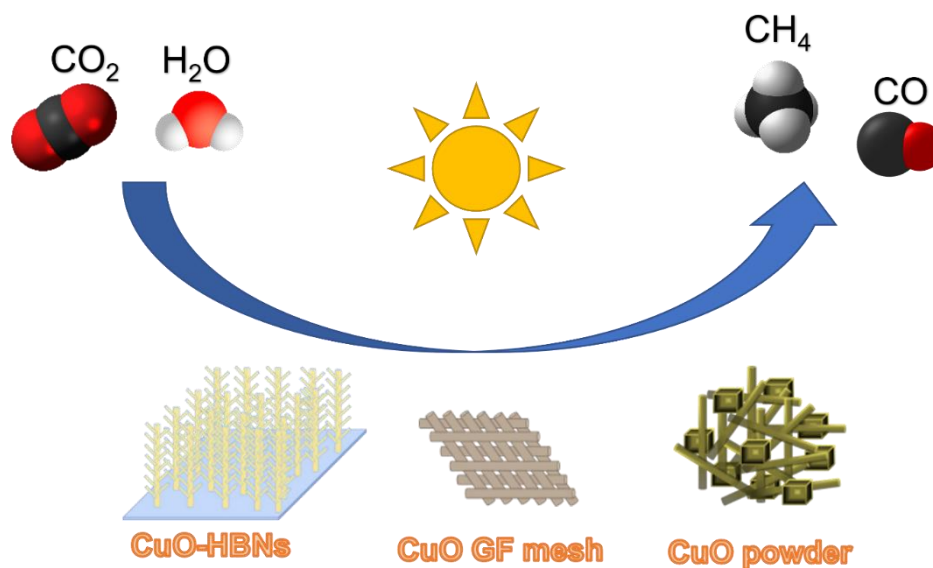
5.1 Aims and objectives

Various conformations of CuO have been proposed in the literature for CO_2 photoreduction; however, the comparison of published results becomes difficult due to the varying experimental conditions, reactor geometry and set-ups. Hence, this study aims to serve as a uniform platform to ascertain the effect of different configurations of CuO on photocatalytic performance and determine the most significant factors for the synthesis of photocatalysts. In this study several conformations of CuO are prepared and tested for CO_2 photoreduction. CuO is examined as a sole photocatalyst and as a co-catalyst supported on titania HBNs. Two general configurations (*i.e.*, powder and coating) were prepared in this study. The powder samples were prepared using precipitation, sonochemical and microwave assisted hydrothermal approaches; whereas the coating samples were prepared on a fiber glass mesh substrate and FTO conductive glass. The FTO samples included titania HBNs, CuO thin film, and CuO-HBNs. These samples were characterised by XRD, Raman, UV-Vis, SEM and XPS to investigate their physical properties.

The publication presented in this chapter is a collaborative work (with other PhD candidates from Heriot-Watt University, UK and the Autonomous University of Nuevo Leon, Mexico), which includes an experimental and a modelling approach. However, this Thesis is focused on the experimental research. Consequently, the modelling section falls out of the scope of this Thesis and will not be included in this chapter. The full version of the paper (along with the supporting information) is available in appendix B. Additionally, since this is a multifaceted comparative study for CuO utilisation with a large number of samples prepared with various synthesis methods and configurations, the titania HBNs sections were removed from the publication for the sake of simplicity and in favour of a straightforward and cohesive narrative for this publication, as requested by the journal reviewer. However, those are important parts for the aim and objectives of this Thesis and consequently the removed parts were added in section 5.11 "Further research (Not published work)" towards the end of the chapter.

The objectives of this work are:

- Fabricate CuO photocatalysts in various conformations and through characterisation study their chemical composition, morphology, and optical properties.

- Through the systematic study establish the most impactful parameters responsible for the performance of the fabricated photocatalysts on CO_2 photoreduction.

- Examine the synergistic behaviour of CuO-HBN and compare with the sole CuO and HBNs photocatalysts.

5.2 Highlights and key findings

5.2.1 Morphological variations and impacts

This chapter examines a series of CuO samples with various conformations. The morphology of the three powder samples, which were synthesized using precipitation, ultrasonication and microwave assisted methods, labelled as CuO P, CuO US, and CuO MW, respectively, were examined using SEM. It was observed that all three samples presented similar morphology consisting of a mixture of nanorods/nanoshards and agglomerated nanoparticles. However, the degree of agglomeration seems higher in CuO P, while CuO MW seems to have the least amount of agglomeration formed and a more predominant concentration of nanorods formed. The three examined samples have

identical chemical composition, as shown in XPS analysis, yet their CH_4 production was significantly impacted by the morphological aspects observed under SEM. CuO P produced only 1 µmol $g_{cat}^{-1} h^{-1}$ while CuO US and CuO MW produced 1.5 and 2.6 µmol $g_{cat}^{-1} h^{-1}$, respectively. These observations indicated that the reduction of agglomerated nanoparticles and the presence of predominant nanorod 1D morphological features of the CuO MW has benefited the CO_2 photoreduction conversion rates.

Similarly to the CuO powder samples, the sample coated on glass fiber mesh and the sample grown as thin film on FTO conductive glass slide were labelled as CuO coat and CuO TF, respectively. The samples demonstrated significant morphological differences when examined under SEM imaging. The CuO coating on the glass fiber mesh exhibited a homogeneous coverage of nanorods growing in random chaotic orientation forming 1-3D nanostructures, with large gaps for light penetration throughout the material. The CuO TF sample demonstrated a different morphology, in which the FTO glass surface was covered by a thin layer of numerous agglomerated 0D nanoparticles forming a 2D overlayer. The overlayer was not homogeneous enough, as cracks were observed under SEM, forming a "patchy" overlayer. Under SEM imaging the FTO coating could be observed through the cracks. Both coated samples (CuO coat and CuO TF) significantly outperformed the powder samples in terms of CO_2 conversion. Nonetheless, the CuO coat sample with the homogeneous 1-3D nanorod structure produced significantly higher CH_4 production (56.3 µmol $g_{cat}^{-1} h^{-1}$) compared to the CuO TF sample (12.7 µmol $g_{cat}^{-1} h^{-1}$). The superior performance of the CuO coat sample was attributed to the reduced agglomeration, likely due to its immobilisation on the glass fiber mesh when compared to the powder counterparts. Additionally, Na_2O originating from the mesh substrate was found and this is believed to have enhanced the CO_2 adsorption leading to higher conversion rates.

5.2.2   *CuO-HBNs compound thin film performance in CO₂ photoreduction*

As mentioned above, CuO TF produced 12.7 µmol $g_{cat}^{-1} h^{-1}$ of CH_4 which was the sole product of the reaction. The pristine titania HBNs were also examined under these experimental conditions and showed a 669 µmol $g_{cat}^{-1} h^{-1}$ production of CO, and 15.5 µmol $g_{cat}^{-1} h^{-1}$ of CH_4, exhibiting a high conversion rate and ~ 98% selectivity towards CO. The high photocatalytic performance of the titania HBNs was largely attributed to the 1-3D nanorod microstructure, and the benefits it provides (light harvesting, charge separation etc.), as described in detail in Chapter 4. However, the CuO-HBNs sample

demonstrated a significantly reduced conversion rate (compared to titania HBNs), producing only 7.3 and 3.8 µmol g_{cat}^{-1} h^{-1} of CO and CH_4, respectively. This reduced conversion rate was attributed to the shading effects of the CuO overlayer that was developed on the HBNs surface during the CuO deposition step. Briefly, due to the CuO being deposited on top of the HBNs using the spin coating technique, an overlayer of CuO was formed. The overlayer resulted in shading large sections of the HBNs, therefore hindering the photocatalytic reaction. Additionally, the HBNs were believed to provide a substrate that could help with CuO dispersion, however under SEM examination the CuO particles seemed to have agglomerated in clusters on the HBNs hindering the materials performance. The CO production observed, was attributed to the partially exposed HBNs. More information can be found in section 5.11. However, the addition of CuO to the HBNs material has shown to increase the CH_4 selectivity of the material from ~2% to ~31% when compared to titania HBNs. Additionally, after the incorporation of CuO onto the HBNs synthesis, band gap narrowing was observed, which reduced the band gap energy from 3.6 to 3.3 eV, thus, improving the light wavelength absorption range of the CuO-HBNs material. As a result of this observations, CuO was deposited using the solvothermal approach in future research as described in Chapter 3, in an attempt to remedy the issues observed with this material synthesis.

5.3 Research impact

Through comparisons drawn from this study it was found that morphological variations, photocatalyst immobilisation and the combination of morphology and immobilisation can greatly affect the photocatalytic behaviour of a photocatalyst of the same chemical compound, specifically CuO. It was found that the powder CuO conformations synthesised with 3 different synthesis methods presented significantly varying photocatalytic activity. Through further characterisation it was deducted that morphological alterations such as the ratio of 1D nanorods features to agglomerated nanoparticles can have an impact on the photocatalytic behaviour (CuO P: 1 µmol g_{cat}^{-1} h^{-1} to CuO MW: 2.6 µmol g_{cat}^{-1} h^{-1}). An even greater impact in conversion rates was observed when the CuO photocatalyst was prepared as thin-film (CuO-TF: 12.7 µmol g_{cat}^{-1} h^{-1}) and the synergistic effects when both morphological features and immobilisation was applied produced the best performing photocatalyst (CuO coat: 56.3 µmol g_{cat}^{-1} h^{-1}). It was also found that the presence of Na_2O can enhance the adsorption of CO_2 leading to higher conversion values. Additionally, comparisons and observations were made

91

regarding the use of CuO, titania HBNs and the compound CuO-HBNs for CO_2 photoreduction to investigate the synergistic effects of the two materials.

5.4   Personal development

The current research required the synthesis of seven different samples, including powder form and coatings supported on substrates. Apart from the large variety of synthesis techniques used, choosing the correct characterisation techniques that are applicable to all samples, or finding ways to modify the samples/sample-holders in order to fit certain characterisation techniques was required. One example of such modification would be the custom-made powder loading sample holder that was designed and developed by the team with support from the workshop (manufacturing process) for the UV-Vis characterisation of the powder samples. This holder allowed for the UV-Vis characterisation of powder samples and coated material on substrates or thin-films. Also, the custom-made photo-reactor, which was designed to fit all the samples, glass fiber mesh, FTO glass slides and powder, while maintaining the same inner volume within the closed system for the results to be comparable. These parts were manufactured by the workshop, yet the design was entirely up to the research team. The parts had to be very accurately designed to allow for efficient operation of the characterisation machine or reaction while accommodating the various samples. Choosing the suitable material was also a very important parameter as well as the capabilities of the workshop to achieve the desired accuracy with each material. Close collaboration and constant communication was maintained with the workshop in the manufacturing process to ensure the parts where accurately manufactured. Overcoming such issues and finding viable practical solutions was a challenging and stimulating process.

As mentioned earlier, the publication presented in this chapter was a collaboration project, which comes with its own set of challenges. The most important challenge was maintaining effective communication between all the researchers involved. Things like overseas communication due to time zone differences (Mexico-UK) and language barriers were all challenges that required a careful approach. This experience has certainly provided plenty opportunities for personal development for working in a collaborative research project.

Publication 2

Title: Comparative Study of CO_2 Photoreduction Using Different Conformations of CuO Photocatalyst: Powder, Coating on Mesh and Thin Film

Authors: Manuel Alejandro Ávila-López[‡a], Stelios Gavrielides[‡b], XiaoJiao Luo[‡b], Abah Ezra Ojoajogwu[b], Jeannie Z. Y. Tan[b*], E. Luévano-Hipólito[c*], Leticia M. Torres-Martínez[a*], M. Mercedes Maroto-Valer[b*]

‡ **These authors contributed equally.**

Status: Published

Abstract

The use of CuO-based photocatalysts for CO_2 photoreduction has been extensively reported in the literature. However, the comparison of the photocatalytic activity and selectivity from the published results becomes difficult due to different experiment conditions (i.e., synthesis method, configuration of photocatalyst, flow rate of gas, water content, light intensity) and reactor geometry employed. Hence, in this work different conformations of CuO-based photocatalyst, namely powder (i.e., synthesized using precipitation, sonochemical and hydrothermal-microwave treatment), coating on glass fiber mesh, and thin film, were tested using the same photoreactor and experimental conditions. All CuO photocatalysts exhibited 100% product selectivity towards CH_4 over CO and the CuO coating on the glass fiber mesh exhibited the highest production of CH_4 (56.3 $\mu mol\ g_{cat}^{-1}\ h^{-1}$). The morphology, particle size, particle dispersity, and presence of impurities/defects within the CuO photocatalysts had a significant effect on photocatalytic activity. A numerical model, which was built using COMSOL, revealed that the experimental data obtained in this simulated photocatalytic activity study fitted well, however, further optimization was needed.

4.5 Introduction

CO_2 is the most abundant anthropogenic greenhouse gas responsible for global warming.[1, 2] Various mitigation approaches have been proposed to decrease CO_2 emissions, including CO_2 conversion and utilization (CCU).[3-5] Solar energy to drive the photoreduction of CO_2 into chemicals and fuels provides an interesting approach for the production of syngas (CO and H_2), CH_3OH, CH_4, HCOOH and HCOH amongst others .[6-12]

Photocatalyst requirements, including a high affinity towards CO_2, rapid adsorption/desorption kinetics, high thermal and mechanical stability and high specific surface area with active sites, have been proposed to enhance the photocatalytic conversion of CO_2 into value-added products.[13] In view of this, transition metal oxides represent an excellent option since they can desorb the adsorbed gas at a relatively low temperature (<200°C) compared to alkali metals and alkaline metal oxides.[13] In addition, they are non-toxic and abundantly available. Among the transition metal oxides, copper-based metal oxides (i.e., Cu_2O, CuO, Cu metal) are the most widely reported materials for CO_2 photoreduction.[14, 15] This is because CuO possesses the highest electronegativity and highest number of basic sites for CO_2 adsorption and a more

favorable CO_2 adsorption capability (ΔH= -45 kJ mol^{-1}) compared to other transition metal oxides.[16, 17]

Many studies have demonstrated the use of CuO as photocatalyst for CO_2 reduction,[8, 18-23] , as summarized in Table B.S1.   However, the comparison of the results from the literature is challenging due to different synthesis approaches, experimental conditions, and geometry of photoreactor employed. Hence, in this study, the comparison of CuO photocatalyst in different conformations (*i.e.,* powder, thin film, and coatings on glass fiber mesh) is investigated under the same experimental conditions. Moreover, three commonly used synthesis methods, including precipitation, sonochemical, and microwave synthesis are employed to fabricate powder samples.

In addition to the development of photocatalysts for CO_2 photoreduction, significant work has been devoted to developing advanced photoreactors in an attempt to improve the current very low conversions.[24, 25]   To address these engineering challenges, a validated Multiphysics model for CO_2 photoreduction under UV-vis light irradiation was developed herein. The model developed was coupled with computation fluid dynamics, mass transport, reaction kinetic and light transport in a continuous flow reactor. Three essential factors (*e.g.*, CO_2 flow rate, inlet H_2O mole fraction and light intensity) in the CO_2 photoreduction were simulated. This numerical modelling is also expected to improve our understanding of the CO_2 photoreduction mechanism, and thereby, provide a useful tool to optimize the reaction process.

5.6 Experimental procedure

Materials synthesis

 Powder

a. Precipitation method

5.98 g of Cu(CH$_3$COO)$_2$·H$_2$O (Fermont, 99%) was dissolved in 40 mL of deionized water (DI). Then, 10 mL of 0.6 M of NaOH (Fermont, 99%) was added dropwise into the solution. The solution was then heated for 3 h at 80 °C under vigorous stirring. The dark brown precipitate was washed with sufficient DI water, for remove all the possible residual precursor. The collected powder was dried in the oven at 80 °C overnight and the sample obtained was denoted as CuO P.

b. Sonochemical method

The CuO powder sample was synthesized following a procedure reported previously.[26]   Briefly, 0.38 M of $Cu(CH_3COO)_2 \cdot H_2O$ solution was dissolved in DI water. Then, 0.6 M of NaOH was added dropwise into the first solution with vigorous stirring at 50 °C. The resulted solution was exposed to sonochemical energy for 25 min using an equipment Hielscher's UP200Ht at 100 W, with capacitance and an amperage of 50 and 20%, respectively. After the sonication treatment, the resulted brown suspension was washed with DI water for three times. Finally, the dark brown powder obtained, which denoted as CuO US, was dried in the oven at 80 °C overnight.

c. Microwave-hydrothermal method

An aqueous solution of 0.6 M of $Cu(CH_3COO)_2 \cdot H_2O$ was prepared under vigorous stirring for 30 minutes. Then, 0.6 M of NaOH was added dropwise. After that, the mixture was treated in a microwave reactor (Mars 6) at 80 °C with 300 W for 60 min. The resulted precipitate was washed with DI water and centrifuged a few times until the water was clear. Finally, the powder obtained was dried at 80°C for 12 h and the resultant sample was denoted as CuO MW.

Coating

A glass fiber mesh with a grit slit of 2.7 nm was used as the substrate for CuO coating fabrication. Firstly, the glass fiber substrate was cleaned with acetone, methanol, and then DI water under sonication for 20 min and then dried at 80 °C overnight. Then, the cleaned glass fiber mesh substrates were placed in an autoclave that was filled with 0.06 M of $Cu(CH_3COO)_2 \cdot H_2O$ solution. After that, 0.6 M of NaOH was added dropwise into the solution under vigorous stirring. Next, the autoclave was placed in the microwave reactor at 80 °C with 300 W for 60 min. The resulting brown coating on the glass fiber mesh was washed with DI water and centrifuged a few times until the water was clear and then dried at 80 °C overnight and the sample denoted as CuO Coat.

Thin film

Fluorine-doped tin oxide (FTO) TEC-15 glass was purchased from Ossila (2.5 cm x 2.5 cm, roughness of 12.5 nm, FTO layer thickness of 200 nm, 83.5% transmission and resistivity of 12-14 Ω cm^{-1}). The FTO substrate was cleaned before use using a mixture of isopropanol, water, and acetone with a 1:1:1 ratio. The FTO glass was submerged into the solution and placed in a sonication bath for 1 h. The FTO glass was then removed and dried in air for 30 min at 75 °C on a hot plate.

Copper (II) acetate (Aldrich, 98%) solution was prepared using 2.742 g in 50 mL of ethanol, forming solution A. Then, solution A was stirred for 30 minutes. After that, 12 µL of diethanolamine ($C_4H_{11}NO_2$, Aldrich ≥98%) and 25 µg of ethylene glycol ($C_2H_6O_2$, Alfa Aesar ≥99%) were added into solution A and stirred for 30 and 60 min, respectively, obtaining solution B that was used to fabricate CuO thin film using a spin coater (Model P6700). Solution B was added drop by drop onto a cleaned FTO glass, which was placed on the sample stage of the spin coater spinning at 3000 rpm. After that, the FTO coated was dried in air at 100 °C for 10 min and then calcined at 400 °C (ramp rate: 10 °C min^{-1}) for 1 h, with the resulting sample labelled as CuO TF.

5.7 Characterization

The samples morphology was analyzed using Scanning Electron Microscopy (SEM, JEOL 6490). To investigate the crystallinity and phase identification, X-ray diffraction (XRD) patterns were obtained using a Bruker D8 Advanced Diffractometer equipped with Cu Kα radiation (λ= 1.5418 Å) and compared with the ICDD-JCPDS powder diffraction file database; and Raman spectra were collected using a Renishaw *inVia* Raman Microscope with 785 nm excitation source. Diffuse reflectance of all the samples was measured using a Perkin Elmer Lambda 950 UV-vis equipped with an integrating sphere (150 mm). X-ray photoelectron spectrum (XPS) analysis were performed using a Thermo Fisher Scientific NEXSA spectrometer. The samples were analysed using a micro-focused monochromatic Al X-ray source (19.2 W) over an area of approximately 100 microns. Data were recorded at pass energies of 200 eV for survey scans and 50 eV for high resolution scan with 1 eV and 0.1 eV step sizes, respectively. Charge neutralisation of the sample was achieved using a combination of both low energy electrons and argon ions. C 1s electron at 284.8 eV was used as standard reference to calibrate the photoelectron energy shift. All the data analysis was performed on the CasaXPS software (version: 2.3.20rev1.0). Fourier Transform Infrared spectroscopy (FTIR), which was performed on Thermo Nicolet iS50 (1000-4000 cm^{-1}), was used to characterize the surface of the materials. *Operando* Diffuse Reflectance Infrared Fourier Transform Spectroscopy (DRIFTS) experiments were conducted on Agilent Cary 600 series spectrometer equipped with Harrick Praying Mantis reaction cell. The gas inlet of the cell was directly connected to a flow system equipped with mass flow controllers and a temperature controller. The cell outlet was connected to the mass spectrometer Hiden QGA MS. In each experiment, 20 mg of crushed powder was placed in the cell. Before

reaction, the KBr background was collected in presence of CO_2 which was flowing through bubbler. 64 scans were collected per spectrum with a spectral resolution of 4 cm^{-1} and in the spectral range of 4000-400 cm^{-1}. The experiment was performed under UV-vis irradiation at 24 and 40 °C and dark (24 °C) conditions to simulate the experimental conditions within the photocatalytic reactor.

5.8 CO_2 Photoreduction tests

The CO_2 photocatalytic reduction tests were performed under UV-visible light irradiation using the experimental set-up and procedure as described in the authors published work.[27] Briefly, the sample was loaded in the middle of the photoreactor. To purge the system, three repetitive steps of placing the system under vacuum to -1 bar and the vacuum released with CO_2 (99.995%) to 1 bar were performed. The CO_2 was then released through the injection port of the gas chromatograph (GC, Agilent, Model 7890B series), leaving a positive pressure of 0.2 bar, before the system was sealed and placed under vacuum overnight before each measurement. The flow rate of CO_2 was set to 0.35 mL min^{-1} and passed through the temperature controlled (±0.1 °C) aluminium body saturator for at least 16 h to allow the system to equilibrate. Relative humidity (±1.8% RH) was measured using an inline Sensirion SHT75 humidity sensor potted (MG Chemicals 832HD) into a Swagelok 1/4" T-piece. The temperature of the photoreactor (40 °C) was controlled using a hotplate and the surface of the coated photocatalyst measured using a Radley's pyrometer (±2.0 °C). An OmniCure S2000 with 300-600 nm wavelength was used as the light source was placed 30 mm above the surface of the investigated sample. The light source produced an Irradiance (150 mWcm^{-2}) at the exit of the fiber optic light guide was measured before each experiment using an OmniCure R2000 radiometer (±5%). The fiber optic was inserted into a lens and the entire photoreactor surface was illuminated. An inline GC) with a Hayesep Q column (1.5 m), 1/16 inch OD, 1 mm OD), Molecular Sieve 13X (1.2 m), 1/16-inch OD, 1 mm ID), thermal conductivity detector (TCD), nickel catalyzed methanizer and flame ionization detector (FID) was used to analyze the output of the photoreactor every four minutes. The GC was calibrated using 1000 ppm calibration gas (H_2, CO, O_2 and CH_4) in a balance of Ar gas) that was further diluted with Ar (99.995%) using mass flow controllers to 17.04, 4.62 and 1 ppm using the FID detector for CH_4 and CO, respectively, and 69.49, 34.72 and 17.04 ppm using the TCD detector for H_2 and O_2.

The CO_2 utilization rate was determined by taking the molar percentage of CO_2 inlet: CO_2 outlet as the amount of CO_2 consumed. The cycling test (*i.e.*, 3 runs) was performed using the optimized sample, which was cleaned with DI water and dried on a hotplate at 100 °C for 2 h before each run.

The quantum yield (ϕ) was measured under similar photocatalytic reaction conditions using the same light source (OmniCure S2000 with 300-600 nm wavelength). The incident flux was determined by a Laboratory Spectroradiometer (Apogee Instruments). The ϕ values of CH_4 evolution for the CO_2 photoreduction reaction were calculated according to the following equation Eq. 5.1:

$$\phi CH_4 \ (300\text{-}600 \ nm) = \frac{amount \ of \ product \ formed}{amount \ of \ photons \ adsorbed \ in \ the \ range \ of \ 300-600 \ nm} \qquad \text{Eq. 5.1}$$

5.9 Simulation studies

(missing part of text, for the full version see Appendix:B)

5.10 Results and discussion

Crystal phase

The powder samples synthesized using different approaches (*i.e.*, precipitation, ultrasonication and microwave synthesis) exhibited the monoclinic phase of CuO (JCPDS: 45-0937, Figure 5.1a-c). The peaks at 32.5, 35.8 and 38.6º corresponded to the (110), (-111) and (111) planes, respectively. The most intense peak at $2\theta = 38.6°$ was used to estimate the crystallite size of the samples, which was 10-12 nm.

The crystal phase of CuO Coat also exhibited monoclinic phase (JCPDS: 45-0937, Figure 5.1d). However, the signal-to-noise of the XRD pattern in CuO Coat was much lower than that for CuO P, CuO US and CuO MW due to the low thickness of the coating on the glass fiber mesh. The XRD pattern of sample CuO TF (Figure 5.1f) only revealed a strong diffraction at $2\theta = 37°$, corresponding to the FTO conductive thin film (Figure 5.1e). This was due to the overshadow of the diffraction pattern of the conductive thin film. Hence, Raman spectroscopy, which is much more sensitive towards the vibration of the crystal lattice, was employed.[28] Three bands centered at 287, 341, and 615 cm^{-1}, which were attributed to A_g, B_{1g}, and, B_{2g} modes of CuO, respectively, were observed in samples CuO TF (Figure B.S1a).[29-32] However, these CuO peaks were broadened and slightly red-shifted, attributing to different sizes of the CuO particles (further discussed in the next section).[30] Sample CuO Coat also exhibited CuO characteristic bands. Additional bands, including PO_4^{3-} ($v1$) (960 cm^{-1}),[33] Si-N-Si (870 cm^{-1}), vibration
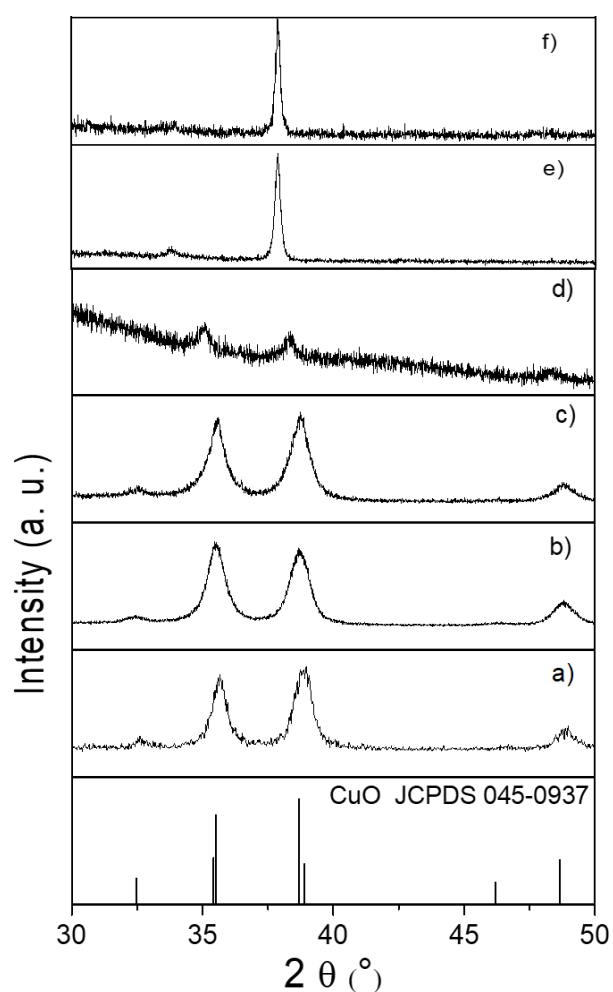

Figure 5.1. XRD patterns of a) CuO P, b) CuO US, c) CuO MW, d) CuO Coat, e) FTO, and f) CuO TF.

outside the plane C-H (760 cm^{-1}), deformation outside the ring C-H (690 cm^{-1}),[34] P-O-P (620 cm^{-1}) were identified originated from the glass fiber mesh substrate (Figure B.S1b and c).

Morphology

The morphology of the fabricated samples was investigated using SEM. Samples CuO P, CuO US and CuO MW possessed a mixture of nanorods and agglomerated nanoparticles (Figure 5.2a-c). The length of the nanorods observed in the sample CuO US (~580 nm, Figure 5.2b) was longer than that in CuO P (~400 nm, Figure 5.2a) and CuO MW (~408 nm, Figure 5.2c). Very similar observation was also obtained on sample CuO Coat, but a more homogeneous nanorods coated on the surface of the glass fiber mesh was observed (~445 nm in length, Figure 5.2d). The CuO TF fabricated revealed a patchy microstructure resulted the broadening and red-shifted of the Raman spectrum in this sample (Figure 5.2f).
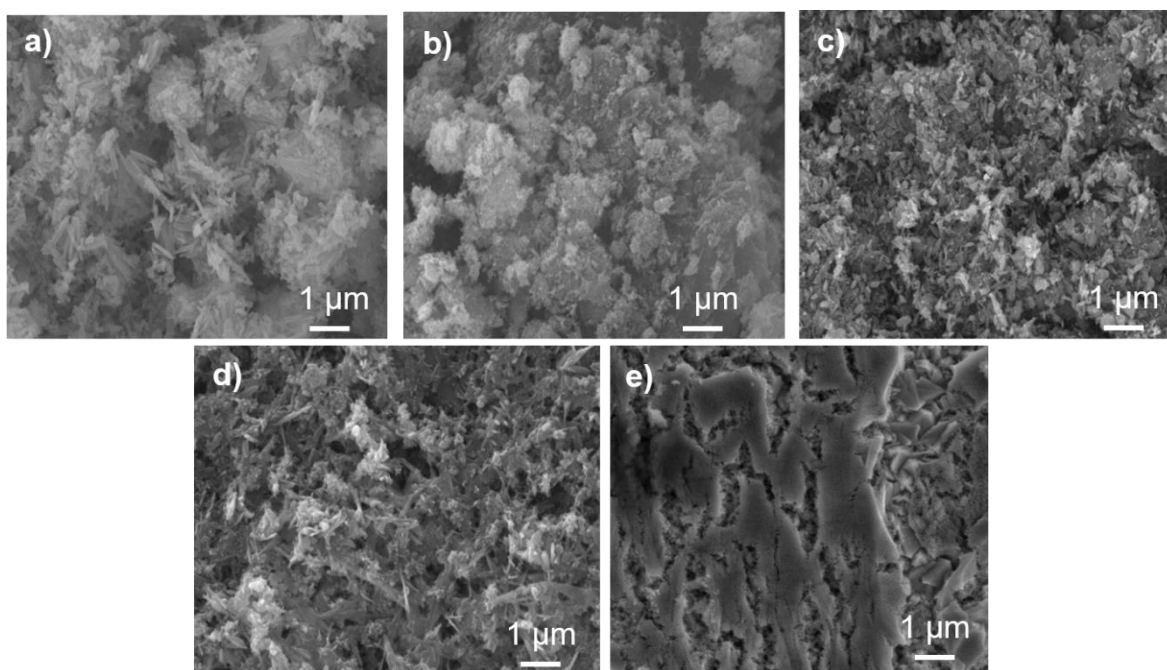

Figure 5.2 - SEM of the a) CuO P, b) CuO US, c) CuO MW, d) CuO Coat, and e) CuO TF.

Optical Properties

The optical properties of the fabricated samples were investigated and analyzed using UV-vis spectroscopy, as shown in Figure 5.3. The band gap energy of was derived using the Kubelka-Munk function from diffuse reflectance. All the fabricated samples showed a band gap of around 1.4-1.5 eV using the (Figure 5.3).
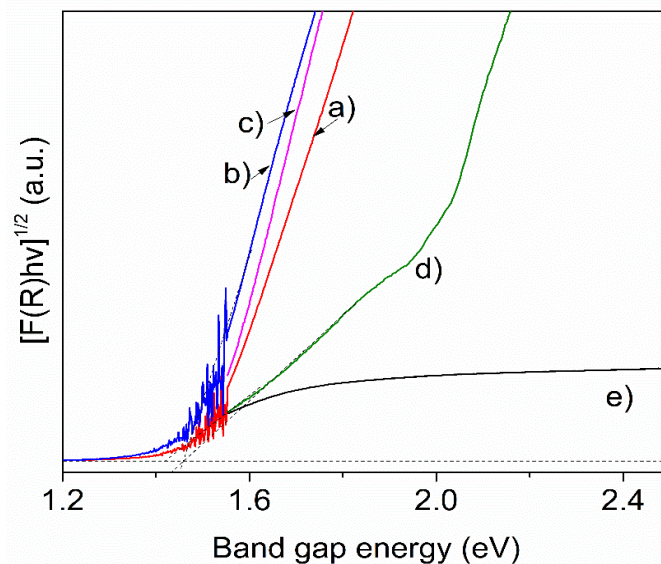
Figure 5.3 - Kubelka-Munk spectra of a) CuO P, b) CuO US, c) CuO MW, d) CuO Coat, and e) CuO TF.

Surface properties

To investigate the surface chemistry of the samples, XPS was performed (Figure 5.4). The XPS survey spectra of samples CuO P, CuO US, CuO MW and CuO TF revealed no
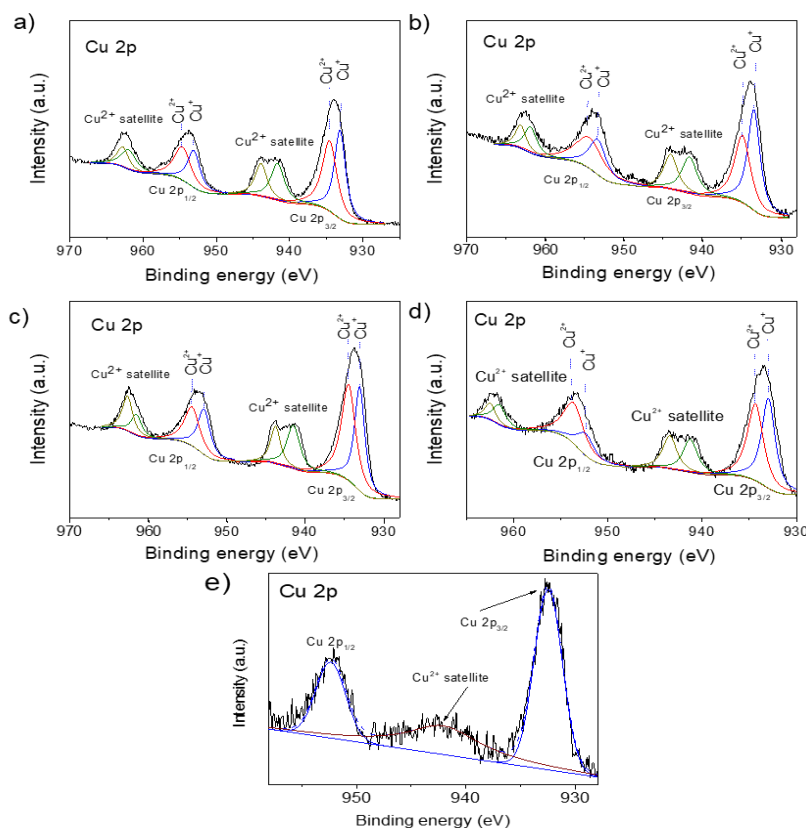

Figure 5.4 - XPS spectra of Cu 2p for a) CuO P, b) CuO US, c) CuO MW, d) CuO Coat, and e) CuO TF.

contamination from the precursors nor substrates, whereas CuO Coat revealed the presence of Na, which was originated from the glass fiber mesh (Figure B.S2).

The Cu 2p spectra of all the samples were deconvoluted into two components. Specifically, the Cu $2p_{3/2}$ (934.5 eV for CuO P and CuO MW; 934.9 eV for CuO US) and Cu $2p_{1/2}$ species (954.7 eV for CuO P and CuO US; 954.6 eV for CuO MW; Figure 5.4a-c). In addition, these components were accompanied by their respective satellite peaks positioning at 961.0-963.9 eV, which are characteristic of Cu^{2+}. Furthermore, the difference between the Cu $2p_{1/2}$ and Cu $2p_{3/2}$ peaks was ~20 eV, which evidenced the oxidation state of the fabricated samples as Cu^{2+}.[35, 36] The presence of Cu^+ on the surface of the fabricated materials was revealed in the peaks centered at 933.1 and 953.1 eV for CuO P; 933.6 and 953.2 eV for CuO US; and 933.1, and 953.0 eV for CuO MW (Figure 5.4a-c).[37] Meanwhile, CuO Coat had the Cu $2p_{3/2}$ peak centered at 934.5 and 934.2 eV and Cu $2p_{1/2}$ peak located at 953.8 eV. Similarly, the difference of Cu $2p_{1/2}$ and Cu $2p_{3/2}$ in CuO Coat remained ~20 eV, confirming the fabricated CuO Coat sample contained Cu (II) (Figure 5.4d). This sample also contained Cu^+ as exhibited in the peak positioned at 933.1 eV (Figure 5.4d) but absent in CuO TF (Figure 5.4e). CuO TF exhibited only the Cu $2p_{3/2}$, Cu $2p_{1/2}$ and Cu satellite peaks at 932.7, 952.4 and 962.1 eV, respectively (Figure 5.4e), confirming the presence of CuO on the thin films.

The high-resolution of O 1s spectrum were deconvoluted into four components (Figure B.S3). The peak centered at 529.5-529.9, were attributed to the O^{2-} in O_L-CuO.[38, 39] Meanwhile, the presence of peak centered at 531.1 (*i.e.*, samples CuO US, and CuO Coat) and 530.2 eV (*i.e.*, sample CuO P and CuO MW) was attributed to V_{Os},[40-42] evidencing the presence of V_{Os} in these samples. Other peaks located at 531.9-532.3 eV were attributed to the oxygen adsorbed on the surface with low coordination.[43, 44]

Photocatalytic activity

The fabricated CuO samples in different conformations were evaluated for the photocatalytic reduction of CO_2 under the light irradiation (300-600 nm) and the quantity of the gaseous products produced (CO and CH_4) were monitored (Table 5.1). In general,

CH$_4$ was the main product produced by all the fabricated CuO samples in the photocatalytic reduction of CO$_2$, whereas CO was generated in very low quantities.
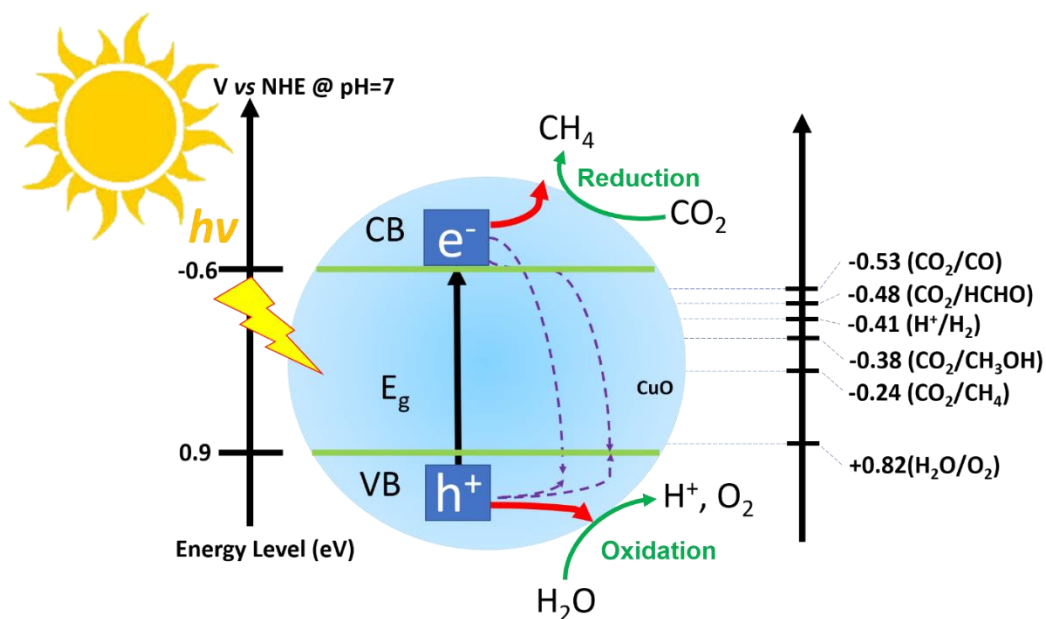
Scheme 5.1 - Schematic illustration of CO$_2$ photocatalytic reduction with H$_2$O using CuO under visible light irradiation.

Table 5.3 - Average products obtained in 4 h from CO$_2$ photoreduction using different configurations of photocatalyst.

Sample name	CH$_4$ (µmol g$_{cat}^{-1}$ h^{-1})
CuO P	1.0
CuO US	1.5
CuO MW	2.6
CuO Coat	56.3
CuO TF	12.7

The CH$_4$ production of the powder samples declined in the order of CuO MW (2.6 µmol g$_{cat}^{-1}$ h^{-1}) > CuO US (1.5 µmol g$_{cat}^{-1}$ h^{-1}) > CuO P (1.0 µmol g$_{cat}^{-1}$ h^{-1}). This could be due to the homogeneity of the particles of the samples fabricated using the microwave-

hydrothermal approach. The action spectra of the CO_2 photoreduction for the fabricated samples is shown in Figure B.S4.

Regarding to the photocatalytic activity of the immobilized photocatalysts, sample CuO TF, which contained only CuO, exhibited 100% selectivity towards CH_4, producing 12.7 µmol g_{cat}^{-1} h^{-1} under visible light irradiation. Sample CuO Coat showed the highest production of CH_4 (56.3 µmol g_{cat}^{-1} h^{-1}), which was approximately 18 times higher than that of CuO MW (*i.e.*, highest among the fabricated powdered samples). The superior performance of CuO Coat ($\phi CH_4 = 0.882$) was due to the reduction of agglomeration and the presence of Na_2O originated from the mesh substrate as shown in the FTIR (Figure 5.5).[45, 46] The presence of Na_2O had significantly enhance the CO_2 adsorption (further discussed in the next paragraph). The CuO Coat, which has the highest CH_4 production was implemented for cycling test (Figure B.S5). The sample was tested for 3 runs and did not show significant reduction in CH_4 production.
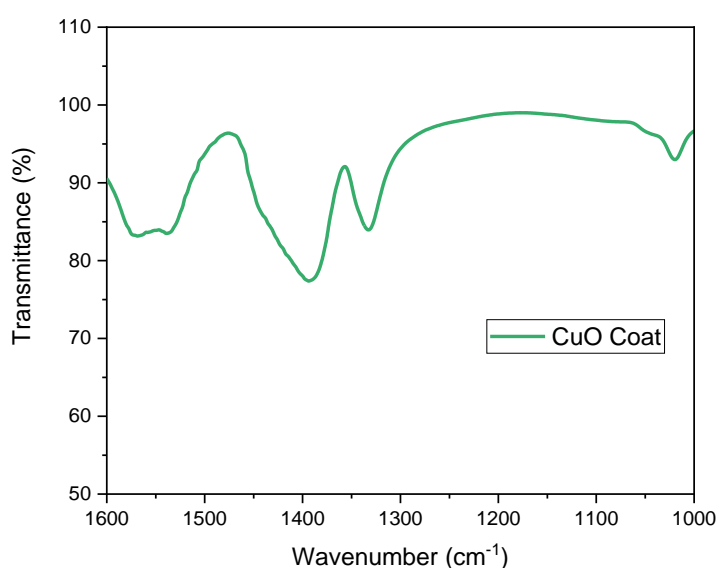

Figure 5.5 - FTIR pattern of CuO Coat upon the exposure of CO_2

The mechanistic study of the best performing sample (*i.e.*, CuO Coat) was conducted using FTIR in the presence of CO_2 (Figure 5.5). A series of bands at 1560 and 1410 cm^{-1}, which could be associated with C−O stretching and symmetry O−C−O vibrational modes, was assigned to monodentate species (linear coordination or carbon coordination).[47, 48] In addition, C−O stretching and symmetry O−C−O vibrational modes, which were shown at 1340 and 1020 cm^{-1} corresponded to the bidentate

105

carbonate.[49]   Based on the results obtained, the CO_2 adsorption and conversion mechanisms in CuO Coat sample was proposed and shown in Scheme 5.2. Briefly, the O and Cu on the surface of CuO Coat acts as a Lewis base site – an active site for CO_2 adsorption and conversion. Then, electrons were transferred to the C and/or O of the CO_2 molecules resulted in the formation of monodentate and bidentate configurations at the surface of CuO Coat.   The hole-electron pairs, which were generated upon light irradiation, traveled to the surface of the photocatalyst and underwent the subsequent oxidation-reduction reactions. CO_2 was reduced to CH_4 and H_2O was oxidized to O_2 and H^+.
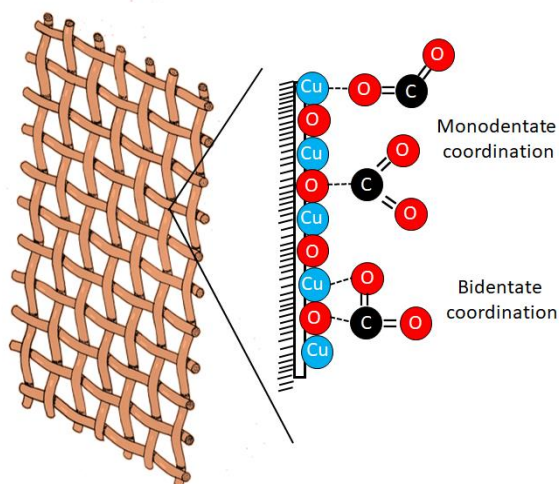
Scheme 5.2 - Schematic illustration of CO_2 adsorption and conversion on the surface of CuO Coat sample.

The CuO coat was analyzed with *operando* DRIFTS to confirm the formation of carbonate species (Figure B.S6). The coating presented a strong adsorption band at 2348 cm^{-1}, which assigns to CO_2 physiosorbed in the surface of the coating, when CO_2 was fed into the reactor and put in contact with the photocatalyst at 24°C in the dark. On the other hand, the bands at around 1620, 1420 and 1296 cm^{-1} were assigned to the asymmetric CO_3 stretching vibration [$v_{as}(CO_3)$], symmetric CO_3 stretching vibration [$v_s(CO_3)$] and O-H deformation vibration [$\delta(O-H)$] of monodentate bicarbonate species (m-HCO_3^{2-}), respectively, were observed upon CO_2 interaction with the coating in the dark.[3, 50] When the coating was irradiated with UV-vis light, the intensity of these bands lowered .The bands at around 1540 and 1384 cm^{-1} corresponds to the [$v_{as}(CO_2)$] and [$v_s(CO_2)$] of

the bidendate formate species (b-HCO_2^{2-}).[51] These results suggested that the CO_2 molecules adsorbed on the surface of CuO coat were mainly m-HCO_3^{2-} and converted to b-HCO_2^{2-} through the reaction with OH^- on the surface or OVs CuO coating. When the reaction temperature increased to 40°C (to emulate the reaction conditions), the bands of m-HCO_3^{2-} continued to decrease, whereas b-HCO_2^{2-} increased steadily. In other words, adsorption of CO_2 and conversion of m-HCO_3^{2-} to b-HCO_2^{2-} were enhanced at elevated temperature, which could favor the formation of CH_4. Therefore, *operando* DRIFT results suggested that the mechanism for the photocatalytic CO_2 reduction route of CuO coat was through the carbene pathway[46, 51].

Simulation study

(Missing part of text, for the full version see Appendix:B)

5.11 Conclusions

CuO photocatalysts with different configurations (powder, thin film, and coatings on glass fiber mesh) were fabricated and their CO_2 photoreduction activity was investigated. Sample CuO Coat with highly dispersed nanorod structure coated on the glass fiber mesh showed the highest CH_4 production from CO_2 (56.3 µmol g_{cat}^{-1} h^{-1}), which was approximately 18 times higher than the powder sample synthesized using the similar method (CuO MW). Combining the experimental and simulated results, the use of highly dispersive nanostructured photocatalyst operated at ~6.0×10^7 ppm and ≤ 2 SCCM of water content and CO_2 flow rate, respectively, could achieve the maximum yield of CO_2 photoreduction at 40 °C.

5.12   Further research (not published work)

The research sections that were originally included in the above manuscript regarding the titania HBN thin film and CuO-HBNs compound thin film are illustrated in the following section as was previously mentioned in section 5.1. These parts are essential for the narrative of this chapter, as one of its main objectives is to examine the use of HBNs as a substrate for CuO and also potential synergistic effects of the composite CuO-HBNs in CO_2 photoreduction. The research presented here is part of the preceding and preliminary work that was presented in Chapter 4. Including this research, helps provide a cohesive understanding of the research presented in this Thesis as a whole.

5.12.1 Material synthesis

FTO Thin film pre-treatment

Fluorine-doped tin oxide (FTO) TEC-15 glass was purchased from Ossila (2.5 cm x 2.5 cm, roughness of 12.5 nm, FTO layer thickness of 200 nm, 83.5% transmission and resistivity of 12-14 Ω cm^{-1}). The FTO substrate was cleaned before use using a mixture of isopropanol, water, and acetone with a 1:1:1 ratio. The FTO glass was submerged into the solution and placed in a sonication bath for 1 h. The FTO glass was then removed and dried in air for 30 min at 75 °C on a hot plate.

Fabrication of CuO and titania HBNs and CuO-HBNs thin film

Copper (II) acetate (Aldrich, 98%) solution was prepared using 2.742 g in 50 mL of ethanol, forming solution A. Then, solution A was stirred for 30 minutes. After that, 12 µL of diethanolamine ($C_4H_{11}NO_2$, Aldrich $\geq$98%) and 25 µg of ethylene glycol ($C_2H_6O_2$, Alfa Aesar $\geq$99%) were added into solution A and stirred for 30 and 60 min, respectively, obtaining solution B that was used to fabricate CuO thin film using a spin coater (Model P6700). Solution B was added drop by drop onto a cleaned FTO glass, which was placed on the sample stage of the spin coater spinning at 3000 rpm. After that, the coated FTO was dried in air at 100 °C for 10 min and then calcined at 400 °C (ramp rate: 10 °C min^{-1}) for 1 h, resulting in the CuO thin film sample.

Hyper-branched titania nanorods (HBNs) were fabricated using a hydrothermal approach. Potassium titanate oxide oxalate (PTO) was dissolved in a mixture of H_2O and Diethylene glycol (DEG) with a ratio of 1:7. The concentration of PTO was 0.05 M. After

30 minutes of vigorous stirring, the precursor solution was transferred to a 100 mL Teflon-lined autoclave along with the FTO glass. The FTO glass was positioned resting against the Teflon-liner walls with the conductive side facing down at approximately 60°. The hydrothermal synthesis was carried out at 180 °C for 9 h. After completing the reaction time, the autoclave was allowed to cool down to room temperature. The titania nanorods were rinsed several times with Milli-Q Type 1 water and ethanol, and then calcined at atmospheric conditions at 550 °C for 1 h.

The fabrication of CuO-HBNs sample followed the synthesis procedure of HBNs synthesis and then followed the CuO synthesis procedure which resulted in the final CuO-HBNs compound material.

5.12.2 Results and Discussion

The XRD pattern samples CuO, HBNs, and CuO-HBNs only revealed the strong diffraction (at $2\theta = 37°$) of the FTO conductive thin film (Figure 5.6). This was due to the overshadow of the diffraction pattern of the conductive thin film as well as the unique morphology of the HBNs that allowed the penetration of the X-ray onto FTO coating of the glass substrate.
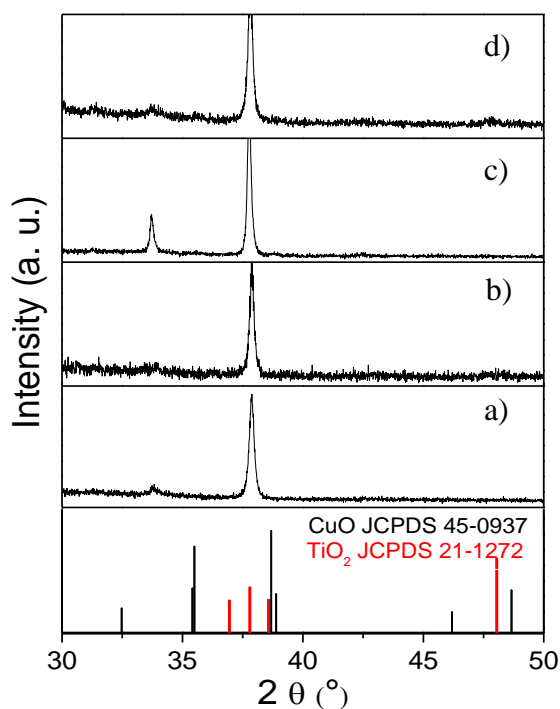

Figure 5.6 - XRD patterns of thin film samples a) blank FTO glass, b) titania HBNs, c) CuO, d) CuO-HBNs.

Since XRD characterization was not conclusive for the thin film samples, due to the overpowering effects of the FTO, Raman spectroscopy was employed. This characterization technique is much more sensitive towards the vibration of the crystal lattice.[28] The Raman bands associated with the anatase phase were revealed at 143, 395, 517, and 638 cm^{-1} in both HBNs containing samples (Figure 5.7a,c).[52-55] In addition, three bands centered at 287, 341, and 615 cm^{-1}, which were attributed to A_g, B_{1g}, and, B_{2g} modes of CuO, respectively, were observed in CuO and CuO-HBNs samples.[30-32, 55] However, these CuO peaks were broadened and slightly red-shifted, attributing to different sizes of the CuO particles (discussed below).
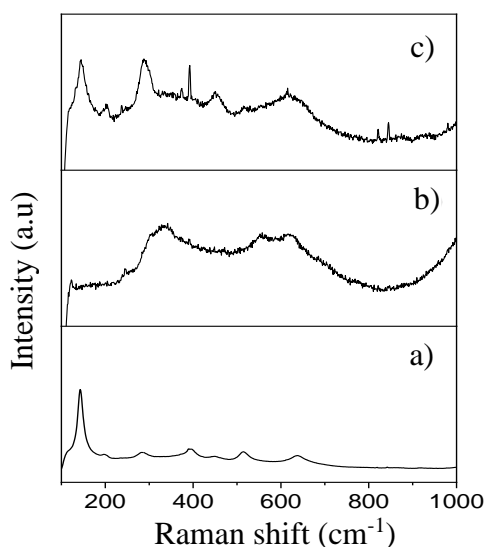

Figure 5.7 - Raman spectra for the thin film samples a) titania HBNs, b) CuO, and c) CuO-HBNs.

Morphology

The fabricated titania HBNs thin-film was coated evenly on the FTO glass. Taking a closer observation, the thin film contained nanorod structures with a highly branched morphology in a 3D orientation (Figure 5.8a). The vertical nanorods were perpendicularly oriented to the FTO glass substrate (Figure 5.8d) and the dimensions of the nanorods were measured as shown in Figure 5.9. The highly branched morphology of the titania HBNs exhibits a nanorod structure with enough space that could promote light penetration through the material and could potentially be a beneficial support for CuO loading to promote dispersion and to prevent the agglomeration of CuO nanoparticles. After the deposition of CuO onto HBNs, a thin over layer on the top of the

HBN nanorods was observed without agglomeration. Furthermore, nano-bridges were formed, linking the HBNs and formed into a 3D network within the sample (Figure 5.8c). However, in the absence of the HBNs, the CuO thin film was agglomerated resulting in a patchy microstructure on the FTO (Figure 5.8b).
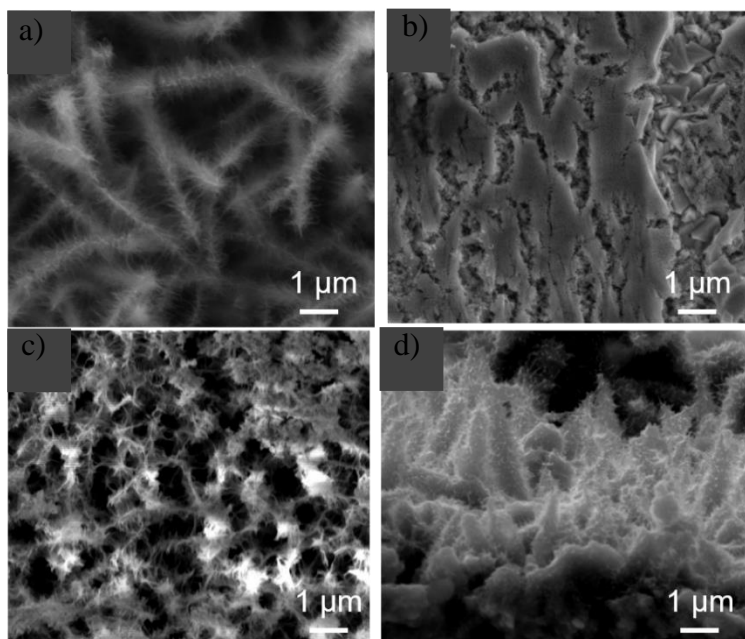

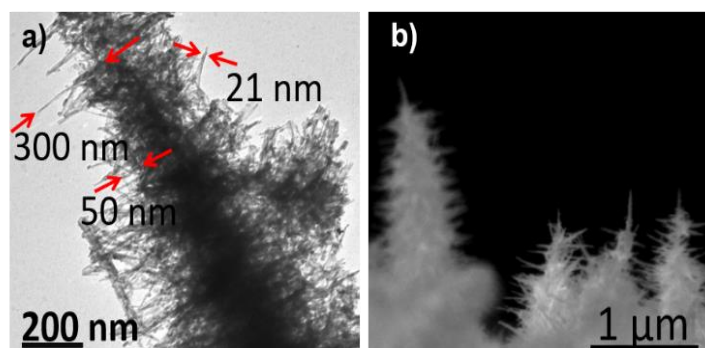Figure 5.8 - SEM imaging of a) titania HBNs, b) CuO, c) CuO-HBNs, and the cross-section view of d) titania HBNs.

Figure 5.9 - Cross-section view of T1 under a) TEM and b) SEM.

111

The optical properties of the fabricated samples were investigated and analyzed using UV-Vis spectroscopy, as shown in Figure 5.10. Interestingly the band gap for the titania HBNs is shown to be narrowed after the incorporation of CuO, from 3.6 to 3.3 eV.
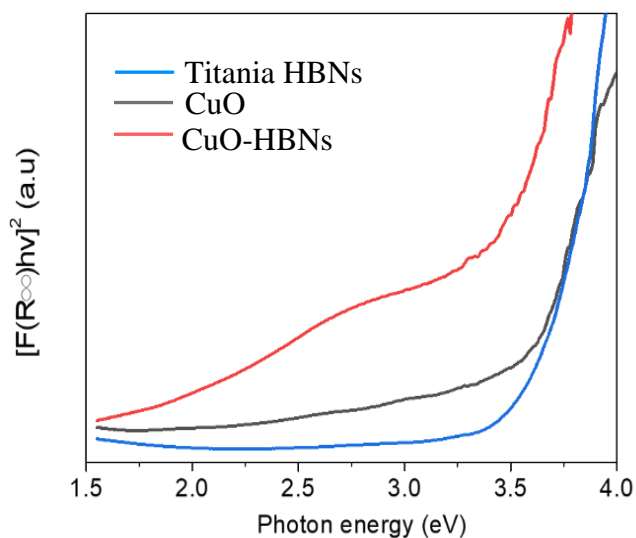

Figure 5.10 - Kubelka-Munk function for the thin film samples.

Surface properties

The CuO-HBNs thin film presented Ti, O and Cu elements in the survey scan. The Ti 2p peak was deconvoluted into two components, in which Ti $2p_{1/2}$ was centered at 471.3 eV and Ti $2p_{3/2}$ was centered at 458.5 eV, indicating Ti^{4+} oxidation state (Figure 5.11). In addition, both Cu containing samples CuO and CuO-HBNs exhibited the Cu $2p_{3/2}$, Cu $2p_{1/2}$ and Cu satellite peaks at 932.7, 952.4 and 962.1 eV, respectively (shown in Figure 5.4e, section 5.10). These observations indicated an oxidation state of Cu^{2+} and confirmed the presence of CuO on the thin films. High resolution XPS spectra at low binding energy region were also collected to investigate the position of the valence band. The valence band of samples CuO and CuO-HBNs was positioned at +1.6 eV, whereas the valence band of titania HBNs was located +2.0 eV. These results indicate that samples CuO and CuO-HBNs may have higher selectivity towards CH_4 than titania HBNs, due to the higher potential to reduce CO_2 to CH_4.[27]
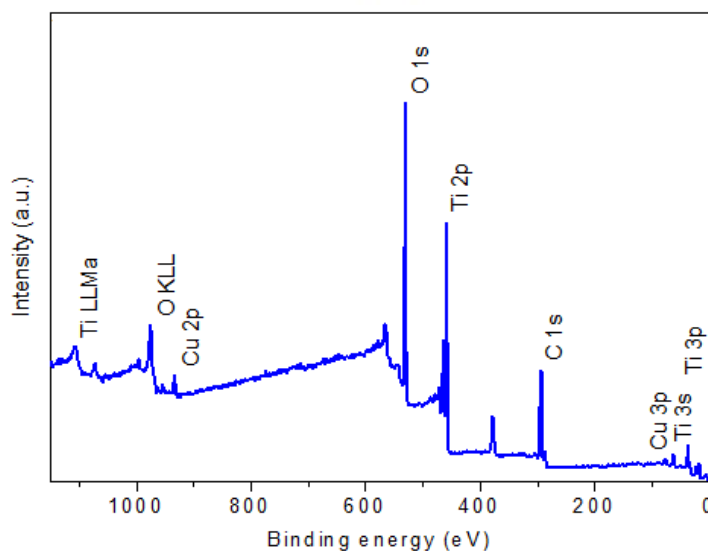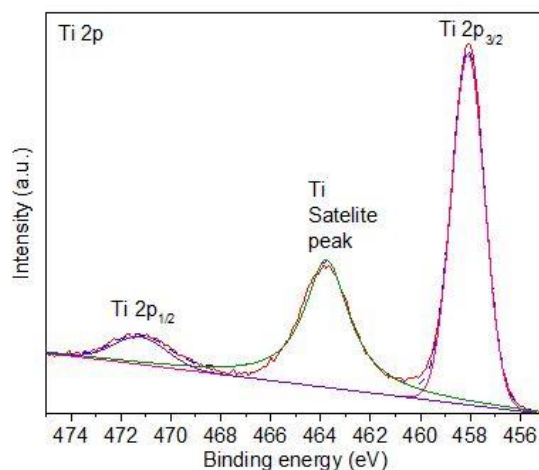
Figure 5.11 - High resolution Ti2p peaks XPS analysis and overall survey scan for CuO-HBNs.

Photoelectrochemical properties

To investigate the photoelectrochemical properties of the fabricated samples, chronoamperometry was carried out (Figure 5.12). The photocurrent generated by titania HBNs and CuO-HBNs samples was 3.3×10^{-7} and -3.2×10^{-6} μA cm^{-2}, respectively (Figure 5.12). The positive photocurrent value of titania HBNs indicated that it is an n-type semiconductor. However, when CuO was loaded, CuO-HBNs revealed a negative photocurrent, exhibiting the characteristic p-type semiconductor. Furthermore, the photocurrent response to the light (*i.e.*, the difference in the current density when the light is on and off) of CuO-HBNs was also improved when compared to the titania HBNs sample. This indicated a surplus of holes available in the valence band of the

photocatalyst that could interact with the water molecule to generate -OH radicals and release H^+ during the CO_2 photoreduction.
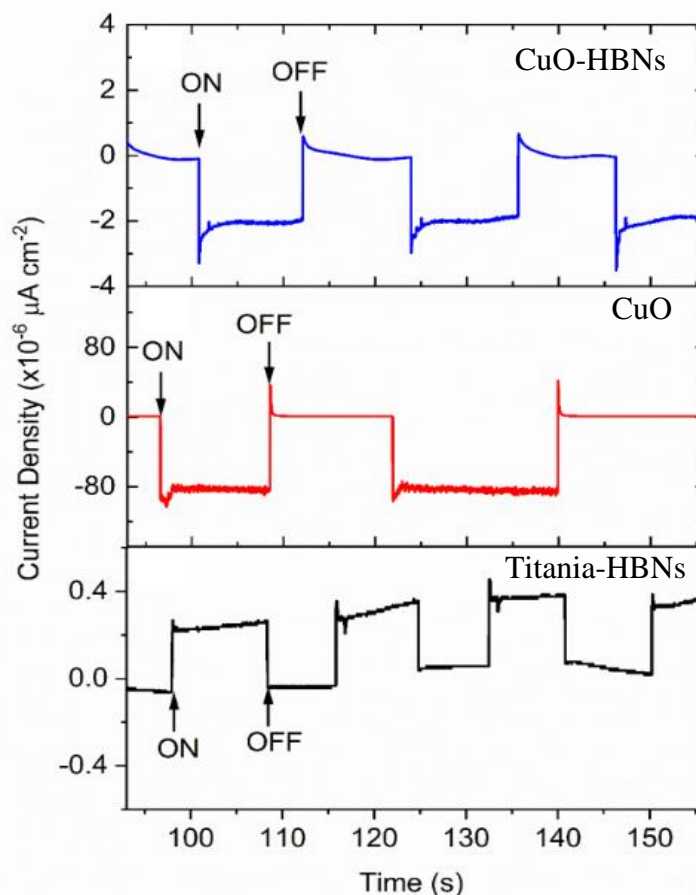
Figure 5.12 - Chronoamperometric pattern of the thin film samples.

Photocatalytic activity

The fabricated samples were evaluated for the photocatalytic reduction of CO_2 under the light irradiation (300-600 nm) and the quantity of the gaseous products produced (CO and CH_4) were monitored (Table 5.2). Titania HBNs produced 668.8 and 15.5 µmol g_{cat}^{-1} h^{-1} of CO and CH_4, respectively. The high production of CO was attributed to the unique morphology of the titania HBNs that could increase the light absorbance and active site exposure. Sample CuO exhibited a 100% selectivity towards CH_4, producing 12.7 µmol g_{cat}^{-1} h^{-1}. When CuO was loaded on the HBNs, the production of CH_4 and CO continued to reduce to only 3.8 and 8.7 µmol g_{cat}^{-1} h^{-1}, respectively. The production of CO in CuO-HBNs was probably attributed to the uncoated titania HBNs with CuO. Interestingly, while the production was reduced, CuO-HBNs showed a significant increase in selectivity

114

towards CH_4 compared to titania HBNs, from 2.26 to 30.37%. The reduced production could be partially attributed to shading effects of the CuO over layer on the titania HBNs, as observed in the SEM analysis (Figure 5.8c).

Table 5.2 - Gas products obtained after 4 h from CO_2 photoreduction using different configurations of photocatalyst.

Sample name	CO (μmol $g_{cat}^{-1} h^{-1}$)	CH_4 (μmol $g_{cat}^{-1} h^{-1}$)
Titania HBNs	669	15.5
CuO	-	12.7
CuO-HBNs	7.30	3.80

References

[1]   Y. Wang, L. Zhao, A. Otto, M. Robinius, and D. Stolten, "A review of post-combustion CO_2 capture technologies from coal-fired power plants," *Energy Procedia,* vol. 114, pp. 650-665, 2017.

[2]   D. Y. Leung, G. Caramanna, and M. M. Maroto-Valer, "An overview of current status of carbon dioxide capture and storage technologies," *Renewable and Sustainable Energy Reviews,* vol. 39, pp. 426-443, 2014.

[3]   L. Liu, C. Zhao, J. Xu, and Y. Li, "Integrated CO_2 capture and photocatalytic conversion by a hybrid adsorbent/photocatalyst material," *Appl. Catal., B,* vol. 179, pp. 489-499, 2015/12/01/ 2015, doi: https://doi.org/10.1016/j.apcatb.2015.06.006.

[4]   A. Crake, K. C. Christoforidis, A. Kafizas, S. Zafeiratos, and C. Petit, "CO_2 capture and photocatalytic reduction using bifunctional TiO_2/MOF nanocomposites under UV–vis irradiation," *Applied Catalysis B: Environmental,* vol. 210, pp. 131-140, 2017/08/05/ 2017, doi: https://doi.org/10.1016/j.apcatb.2017.03.039.

[5]   M. Flores-Flores, E. Luévano-Hipólito, L. M. T. Martínez, G. Morales-Mendoza, and R. Gómez, "Photocatalytic CO_2 conversion by MgAl layered double hydroxides: Effect of Mg2+ precursor and microwave irradiation time," *Journal of Photochemistry and Photobiology A: Chemistry,* vol. 363, pp. 68-73, 2018.

[6]   A. Li *et al.*, "Tunable syngas production from photocatalytic CO_2 reduction with mitigated charge recombination driven by spatially separated cocatalysts," *Chemical science,* vol. 9, no. 24, pp. 5334-5340, 2018.

[7]   G. Qin *et al.*, "Photocatalytic reduction of carbon dioxide to formic acid, formaldehyde, and methanol using dye-sensitized TiO_2 film," *Applied Catalysis B: Environmental,* vol. 129, pp. 599-605, 2013.

[8]   J. Z. Tan, Y. Fernández, D. Liu, M. Maroto-Valer, J. Bian, and X. Zhang, "Photoreduction of CO2 using copper-decorated TiO_2 nanorod films with localized surface plasmon behavior," *Chem. Phys. Lett.,* vol. 531, pp. 149-154, 2012.

[9]   O. Ola and M. M. Maroto-Valer, "Copper based TiO_2 honeycomb monoliths for CO 2 photoreduction," *Catalysis Science & Technology,* vol. 4, no. 6, pp. 1631-1637, 2014 2014.

[10]   W. A. Thompson, C. Perier, and M. M. Maroto-Valer, "Systematic study of sol-gel parameters on TiO_2 coating for CO_2 photoreduction," *Applied Catalysis B: Environmental,* vol. 238, pp. 136-146, 2018.

[11]   D. Liu *et al.*, "On the impact of Cu dispersion on CO_2 photoreduction over Cu/TiO_2," *Catal. Commun.,* vol. 25, pp. 78-82, 2012.

[12]   Y. Chiang and R. Juang, "Surface modifications of carbonaceous materials for carbon dioxide adsorption: a review. J Taiwan Inst Chem Eng 71: 214–234," ed, 2017.

[13]   Q. Wang, J. Luo, Z. Zhong, and A. Borgna, "CO_2 capture by solid adsorbents and their applications: current status and new trends," *Energy Environ. Sci.,* vol. 4, no. 1, pp. 42-55, 2011.

[14]   S. Sun, "Recent advances in hybrid Cu_2O-based heterogeneous nanostructures," *Nanoscale,* vol. 7, no. 25, pp. 10850-10882, 2015.

[15] M. Janczarek and E. Kowalska, "On the origin of enhanced photocatalytic activity of copper-modified titania in the oxidative reaction systems," *Catalysts,* vol. 7, no. 11, p. 317, 2017.

[16] W. N. R. W. Isahak *et al.*, "Adsorption–desorption of CO_2 on different type of copper oxides surfaces: Physical and chemical attractions studies," *Journal of CO_2 Utilization,* vol. 2, pp. 8-15, 2013.

[17] B.-J. Kim, K.-S. Cho, and S.-J. Park, "Copper oxide-decorated porous carbons for carbon dioxide adsorption behaviors," *J. Colloid Interface Sci.,* vol. 342, no. 2, pp. 575-578, 2010.

[18] J.-C. Wang *et al.*, "Enhanced photoreduction CO_2 activity over direct Z-scheme α-Fe_2O_3/Cu_2O heterostructures under visible light irradiation," *ACS applied materials & interfaces,* vol. 7, no. 16, pp. 8631-8639, 2015.

[19] S. I. In, D. D. Vaughn, and R. E. Schaak, "Hybrid CuO-TiO_2− xNx hollow nanocubes for photocatalytic conversion of CO_2 into methane under solar irradiation," *Angew. Chem. Int. Ed.,* vol. 51, no. 16, pp. 3915-3918, 2012.

[20] N. Jantarasorn, O. Mekasuwandumrong, P. Kelly, and P. Praserthdam, "Reactive Magnetron Sputter Deposition of Copper on TiO_2 Support for Photoreduction of CO_2 to CH_4," *IOP Conference Series: Materials Science and Engineering,* vol. 559, no. 1, p. 012017, 2019/06/01 2019, doi: 10.1088/1757-899x/559/1/012017.

[21] Z. Xiong *et al.*, "Selective photocatalytic reduction of CO_2 into CH_4 over Pt-Cu_2O TiO_2 nanocrystals: The interaction between Pt and Cu_2O cocatalysts," *Applied Catalysis B: Environmental,* vol. 202, pp. 695-703, 2017.

[22] A. E. Nogueira, J. A. Oliveira, G. T. da Silva, and C. Ribeiro, "Insights into the role of CuO in the CO_2 photoreduction process," *Sci. Rep.,* vol. 9, no. 1, pp. 1-11, 2019.

[23] M. L. Ovcharov, A. M. Mishura, N. D. Shcherban, S. M. Filonenko, and V. M. Granchak, "Photocatalytic reduction of CO_2 using nanostructured Cu_2O with foam-like structure," *Solar Energy,* vol. 139, pp. 452-457, 2016/12/01/ 2016, doi: https://doi.org/10.1016/j.solener.2016.10.010.

[24] T. Arai, S. Sato, and T. Morikawa, "A monolithic device for CO_2 photoreduction to generate liquid organic substances in a single-compartment reactor," *Energy Environ. Sci.,* 10.1039/C5EE01314C vol. 8, no. 7, pp. 1998-2002, 2015, doi: 10.1039/C5EE01314C.

[25] M. Tahir and N. S. Amin, "Photocatalytic CO_2 reduction and kinetic study over In/TiO_2 nanoparticles supported microchannel monolith photoreactor," *Applied Catalysis A: General,* vol. 467, pp. 483-496, 2013 2013.

[26] M. A. Ávila-López, E. Luévano-Hipólito, and L. M. Torres-Martínez, "CO_2 adsorption and its visible-light-driven reduction using CuO synthesized by an eco-friendly sonochemical method," *Journal of Photochemistry and Photobiology A: Chemistry,* vol. 382, p. 111933, 2019/09/01/ 2019, doi: https://doi.org/10.1016/j.jphotochem.2019.111933.

[27] W. A. Thompson *et al.*, "Systematic study of TiO_2/ZnO mixed metal oxides for CO_2 photoreduction," *RSC Adv.,* 10.1039/C9RA03435H vol. 9, no. 38, pp. 21660-21666, 2019, doi: 10.1039/C9RA03435H.

[28] I. R. Lewis and H. Edwards, *Handbook of Raman spectroscopy: from the research laboratory to the process line.* CRC press, 2001.

[29] S. Guha, D. Peebles, and J. Terence Wieting, "Raman and infrared studies of cupric oxide," *Bull. Mater. Sci.,* vol. 14, no. 3, pp. 539-543, 1991/06/01 1991, doi: 10.1007/BF02744682.

[30] M. Rashad, M. Rüsing, G. Berth, K. Lischka, and A. Pawlis, "CuO and Co_3O_4 nanoparticles: synthesis, characterizations, and Raman spectroscopy," *Journal of Nanomaterials,* vol. 2013, 2013.

[31] H. Goldstein, D.-s. Kim, Y. Y. Peter, L. Bourne, J. Chaminade, and L. Nganga, "Raman study of CuO single crystals," *Physical Review B,* vol. 41, no. 10, p. 7192, 1990.

[32] S. Chakraborty, A. Das, M. R. Begum, S. Dhara, and A. Tyagi, "Vibrational properties of CuO nanoparticles synthesized by hydrothermal technique," in *AIP Conference Proceedings*, 2011, vol. 1349, no. 1: American Institute of Physics, pp. 841-842.

[33] P. Timchenko, E. Timchenko, L. Volova, and O. Frolov, "Chemometric analysis of the Raman spectra for determination of the composition of bones with different porosity," in *Journal of Physics: Conference Series*, 2018, vol. 1135, no. 1: IOP Publishing, p. 012054.

[34] D. A. Long, "Infrared and Raman characteristic group frequencies. Tables and charts George Socrates John Wiley and Sons, Ltd, Chichester, Third Edition, 2001. " *Journal of Raman Spectroscopy,* vol. 35, no. 10, pp. 905-905, 2004, doi: https://doi.org/10.1002/jrs.1238.

[35] D. He, S. Xing, B. Sun, H. Cai, H. Suo, and C. Zhao, "Design and construction of three-dimensional flower-like CuO hierarchical nanostructures on copper foam for high performance supercapacitor," *Electrochim. Acta,* vol. 210, pp. 639-645, 2016.

[36] L. Zhu, H. Li, Z. Liu, P. Xia, Y. Xie, and D. Xiong, "Synthesis of the 0D/3D CuO/ZnO heterojunction with enhanced photocatalytic activity," *The Journal of Physical Chemistry C,* vol. 122, no. 17, pp. 9531-9539, 2018.

[37] J.-Y. Park, K.-A. Lim, R. D. Ramsier, and Y.-C. Kang, "Spectroscopic and morphological investigation of copper oxide thin films prepared by magnetron sputtering at various oxygen ratios," *Bull. Korean Chem. Soc.,* vol. 32, no. 9, pp. 3395-3399, 2011.

[38] Q. Yang, P. Yan, J. Chang, J. Feng, and G. Yue, "Growth of bicrystal CuO microsheets from aqueous solution," *Phys. Lett. A,* vol. 361, no. 6, pp. 493-496, 2007.

[39] Y. Min, T. Wang, and Y. Chen, "Microwave-assistant synthesis of ordered CuO micro-structures on Cu substrate," *Appl. Surf. Sci.,* vol. 257, no. 1, pp. 132-137, 2010.

[40] W. Li, R. Liang, A. Hu, Z. Huang, and Y. N. Zhou, "Generation of oxygen vacancies in visible light activated one-dimensional iodine TiO_2 photocatalysts," *RSC Adv.,* vol. 4, no. 70, pp. 36959-36966, 2014.

[41] H. Yu *et al.*, "Three-in-one oxygen vacancies: whole visible-spectrum absorption, efficient charge separation, and surface site activation for robust CO_2 photoreduction," *Angew. Chem. Int. Ed.,* vol. 58, no. 12, pp. 3880-3884, 2019.

[42] Z.-P. Nie, D.-K. Ma, G.-Y. Fang, W. Chen, and S.-M. Huang, "Concave Bi_2WO_6 nanoplates with oxygen vacancies achieving enhanced electrocatalytic oxygen evolution in near-neutral water," *Journal of Materials Chemistry A,* vol. 4, no. 7, pp. 2438-2444, 2016.

[43] E. Desimoni and B. Brunetti, "X-ray photoelectron spectroscopic characterization of chemically modified electrodes used as chemical sensors and biosensors: a review," *Chemosensors,* vol. 3, no. 2, pp. 70-117, 2015.

[44] S. Jaiswar and K. Mandal, "Evidence of enhanced oxygen vacancy defects inducing ferromagnetism in multiferroic $CaMn_7O_{12}$ manganite with sintering

time," *The Journal of Physical Chemistry C,* vol. 121, no. 36, pp. 19586-19601, 2017.

[45]   L. Proaño, E. Tello, M. A. Arellano-Trevino, S. Wang, R. J. Farrauto, and M. Cobo, "In-situ DRIFTS study of two-step CO_2 capture and catalytic methanation over Ru,"Na_2O"/Al_2O_3 Dual Functional Material," *Appl. Surf. Sci.,* vol. 479, pp. 25-30, 2019.

[46]   M. A. Ávila-López, E. Luévano-Hipólito, and L. M. Torres-Martínez, "CuO coatings on glass fibers: a hybrid material for CO_2 adsorption and photocatalytic reduction to solar fuels," *Journal of Materials Science: Materials in Electronics,* vol. 31, no. 16, pp. 13957-13969, 2020/08/01 2020, doi: 10.1007/s10854-020-03955-x.

[47]   H. Du, C. T. Williams, A. D. Ebner, and J. A. Ritter, "In Situ FTIR Spectroscopic Analysis of Carbonate Transformations during Adsorption and Desorption of CO_2 in K-Promoted HTlc," *Chem. Mater.,* vol. 22, no. 11, pp. 3519-3526, 2010/06/08 2010, doi: 10.1021/cm100703e.

[48]   Y. Liu *et al.*, "Chemical Adsorption Enhanced CO_2 Capture and Photoreduction over a Copper Porphyrin Based Metal Organic Framework," *ACS Applied Materials & Interfaces,* vol. 5, no. 15, pp. 7654-7658, 2013/08/14 2013, doi: 10.1021/am4019675.

[49]   A. Hakim *et al.*, "Studies on CO_2 adsorption and desorption properties from various types of iron oxides (FeO, Fe_2O_3, and Fe_3O_4)," *Industrial & Engineering Chemistry Research,* vol. 55, no. 29, pp. 7888-7897, 2016.

[50]   Y. Kato *et al.*, "Study on carbon dioxide reduction with water over metal oxide photocatalysts," *Surf. Interface Anal.,* vol. 51, no. 1, pp. 40-45, 2019, doi: https://doi.org/10.1002/sia.6542.

[51]   S. N. Habisreutinger, L. Schmidt-Mende, and J. K. Stolarczyk, "Photocatalytic Reduction of CO_2 on TiO_2 and Other Semiconductors," *Angew. Chem. Int. Ed.,* vol. 52, no. 29, pp. 7372-7408, 2013, doi: https://doi.org/10.1002/anie.201207199.

[52]   J. S. Lee, K. H. You, and C. B. Park, "Highly Photoactive, Low Bandgap TiO_2 Nanoparticles Wrapped by Graphene," *Adv. Mater.,* vol. 24, no. 8, pp. 1084-1088, 2012, doi: https://doi.org/10.1002/adma.201104110.

[53]   A. León *et al.*, "FTIR and Raman Characterization of TiO_2 Nanoparticles Coated with Polyethylene Glycol as Carrier for 2-Methoxyestradiol," *Applied Sciences,* vol. 7, no. 1, p. 49, 2017. [Online]. Available: https://www.mdpi.com/2076-3417/7/1/49.

[54]   H. C. Choi, Y. M. Jung, and S. B. Kim, "Size effects in the Raman spectra of TiO2 nanoparticles," *Vib. Spectrosc,* vol. 37, no. 1, pp. 33-38, 2005/01/14/ 2005, doi: https://doi.org/10.1016/j.vibspec.2004.05.006.

[55]   T. Ohsaka, "Temperature Dependence of the Raman Spectrum in Anatase TiO_2" *J. Phys. Soc. Jpn.,* vol. 48, no. 5, pp. 1661-1668, 1980, doi: 10.1143/JPSJ.48.1661.

Chapter 6

Photo-generation of cyclic carbonates using hyper-branched Ru-TiO$_2$
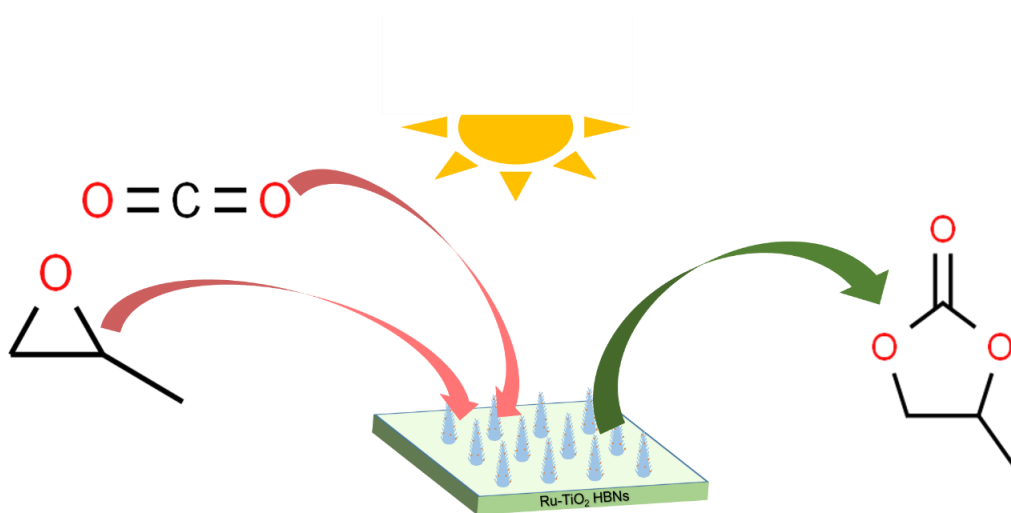
6.1 Aim and objectives

The production of cyclic carbonates (CCs) using CO_2 and epoxides has been industrially available for over 60 years.[1] However, with the shift towards more sustainable and environmentally friendly processes, many researchers have attempted to improve upon the existing homogeneous catalyst. The currently used homogeneous catalysts require high temperatures and pressures, and their corrosive properties necessitate exotic and expensive materials for their reactors.[2, 3] A lot of research has been directed towards heterogeneous catalysts, which provides the added benefit of reduced separation and purification costs in the production line.[1, 4-9] The presented publication`s aim is to investigate the underexplored photocatalytic approach, towards the photo-generation of cyclic carbonates using RuO$_2$-HBNs as photocatalyst. The CO_2 cyclo-addition reaction was performed using mild reaction conditions ~55 °C and 200 kPa for 6 h under solar simulator irradiation as opposed to 100-200 °C and 5000-10000 kPa used in industrial processes with homogeneous catalysts.[10] Following the publication, towards the end of the current chapter is section 6.11 "Further research" which contains unpublished work that followed the research work presented in the publication. In this section, further examination of various photocatalysts take place and valuable comparison are made with the limited amount of research available on the photo-generation of cyclic carbonates.

The objectives of this work are:

- Fabricate a suitable photocatalyst with appropriate modifications to achieve the photocatalytic generation of cyclic carbonates under visible light.
- Perform sufficient experiments to validate that the reaction follows a photocatalytic pathway.
- Aim towards milder reaction conditions compared to the ones currently being used in the industry.
- Consider ease of use of the photocatalyst to avoid complex photocatalyst regeneration and purification steps.

6.2 Highlights and key findings

6.2.1 Fabrication of HBN and visible light absorption

Due to the versatility and enhanced photocatalytic performance of the titania-based hyper-branched nanorods (HBN), as discussed in Chapter 4 and 5, it is worth exploring their utilisation in different photocatalytic reactions. Although HBN morphology had shown to have increased light harvesting, the as-prepared HBNs showed poor visible light performance, due to their wide band gap of 3.6 eV as was shown under UV-Vis examination. To modify the wavelength absorption range of the fabricated HBNs, Ru was incorporated into the synthesis using solvothermal treatment after the fabrication of the HBNs. The resulting Ru-TiO$_2$ HBNs have shown increased visible light absorption which was attributed to the RuO$_2$ nanoparticles found decorating the dendritic microstructures. Furthermore, additional absorption was observed in the range of 350 – 500 nm which was attributed to Ru^{4+} particles doped into the crystal lattice of the TiO$_2$. The above modifications allowed the Ru-TiO$_2$ HBNs to perform under the solar simulator irradiation and successfully facilitate the CO$_2$ cycloaddition reaction.

6.2.2 Photocatalytic approach and control experiments

The photocatalytic performance was evaluated by the conversion of propylene oxide (PO), as the epoxide source, into propylene carbonate (PC). FT-IR was performed using the solution obtained after the reaction before any purification, and a following FT-IR analysis was acquired after the filtration and evaporation steps to purify the product. To ensure the reaction follows a photocatalytic route, two control experiments were

conducted: (i) First, heat and pressure were applied, without a light source nor a photocatalyst. This control experiment aims to investigate if the applied heat and pressure were able to stimulate the CO_2 cycloaddition. In this experiment, no residual product was observed in the evaporation process; (ii) The second control experiment included the best performing RuO_2-TiO_2 HBN photocatalyst, in the absence of the solar simulator irradiation. This control experiment aims to investigate if the reaction follows a photo-catalytic path. The FT-IR spectrum of this experiment showed no residual product produced (Figure 6.8a). The reactions solution for these experiments was prepared using dichloromethane (DCM) to PO ratio of 1:8 and 1.022 mg of DMAP was added per mL of solution. The reaction solution was kept in dark conditions at room temperature.

6.2.3   Effects of Ru concentration and stability

As mentioned in section 5.2.1, the as prepared TiO_2 HBNs showed inferior PC conversion as shown in Figure 6.8 (a,b) (see Publication 3 below). Three variations of Ru loading concentration (0.05, 0.01 and 0.005 M) were used to fabricate Ru-HBNs. When the Ru element was introduced into the photo-catalyst synthesis, the PC conversion improved. It was observed that with lower Ru concentration, the intensity of the trough positioned at 1792 cm^{-1} associated with PC was increased (Figure 6.8a). When Ru concentration was increased from 0.005 to 0.01 M, it was observed that the PC production was almost halved. No significant further product formation was observed when the concentration of Ru was further increased to 0.05 M. The best performing photocatalyst was Ru_{005}-TiO_2 HBN, which had a Ru atomic percentage of 1.11% relative to titania, as determined from the XPS studies.

6.3   Research impact

The contribution in this study lies in that it discusses the underexplored photocatalytic approach for the CO_2 cycloaddition to epoxides for the generation of cyclic carbonates. Prior 2021, there are only 3 publications available discussing the photogeneration of cyclic carbonates, including the current study, to the best of the authors knowledge.[11, 12] It is also the first study to demonstrate the effectiveness of Ru element in the photogeneration of cyclic carbonates. Additionally, this study presents a different reaction solution which does not involve high amounts of solvents as opposed to the other two available publications. In more detail, the reactant (propylene oxide) to solvent ratio for this study is 8:1, while the alternative reaction solution mentioned in the other two available publications has a reactant to solvent ratio of 1:225. The fabricated Ru-TiO_2

HBNs provides an easy catalyst recovery step due to the FTO glass support, which could potentially reduce the cost of the expensive catalyst separation step required with current homogeneous catalysts used in the industry. However, it is important to mention that the conversion rates are not yet comparable with the homogeneous catalysts currently being used in the industry.

6.4   Personal development

The current work was conducted during the first year of this PhD project, and therefore, skills for the challenging synthesis, characterisation techniques, and reactor design and engineering were developed during this study. More importantly, this study was published in the Faraday Discussions 2019 for artificial photosynthesis. Along with this publication, there was a conference oral presentation requirement for the published paper where the research was read beforehand by the audience and discussed at the conference held at Cambridge University. For a first year PhD student to present his work amongst leading researchers in the photocatalysis field in this prestigious conference was both a challenging yet an invaluable experience.

Publication 3

Title: Photo-generation of Cyclic Carbonates Using Hyper-branched Ru-TiO$_2$.

Authors: Gavrielides Stelios, Jeannie Z. Y. Tan, Eva Sanchez Fernandez and M. Mercedes Maroto-Valer

Status: Published

Abstract

Anthropogenic CO_2 is the main contributor to the increased concentration of greenhouse gases in the atmosphere, and thus utilising waste CO_2 for the production of valuable chemicals is a very appealing strategy for reducing CO_2 emissions. The catalytic fixation of CO_2 with epoxides to produce cyclic carbonates has gained increasing attention from the research community in search of an alternative to the homogeneous catalytic routes, which are currently being used in industry. A novel photocatalytic heterogeneous approach to generate cyclic carbonates is demonstrated in this work. Hyper-branched microstructured Ru modified TiO_2 nanorods decorated with RuO_2 nanoparticles, supported on fluorine-doped tin oxide (FTO) glass were fabricated for the first time and were used to catalyse the photo-generation of propylene carbonates from propylene oxides. Propylene carbonate was used as a reference for cyclic carbonates. The photo-generation of cyclic carbonates from epoxides and CO_2 was carried out at a maximum temperature of 55 °C and 200 kPa in a stainless steel photoreactor with a quartz window, under solar irradiation. The best performing photocatalyst exhibited an estimated selectivity of 83% towards propylene carbonates under the irradiation of solar simulator.

5.5 Introduction

Humankind relies heavily on fossil fuels as the primary energy source, producing CO_2 as a by-product, which is released into the atmosphere. The increased level of anthropogenic CO_2 emissions is one of the most vital contributors to climate change. In this regard, the research community has been trying to address this challenge by developing alternative energy sources, increasing efficiency and carbon capture, utilisation and storage (CCUS).[13] Utilising CO_2 in the production of commercially valuable chemicals and fuels has recently attracted much attention.[14] CO_2, is often a good source of C-building blocks for various organic synthesis, as it is abundant and low-cost.[15] Using waste CO_2 as a feedstock for chemical reactions not only offers a more sustainable route to generate value-added products, but also contributes to CO_2 fixation.[13, 16]

The synthesis of cyclic carbonates (CCs) through the coupling of CO_2 and epoxides has been commercially available for over 60 years and is one of the most promising CO_2 utilisation industrial applications.[13] CCs are valuable as monomers, small molecules[17] and polymer intermediates,[18] pharmaceuticals[19], and fine chemical intermediates.[15] In addition, the most important and rapidly growing application of CCs lies in Li-ion batteries, in which CCs are used as electrolytes.[20]

Nowadays, Li-ion batteries power most of the portable electronic devices and their application in electronic vehicles is becoming very popular.[20] Due to the future projected demands for Li-ion batteries, the current industrial production of Li-ion is rapidly increasing.

Current commercial process for CCs synthesis uses homogeneous catalysts, such as quaternary ammonium[2] or phosphonium halides. Although these catalysts are inexpensive, they suffer from low efficiencies and require high temperature and pressure.[21] More specifically, the reaction conditions were reported to be at 100-200 °C, and 50-100 bar.[22] Additionally, due to their corrosive nature, special reactor materials are necessary, which further increases the production cost. Hence, in recent decades, new approaches have been developed for the production of CCs.[4-6, 23] Many researchers used homogeneous catalysts, such as (salen)Cr(III) complexes[15], (salen)Co(III),[24] (salen)Mn(III),[25] and supramolecular metal complexes[26] to catalyse the production of CCs. However, several drawbacks were detected have been reported for these developed homogeneous catalysts, including low catalyst stability, reactivity and air sensitivity.[15, 20] Furthermore, the recovery of these homogeneous catalysts, and the purification of the product is challenging, expensive and time-consuming.[13]

Recently, heterogeneous catalysts for the synthesis of CCs have been developed because of the easy separation of fluids from the solid catalyst, convenient handling and catalyst regeneration.[7, 13] For example, Zn-ZIF-67-MOFs,[8] Fe(III)[9] and bimetallic complexes[27] have been developed to catalyse the production of CCs from CO_2 and epoxide.

Photocatalysis has received much attention from the research community in the recent years due to its sustainability aspect and its high performance in a variety of applications, including photo-generation of H_2,[28-31] photoreduction of CO_2 for the production of fine chemicals and solar fuels,[32-34] and air and water purification.[35-37] TiO_2 is the most widely used photo-catalyst for these applications because it is non-toxic, thermally and chemically very stable, abundantly available and has good photo-response under UV light irradiation.[11, 38]

Very recently, Prajapati *et al*. demonstrated the first photocatalytic synthesis of CCs using cobalt phtalocyanine grafted on TiO_2. The synthesized photocatalyst revealed 94.2% of conversion after 24 h of irradiation at 25 °C and 1 atm. Additionally, the

photocatalysis route has shown promising performance and provides a safer route with milder reaction conditions, compared to other heterogeneous catalysts, which were reported to require temperatures up to 80-150 °C and pressure of 10 - 30 bar.[7]

To further explore the photogeneration of CCs using TiO_2-based heterogeneous photocatalysts, the use of a thin film photocatalyst is proposed here to eliminate the need of separation step to recycle the catalyst, as well as to ease the handling of photocatalyst. To the best of the authors' knowledge, the photo-generation of CCs using a thin film photocatalyst has not been reported in the literature. TiO_2 is a wide band gap semiconductor, and thus, it is photo-active predominantly in the UV range. To address this issue, the addition of foreign elements that are active in the visible light region are employed. RuO_2 decorating the TiO_2 are known to increase the overall absorbance of the RuO_2/TiO_2 material in the visible light region.[39] Therefore, the combination of Ru^{4+} doping and RuO_2 decoration on the TiO_2 can greatly increase the absorbance in the visible light region, and in turn making the use of solar light viable.[40] Furthermore, RuO_2 has high chemical stability, and electrical conductivity. The combination of RuO_2 with TiO_2 has been reported to improve charge separation, hindering the recombination process which should enhance the photocatalytic activity of the material.[39] This effect is attributed to the position of RuO_2 valence and conduction band relative to those of TiO_2. Therefore, in this work, Ru_x-TiO_2 thin film supported on the fluorine-doped tin oxide (FTO) glass is proposed for photogeneration of CCs.

Moreover, in order to provide large surface area with more exposed active sites and superior light scattering capability, fast electron transport and efficient charge collection, the hyper-branched nanorods (HBN), are synthesized. These HBN have been reported to exhibit improved optical and photoelectrical properties which resulted in improved photo-conversion reactions.[41] Hence, the HBN were modified with Ru to be used as a novel Ru_x-TiO_2 photocatalyst for the photogeneration of CCs.

6.6 Experimental procedure

Materials & synthesis

Fluorine-doped tin oxide (FTO) glass TEC-15 was purchased from Ossila (dimensions 2.5 cm x 2.5 cm, roughness of 12.5 nm, FTO layer thickness of 200 nm, 83.5% transmission and resistivity of 12-14 Ω.cm^{-1}). Potassium titanium oxide oxalate dihydrate (PTO, ≥98.0%), diethylene glycol (DEG, 99.0%), bis(cyclopentadienyl)ruthenium

$((C_5H_5)_2Ru$, 98.0%), n-hexane $(C_6H_{14},$ 95.0%), propylene oxide (PO, 99.0%), dichloromethane (DCM, CH_2Cl_2, 99.8%), 4-(dimethylamino)pyridine (DMAP, 99.0%), propylene carbonate (PC, 99.7% anhydrous) and polyethylene glove Atmosbag were purchased from Sigma-Aldrich. Isopropanol (IPA, 99.5%), acetone (>95.0%) and ethanol (99.0%) were procured from Fisher Scientific. All chemicals were used without any further purification. All aqueous solutions were prepared using Milli-Q ultrapure type 1 water (18.2 MΩ.cm) collected from a Millipore system.

The FTO glass was cleaned prior to use with a solution of H_2O, IPA, and Acetone in a ratio of 1:1:1, for 1 h in the sonicator and air dried at 75 °C for 30 mins.

Hyper-branched nanorods (HBNs) of TiO₂ were fabricated using a hydrothermal approach. PTO was dissolved in a mixture of H_2O and DEG with a ratio of 1:7. The concentration of PTO was 0.05 M. After 30 minutes of vigorous stirring, the precursor solution was transferred to a 100 mL Teflon-lined autoclave along with the FTO glass. The FTO glass was positioned resting against the Teflon-liner walls with the conductive side facing down at approximately 60°. The hydrothermal synthesis was carried out at 180 °C for 9 h. After completing the reaction time, the autoclave was allowed to cool down to room temperature. The TiO_2 nanorods were rinsed several times with Milli-Q Type 1 water and ethanol, and then calcined at atmospheric conditions at 550 °C for 1 h.

The Ru loaded TiO₂ (Ruₓ-TiO₂) was synthesized under dry nitrogen atmosphere, in a polyethylene Atmos glove bag. A known amount of bis(cyclopentadienyl)ruthenium $(C_5H_5)_2Ru$, was dissolved in n-hexane (C_6H_{14}) and stirred vigorously at 40 °C until a clear solution was obtained. Three different concentrations of Ru precursor were synthesised, namely 0.05 M, 0.01 M, and 0.005 M that are denoted as Ru_{05}-TiO_2, Ru_{01}-TiO_2, and Ru_{005}-TiO_2, respectively. The TiO_2 loaded FTO glass was heated to 150 °C for 1 h to remove adsorbed water and was then allowed to cool to room temperature in dry air. The TiO_2 loaded FTO glass was then placed into the teflon liner resting against its walls at roughly 60 ° with the coated surface facing down. The ruthenium precursor liquid was added to the Teflon-liner to cover the entire FTO surface (25 ml). The Teflon liner was then transferred into the autoclave and was placed in the oven at 180 °C for 30 h. The Ru_x-TiO_2 FTO glass was then rinsed with n-hexane in dry nitrogen. It was then calcined to 400 °C for 10 h under dry air atmosphere with a ramp rate of 10 °C min⁻¹.

6.7 Characterization

The morphology of the synthesized products was examined by a field emission scanning electron microscope (FE-SEM, FEI Quanta 200 F). Further investigation on the morphology and the element composition of the samples was carried out using a transmission electron microscope (TEM) and high resolution HR-TEM (FEI Titan Themis 200) equipped with an energy dispersive X-ray spectroscope (EDX) detector operated at 200 kV. The samples were sonicated in ethanol for 5 min and then a few drops of the solution were placed on a carbon-coated copper TEM grid. Crystallinity and phase identification of the synthesized products were performed using powder X-ray diffraction (XRD, Bruker D8 Advanced Diffractometer) equipped with Cu Kα radiation ($\lambda = 1.5418$ Å). Raman spectra were collected using a Renishaw *inVia* Raman Microscope with 785 nm excitation source. The diffuse reflectance was measured using a Perkin Elmer Lambda 950 UV-vis equipped with an integrating sphere (150 mm) and the band gap energy was estimated using the Kubelka Munk function. X-ray photoelectron spectroscopy (XPS) was performed on a Scienta 300 XPS machine incorporating with a rotating AlKα X-ray source operating at 13 kV x 333 mA (4.33 kW). Electron analysis was performed using a 300 cm radius hemispherical analyser and lens system. The electron counting system consist of a multichannel plate, phosphorescent screen and CCD camera. All multichannel detection counting is done using proprietary Scienta software. The elements present were determined *via* a wide energy range survey scan (200 mW step, 20 ms dwell time, 150 eV pass energy and summed over 3 scans). The high resolution scans were performed at a similar pass energy (150 eV), but a step size of 20 mV. A dwell time of 533 ms was used and accumulated over 3 scans. The instrument operated at a base pressure of 1 x 10^{-9} mbar; the energy scale is calibrated using the Au 4f, Ag 3d and Cu 2p emission lines, where the half width of the Au $4f_7$ emission line is approximately 1.0 eV. All data analysis and peak fitting were performed using the CaseXPS software.

6.8 Photocatalysis

The reaction solution was prepared with DCM and PO in a 1:8 ratio, adding 1.022 mg of DMAP per mL of solution, and was kept in the dark at room temperature. The solution was then transferred to the stainless-steel Teflon-lined pressurized photo-reactor (Scheme 1) along with the photocatalyst. Two control experiments were performed, one with the absence of photocatalyst and light, and one with the absence of light, keeping all the rest

reaction conditions the same. The temperature throughout the experiment was measured using a pyrometer from the outside of the reactor that ranged between 40-55 °C. For the experiments incorporating photocatalysts, four pieces of Ru_x-TiO_2 coated FTO glasses were supported on a custom-made photocatalyst stage, as shown in Scheme 6.1. The stage was positioned directly below the quartz glass to be irradiated with the AM1.5G solar simulator directly (1 sun equivalent, 100 Wm^{-2}, 92250 A Newport, USA) while being submerged in the reaction solution. The reaction solution was bubbled with CO_2 and pressurised in CO_2 atmosphere, throughout the experiment. The 500 mL photo-reactor was supplied with continuous CO_2 and the pressure was maintained at 200 kPa using a bubbler. The reaction was conducted under the solar simulator for 6 h. After the reaction time was completed, the unreacted substrate and solvent were removed *in vacuo* and the products were then isolated using a rotary evaporator. The products were then identified using a FTIR spectrometer Perkin Elmer Frontier.
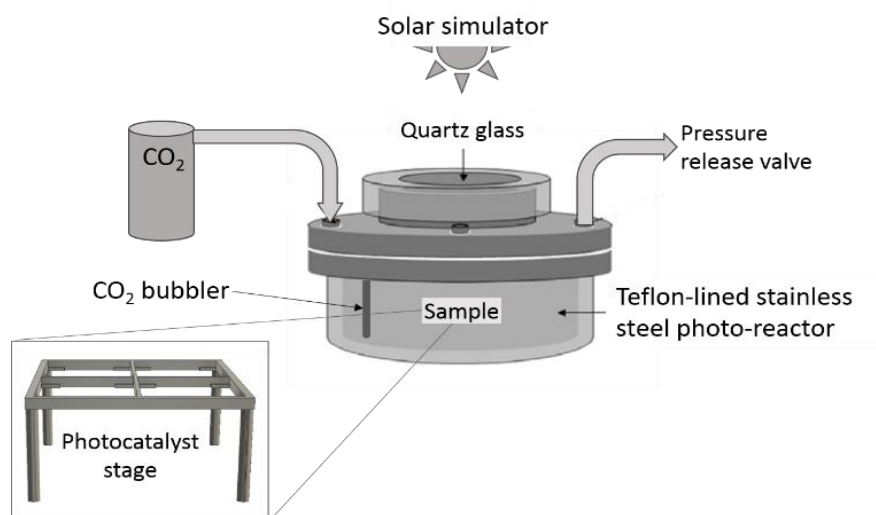
Scheme 6.3 - Schematic diagram of the photocatalysis setup and photocatalytic stage.

6.9 Results and discussion

The as-prepared TiO_2 and the fabricated Ru_x-TiO_2 thin film samples synthesized using solvothermal treatment followed by calcination exhibited homogeneous coating on the FTO glass. All the prepared samples were examined using XRD. In addition to the XRD pattern of the FTO coating on the glass, the crystallinity of anatase TiO_2 was also observed in all the samples (Figure 6.1). The peaks positioned at 25.4 and 48.1° were assigned to the (101) and (200) planes of anatase. No ruthenium related peak was observed in the XRD patterns of the fabricated Ru_x-TiO_2 samples. This was probably due

to the low concentration of Ru deposited on the glass. However, it is observed that with higher concentration of Ru loading the crystallinity of the sample is steadily decreasing suggesting that the Ru particles have been doped into the crystal lattice of the TiO_2 HBNs.

Raman spectroscopy is more sensitive and capable of characterising the crystal structure,[42] therefore, it was used in to further investigate the crystal phases present on the TiO_2-based thin film samples. The Raman patterns of the as-prepared TiO_2 and Ru_x-TiO_2 samples are shown in Figure 6.2. The Raman feature of the anatase phase, positioned at 143, 395, 517, and 638 cm^{-1} are associated with the E_g, B_{1g}, A_{1g}, and E_g vibrations, respectively, was present in all the fabricated sample.[43-47] Under close inspection, the main anatase peak of sample Ru_{05}-TiO_2 positioned at 143 cm^{-1} was shifted to 149 cm^{-1}, whereas the peak positioned at 638 cm^{-1} was shifted to 621 cm^{-1}. When the concentration of Ru was lowered down to 0.01 and 0.005 M, these shifts were reduced. These shifts are speculated to be attributed to lattice substitution of Ru into TiO_2.[48] Additionally, Raman feature of potassium titanate (PT) positioned at 285 and 444 cm^{-1}, was also observed, indicating potassium contamination from the titania precursor, PTO (Figure 6.2).[49] The PT and anatase peak intensities seem to have an inverse relationship, where one increases, while the other one decreases. However, a general trend can be observed, where PT peaks are found to increase in the Ru_x-TiO_2 samples. This corresponds to the loss of crystallinity observed in the XRD patterns (Figure 6.1) due to lattice substitution of Ti with Ru, which lowers the intensity of the anatase phase peaks No ruthenium related peak was found on the Raman spectra of the Ru_x-TiO_2 samples. This is probably due to the small particle size of RuO_2 (discussed in the next
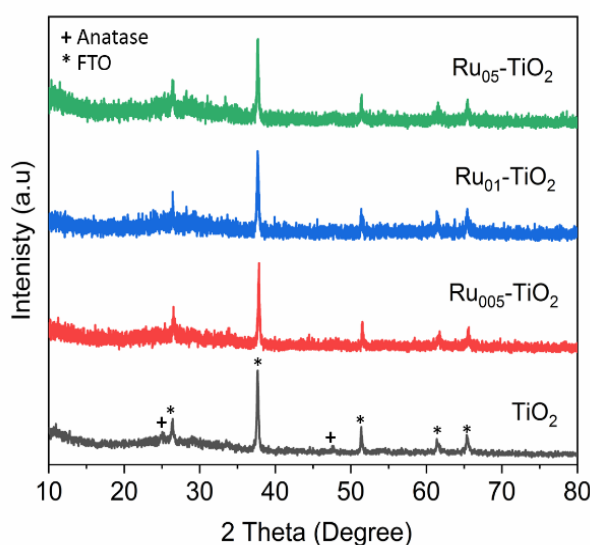

Figure 6.1 - XRD pattern of the as prepared TiO_2 and Ru_x-TiO_2 samples.

section) and low concentration, along with the low intensity Raman excitation source (785 nm).
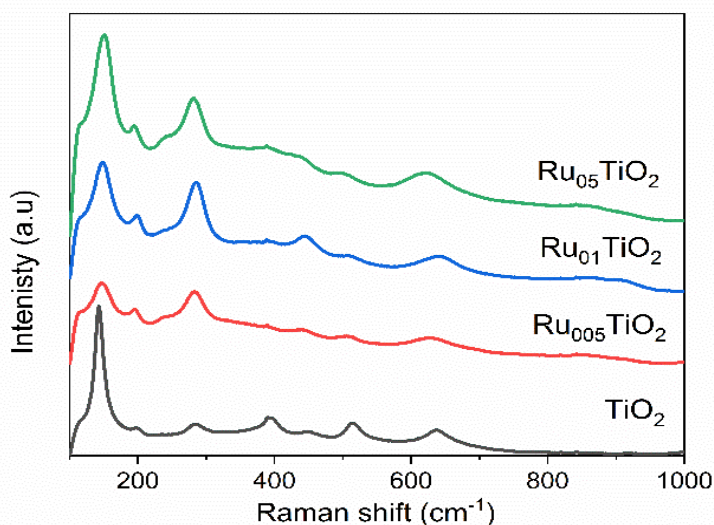

Figure 6.2 - Raman pattern of the as-prepared TiO_2 and Ru_x-TiO_2 samples.

The morphology of the HBN structure of the titania was examined using SEM (Figure 6.3). The microstructured as-prepared TiO_2 was evenly coated on the FTO (Figure 6.3a). Each nanorod exhibited a vertically oriented spine with a highly branched nanostructure (inset of Figure 6.3a). When different concentration of Ru was loaded onto the TiO_2 HBN *via* solvothermal treatment, no significant alteration was observed in the Ru_x-TiO_2 samples (Figure 6.3b-d). However, there were noticeable nanoparticles deposited on the
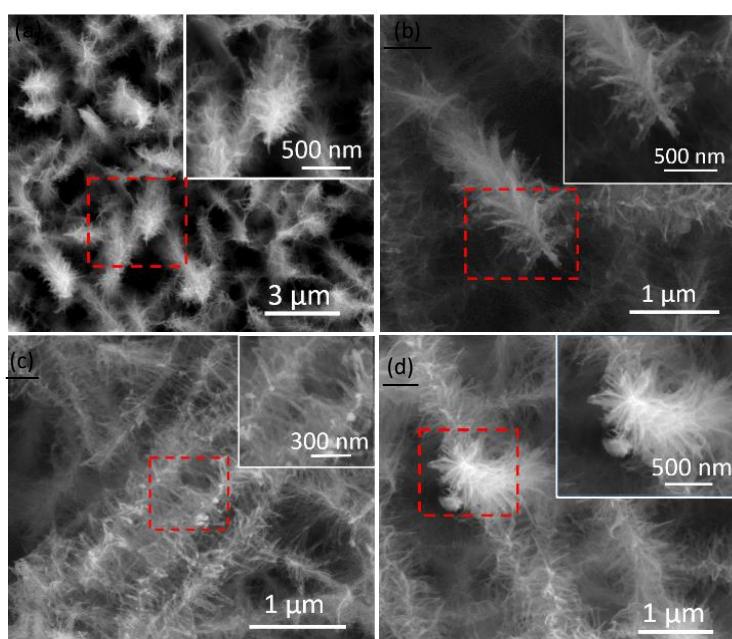

Figure 6.3 - SEM images, with high magnification inserts indicated by the red border, of (a) as-prepared TiO_2, (b) Ru_{005}-TiO_2, (c) Ru_{01}-TiO_2, and (d) Ru_{05}-TiO_2.

spine and the nano-branches of TiO_2 HBNs, which could be attributed to the agglomeration of the RuO_2 nanoparticles (inset of Figure 6.3b-d).

The cross-section view of the as-prepared TiO_2 coating revealed the morphology of the HBNs attaching to the FTO glass (Figure 6.4a). The growth of nano-branches of TiO_2 HBNs was perpendicular to the FTO and was supported on a base layer of TiO_2 with 1-2 µm of thickness, which had dense and thick structures. The base layer was attached on the FTO coating on the glass. Taking a closer look at the tip of the TiO_2 nanorods, the length of the nanorod spine was measured between 1-5 µm (Figure 6.4b), whereas the nano-branches grown on the spine were ranged from 50-300 nm (Figure 6.4c). The nano-branches structure was proposed to provide high surface area exposing more active sites for the photocatalytic reaction and the loading of Ru element.[41]
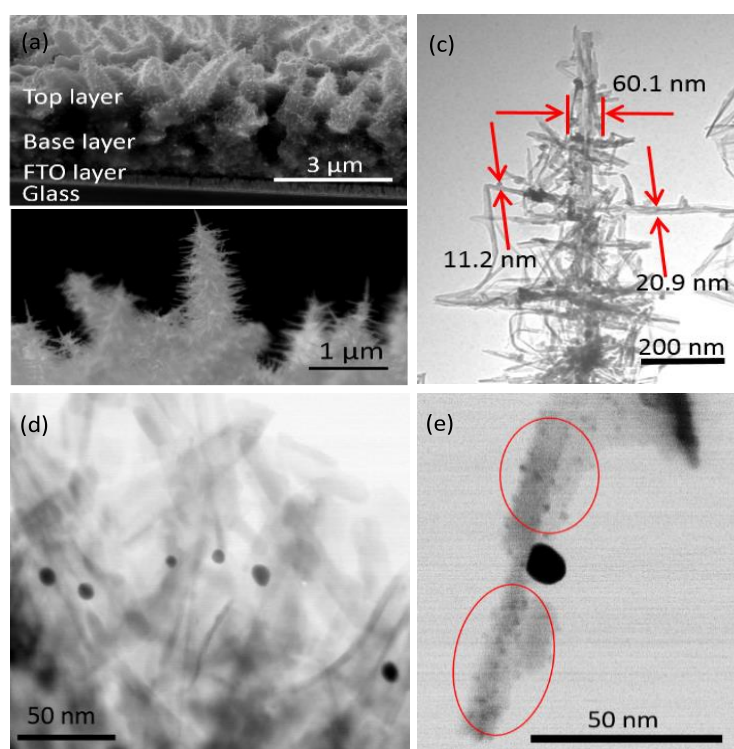

Figure 6.4 - SEM cross-section view of the as-prepared TiO_2 sample (a, b). TEM image of a single Ru_{01}-TiO_2 HBN with thickness measurements (c). Low (d) and high (e) magnification of HR-TEM images of Ru_{05}-TiO_2 sample.

The thickness of the HBN spine and nano-branches as well as the diameter of the loaded RuO_2 nanoparticles were ~60.1, 20.9, 11.2 nm, respectively (Figure 6.4c). The size of the loaded RuO_2 nanoparticles in Ru_{05}-TiO_2 sample was ~11.5 nm (Figure 6.4d). Furthermore, numerous nanoparticles of a much smaller size compared to the vicinity

RuO_2 nanoparticles, were observed in the Ru_{05}-TiO_2 sample (Figure 6.4e). These highly dispersed nanoparticles present on the TiO_2 HBNs were ranged 1-4 nm in diameter. The EDX mapping on HR-TEM evidenced the presence of RuO_2 nanoparticles distributed along the TiO_2 HBNs. It can also be observed that Ru particles are detected in the lattice of the HBNs (Figure 6.5).
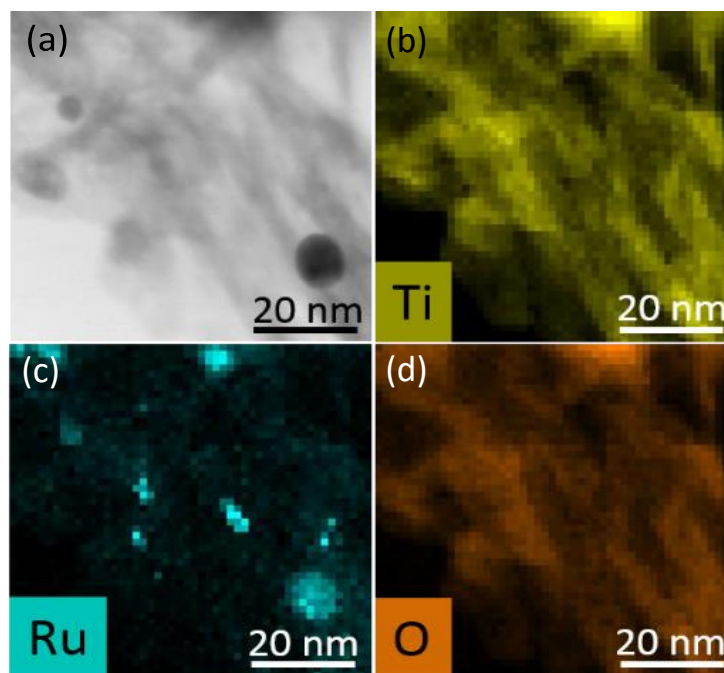

Figure 6.5 - HR-TEM EDX mapping for Ru_{05}-TiO_2 sample.

X-ray photoelectron spectroscopy (XPS) was performed to investigate the surface properties of the fabricated TiO_2 and Ru_x-TiO_2 thin films and to estimate the amount of Ru loaded on the TiO_2 thin film (Figure 6.6). The Ru $3d_{5/2}$, and $3d_{3/2}$ peaks (dark shaded area in Figure 6.6), which centred at 281.0 and 285.4 eV, respectively, were present in all the Ru_x-TiO_2 samples. These peaks were attributed to Ru^{4+}, indicating RuO_2 NPs were loaded onto TiO_2.[50, 51] Ru^{4+} particles seem to have replaced Ti^{4+} in the HBN lattice as shown from the EDX studies (Figure 6.6), as well as Raman peak shifts (Figure 6.2) and XRD crystallisation decrease (Figure 6.1). The area was analysed and the concentration of Ru was estimated to be 2.82, 1.45, and 1.11 at% for the Ru_{05}-TiO_2, Ru_{01}-TiO_2, and Ru_{005}-TiO_2, respectively. As expected, no Ru peak was observed in the as-prepared TiO_2 sample. Nevertheless, the XPS spectra revealed the peak for K centred at 293.0 eV (data not shown), confirming the presence of potassium titanate in all of the thin film samples, as observed in the Raman pattern (Figure 6.2).[52] The C1s peaks shown centred at 283

eV, 286 eV, and 288 eV (not shaded) are ascribed to adventitious carbon contamination due to atmosphere exposure of the samples[53].
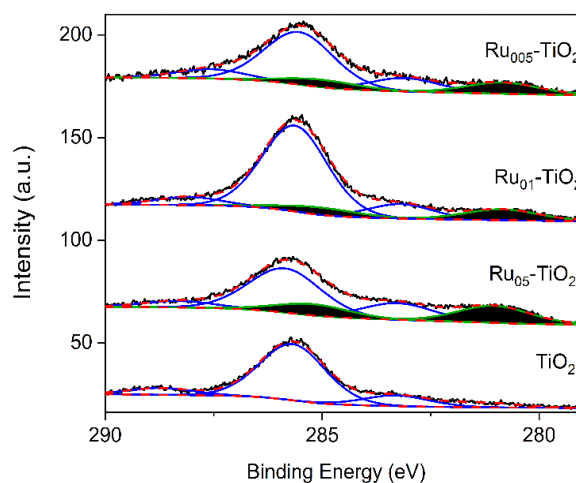

Figure 6.6 - XPS spectra of the as-prepared TiO_2 and Ru_x-TiO_2 samples. The shaded area represented the Ru area under the curve.

The optical properties of the synthesized thin films were investigated using UV-Vis spectroscopy. Diffuse reflectance of the as-prepared TiO_2 and Ru_x-TiO_2 samples was measured and the band gap energy was estimated using the Kubelka-munk function (Figure 6.7a). The band gap energy of the as prepared TiO_2 was ~3.6 eV, which is larger than the anatase phase of TiO_2 (~3.2 eV). The band gap widening is attributed to the quantum confinement effect of the nanostructures.[54-56] The band gap energy for the Ru_{005}-TiO_2, Ru_{01}-TiO_2, and Ru_{05}-TiO_2, was ~3.54, 3.53 and 3.49 eV, respectively. Although the shift of the band gap energy observed in the Ru_x-TiO_2 samples was not significant, the band gap energy decreased with increasing Ru concentration. This phenomenon is very likely due to the Ru^{4+} present in the crystal lattice of the titania, matching the observations made earlier from EDX, XRD and in the Raman pattern of Ru_{05}-TiO_2 (Figures 6.1,6.2 and 6.6 respectively).[57] As confirmed by the XPS , Ru^{4+} was doped into the crystal lattice replacing Ti^{4+}, which explains the increased absorbance in the region of 350-500 nm that is observed in Figure 6.7(a,b).[57-60] Another observation is that the overall absorbance increased with the Ru loading concentration. The overall increase in absorbance, for wavelengths longer than 500nm, is attributed to the RuO_2 decorated on the surface of the TiO_2 HBNs.[39] The synergistic effects of the Ru^{4+} doping and RuO_2 decoration on the TiO_2 are shown to greatly enhance the visible light absorption of the Ru_x-TiO_2 samples, making the use of a solar simulator for the photo-generation of cyclic carbonates a viable option.
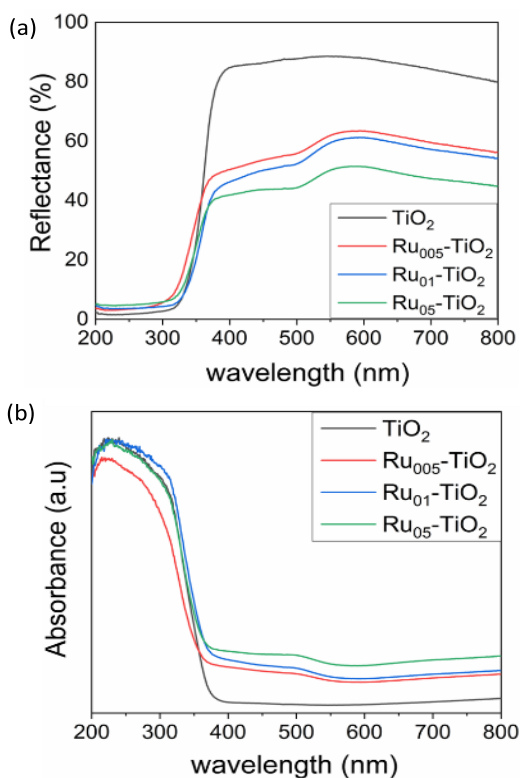
Figure 6.7 **-** Diffuse reflectance (a) and absorbance (b) of
the as-prepared TiO_2 and the Ru_x-TiO_2 samples.

Photocatalysis studies

The photocatalytic activity of the fabricated samples was evaluated with the photo-conversion of PO into PC under the irradiation of a simulated solar lamp. PC was used as a reference for CCs. A control experiment performed in the absence of photocatalyst and light was conducted. No PC was obtained as revealed in the FTIR pattern of the control experiment (Figure 6.8a). Only the tertiary –CH and anti-symmetry of -CH_3 and –CH_2, positioned at 2847.4, 2921.2 and 2953.1 cm^{-1}, respectively, were observed, and these were attributed to the PO moiety.[61] The as-prepared TiO_2 HBN catalyst, which was placed into the PO solution for 6 h under irradiation of the simulated solar lamp, showed no conversion. In contrast, for the fabricated Ru_x-TiO_2 photocatalyst, the trough positioned at 1792 cm^{-1} was observed, which corresponds to one of the characteristic peaks of the cyclic carbonate group.[61] The intensity of this trough increased with decreased Ru concentration. This phenomenon indicated that higher amount of PC was photo-generated with lower amount of Ru loading (Figure 6.8a). When the Ru loading was increased from 0.005 to 0.01 M, the photo-generation of PC was reduced to ~50% compared to that of Ru_{005}-TiO_2 sample. Further increasing the Ru loading, however, did not reduce the photo-generation of PC significantly.
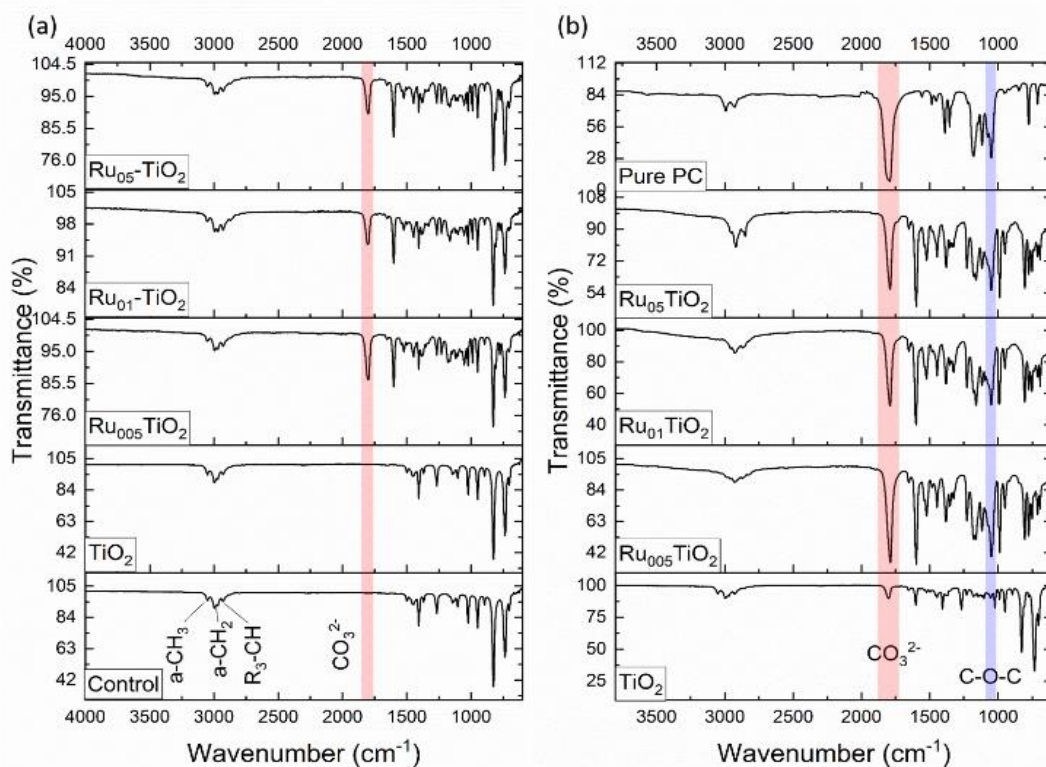
136

Figure 6.8 - (a) FTIR pattern of the solution obtained before evaporation from the fabricated Ru_x-TiO_2 and the control experiment without light and photocatalyst; (b) evaporated products with the fabricated Ru_x-TiO_2 photocatalysts and pure cyclic propylene carbonate as reference.

To further investigate the selectivity and purity of the photo-generation of PC, the solution was purified through evaporation to remove the DCM and unreacted PO. Then, the residue solution was analysed using FTIR (Figure 6.8b). The intensity of the trough, which positioned at 1792 cm^{-1}, for all the Ru_x-TiO_2 samples was enhanced in the purified solutions. The as prepared TiO_2 HBN photocatalyst presented a weak trough at 1792 cm^{-1}, indicating small amount of CCs were produced. This confirms that the reaction is possible without the Ru doping on the TiO_2 HBNs photocatalyst; however, the doping greatly enhances its performance based on the intensity of the trough evident in Figure 8b. On the other hand, the control experiment solution when evaporated had no residual solution left, as expected. The Ru_{005}-TiO_2 sample exhibited the highest intensity among the Ru_x-TiO_2 samples, indicating a high selectivity towards PC. Relatively to the intensity of the pure PC trough, the selectivity of each sample towards PC were estimated to be 83, 62 and 57 % for Ru_{005}-TiO_2, Ru_{01}-TiO_2, and Ru_{05}-TiO_2 samples, respectively. Moreover, another trough centred at 1048 cm^{-1}, which was assigned to another characteristic peak of the CC group (C-O-C), was present in the pure PC solution. The same trough was

observed in the solution after the photocatalytic reaction with Ru_x-TiO_2 samples, confirming PC was photo-generated by the Ru_x-TiO_2 samples. An additional peak centred at 1598 cm^{-1}, which is attributed to the C=N bond, presented in all the solution after the photocatalytic reaction with Ru_x-TiO_2 samples but was absent in the pure PC solution.[62] The emergence of this peak was very likely due to the dissolution of DMAP that was used as an additive in the reacting solution.

6.10 Conclusions

TiO_2 HBN thin films have been synthesised *via* a 2-step hydrothermal method, doped with Ru^{4+} and decorated with different amount of RuO_2 nanoparticles. These novel hyper-branch microstructured TiO_2 thin films doped and loaded with Ru^{4+}/RuO_2 exhibited enhanced visible light absorption when compared to the pristine TiO_2 thin film. The size of the loaded RuO_2 nanoparticles ranged from 10 to 15 nm. The best performing amount of Ru loaded onto TiO_2 herein was 0.005 M, which was 1.11 at% Ru relative to TiO_2 as shown in the XPS analysis. The photo-generation of PC using Ru_{005}-TiO_2 sample had an estimated selectivity of 83% towards the CC. Further quantification of the selectivity measurements will be determined using gas chromatography (GC). In the absence of Ru_x-TiO_2 photocatalyst and light, no product was obtained. These novel FTO supported photocatalysts, which eliminate the need of a catalyst separation step, are the first to be reported so far. The photocatalytic approach is a newly proposed concept for the generation of CCs. Compared to the heterogeneous counterparts, which typically require temperatures up to 80-150 °C and pressure of 10-30 bar, as well as the homogeneous catalysts that currently used in industry, at 100-200 °C, and 50-100 bar, the photocatalytic approach requires temperatures up to 55 °C and 2 bar. Therefore, this approach could potentially become a significant advantage for industrial applications.

6.11   Further research (not published work)

In the following section complimentary research is initially discussed (6.11.1) in order to validate assumptions made in Publication 3. In more detail NMR analysis was performed to validate the assumption that the observed FT-IR trough at 1792 cm^{-1} was correctly attributed to photogenerated cyclic propylene carbonate and was not generated from other carbonate species.   In the following section 6.11.2, further research took place incorporating the findings from Chapter 4, to the photogeneration of cyclic carbonates. The fabricated photocatalysts HBNs BP, HBNs AP, RuO$_2$-HBNs and CuO-HBNs were tested and their performance was recorded for the photogeneration of cyclic carbonates. Lastly, in section 6.11.3 a comparison is drawn between photocatalysts and reaction setups with Prajapati et al. research.   Prajapati et al. was the first publication to demonstrate the photocatalytic conversion of cyclic carbonates while publication 3 shown in this chapter, followed a few months later. Interestingly, these two publications use significantly different reaction setups, meaning different photoreactors, reaction solutions, reaction conditions and photocatalysts. Since there is a limited literature available on the photogeneration of cyclic carbonates, constructive comparisons are drawn between the two studies. Initially, the photocatalyst used in Prajapati et al. study is re-produced and tested in the reaction setup of Publication 3. Then the reaction setup of Prajapati et al. study is reproduced (with certain differentiations to fit the existing photoreactor as discussed in section 6.11.3) and the RuO$_2$-HBNs photocatalyst is tested in that reaction setup.

6.11.1 Complimentary research (NMR analysis)

In the above publication, the compound attributed to the 1792 cm^{-1} trough in the FT-IR analysis was assumed to be propylene carbonate (PC).   However, it is possible that polypropylene carbonate or other non-cyclic carbonates could have produced the trough observed at 1792 cm^{-1} in the FT-IR analysis (Figure 6.8a,b). To verify the genuine product of the reaction was cyclic propylene carbonate, NMR analysis were conducted. The purified solution (50 µl) was dissolved in 1.0 ml of Chloroform-D and then examined under both ^{1}H and ^{13}C NMR (AV400 Bruker). The ^{1}H NMR has shown a doubleted signal at 1.5 ppm (Figure 6.9a). This upfield signal is associated with the CH$_3$ group far away from oxygen atoms, and the doubleted signal splitting is explained by the neighbouring CH group. The triplet signals associated with the CH$_2$ group are found at

3.95 and 4.5 ppm, respectively. Lastly, the most downfield signal at 4.81 ppm, associated with the CH group which is closer to the oxygen atoms causing a de-shielding effect, and is split into 6 peaks by the five neighbouring hydrogen atoms. Signals from the CH_3, CH_2, and CH group were identified as well as the C=O functional group in the ^{13}C NMR spectrum as shown in Figure 6.9b. Similar spectra of cyclic PC for both ^1H and ^{13}C NMR are found in the supporting information of Prajapati et al. publication.[11]
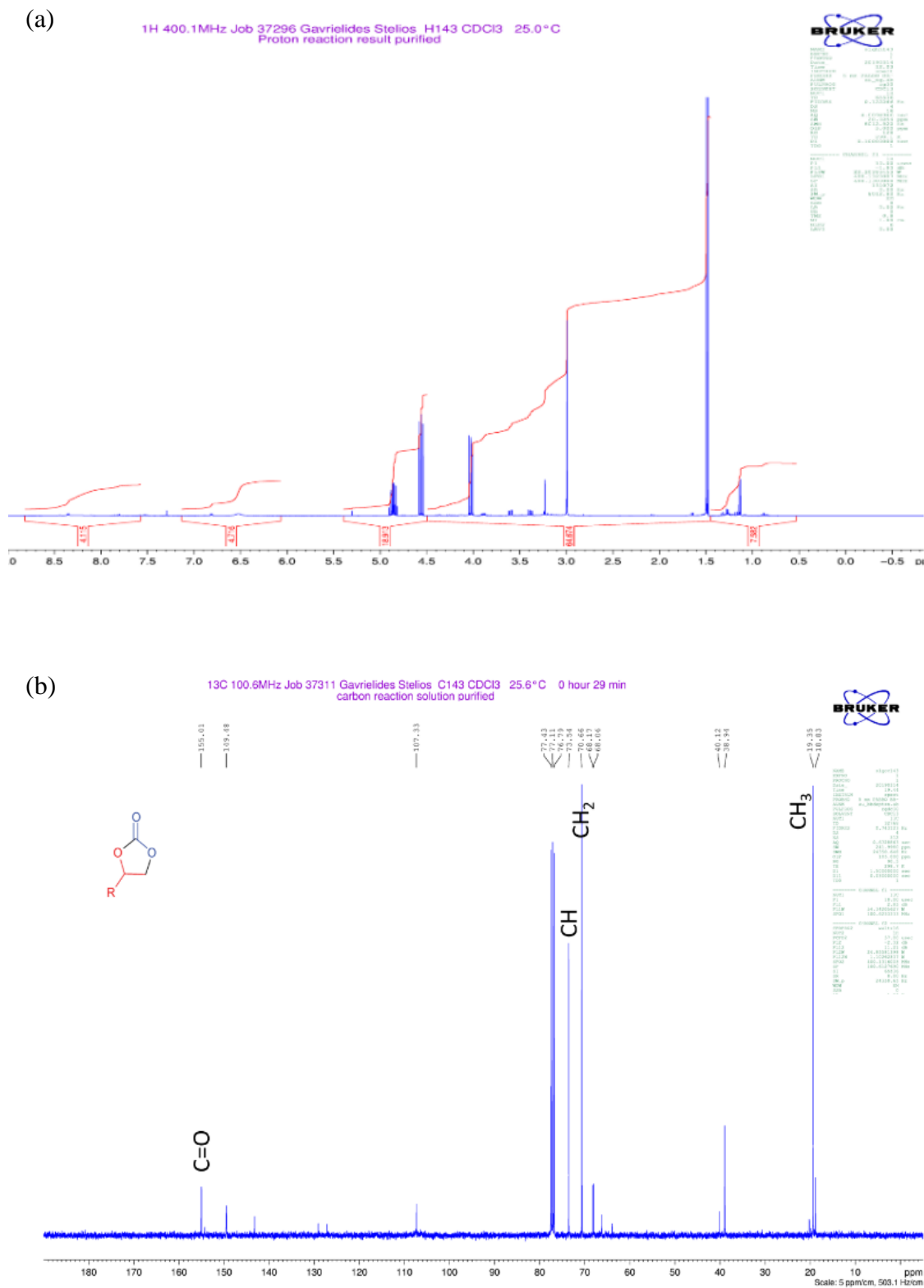
(a)

(b)

Figure 6.9 - (a) ^{1}H NMR and (b) ^{13}C NMR spectra of purified reaction solution using Ru$_{005}$-TiO$_2$ HBNs for photogeneration of cyclic carbonates indicating signals associated with cyclic propylene carbonate.

6.11.2 Incorporation of findings of Chapter 4

Effects of protonation treatment

After the findings of the research conducted in the 1st publication (Chapter 4), and the positive optical and electrical effects that were observed utilising the protonation treatment on the HBN samples, it was intriguing to investigate the protonated HBNs performance on the photogeneration of cyclic carbonates. Therefore, the synthesis procedure that was described in section 4.6 was followed and the HBNs BP and HBNs AP samples were synthesized and tested in the CCs reaction utilising the same experimental conditions presented in publication 3. The conversion calculations were done by weight comparison, as shown in Table 6.1. The HBNs AP have outperformed the HBNs BP with a conversion of 1.41% as opposed to 1.14%. These results agreed with previous characterisation observations regarding increased optical performance and enhanced electron transfer for HBNs AP, as discussed in Chapter 4.

Effects of RuO_2 and CuO

The RuO_2-HBNs and CuO-HBNs prepared in section 4.6 (Chapter 4) were also synthesized and examined for the photogeneration of cyclic carbonates. According to the findings on Chapter 4 (photocurrent experiment), the RuO_2-HBNs have shown enhanced electronic properties when compared to CuO-HBNs. On the other hand, CuO-HBNs have shown improved optical properties yet yielded modest conversion rates due to charge recombination. When the RuO_2-HBNs and CuO-HBNs were tested on the photogeneration of CCs, a similar performance was observed, where RuO_2-HBNs outperformed all the other fabricated photocatalyst with 1.65% conversion while CuO-HBNs have shown a 1.08% conversion, as shown in Table 6.1.

Control experiments

Two control experiments were performed to ensure the photocatalytic pathway of the reaction and the contribution of the photocatalyst: (1) using the best performing RuO_2-HBNs photocatalyst in the absence of light, and (2) with light but without a photocatalyst. The rest of the reaction conditions remained the same. The two control experiments have shown a 0.32 and 0.24% conversion, respectively. The small amount of conversion observed was expected, given than the cycloaddition of CO_2 to epoxides is a spontaneous reaction (Table 6.1).

6.11.3 Constructive comparisons between studies

CoPc-TiO_2 performance

The cobalt phthalocyanine grafted on titanium dioxide (CoPc-TiO$_2$) photocatalyst reported in Prajapati et al. publication, was re-produced and examined in the same reactor and reaction conditions as publication 3, to compare the performance of the photocatalyst samples.[11] The CoPc-TiO$_2$ powder was suspended in water and loaded on FTO slides for the photocatalytic reaction. The CoPc-TiO$_2$ slides where tested in the photogeneration of CCs reaction and have shown a modest performance of 0.66% conversion (Table 6.1). Despite its modest performance in the current reactor and setup, this photocatalyst was reported to have very high performance in Prajapati reaction setup.[11] This could be attributed to the reaction configuration, which was are very different in terms of scale (225 ml vs 15 ml as reported), solvent content (1:8 vs 225:1), photocatalyst presentation (thin-films vs powder), reactor configurations and light sources. Therefore, this result of modest performance can only be used as a comparison with the photocatalysts used in the examined reaction system.

In the following Table 6.1 and 6.2 the quantification of the conversion yields is shown, and the procedure is explained below. The conversion yield was measured as the weight percentage of cyclic carbonates produced compared to the reaction solution recovered (which accounts for the overall weight of CCs and unreacted PO). The "Empty Vessel" column refers to the measured empty glass vial weight that will be used for the quantification. The "Before evaporation" column refers to the measured weight of the reaction solution out of the reactor when the reaction was finished, which includes the glass vial`s weight. "Impurified solution" is the "Before evaporation" column subtracting the "Empty Vessel" weight, which leaves the reaction solution`s calculated weight. To remove the weight of the solvents included in the reaction solution and account only for the unreacted PO and CCs, the percentage of the solvents is removed from the "Impurified solution" weight, resulting in the calculated column "Impur. Sol. w/o solvent". To find the weight of the cyclic carbonates and divide it by the "Impur. Sol. w/o solvent", the recovered reaction solution was evaporated, and the measured weight of the remaining solution was measured as column "After evaporation" which includes the weight of the glass vial and the converted cyclic carbonates weight. The glass vial`s weight was removed to calculate the "Remaining solution" column by subtracting "Empty vessel" measured weight. The conversion was the calculated using the "Remaining solution" divided by "Impur. Sol w/o solvent" columns, presented as a weight percentage at the "Conversion" column.

Table 6.1 - Weight conversion rate measurements for cyclic carbonate reaction. Explanations: *Impurified solution is "before evaporation" minus "empty vessel" weight. *Impur. Sol. w/o solvent is "Impurified solution" minus the percentage of solvents in the reaction system (1:8). *Remaining solution is "After evaporation" minus "Empty Vessel".

| Sample name	Empty Vessel	Before evaporation	Impurified solution	Impur. Sol. w/o solvent	After evaporation	Remaining solution	Conversion
	(g)	(g)	(g)	(g)	(g)	(g)	(%)
HBN bp	71.41	148.291	76.881	68.339	72.186	0.776	1.14%
HBN ap	71.41	164.141	92.731	82.428	72.575	1.165	1.41%
RuO$_2$ HBN	71.41	140.157	68.747	61.108	72.416	1.006	1.65%
CuO HBN	71.414	135.961	64.547	57.375	72.033	0.619	1.08%
Ctrl 1 (no light, Ru cat.)	71.41	139.282	67.872	60.331	71.603	0.193	0.32%
Ctrl 2 (light, no cat.)	71.41	149.141	77.731	69.094	71.578	0.168	0.24%
CoPc-TiO$_2$	71.41	148.691	77.281	68.694	71.865	0.455	0.66%
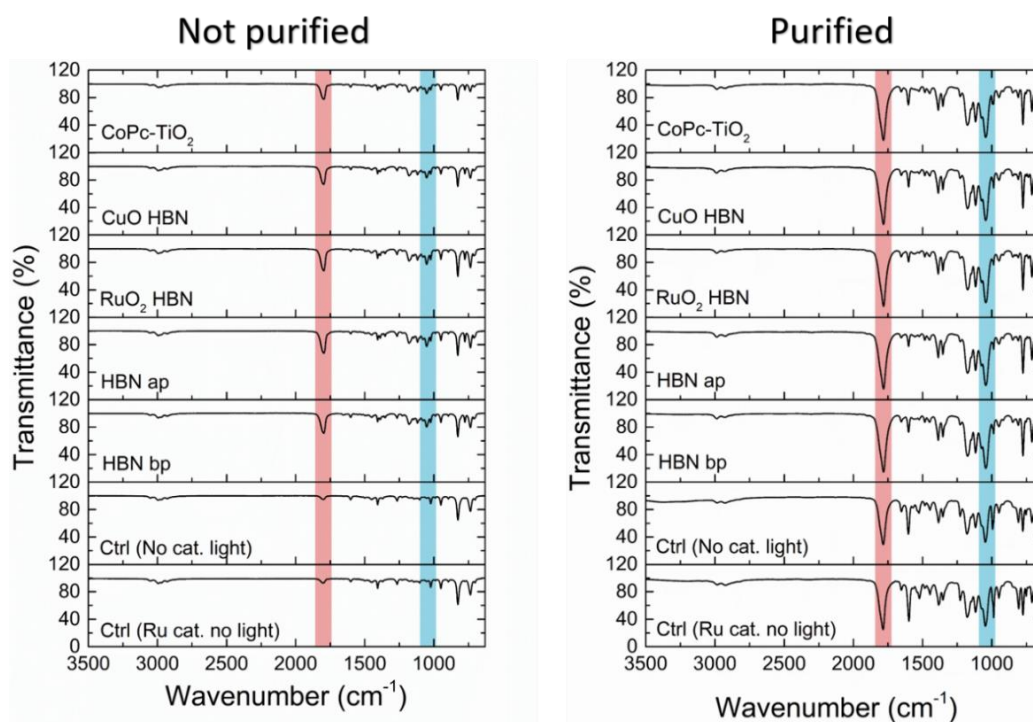
Figure 6.10 - FT-IR spectra of "not purified" and "purified" reaction solutions for all the photocatalysts described above including control experiments.

FT-IR spectra were acquired for all the above mentioned photocatalysts as well as the control experiments. Two spectra were acquired for each material, the "not purified", and "purified" as can be seen in Figure 6.10. "Not purified" is the acquired solution before it has passed through the rotary evaporator step, therefore containing unreacted PO, reaction product PC, and solvents. The "purified" column is spectra acquired after the evaporation step where only the product of the reaction is present. The peaks related to the cyclic carbonate product are highlighted as was presented in Publication 3 section 6.9.

Alternative reaction solution and conditions

Another experiment was conducted where the reaction solution and experimental conditions mentioned in the literature were incorporated.[11] The reaction solution described in Prajapati study is referred to as "alternative reaction solution" for purposes of differentiation with the reaction solution described in Publication 3. The alternative reaction solution was produced and the reaction was scaled from 15 ml up to 225 ml in order to fit the existing reactor system. The examined alternative reaction solution contained 150 ml of acentontrile, 75 ml of methanol, 1.5 mmol of tetrabutylammonium bromide (TBAB) and 15 mmol of the reactant propylene oxide. It was prepared and vigorously stirred for 30 minutes and kept in dark conditions. The performance of CoPc-TiO$_2$ and RuO$_2$-HBNs samples was analysed using similar experimental conditions described in literature from Prajapati et al.[11] No external heat was applied and the reaction was irradiated with visible light for 24 h. The main difference from the reported conditions is that in Prajapati et al`s publication, a 20 W LED (Model No. HP-FL-20W-F-Hope LED Opto-Electric Co., Ltd., $\lambda > 400$ nm) was used in Prajapati et al. study instead of the solar simulator AM1.5G (1 sun equivalent, 100 Wm^{-2}, 92250 A Newport, USA) used in the current study. The CoPc-TiO$_2$ performed much better in these conditions achieving a 78 % conversion, while the RuO$_2$-HBN has managed to reach slightly higher conversion of 85% (Table 6.2). All calculations were done exactly as described above for Table 6.1.

Table 6.2 - Weight conversion rate measurements for cyclic carbonate reaction using the alternative reaction solution. Explanations: *Impurified solution is "before evaporation" minus "empty vessel" weight. *Impur. Sol. w/o solvent is "Impurified solution" minus the percentage of solvents in the reaction system (225:1). *Remaining solution is "After evaporation" minus "Empty Vessel". *Conversion is "remaining solution"/"Impur. Sol. w/o solvent".

Sample name	Empty Vessel	Before evaporation	Impurified solution	Impur. Sol. w/o solvent	After evaporation	Remaining solution	Conversion
	(g)	(g)	(g)	(g)	(g)	(g)	(%)
CoPc-TiO$_2$	71.41	136.322	64.912	0.287	71.633	0.223	78
RuO$_2$ HBN	76.463	145.181	68.718	0.304	76.72	0.257	85

References

[1]   E. Alper and O. Y. Orhan, "CO$_2$ utilization: Developments in conversion processes," *Petroleum,* vol. 3, no. 1, pp. 109-126, 2017.

[2]   L. Wang, P. Li, X. Jin, J. Zhang, H. He, and S. Zhang, "Mechanism of fixation of CO2 in the presence of hydroxyl-functionalized quaternary ammonium salts," *Journal of CO$_2$ Utilization,* vol. 10, pp. 113-119, 2015.

[3]   J. A. Castro-Osma, M. North, and X. Wu, "Synthesis of cyclic carbonates catalysed by chromium and aluminium salphen complexes," *Chemistry–A European Journal,* vol. 22, no. 6, pp. 2100-2107, 2016.

[4]   H. Kawanami and Y. Ikushima, "Chemical fixation of carbon dioxide to styrene carbonate under supercritical conditions with DMF in the absence of any additional catalysts," *Chemical Communications,* no. 21, pp. 2089-2090, 2000.

[5]   H. S. Kim, J. J. Kim, B. G. Lee, O. S. Jung, H. G. Jang, and S. O. Kang, "Isolation of a pyridinium alkoxy ion bridged dimeric zinc complex for the coupling reactions of CO$_2$ and epoxides," *Angewandte Chemie International Edition,* vol. 39, no. 22, pp. 4096-4098, 2000.

[6]   A. Decortes, A. M. Castilla, and A. W. Kleij, "Salen-complex-mediated formation of cyclic carbonates by cycloaddition of CO$_2$ to epoxides," *Angew. Chem. Int. Ed.,* vol. 49, no. 51, pp. 9822-9837, 2010.

[7]   V. B. Saptal and B. M. Bhanage, "Current advances in heterogeneous catalysts for the synthesis of cyclic carbonates from carbon dioxide," *Curr. Opin. Green Sustain. Chem.,* vol. 3, pp. 1-10, 2017/02/01/ 2017, doi: https://doi.org/10.1016/j.cogsc.2016.10.006.

[8]   A. Zanon, S. Chaemchuen, B. Mousavi, and F. Verpoort, "1 Zn-doped ZIF-67 as catalyst for the CO$_2$ fixation into cyclic carbonates," *Journal of CO2 Utilization,* vol. 20, pp. 282-291, 2017.

[9]   A. Buonerba *et al.*, "Novel iron(iii) catalyst for the efficient and selective coupling of carbon dioxide and epoxides to form cyclic carbonates," *Catalysis Science & Technology,* 10.1039/C4CY01187B vol. 5, no. 1, pp. 118-123, 2015, doi: 10.1039/C4CY01187B.

[10]   I. Korosteleva, N. Markova, N. Kolesnichenko, N. Ezhova, S. Khadzhiev, and N. Trukhmanova, "Catalytic synthesis of propylene carbonate from propylene oxide and carbon dioxide in the presence of rhodium complexes modified with organophosphorus ligands and chitosan," *Petroleum Chemistry,* vol. 53, no. 6, pp. 412-417, 2013.

[11]   P. K. Prajapati, A. Kumar, and S. L. Jain, "First Photocatalytic Synthesis of Cyclic Carbonates from CO$_2$ and Epoxides Using CoPc/TiO$_2$ Hybrid under Mild Conditions," *ACS Sustain. Chem. Eng.,* vol. 6, no. 6, pp. 7799-7809, 2018/06/04 2018, doi: 10.1021/acssuschemeng.8b00755.

[12]   M. Bakiro, S. H. Ahmed, and A. Alzamly, "Cycloaddition of CO$_2$ to propylene oxide using BiNbO4/NH2-MIL-125(Ti) composites as visible-light photocatalysts," *Journal of Environmental Chemical Engineering,* vol. 8, no. 6, p. 104461, 2020/12/01/ 2020, doi: https://doi.org/10.1016/j.jece.2020.104461.

[13]   E. Alper and O. Yuksel Orhan, "CO$_2$ utilization: Developments in conversion processes," *Petroleum,* vol. 3, no. 1, pp. 109-126, 2017/03/01/ 2017, doi: https://doi.org/10.1016/j.petlm.2016.11.003.

[14]   M. Aresta and A. Dibenedetto, "Utilisation of CO$_2$ as a chemical feedstock: opportunities and challenges," *Dalton Trans.,* 10.1039/B700658F no. 28, pp. 2975-2992, 2007, doi: 10.1039/B700658F.

[15] R. L. Paddock and S. T. Nguyen, "Chemical CO_2 fixation: Cr (III) salen complexes as highly efficient catalysts for the coupling of CO_2 and epoxides," *J. Am. Chem. Soc.,* vol. 123, no. 46, pp. 11498-11499, 2001.

[16] M. North, R. Pasquale, and C. Young, "Synthesis of cyclic carbonates from epoxides and CO_2," *Green Chemistry,* vol. 12, no. 9, pp. 1514-1539, 2010.

[17] J. H. Clements, "Reactive applications of cyclic alkylene carbonates," *Industrial & Engineering Chemistry Research,* vol. 42, no. 4, pp. 663-674, 2003.

[18] S. Fukuoka *et al.*, "A Novel Non-Phosgene Process for Polycarbonate Production from CO_2: Green and Sustainable Chemistry in Practice," *Catalysis Surveys from Asia,* journal article vol. 14, no. 3, pp. 146-163, September 01 2010, doi: 10.1007/s10563-010-9093-5.

[19] G. Cascio, E. Manghisi, R. Porta, and G. Fregnan, "N-Phenylpiperazine derivatives with hypocholesterolemic activity," *Journal of medicinal chemistry,* vol. 28, no. 6, pp. 815-818, 1985.

[20] J. W. Comerford, I. D. Ingram, M. North, and X. Wu, "Sustainable metal-based catalysts for the synthesis of cyclic carbonates containing five-membered rings," *Green Chemistry,* vol. 17, no. 4, pp. 1966-1987, 2015.

[21] J. Castro-Osma, J. Comerford, M. North, and X. Wu, "Green Syntheses of Cyclic Carbonates."

[22] I. G. Korosteleva, N. A. Markova, N. V. Kolesnichenko, N. N. Ezhova, S. N. Khadzhiev, and N. I. Trukhmanova, "Catalytic synthesis of propylene carbonate from propylene oxide and carbon dioxide in the presence of rhodium complexes modified with organophosphorus ligands and chitosan," *Petrol. Chem.,* vol. 53, no. 6, pp. 412-417, 2013/11/01 2013, doi: 10.1134/S0965544113060108.

[23] M. North and R. Pasquale, "Mechanism of cyclic carbonate synthesis from epoxides and CO_2," *Angewandte Chemie,* vol. 121, no. 16, pp. 2990-2992, 2009.

[24] X.-B. Lu *et al.*, "Asymmetric Catalysis with CO_2: Direct Synthesis of Optically Active Propylene Carbonate from Racemic Epoxides," *J. Am. Chem. Soc.,* vol. 126, no. 12, pp. 3732-3733, 2004/03/01 2004, doi: 10.1021/ja049734s.

[25] F. Jutz, J.-D. Grunwaldt, and A. Baiker, "Mn(III)(salen)-catalyzed synthesis of cyclic organic carbonates from propylene and styrene oxide in "supercritical" CO_2," *Journal of Molecular Catalysis A: Chemical,* vol. 279, no. 1, pp. 94-103, 2008/01/02/ 2008, doi: https://doi.org/10.1016/j.molcata.2007.10.010.

[26] J. Peng, H.-J. Yang, Y. Geng, Z. Wei, L. Wang, and C.-Y. Guo, "Novel, recyclable supramolecular metal complexes for the synthesis of cyclic carbonates from epoxides and CO_2 under solvent-free conditions," *Journal of CO_2 Utilization,* vol. 17, pp. 243-255, 2017/01/01/ 2017, doi: https://doi.org/10.1016/j.jcou.2016.10.013.

[27] J. Peng, H.-J. Yang, N. Song, and C.-Y. Guo, "An effective Ni/Zn catalyst system for the chemical fixation of carbon dioxide with epoxides," *Journal of CO_2 Utilization,* vol. 9, pp. 16-22, 2015/03/01/ 2015, doi: https://doi.org/10.1016/j.jcou.2014.11.002.

[28] V. Preethi and S. Kanmani, "Photocatalytic hydrogen production," *Materials Science in Semiconductor Processing,* vol. 16, no. 3, pp. 561-575, 2013/06/01/ 2013, doi: https://doi.org/10.1016/j.mssp.2013.02.001.

[29] G. L. Chiarello, M. V. Dozzi, and E. Selli, "TiO2-based materials for photocatalytic hydrogen production," *Journal of Energy Chemistry,* vol. 26, no. 2, pp. 250-258, 2017/03/01/ 2017, doi: https://doi.org/10.1016/j.jechem.2017.02.005.

[30] R. D. Tentu and S. Basu, "Photocatalytic water splitting for hydrogen production," *Current Opinion in Electrochemistry,* vol. 5, no. 1, pp. 56-62, 2017/10/01/ 2017, doi: https://doi.org/10.1016/j.coelec.2017.10.019.

[31] H. Ahmad, S. K. Kamarudin, L. J. Minggu, and M. Kassim, "Hydrogen from photo-catalytic water splitting process: A review," *Renewable and Sustainable Energy Reviews,* vol. 43, pp. 599-610, 2015/03/01/ 2015, doi: https://doi.org/10.1016/j.rser.2014.10.101.

[32] D. Kong, J. Z. Y. Tan, F. Yang, J. Zeng, and X. Zhang, "Electrodeposited Ag nanoparticles on TiO_2 nanorods for enhanced UV visible light photoreduction CO_2 to CH_4," *Applied Surface Science,* vol. 277, pp. 105-110, 2013/07/15/ 2013, doi: https://doi.org/10.1016/j.apsusc.2013.04.010.

[33] J. Z. Y. Tan, Y. Fernández, D. Liu, M. Maroto-Valer, J. Bian, and X. Zhang, "Photoreduction of CO_2 using copper-decorated TiO_2 nanorod films with localized surface plasmon behavior," *Chem. Phys. Lett.,* vol. 531, pp. 149-154, 2012/04/02/ 2012, doi: https://doi.org/10.1016/j.cplett.2012.02.016.

[34] J. Zhao, Y. Li, Y. Zhu, Y. Wang, and C. Wang, "Enhanced CO_2 photoreduction activity of black TiO_2−coated Cu nanoparticles under visible light irradiation: Role of metallic Cu," *Applied Catalysis A: General,* vol. 510, pp. 34-41, 2016/01/25/ 2016, doi: https://doi.org/10.1016/j.apcata.2015.11.001.

[35] J. Z. Y. Tan *et al.*, "High-Performance Coral Reef-like Carbon Nitrides: Synthesis and Application in Photocatalysis and Heavy Metal Ion Adsorption," *ACS Applied Materials & Interfaces,* vol. 9, no. 5, pp. 4540-4547, 2017/02/08 2017, doi: 10.1021/acsami.6b11427.

[36] P. Blanchet and V. Landry, "13 - Nanocomposite coatings and plasma treatments for wood-based products," in *Wood Composites*, M. P. Ansell Ed.: Woodhead Publishing, 2015, pp. 335-355.

[37] H. Koinuma *et al.*, "Chapter 11.1.11 - Combinatorial Nanoscience and Technology for Solid-State Materials," in *Handbook of Advanced Ceramics (Second Edition)*, S. Somiya Ed. Oxford: Academic Press, 2013, pp. 1103-1124.

[38] J. Schneider *et al.*, "Understanding TiO_2 Photocatalysis: Mechanisms and Materials," *Chem. Rev.,* vol. 114, no. 19, pp. 9919-9986, 2014/10/08 2014, doi: 10.1021/cr5001892.

[39] J. Tian *et al.*, "RuO_2/TiO_2 nanobelt heterostructures with enhanced photocatalytic activity and gas-phase selective oxidation of benzyl alcohol," *Solar Energy Materials and Solar Cells,* vol. 151, pp. 7-13, 2016/07/01/ 2016, doi: https://doi.org/10.1016/j.solmat.2016.02.017.

[40] F. Yoshitomi, K. Sekizawa, K. Maeda, and O. Ishitani, "Selective formic acid production via CO_2 reduction with visible light using a hybrid of a perovskite tantalum oxynitride and a binuclear ruthenium (II) complex," *ACS applied materials & interfaces,* vol. 7, no. 23, pp. 13092-13097, 2015.

[41] W.-Q. Wu, H.-S. Rao, H.-L. Feng, X.-D. Guo, C.-Y. Su, and D.-B. Kuang, "Morphology-controlled cactus-like branched anatase TiO_2 arrays with high light-harvesting efficiency for dye-sensitized solar cells," *Journal of Power Sources,* vol. 260, pp. 6-11, 2014.

[42] Y. Gong, C. Lee, and C. Yang, "Atomic force microscopy and Raman spectroscopy studies on the oxidation of Cu thin films," *Journal of Applied Physics,* vol. 77, no. 10, pp. 5422-5425, 1995.

[43] J. S. Lee, K. H. You, and C. B. Park, "Highly photoactive, low bandgap TiO_2 nanoparticles wrapped by graphene," *Advanced Materials,* Article vol. 24, no. 8, pp. 1084-1088, 2012, doi: 10.1002/adma.201104110.

[44] A. León *et al.*, "FTIR and Raman characterization of TiO$_2$ nanoparticles coated with polyethylene glycol as carrier for 2-methoxyestradiol," *Applied Sciences,* vol. 7, no. 1, p. 49, 2017.

[45] H. C. Choi, Y. M. Jung, and S. B. Kim, "Size effects in the Raman spectra of TiO2 nanoparticles," *Vib. Spectrosc,* vol. 37, no. 1, pp. 33-38, 2005/01/14/ 2005, doi: https://doi.org/10.1016/j.vibspec.2004.05.006.

[46] T. Ohsaka, "Temperature dependence of the Raman spectrum in anatase TiO$_2$," *Journal of the Physical Society of Japan,* vol. 48, no. 5, pp. 1661-1668, 1980.

[47] Y. Zhang, C. X. Harris, P. Wallenmeyer, J. Murowchick, and X. Chen, "Asymmetric lattice vibrational characteristics of rutile TiO$_2$ as revealed by laser power dependent Raman spectroscopy," *The Journal of Physical Chemistry C,* vol. 117, no. 45, pp. 24015-24022, 2013.

[48] W.-K. Jo, S. Kumar, M. A. Isaacs, A. F. Lee, and S. Karthikeyan, "Cobalt promoted TiO$_2$/GO for the photocatalytic degradation of oxytetracycline and Congo Red," *Applied Catalysis B: Environmental,* vol. 201, pp. 159-168, 2017/02/01/ 2017, doi: https://doi.org/10.1016/j.apcatb.2016.08.022.

[49] X. Liu and N. Coville, *A Raman Study of Titanate Nanotubes*. 2005, pp. 110-115.

[50] X. Wei *et al.*, "A Bowknot-like RuO$_2$ quantum dots@ V$_2$O$_5$ cathode with largely improved electrochemical performance," *Phys. Chem. Chem. Phys.,* vol. 16, no. 35, pp. 18680-18685, 2014.

[51] S. Kaliaguine, "Application of surface science techniques in the field of zeolitic materials," in *Studies in Surface Science and Catalysis*, vol. 102, H. Chon, S. I. Woo, and S. E. Park Eds.: Elsevier, 1996, pp. 191-230.

[52] Q. Wang, Z. Guo, and J. S. Chung, "Formation and structural characterization of potassium titanates and the potassium ion exchange property," *Mater. Res. Bull.,* vol. 44, no. 10, pp. 1973-1977, 2009/10/01/ 2009, doi: https://doi.org/10.1016/j.materresbull.2009.06.009.

[53] M. Descostes, F. Mercier, C. Beaucaire, P. Zuddas, and P. Trocellier, "Nature and distribution of chemical species on oxidized pyrite surface: Complementarity of XPS and nuclear microprobe analysis," *Nucl. Instrum. Meth. B,* vol. 181, no. 1, pp. 603-609, 2001/07/01/ 2001, doi: https://doi.org/10.1016/S0168-583X(01)00627-9.

[54] E. Roduner, "Size matters: why nanomaterials are different," *Chemical Society Reviews,* vol. 35, no. 7, pp. 583-592, 2006.

[55] M. A. Siddiqui, V. S. Chandel, and A. Azam, "Comparative study of potassium hexatitanate (K$_2$Ti$_6$O$_{13}$) whiskers prepared by sol–gel and solid state reaction routes," *Appl. Surf. Sci.,* vol. 258, no. 19, pp. 7354-7358, 2012/07/15/ 2012, doi: https://doi.org/10.1016/j.apsusc.2012.04.018.

[56] T. Takagahara and K. Takeda, "Theory of the quantum confinement effect on excitons in quantum dots of indirect-gap materials," *Phys. Rev. B,* vol. 46, no. 23, pp. 15578-15581, 12/15/ 1992, doi: 10.1103/PhysRevB.46.15578.

[57] T.-D. Nguyen-Phan *et al.*, "Three-dimensional ruthenium-doped TiO$_2$ sea urchins for enhanced visible-light-responsive H 2 production," *Physical Chemistry Chemical Physics,* vol. 18, no. 23, pp. 15972-15979, 2016.

[58] T. Ohno, F. Tanigawa, K. Fujihara, S. Izumi, and M. Matsumura, "Photocatalytic oxidation of water by visible light using ruthenium-doped titanium dioxide powder," *Journal of Photochemistry and Photobiology A: Chemistry,* vol. 127, no. 1, pp. 107-110, 1999/10/01/ 1999, doi: https://doi.org/10.1016/S1010-6030(99)00128-8.

[59] H. Huang *et al.*, "A Long-Lived Mononuclear Cyclopentadienyl Ruthenium Complex Grafted onto Anatase TiO2 for Efficient CO_2 Photoreduction," *Angewandte Chemie International Edition,* vol. 55, no. 29, pp. 8314-8318, 2016.

[60] M. T. Uddin *et al.*, "Preparation of RuO_2/TiO_2 Mesoporous Heterostructures and Rationalization of Their Enhanced Photocatalytic Properties by Band Alignment Investigations," *The Journal of Physical Chemistry C,* vol. 117, no. 42, pp. 22098-22110, 2013/10/24 2013, doi: 10.1021/jp407539c.

[61] L. Zhang, X. Luo, Y. Qin, and Y. Li, "A novel 2,5-furandicarboxylic acid-based bis(cyclic carbonate) for the synthesis of biobased non-isocyanate polyurethanes," *RSC Adv.,* 10.1039/C6RA25045A vol. 7, no. 1, pp. 37-46, 2017, doi: 10.1039/C6RA25045A.

[62] V. Kuryanov, M. K Tokarev, T. A Chupakhina, V. Ya, and Chirva, *The Synthesis of N-Acetylglucosamine Heteroaromatic N-β-Glycosides under Phase Transfer Conditions: Part III. l,2,4-Triazolin-3-one Glucosaminides*. 2011, pp. 602-608.

Chapter 7

Conclusions and future work

7.1 Introductory chapters summary

As a summary of the introductory chapters, an overview of the UK and Scottish energy sector is presented. The concept and role of CCUS towards decarbonisation of the energy sector as well as placing of CO_2 utilisation technology within the overall CCUS technology scheme is discussed. Furthermore, the policies regarding CCUS incorporation plans in the UK are reported and critically reviewed. Further along, the underlying principles of photochemistry and photocatalysis are introduced. Mainly, electromagnetic irradiation is analysed and its interaction with matter. Light absorption principles are discussed as well as the resulting excitation and relaxation processes. A section on CO_2 photoreduction and CO_2 cycloaddition to epoxides follows before introducing the overall aim and objectives for the current thesis towards the end of chapter 1.

In chapter 2, a detailed discussion on the subject of material design and morphology takes place. Several material design techniques, morphological alterations and material modifications are analysed as to how they impact the properties of material and its photocatalytic behaviour. The wide topic of morphological alterations is explored in respect of shape, texture, particle size, porosity, and architecture. Plentiful examples are drawn from the literature and presented in this chapter. The photocatalyst immobilisation in the form of thin films is also discussed, along with materials that have been previously used as supports, and the potential benefits that these techniques could offer. A significant part of the chapter is devoted to photocatalyst modification techniques, such as elemental doping and heterojunction formation. These techniques are analysed in terms of the optical and electronic properties they can offer, accompanied by examples of how researchers have implemented them before, to affect their material`s photocatalytic performance. It is crucial to understand the potential effects of each modification technique and apply to the photocatalyst material accordingly. To conclude chapter 2, the last section discussed the hydrothermal and solvothermal synthesis technique. Chapter 3 describes how the HBNs morphology synthesis protocol was developed and reviews analytical techniques used as part of this thesis. The topics

discussed in chapters 2-3 are applied techniques that are used in the experimental section of this thesis (chapters 4-6) but it is not an exhaustive list.

7.2 Concluding remarks

A new purpose-build photocatalytic thin-film material with 1-3D hyperbranched morphology is now an available option for CO_2 utilisation reactions. It demonstrates enhanced optical and electronic properties along with potential for tuneability and ease of use. The HBNs have shown promising results in terms of both conversion and selectivity on photocatalytic reactions such as CO_2 photoreduction and photo-generation of cyclic carbonates. Furthermore, the HBNs use could potentially be expanded to other CO_2 utilisation reactions, as discussed in section 7.3.

This thesis provides a comprehensive framework of experimental research regarding purpose-build fabrication of photocatalysts with focus on CO_2 utilisation applications. The main objectives of this thesis are addressed through the experimental work and published articles presented in chapters 4,5 and 6. As was outlined in section 1.6, the main objectives for the fabrication of an efficient purpose build material consider electronic properties, optical properties, introduced tuneability and control, and ease of use of the photocatalytic material.

The electronic properties of the photocatalyst were enhanced with various techniques. Firstly, the material selection ensured thermodynamically favourable electrochemical potential for the specific CO_2 utilisation reactions. As was discussed in chapter 1 this is a fundamental property for a functioning photocatalysts and can influence the ability of the material to perform the reaction as well as its conversion rates and product selectivity. Also, the complex 1-3D superstructure provides improved charge mobility of photoexcited particles due to its composition of 1D lower dimension building blocks.[1] The loading RuO_2 and CuO on the HBNs have also allowed for modified electronic properties.[2, 3] The RuO_2 enhanced charge separation reducing the charge recombination rate leading to enhanced conversion rates, while CuO loading provided a narrower band gap, but acted as a recombination centre leading to modest conversion rates despite the increased wavelength absorption range. These have been explored predominantly in chapters 4 and 5.

Apart from improving charge mobility, the 1-3D hierarchical superstructure has shown to have significantly improved light harvesting capabilities of the photocatalyst. Photo-radiometer measurements have shown an increase in absorbed photon flux from

28.6 μmol m^{-2} s^{-1} up to 48.2 μmol m^{-2} s^{-1} when compared to P25.[2] This was attributed to the hyperbranched morphology and its light scattering capabilities. Additionally, the optical properties were enhanced utilising the incorporation of foreign compounds as shown in chapters 4 and 6. For example, the HBNs have a wide band gap of ~3.6 eV which necessitates high energy UV irradiation for charge excitation. However, after the incorporation of foreign compounds, the RuO_2-HBNs were able to successfully perform the cyclic carbonates reaction under solar simulator irradiation.[4]

Introducing tuneability to a photocatalyst provides control over product selectivity and conversion rates. This level of control was achieved using a facile protonation treatment on HBNs BP in chapter 4. When HBNs BP were presented to CO_2 photoreduction the primary product of the reaction was CO with a selectivity of 91% and 7.9 μmol g_{cat}^{-1} h^{-1} conversion. When the simple protonation treatment was applied (HBNs AP) the product selectivity was shifted to 64% towards CH_4 and the conversion rate was increased to 8.7 μmol g_{cat}^{-1} h^{-1}. This tuneability control was achieved by adjusting the ratio of the titanates to anatase phase on the HBNs material.[2] Enhanced light absorption and higher charge mobility were observed as described in chapter 4. When further modifications were applied to the photocatalyst, the selectivity of the reaction was increased reaching up to 74% towards CH_4 with 5.4 μmol g_{cat}^{-1} h^{-1} conversion.

Lastly, careful consideration of the presentation of a photocatalyst to the reaction is important. Ease of use of a photocatalytic material can help eliminate the need of costly processes like separation and purification steps.[4] An example can be drawn from chapter 6. The HBNs thin films, which was supported on FTO glass, provide an easy separation step from the liquid reaction solution without the need for complex separation or filtration steps. Costly separation and filtration steps are one of the main drawbacks of homogeneous photocatalysts that are currently being used industrially to catalyse this reaction.[5, 6] This contributes to the 4th objective as stated in Section 1.6.

7.3 Future development

The following section is a list of recommended future work for the expansion of the research work presented in this thesis.

Direct implementation of HBNs material. As mentioned, the titania HBNs photocatalyst was fabricated with photocatalytic CO_2 Utilisation applications in mind. However, photoelectrochemical reactions can be easily investigated without the need of

significant modifications (if any). For example, the material could be used for the photoelectrochemical reduction of CO_2 as a photoanode in a photoelectrochemical cell (PEC). The HBNs thin films are already grown on transparent conductive FTO glass as thin-films which could be incorporated into the PEC. Furthermore, it possesses thermodynamically favourable electrochemical potentials for the reduction of CO_2 and has exhibited good light harvesting and electron transfer. PEC systems tend to offer better efficiencies when compared to photocatalytic reaction as the PEC can promote charge separation through the electric field induced by the external bias.[7]

Exploring photogeneration of cyclic carbonates (CCs). To improve upon the conversion efficiencies and our understanding of the photogenerated CCs utilising CO_2 and epoxides, a few recommendations are presented. Since this is a recently discovered photocatalytic reaction, there are multiple unexplored perspectives to be researched. With this in mind, a flow photoreactor set-up is proposed as shown in Figure 7.1. The photocatalytic reaction in the current thesis was performed in a relatively large 500 mL photoreactor. At this scale and set-up, there are several reactor related considerations, which cannot be sufficiently or conveniently controlled. The proposed photoreactor geometry has an overall reaction chamber of 7.85 cm^3 with a 2D geometry (Dimensions; surface area 78.5 cm^2 x 0.1 cm depth). This geometry will ensure good illumination of the photoreactor chamber. Also, the 2D geometry can increase contact of reactants with photocatalyst thin film in the presence of irradiation. The mixing ratio of reactants could be better controlled and varied as needed for research purposes. Easy and more accurate control of heating could be achieved with line heating, sensors and a significantly smaller reactor body which is easier to raise temperature and cool down. Controllable time under reactants-photocatalyst contact by adjustable flow of the mass flow controller (MFC) and syringe pump (SP). An in-line back pressure regulator would allow for experimentation with a pressurised photoreactor. More importantly, the proposed set-up will dramatically reduce the time required for each experiment and would allow for sufficient amount of experiments to define the most impactful factors for this photocatalytic reaction. A mass spectrometer and gas chromatograph could be used to accurately analyse the reaction product. An important consideration is that epoxides and CO_2 can be corrosive to certain material commonly used in reactor rigs, such as sealing O-rings. However, there is a selection of materials that are resistant to these chemicals and are available as sealing O-rings, such as PTFE, PEEK and Kalrez.

Unexplored synergies. The addition of foreign elements such as RuO_2 and CuO on the HBNs have shown interesting results. However, CuO have consistently demonstrated modest conversion rates and photocurrent response despite the enhanced optical properties demonstrated by photo-radiometer and UV-Vis measurements. This was attributed to recombination centres formed which hindered the photocatalytic processes. It would be interesting to examine ways to reduce the recombination centres and improve the photocatalytic performance of the CuO-HBNs. In addition to reducing the CuO loading concentration as a way to reduce recombination centres, RuO_2 has shown the ability to improve charge mobility, suggesting that the incorporation of RuO_2 could be beneficial to the photocatalyst. Since the two materials offered complimenting properties to the HBNs, it is worth examining potential synergistic effects on HBNs photocatalysts. The suggested material would require 1 hydrothermal synthesis for the HBNs followed by two solvothermal synthesis for RuO_2 and CuO loading. The following procedure should be considered as a starting point. Initially the fabrication of HBNs AP using the hydrothermal process as described in chapter 4, after calcination the 0.005 M loading of Ru using solvothermal treatment as described in chapter 4, recalcination at 400 °C for 10 h and then the addition of CuO following the procedure for chapter 4 with a reduced concentration at 0.0005 M CuO followed by a second recalcination at 400 °C for 10 h.
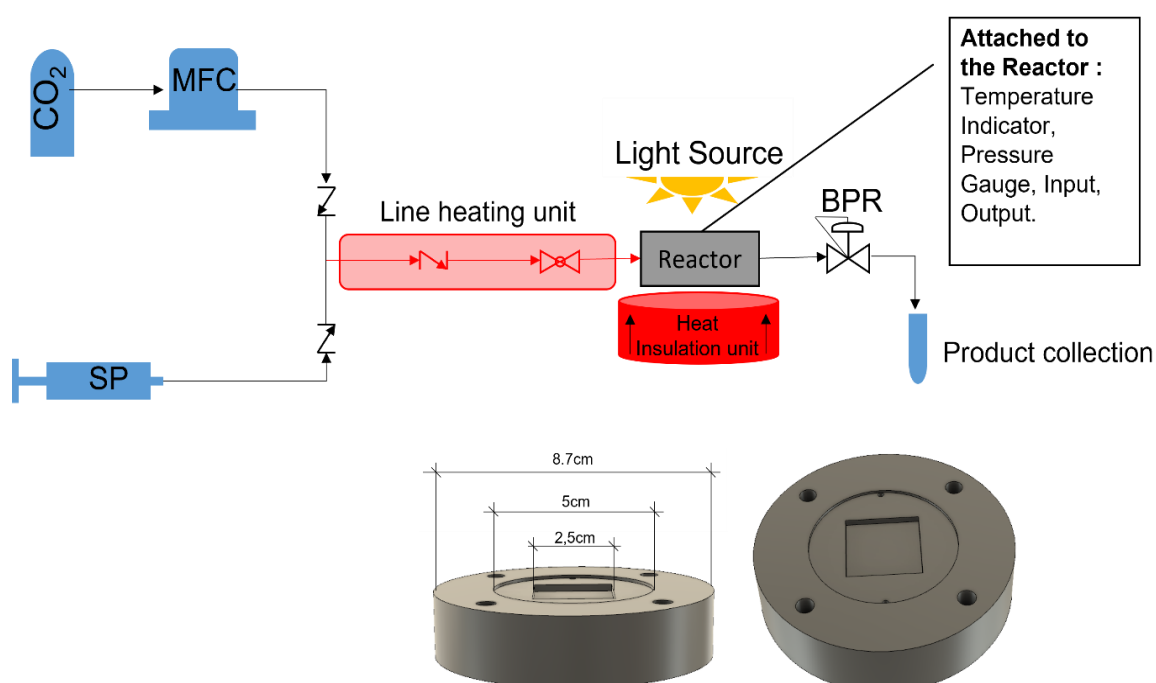

Figure 7.1 - Schematic representation of proposed flow photoreactor set-up for the photogeneration of Cyclic Carbonates.

References

[1]   Y. Ma, X. Wang, Y. Jia, X. Chen, H. Han, and C. Li, "Titanium Dioxide-Based Nanomaterials for Photocatalytic Fuel Generations," *Chem. Rev.,* vol. 114, no. 19, pp. 9987-10043, 2014/10/08 2014, doi: 10.1021/cr500008u.

[2]   G. Stelios, J. Z. Y. Tan, and M. M. Maroto-Valer, "Hierarchical hyper-branched titania nanorods with tuneable selectivity for CO_2 photoreduction," *RSC Adv.,* 10.1039/D1RA05414G vol. 11, no. 51, pp. 32022-32029, 2021, doi: 10.1039/D1RA05414G.

[3]   M. A. Ávila-López *et al.*, "Comparative study of CO_2 photoreduction using different conformations of CuO photocatalyst: Powder, coating on mesh and thin film," *Journal of CO_2 Utilization,* vol. 50, p. 101588, 2021/08/01/ 2021, doi: https://doi.org/10.1016/j.jcou.2021.101588.

[4]   S. Gavrielides, J. Z. Y. Tan, E. S. Fernandez, and M. M. Maroto-Valer, "Photo-generation of cyclic carbonates using hyper-branched Ru–TiO_2," *Faraday Discuss.,* 10.1039/C8FD00181B vol. 215, no. 0, pp. 407-421, 2019, doi: 10.1039/C8FD00181B.

[5]   E. Alper and O. Y. Orhan, "CO_2 utilization: Developments in conversion processes," *Petroleum,* vol. 3, no. 1, pp. 109-126, 2017.

[6]   V. B. Saptal and B. M. Bhanage, "Current advances in heterogeneous catalysts for the synthesis of cyclic carbonates from carbon dioxide," *Current Opinion in Green and Sustainable Chemistry,* vol. 3, pp. 1-10, 2017/02/01/ 2017, doi: https://doi.org/10.1016/j.cogsc.2016.10.006.

[7]   X. Chang, T. Wang, P. Yang, G. Zhang, and J. Gong, "The Development of Cocatalysts for Photoelectrochemical CO_2 Reduction," *Adv. Mater.,* vol. 31, no. 31, p. 1804710, 2019, doi: https://doi.org/10.1002/adma.201804710.

Appendix A – Supplementary information for publication 1

The following figures were submitted and published as supplementary information for publication 1 presented in chapter 4.
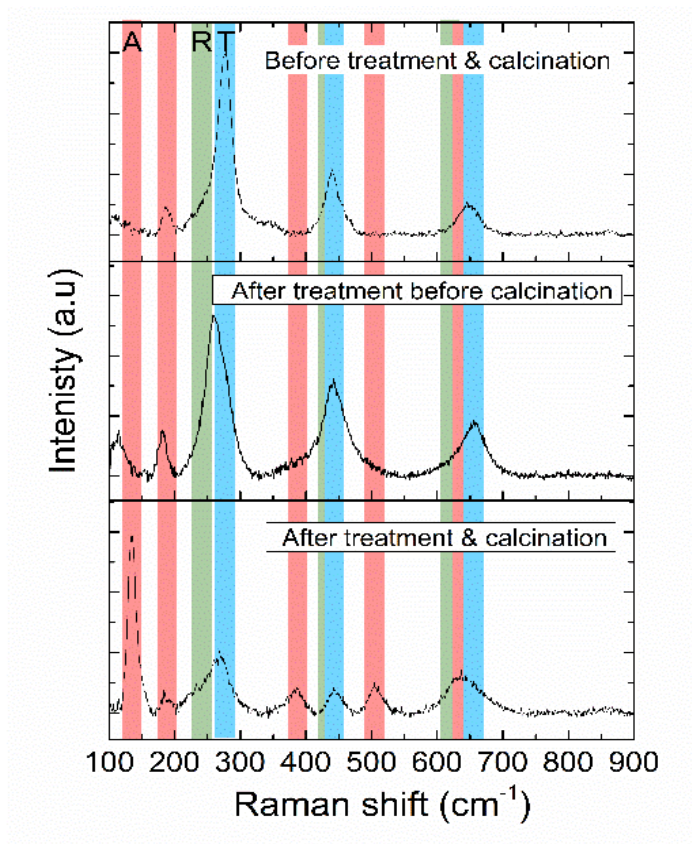

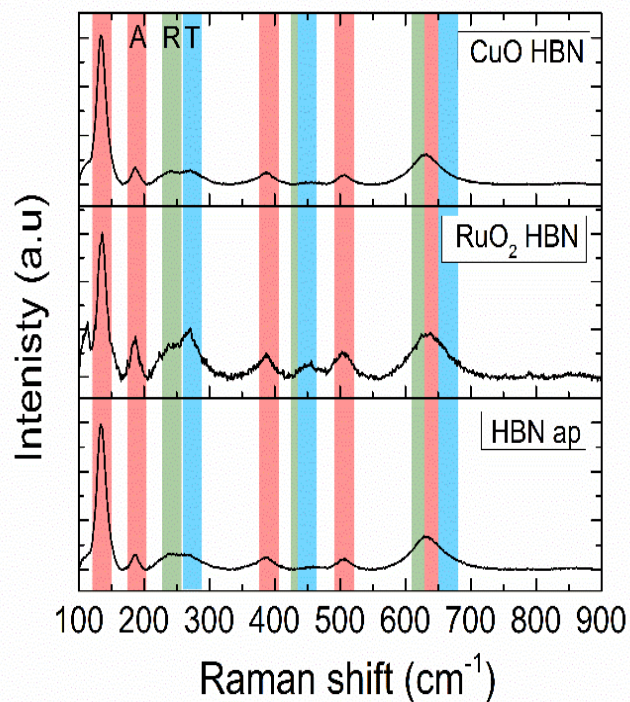Figure A.1 - Raman spectra investigation of the phase altering step from potassium titanates to anatase phase.

Figure A.2 - Raman spectra of the RuO_2 HBN and CuO HBN samples with as-prepared HBN ap. The figure shows very similar spectra with no Ru or Cu related peaks.
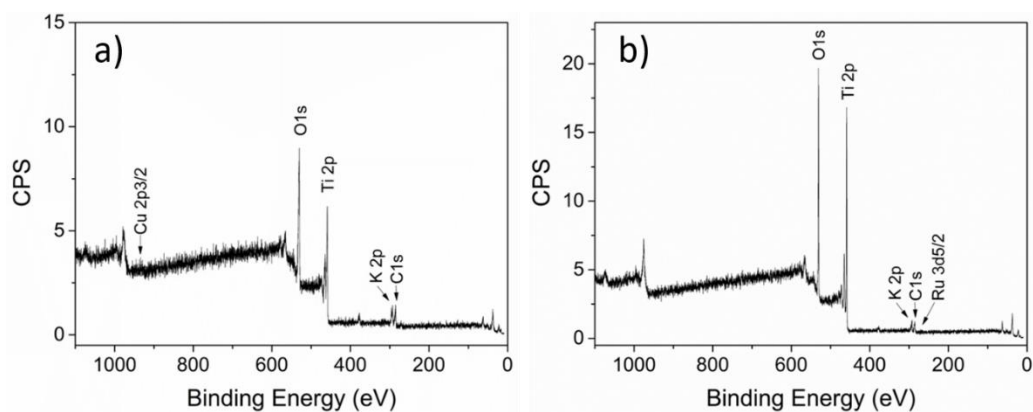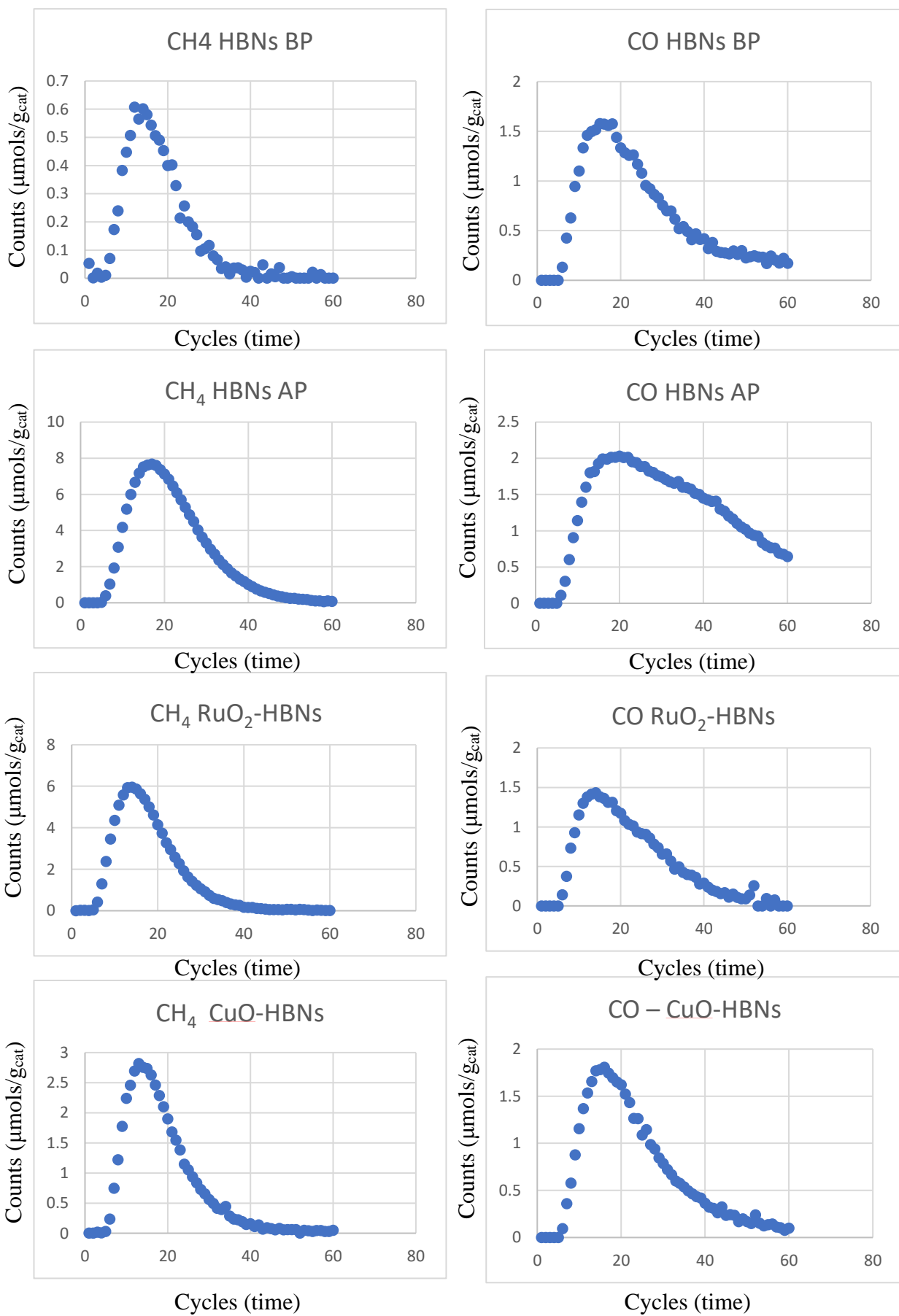

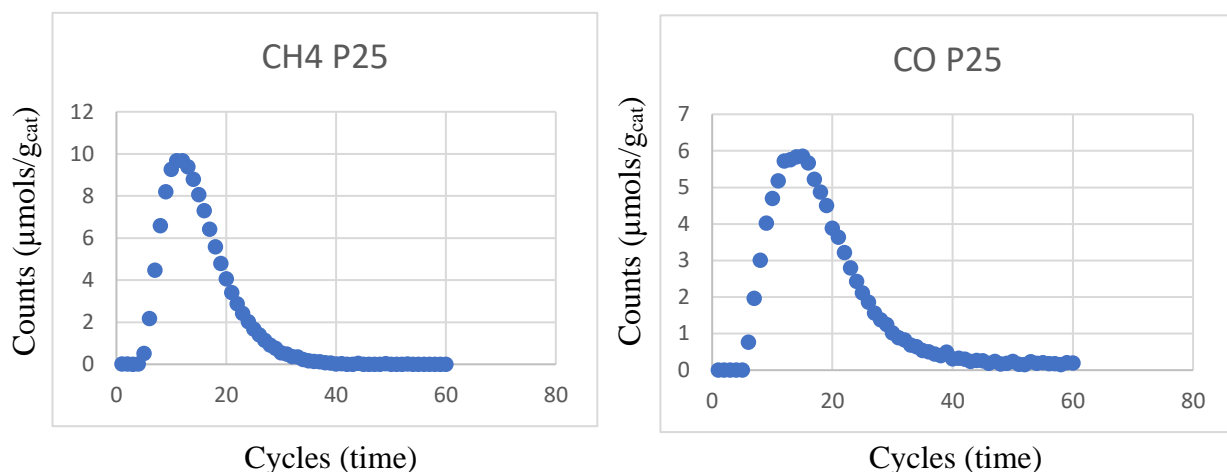Figure A.3 - XPS survey spectra for a) CUO HBN and b) RuO_2 HBN samples with annotated peaks.

Figure A.4 – Gaseous products production (µmols/g$_{cat}$) plotted against GC cycles for all the examined samples. Each cycle takes 4 minutes to complete, the data above represent 4 hours of reaction.
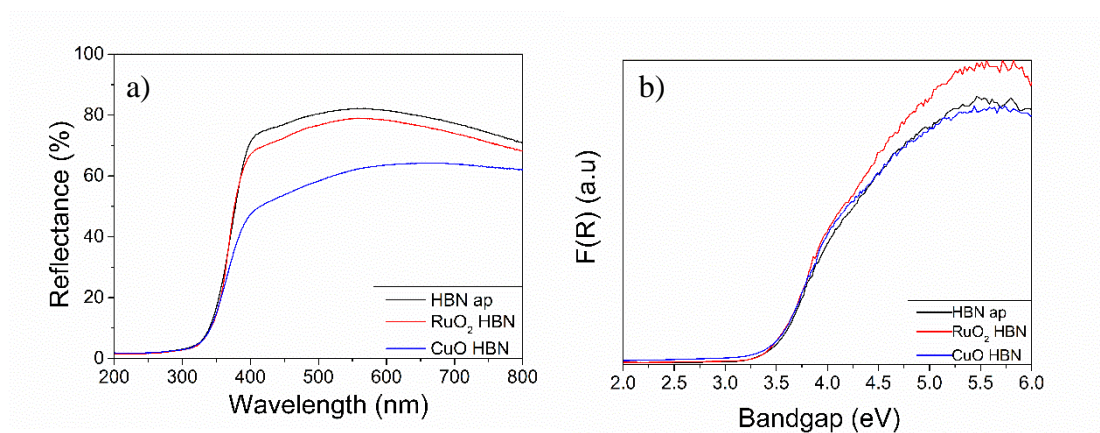

Figure A.5 - a) Funmi reflectance and b) Kubelka Munk spectra of the HBN ap, RuO$_2$ HBN and CuO HBN samples.

Appendix B - Publication 2 (full article + supporting information)

B.1 Full Article

Comparative Study of CO₂ Photoreduction Using Different Conformations of CuO Photocatalyst: Powder, Coating on Mesh and Thin Film

Manuel Alejandro Ávila-López[‡a], Stelios Gavrielides[‡b], XiaoJiao Luo[‡b], Abah Ezra Ojoajogwu[b], Jeannie Z. Y. Tan[b*], E. Luévano-Hipólito[c*], Leticia M. Torres-Martínez[a*], M. Mercedes Maroto-Valer[b*]

‡**These authors contributed equally.**

a. Universidad Autónoma de Nuevo León, Facultad de Ingeniería Civil-Departamento de Ecomateriales y Energía, Cd. Universitaria, C.P. 66455 San Nicolás de los Garza, NL, México.

b. Research Centre of Carbon Solutions (RCCS), School of Engineering & Physical Sciences, Heriot-Watt University, Edinburgh, United Kingdom.

c. CONACYT- Universidad Autónoma de Nuevo León, Facultad de Ingeniería Civil-Departamento de Ecomateriales y Energía, Cd. Universitaria, C.P. 66455 San Nicolás de los Garza, NL, México.

Abstract

The use of CuO-based photocatalysts for CO2 photoreduction has been extensively reported in the literature. However, the comparison of the photocatalytic activity and selectivity from the published results becomes difficult due to different experiment conditions (i.e., synthesis method, configuration of photocatalyst, flow rate of gas, water content, light intensity) and reactor geometry employed. Hence, in this work different conformations of CuO-based photocatalyst, namely powder (i.e., synthesized using precipitation, sonochemical and hydrothermal-microwave treatment), coating on glass fiber mesh, and thin film, were tested using the same photoreactor and experimental

conditions. All CuO photocatalysts exhibited 100% product selectivity towards CH4 over CO and the CuO coating on the glass fiber mesh exhibited the highest production of CH4 ($56.3 \ \mu mol \ g_{cat}^{-1} \ h^{-1}$). The morphology, particle size, particle dispersity, and presence of impurities/defects within the CuO photocatalysts had a significant effect on photocatalytic activity. A numerical model, which was built using COMSOL, revealed that the experimental data obtained in this simulated photocatalytic activity study fitted well, however, further optimization was needed.

Introduction

CO_2 is the most abundant anthropogenic greenhouse gas responsible for global warming.[1, 2] Various mitigation approaches have been proposed to decrease CO_2 emissions, including CO_2 conversion and utilization (CCU).[3-5] Solar energy to drive the photoreduction of CO_2 into chemicals and fuels provides an interesting approach for the production of syngas (CO and H_2), CH_3OH, CH_4, HCOOH and HCOH amongst others .[6-12]

Photocatalyst requirements, including a high affinity towards CO_2, rapid adsorption/desorption kinetics, high thermal and mechanical stability and high specific surface area with active sites, have been proposed to enhance the photocatalytic conversion of CO_2 into value-added products.[13] In view of this, transition metal oxides represent an excellent option since they can desorb the adsorbed gas at a relatively low temperature (<200°C) compared to alkali metals and alkaline metal oxides.[13] In addition, they are non-toxic and abundantly available. Among the transition metal oxides, copper-based metal oxides (*i.e.*, Cu_2O, CuO, Cu metal) are the most widely reported materials for CO_2 photoreduction.[14, 15] This is because CuO possesses the highest electronegativity and highest number of basic sites for CO_2 adsorption and a more favorable CO_2 adsorption capability ($\Delta H= -45 \ kJ \ mol^{-1}$) compared to other transition metal oxides.[16, 17]

Many studies have demonstrated the use of CuO as photocatalyst for CO_2 reduction,[8, 18-23] , as summarized in Table S1. However, the comparison of the results from the literature is challenging due to different synthesis approaches, experimental conditions, and geometry of photoreactor employed. Hence, in this study, the comparison of CuO photocatalyst in different conformations (*i.e.,* powder, thin film, and coatings on glass fiber mesh) is investigated under the same experimental conditions. Moreover,

three commonly used synthesis methods, including precipitation, sonochemical, and microwave synthesis are employed to fabricate powder samples.

In addition to the development of photocatalysts for CO_2 photoreduction, significant work has been devoted to developing advanced photoreactors in an attempt to improve the current very low conversions.[24, 25] To address these engineering challenges, a validated Multiphysics model for CO_2 photoreduction under UV-vis light irradiation was developed herein. The model developed was coupled with computation fluid dynamics, mass transport, reaction kinetic and light transport in a continuous flow reactor. Three essential factors (*e.g.*, CO_2 flow rate, inlet H_2O mole fraction and light intensity) in the CO_2 photoreduction were simulated. This numerical modelling is also expected to improve our understanding of the CO_2 photoreduction mechanism, and thereby, provide a useful tool to optimize the reaction process.

Experimental Procedure

Materials synthesis

Powder

a. Precipitation method

5.98 g of $Cu(CH_3COO)_2 \cdot H_2O$ (Fermont, 99%) was dissolved in 40 mL of deionized water (DI). Then, 10 mL of 0.6 M of NaOH (Fermont, 99%) was added dropwise into the solution. The solution was then heated for 3 h at 80 °C under vigorous stirring. The dark brown precipitate was washed with sufficient DI water, for remove all the possible residual precursor. The collected powder was dried in the oven at 80 °C overnight and the sample obtained was denoted as CuO P.

b. Sonochemical method

The CuO powder sample was synthesized following a procedure reported previously.[26] Briefly, 0.38 M of $Cu(CH_3COO)_2 \cdot H_2O$ solution was dissolved in DI water. Then, 0.6 M of NaOH was added dropwise into the first solution with vigorous stirring at 50 °C. The resulted solution was exposed to sonochemical energy for 25 min using an equipment Hielscher's UP200Ht at 100 W, with capacitance and an amperage of 50 and 20%, respectively. After the sonication treatment, the resulted brown suspension was washed with DI water for three times. Finally, the dark brown powder obtained, which denoted as CuO US, was dried in the oven at 80 °C overnight.

c. Microwave-hydrothermal method

An aqueous solution of 0.6 M of $Cu(CH_3COO)_2 \cdot H_2O$ was prepared under vigorous stirring for 30 minutes. Then, 0.6 M of NaOH was added dropwise. After that, the mixture was treated in a microwave reactor (Mars 6) at 80 °C with 300 W for 60 min. The resulted precipitate was washed with DI water and centrifuged a few times until the water was clear. Finally, the powder obtained was dried at 80°C for 12 h and the resultant sample was denoted as CuO MW.

Coating

A glass fiber mesh with a grit slit of 2.7 nm was used as the substrate for CuO coating fabrication. Firstly, the glass fiber substrate was cleaned with acetone, methanol, and then DI water under sonication for 20 min and then dried at 80 °C overnight. Then, the cleaned glass fiber mesh substrates were placed in an autoclave that was filled with 0.06 M of $Cu(CH_3COO)_2 \cdot H_2O$ solution. After that, 0.6 M of NaOH was added dropwise into the solution under vigorous stirring. Next, the autoclave was placed in the microwave reactor at 80 °C with 300 W for 60 min. The resulting brown coating on the glass fiber mesh was washed with DI water and centrifuged a few times until the water was clear and then dried at 80 °C overnight and the sample denoted as CuO Coat.

Thin film

Fluorine-doped tin oxide (FTO) TEC-15 glass was purchased from Ossila (2.5 cm x 2.5 cm, roughness of 12.5 nm, FTO layer thickness of 200 nm, 83.5% transmission and resistivity of 12-14 Ω cm^{-1}). The FTO substrate was cleaned before use using a mixture of isopropanol, water, and acetone with a 1:1:1 ratio. The FTO glass was submerged into the solution and placed in a sonication bath for 1 h. The FTO glass was then removed and dried in air for 30 min at 75 °C on a hot plate.

Copper (II) acetate (Aldrich, 98%) solution was prepared using 2.742 g in 50 mL of ethanol, forming solution A. Then, solution A was stirred for 30 minutes. After that, 12 µL of diethanolamine ($C_4H_{11}NO_2$, Aldrich $\geq$98%) and 25 µg of ethylene glycol ($C_2H_6O_2$, Alfa Aesar $\geq$99%) were added into solution A and stirred for 30 and 60 min, respectively, obtaining solution B that was used to fabricate CuO thin film using a spin coater (Model P6700). Solution B was added drop by drop onto a cleaned FTO glass, which was placed on the sample stage of the spin coater spinning at 3000 rpm. After that, the FTO coated was dried in air at 100 °C for 10 min and then calcined at 400 °C (ramp rate: 10 °C min^{-} ^{1}) for 1 h, with the resulting sample labelled as CuO TF.

Characterization

The samples morphology was analyzed using Scanning Electron Microscopy (SEM, JEOL 6490). To investigate the crystallinity and phase identification, X-ray diffraction (XRD) patterns were obtained using a Bruker D8 Advanced Diffractometer equipped with Cu Kα radiation (λ= 1.5418 Å) and compared with the ICDD-JCPDS powder diffraction file database; and Raman spectra were collected using a Renishaw *inVia* Raman Microscope with 785 nm excitation source. Diffuse reflectance of all the samples was measured using a Perkin Elmer Lambda 950 UV-vis equipped with an integrating sphere (150 mm). X-ray photoelectron spectrum (XPS) analysis were performed using a Thermo Fisher Scientific NEXSA spectrometer. The samples were analysed using a micro-focused monochromatic Al X-ray source (19.2 W) over an area of approximately 100 microns. Data were recorded at pass energies of 200 eV for survey scans and 50 eV for high resolution scan with 1 eV and 0.1 eV step sizes, respectively. Charge neutralisation of the sample was achieved using a combination of both low energy electrons and argon ions. C 1s electron at 284.8 eV was used as standard reference to calibrate the photoelectron energy shift. All the data analysis was performed on the CasaXPS software (version: 2.3.20rev1.0). Fourier Transform Infrared spectroscopy (FTIR), which was performed on Thermo Nicolet iS50 (1000-4000 cm^{-1}), was used to characterize the surface of the materials. *Operando* Diffuse Reflectance Infrared Fourier Transform Spectroscopy (DRIFTS) experiments were conducted on Agilent Cary 600 series spectrometer equipped with Harrick Praying Mantis reaction cell. The gas inlet of the cell was directly connected to a flow system equipped with mass flow controllers and a temperature controller. The cell outlet was connected to the mass spectrometer Hiden QGA MS. In each experiment, 20 mg of crushed powder was placed in the cell. Before reaction, the KBr background was collected in presence of CO_2 which was flowing through bubbler. 64 scans were collected per spectrum with a spectral resolution of 4 cm^{-1} and in the spectral range of 4000-400 cm^{-1}. The experiment was performed under UV-vis irradiation at 24 and 40 °C and dark (24 °C) conditions to simulate the experimental conditions within the photocatalytic reactor.

CO_2 Photoreduction tests

The CO_2 photocatalytic reduction tests were performed under UV-visible light irradiation using the experimental set-up and procedure as described in the authors published

work.[27] Briefly, the sample was loaded in the middle of the photoreactor. To purge the system, three repetitive steps of placing the system under vacuum to -1 bar and the vacuum released with CO_2 (99.995%) to 1 bar were performed. The CO_2 was then released through the injection port of the gas chromatograph (GC, Agilent, Model 7890B series), leaving a positive pressure of 0.2 bar, before the system was sealed and placed under vacuum overnight before each measurement. The flow rate of CO_2 was set to 0.35 mL min^{-1} and passed through the temperature controlled ($\pm$0.1 °C) aluminium body saturator for at least 16 h to allow the system to equilibrate. Relative humidity ($\pm$1.8% RH) was measured using an inline Sensirion SHT75 humidity sensor potted (MG Chemicals 832HD) into a Swagelok 1/4" T-piece. The temperature of the photoreactor (40 °C) was controlled using a hotplate and the surface of the coated photocatalyst measured using a Radley's pyrometer ($\pm$2.0 °C). An OmniCure S2000 with 300-600 nm wavelength was used as the light source was placed 30 mm above the surface of the investigated sample. Irradiance (150 mWcm^{-2}) at the exit of the fiber optic light guide was measured before each experiment using an OmniCure R2000 radiometer ($\pm$5%). An inline GC) with a Hayesep Q column (1.5 m), 1/16 inch OD, 1 mm OD), Molecular Sieve 13X (1.2 m), 1/16-inch OD, 1 mm ID), thermal conductivity detector (TCD), nickel catalyzed methanizer and flame ionization detector (FID) was used to analyze the output of the photoreactor every four minutes. The GC was calibrated using 1000 ppm calibration gas (H_2, CO, O_2 and CH_4) in a balance of Ar gas) that was further diluted with Ar (99.995%) using mass flow controllers to 17.04, 4.62 and 1 ppm using the FID detector for CH_4 and CO, respectively, and 69.49, 34.72 and 17.04 ppm using the TCD detector for H_2 and O_2.

The CO_2 utilization rate was determined by taking the molar percentage of CO_2 inlet: CO_2 outlet as the amount of CO_2 consumed. The cycling test (*i.e.*, 3 runs) was performed using the optimized sample, which was cleaned with DI water and dried on a hotplate at 100 ºC for 2 h before each run.

The quantum yield (ϕ) was measured under similar photocatalytic reaction conditions using the same light source (OmniCure S2000 with 300-600 nm wavelength). The incident flux was determined by a Laboratory Spectroradiometer (Apogee Instruments). The ϕ values of CH_4 evolution for the CO_2 photoreduction reaction were calculated according to the following equation:

ϕCH_4 (300-600 nm) =

$$\frac{amount\ of\ product\ formed}{amount\ of\ photons\ adsorbed\ in\ the\ range\ of\ 300-600\ nm}$$

Simulation studies

COMSOL Multiphysics version 5.3 was used to solve the numerical equations and develop a stationary numerical model for CO_2 photoreduction. The model built was validated with the experimental data obtained in this study. A three-dimensional continuous flow reactor was simulated. The following general assumptions were made: (1) steady state laminar flow of incompressible Newtonian fluid with constant physical properties; (2) all gases were assumed as ideal gases; and (3) the whole reactor was assumed isothermal with temperature of 298 K, which means the Arrhenius expressions were ignored in the model. To assure the accuracy of the solutions obtained, a grid independence check was conducted. The computational domain of the 3D models developed for samples CuO MW, CuO Coat and CuO TF were mainly discretized with tetrahedral, prism and triangular elements. Direct solution procedure was conducted by using the Multifrontal Massively Parallel Solver. The abbreviations and symbols used are listed in Table S2 and a summary of all parameters used are presented in Table S3.

Results and Discussion

Crystal phase

The powder samples synthesized using different approaches (*i.e.*, precipitation, ultrasonication and microwave synthesis) exhibited the monoclinic phase of CuO (JCPDS: 45-0937, Figure B.1a-c). The peaks at 32.5, 35.8 and 38.6º corresponded to the (110), (-111) and (111) planes, respectively. The most intense peak at $2\theta = 38.6°$ was used to estimate the crystallite size of the samples, which was 10-12 nm.

The crystal phase of CuO Coat also exhibited monoclinic phase (JCPDS: 45-0937, Figure 1d). However, the signal-to-noise of the XRD pattern in CuO Coat was much lower than that for CuO P, CuO US and CuO MW due to the low thickness of the coating on the glass fiber mesh. The XRD pattern of sample CuO TF (Figure B.1f) only revealed a strong diffraction at $2\theta = 37°$, corresponding to the FTO conductive thin film (Figure B.1e). This was due to the overshadow of the diffraction pattern of the conductive thin film. Hence, Raman spectroscopy, which is much more sensitive towards the vibration of the crystal lattice, was employed.[28] Three bands centered at 287, 341, and 615 cm^{-1}, which were attributed to A_g, B_{1g}, and, B_{2g} modes of CuO, respectively, were observed in samples CuO TF (Figure S1a).[29-32] However, these CuO peaks were broadened and slightly red-shifted, attributing to different sizes of the CuO particles (further discussed in the next section).[30] Sample CuO Coat also exhibited CuO characteristic bands. Additional bands, including PO_4^{3-} ($v1$) (960 cm^{-1}),[33] Si-N-Si (870 cm^{-1}), vibration outside the plane C-H (760 cm^{-1}), deformation outside the ring C-H (690 cm^{-1}),[34] P-O-
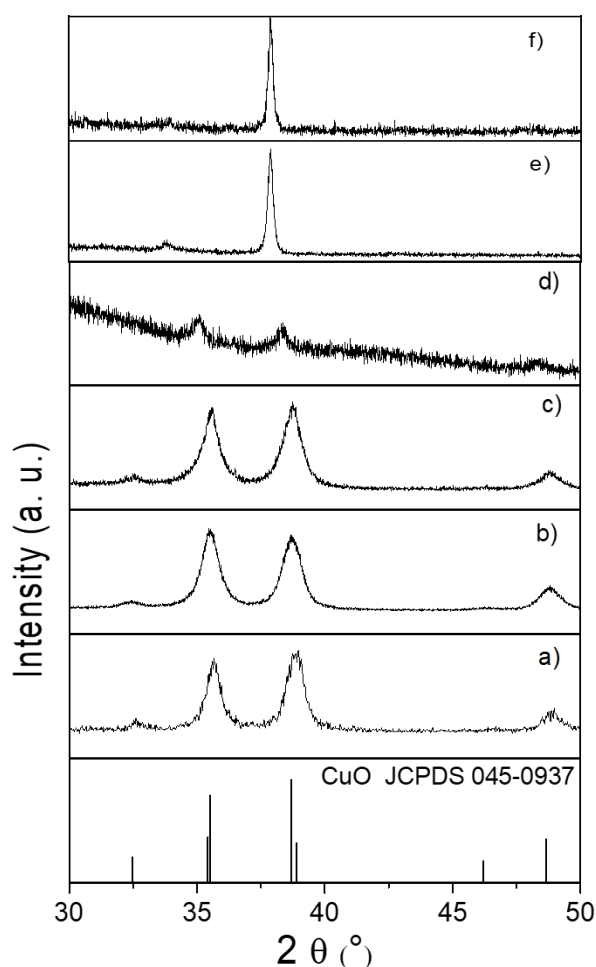

Figure B.1 - XRD patterns of a) CuO P, b) CuO US, c) CuO MW, d) CuO Coat, e) FTO, and f) CuO TF.

P (620 cm^{-1}) were identified originated from the glass fiber mesh substrate (Figure B.S1b and c).

Morphology

The morphology of the fabricated samples was investigated using SEM. Samples CuO P, CuO US and CuO MW possessed a mixture of nanorods and agglomerated nanoparticles (Figure B.2a-c). The length of the nanorods observed in the sample CuO US (~580 nm, Figure B.2b) was longer than that in CuO P (~400 nm, Figure B.2a) and CuO MW (~408 nm, Figure B.2c). Very similar observation was also obtained on sample CuO Coat, but a more homogeneous nanorods coated on the surface of the glass fiber mesh was observed (~445 nm in length, Figure B.2d). The CuO TF fabricated revealed a patchy microstructure resulted the broadening and red-shifted of the Raman spectrum in this sample (Figure B.2f).
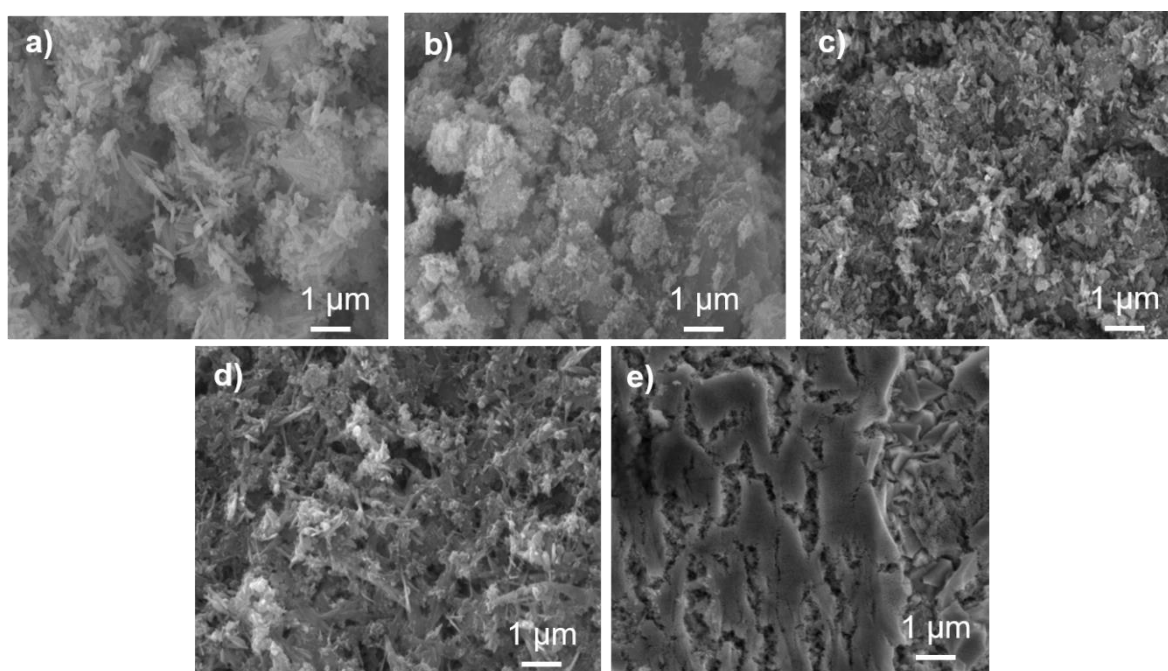

Figure B.2 - SEM of the a) CuO P, b) CuO US, c) CuO MW, d) CuO Coat, and e) CuO TF.

Optical Properties

The optical properties of the fabricated samples were investigated and analyzed using UV-vis spectroscopy, as shown in Figure B.3. The band gap energy of was derived using the Kubelka-Munk function from diffuse reflectance. All the fabricated samples showed a band gap of around 1.4-1.5 eV using the (Figure B.3).
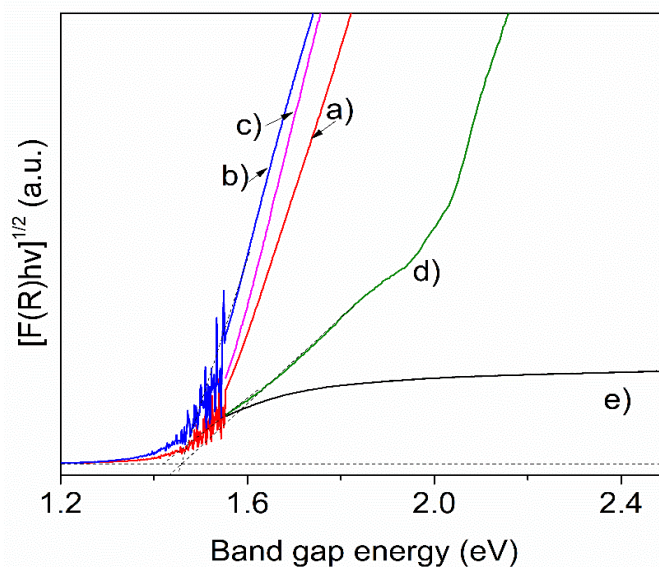
Figure B.3 - Kubelka-Munk spectra of a) CuO P, b) CuO US, c) CuO MW, d) CuO Coat, and e) CuO TF.

Surface properties

To investigate the surface chemistry of the samples, XPS was performed (Figure B.4). The XPS survey spectra of samples CuO P, CuO US, CuO MW and CuO TF revealed no contamination from the precursors nor substrates, whereas CuO Coat revealed the presence of Na, which was originated from the glass fiber mesh (Figure B.S2).

The Cu 2p spectra of all the samples were deconvoluted into two components. Specifically, the Cu $2p_{3/2}$ (934.5 eV for CuO P and CuO MW; 934.9 eV for CuO US) and Cu $2p_{1/2}$ species (954.7 eV for CuO P and CuO US; 954.6 eV for CuO MW; Figure 4a-c). In addition, these components were accompanied by their respective satellite peaks positioning at 961.0-963.9 eV, which are characteristic of Cu^{2+}. Furthermore, the difference between the Cu $2p_{1/2}$ and Cu $2p_{3/2}$ peaks was ~20 eV, which evidenced the oxidation state of the fabricated samples as Cu^{2+}.[35, 36] The presence of Cu^+ on the surface of the fabricated materials was revealed in the peaks centered at 933.1 and 953.1 eV for CuO P; 933.6 and 953.2 eV for CuO US; and 933.1, and 953.0 eV for CuO MW (Figure B.4a-c).[37] Meanwhile, CuO Coat had the Cu $2p_{3/2}$ peak centered at 934.5 and 934.2 eV and Cu $2p_{1/2}$ peak located at 953.8 eV. Similarly, the difference of Cu $2p_{1/2}$ and Cu $2p_{3/2}$ in CuO Coat remained ~20 eV, confirming the fabricated CuO Coat sample contained Cu (II) (Figure B.4d). This sample also contained Cu^+ as exhibited in the peak positioned at 933.1 eV (Figure B.4d) but absent in CuO TF (Figure B.4e). CuO TF

171

exhibited only the Cu $2p_{3/2}$, Cu $2p_{1/2}$ and Cu satellite peaks at 932.7, 952.4 and 962.1 eV, respectively (Figure B.4e), confirming the presence of CuO on the thin films.

The high-resolution of O 1s spectrum were deconvoluted into four components (Figure B.S3). The peak centered at 529.5-529.9, were attributed to the O^{2-} in O_L-CuO.[38, 39] Meanwhile, the presence of peak centered at 531.1 (*i.e.*, samples CuO US, and CuO Coat) and 530.2 eV (*i.e.*, sample CuO P and CuO MW) was attributed to V_{Os},[40-42] evidencing the presence of V_{Os} in these samples. Other peaks located at 531.9-532.3 eV were attributed to the oxygen adsorbed on the surface with low coordination.[43, 44]

High resolution XPS spectra at low binding energy region were also collected to investigate the position of the valence band. The valence band of the fabricated samples
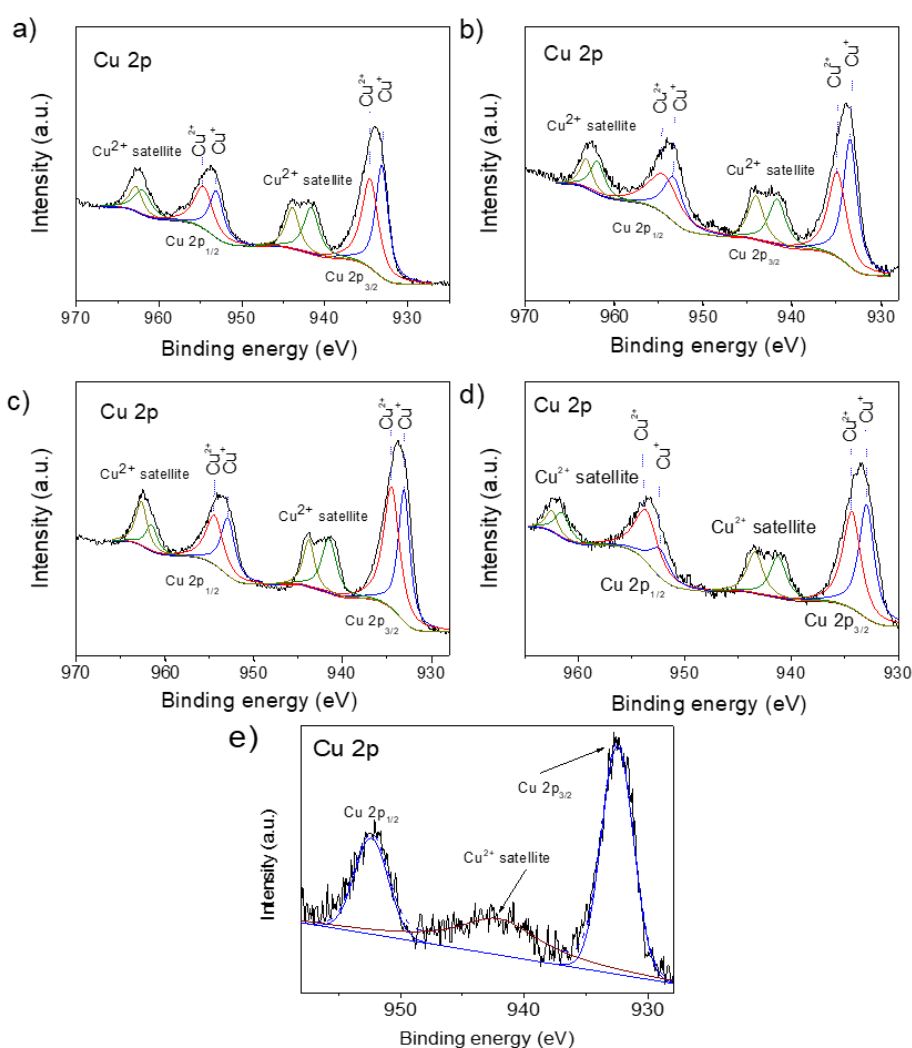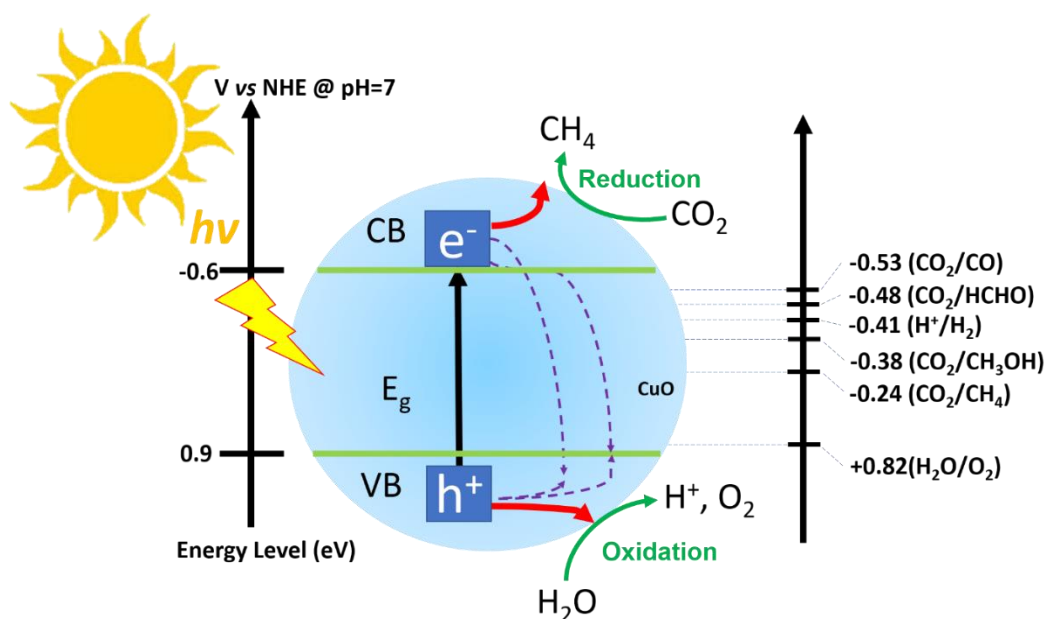

Figure B.4 - XPS spectra of Cu 2p for a) CuO P, b) CuO US, c) CuO MW, d) CuO Coat, and e) CuO TF.

was positioned at ~1.6 eV, indicating the CuO-based sample possessed sufficient potential to reduce CO_2 to CH_4 (Scheme 1).[45]

.

Scheme B.4 - Schematic illustration of CO_2 photocatalytic reduction with H_2O under using CuO under visible light irradiation.

Photocatalytic activity

The fabricated CuO samples in different conformations were evaluated for the photocatalytic reduction of CO_2 under the light irradiation (300-600 nm) and the quantity of the gaseous products produced (CO and CH_4) were monitored (Table B.1). In general, CH_4 was the main product produced by all the fabricated CuO samples in the photocatalytic reduction of CO_2, whereas CO was generated in very low quantities.

Table B.4 - Average products obtained in 4 h from CO_2 photoreduction using different configurations of photocatalyst.

Sample name	CH_4 (μmol $g_{cat}^{-1} h^{-1}$)
CuO P	1.0
CuO US	1.5

CuO MW	2.6
CuO Coat	56.3
CuO TF	12.7

The CH_4 production of the powder samples declined in the order of CuO MW (2.6 µmol g_{cat}^{-1} h^{-1}) > CuO US (1.5 µmol g_{cat}^{-1} h^{-1}) > CuO P (1.0 µmol g_{cat}^{-1} h^{-1}). This could be due to the homogeneity of the particles of the samples fabricated using the microwave-hydrothermal approach. The action spectra of the CO_2 photoreduction for the fabricated samples is shown in Figure S4.

Regarding to the photocatalytic activity of the immobilized photocatalysts, sample CuO TF, which contained only CuO, exhibited 100% selectivity towards CH_4, producing 12.7 µmol g_{cat}^{-1} h^{-1} under visible light irradiation. Sample CuO Coat showed the highest production of CH_4 (56.3 µmol g_{cat}^{-1} h^{-1}), which was approximately 18 times higher than that of CuO MW (*i.e.*, highest among the fabricated powdered samples). The superior performance of CuO Coat (ϕCH_4 = 0.882) was due to the reduction of agglomeration and the presence of Na_2O originated from the mesh substrate as shown in the FTIR (Figure B.5).[46, 47] The presence of Na_2O had significantly enhance the CO_2 adsorption (further discussed in the next paragraph). The CuO Coat, which has the highest CH_4 production was implemented for cycling test (Figure B.S5). The sample was tested for 3 runs and did not show significant reduction in CH_4 production.
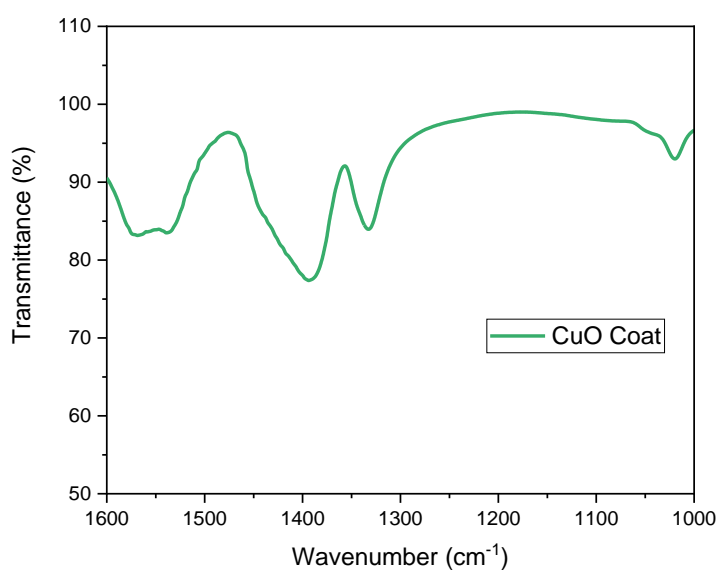
Figure B.5 - FTIR pattern of CuO Coat upon the exposure of CO_2

The mechanistic study of the best performing sample (*i.e.*, CuO Coat) was conducted using FTIR in the presence of CO_2 (Figure B.5). A series of bands at 1560 and 1410 cm^{-1}, which could be associated with C−O stretching and symmetry O−C−O vibrational modes, was assigned to monodentate species (linear coordination or carbon coordination).[48, 49] In addition, C−O stretching and symmetry O−C−O vibrational modes, which were shown at 1340 and 1020 cm^{-1} corresponded to the bidentate carbonate.[50] Based on the results obtained, the CO_2 adsorption and conversion mechanisms in CuO Coat sample was proposed and shown in Scheme B.2. Briefly, the O and Cu on the surface of CuO Coat acts as a Lewis base site – an active site for CO_2 adsorption and conversion. Then, electrons were transferred to the C and/or O of the CO_2 molecules resulted in the formation of monodentate and bidentate configurations at the surface of CuO Coat. The hole-electron pairs, which were generated upon light irradiation, traveled to the surface of the photocatalyst and underwent the subsequent oxidation-reduction reactions. CO_2 was reduced to CH_4 and H_2O was oxidized to O_2 and H^+.
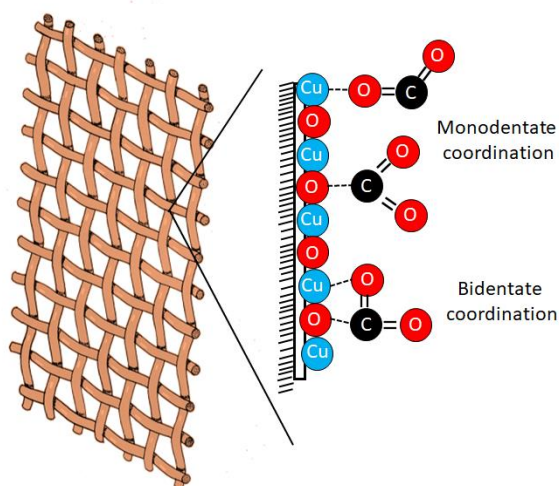
Scheme B.5 - Schematic illustration of CO_2 adsorption and conversion on the surface of CuO Coat sample.

The CuO coat was analyzed with *operando* DRIFTS to confirm the formation of carbonate species (Figure B.S6). The coating presented a strong adsorption band at 2348

cm^{-1}, which assigns to CO_2 physiosorbed in the surface of the coating, when CO_2 was fed into the reactor and put in contact with the photocatalyst at 24°C in the dark. On the other hand, the bands at around 1620, 1420 and 1296 cm^{-1} were assigned to the asymmetric CO_3 stretching vibration [$v_{as}(CO_3)$], symmetric CO_3 stretching vibration [$v_s(CO_3)$] and O-H deformation vibration [δ(O-H)] of monodentate bicarbonate species (m-HCO_3^{2-}), respectively, were observed upon CO_2 interaction with the coating in the dark.[3, 51] When the coating was irradiated with UV-vis light, the intensity of these bands lowered. The bands at around 1540 and 1384 cm^{-1} corresponds to the [$v_{as}(CO_2)$] and [$v_s(CO_2)$] of the bidendate formate species (b-HCO_2^{2-}).[52] These results suggested that the CO_2 molecules adsorbed on the surface of CuO coat were mainly m-HCO_3^{2-} and converted to b-HCO_2^{2-} through the reaction with OH$^-$ on the surface or OVs CuO coating. When the reaction temperature increased to 40°C (to emulate the reaction conditions), the bands of m-HCO_3^{2-} continued to decrease, whereas b-HCO_2^{2-} increased steadily. In other words, adsorption of CO_2 and conversion of m-HCO_3^{2-} to b-HCO_2^{2-} were enhanced at elevated temperature, which could favor the formation of CH_4. Therefore, *operando* DRIFT results suggested that the mechanism for the photocatalytic CO_2 reduction route of CuO coat was through the carbene pathway[47, 52].

Simulation study

To gain insight in the coupled physical/chemical processes, parametric simulations (CO_2 gas flow, humidity, and light intensity) were performed. The simulated photocatalytic activity values obtained from the constructed models using COMSOL multiphysics software matched well with the experimental results as shown in Figure B.6. The simulation revealed that the flow rate of CO_2 had almost no effect on the photoreduction reaction rate (Figure B.6a). However, the simulated CO_2 utilization rate dropped rapidly with increasing CO_2 flow rates for values up to 5 SCCM (Figure B.6d). Further increasing the CO_2 flow rates would eventually lead to zero CO_2 utilization rate. This phenomenon was expected due to the reduction of contact time between the gas (CO_2) and solid (photocatalyst) phases at high flow rate as reported in other work.[53]

Increasing the water content exhibited a remarkable improvement in the reaction rate, (Figure B.6b) and CO_2 utilization rate (Figure B.6e), especially for sample CuO MW. Hence, the simulated results indicated that the water content for the CO_2

photoreduction was far below the saturation point. Further increasing the water content will promote the photocatalytic reduction of CO_2.

The light intensity applied to stimulate the CO_2 photoreduction reaction strongly depended on the properties of the photocatalyst, including microstructure, surface area, etc. For instance, sample CuO Coat with rod-shape nanostructure exhibited the highest reaction rate and CO_2 utilization rate; whereas samples CuO TF and CuO MW with patchy-structures and agglomeration revealed a much lower performance (Figure B.6c and f).
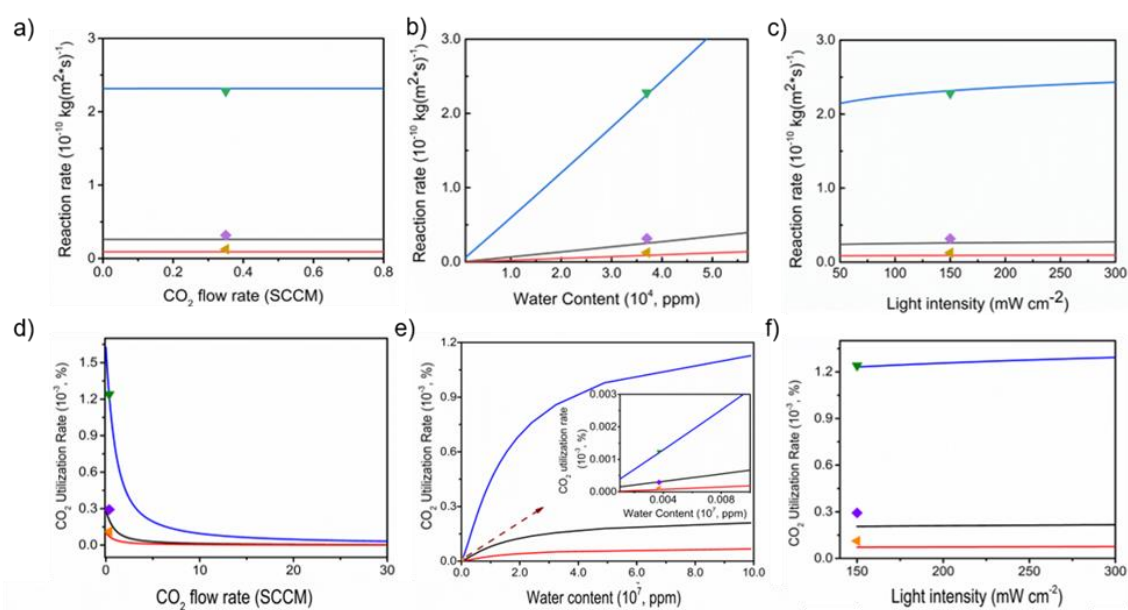

Figure B.6. Simulated patterns (lines: black- CuO TF, orange- CuO MW, blue- CuO Coat) and experimental results (purple ◆: CuO TF, orange ◣: CuO TF, green ▼: CuO TF) of the CO_2 photoreduction reaction rate and CO_2 utilization rate influenced by the (a and d) CO_2 flow rate, (b and e) water content, (c and f) light intensity.

Conclusions

CuO photocatalysts with different configurations (powder, thin film, and coatings on glass fiber mesh) were fabricated and their CO_2 photoreduction activity was investigated. Sample CuO Coat with highly dispersed nanorod structure coated on the glass fiber mesh showed the highest CH_4 production from CO_2 (56.3 μmol g_{cat}^{-1} h^{-1}), which was approximately 18 times higher than the powder sample synthesized using the similar method (CuO MW). Combining the experimental and simulated results, the use of highly dispersive nanostructured photocatalyst operated at ~6.0×10^7 ppm and ⩽2 SCCM of

water content and CO_2 flow rate, respectively, could achieve the maximum yield of CO_2 photoreduction at 40 °C.

Conflicts of interest

There are no conflicts to declare.

Acknowledgements

Supporting Information.

Tabulated results of CO_2 photoreduction efficiency from the literature; List of abbreviations and symbols used in the simulation study; Parameters used in the simulation study for different samples; XPS survey scan of the samples; high resolution O 1s spectra of the samples; chronoamperometric pattern of the fabricated samples.

Author Information

Corresponding Author

*Dr. Jeannie Z. Y. Tan

E-mail: j.tan@hw.ac.uk

*Prof. M. Mercedes Maroto-Valer

E-mail: m.maroto-valer@hw.ac.uk

*E. Luévano-Hipólito

E-mail: eluevano@conacyt.mx, edith.luevanohp@uanl.edu.mx

*Leticia M. Torres-Martínez

E-mail: leticia.torresgr@uanl.edu.mx

Author Contributions

The manuscript was written through contributions of all authors. All authors have given approval to the final version of the manuscript. ‡These authors contributed equally.

Funding Sources

B.2 Supporting information

Tabulated results of CO_2 photoreduction efficiency from the literature; List of abbreviations and symbols used in the simulation study; Parameters used in the simulation study for different samples; XPS survey scan of the samples; high resolution O 1s spectra of the samples; chronoamperometric pattern of the fabricated samples.

Table B.S.1 **-** Analysis of CuO based photocatalysts used for CO_2 photoreduction reported in the literature.

Photocatalytic material	CO_2 photocatalytic reduction product (s) (μmol $g_{cat}^{-1}h^{-1}$)	Operating conditions	Ref.
Cu_2O-$CuO/TiO_2/FTO$	CH_4: 0.5	- Catalyst mass: 1.0 g -Reactor: Continuous - Light source: 8 W UVA, 3.25 mW/cm^2 Range 365 nm -Pressure: 1.01 bar -Temperature: No reported	[8]
α-Fe_2O_3/Cu_2O/glass	CO:1.67	-Catalyst mass:0.1 g -Reactor: Continuous -Light source: Lamp 300 W Xe (λ> 400 nm) -Pressure: 3.0 bar. -Temperature: 40°C.	[18]
CuO-TiO_2-xNx	CH_4: 1.30	-Mass used: 0.1 g	[19]

		-Reactor: Batch	
		-Lamp: 300 W Xe	
		-Pressure: 0.1 bar	
		-Temperature: No reported	
TiO$_2$/Cu	CH$_4$: 1.86	-Catalyst mass:0.5 g	[20]
		-Reactor: Continuous	
		-Light source: UV-light 16 W	
		-Pressure: No reported	
		-Temperature: No reported	
Pt-Cu$_2$O/TiO$_2$	CH$_4$: 1.42 CO:0.05	-Catalyst mass:0.02 g	[21]
		-Reactor: Batch	
		-Light source: Lamp 300 W Xe (λ> 400 nm) 20.5 mW cm^{-2}	
		-Pressure: 0.71 bar	
		-Temperature: 20 °C	
CuO	CH$_4$: 39.5	-Catalyst mass: 0.3 g, sacrifice agent: NaOH	[22]
		-Reactor: Batch	
		-Light source: 5 W UVC lamp, 5.5 mW cm^{-2}	
		-Pressure: No reported	
		-Temperature: 25°C	
Cu$_2$O/Cu	CH$_4$: 15.9	-Catalyst mass: 0.003 g	[23]
		-Reactor: Batch	
		-Light source: 125 W Hg lamp	

-Pressure: No reported

-Temperature: No reported

Table B.S.2 - Abbreviations and symbols used in the simulation study.

CFD computational fluid dynamic	$\mathbf{K_{CO2}}$ ratio of rate constant for adsorption and desorption of CO_2
SCCM standard cubic centimeters per minute	**I** light intensity
R reaction rate of photochemical reduction,	$\mathbf{K_0}$ permeability coefficient, m^2
$\mathbf{K_{H2O}}$ ratio of rate constant for adsorption and desorption of H_2O	D_j^{eff} effective diffusivity of species j, $m^2 \cdot s^{-1}$
k rate constant of photochemical reduction	N_j flux of mass transport, $kg \cdot m^{-3} \cdot s^{-1}$
p (partial) pressure, Pa	**R** gas constant, $8.314\ J \cdot mol^{-1} \cdot K^{-1}$
T temperature, K	**u** velocity field, $m^3 \cdot s^{-1}$
V volume fraction	y_j mole fraction of component j
α reaction order of photochemical reduction	ε_m porosity
μ dynamic viscosity of fluid, Pa·s	τ_m tortuosity
ρ density	D_j^m mass-average Stefan-Maxwell diffusivity
D_j diffusion coefficient	D_j^K Knudsen diffusivity

Table B.S.3 - Parameters used in the simulation study for different samples.

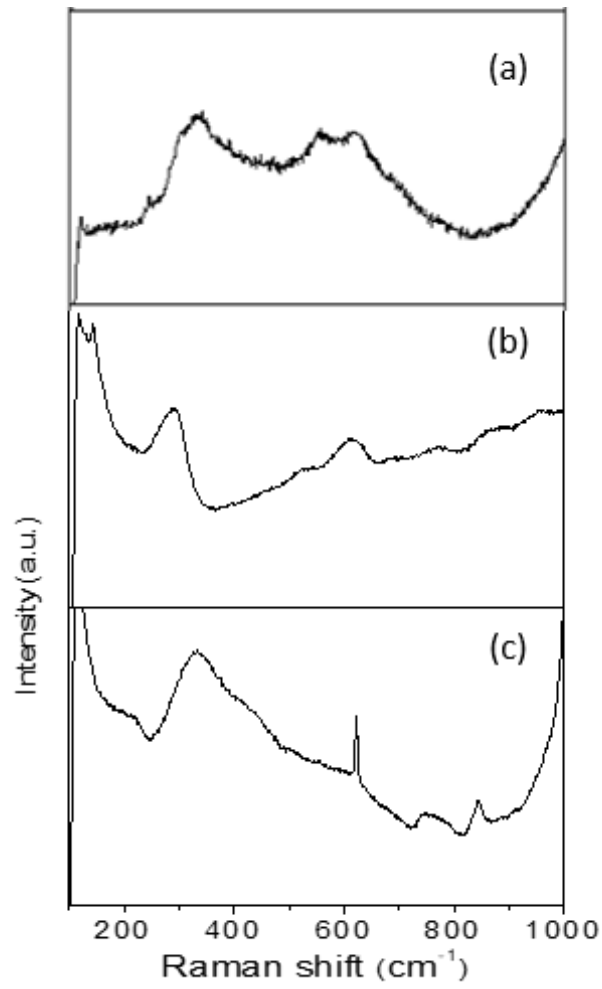| Parameter	Value	Unit
Photoreactor inlet gas flow rate	0.35	SCCM
Humidity	30030	ppm
Light Intensity	150	mW cm^{-2}
Temperature	293	K

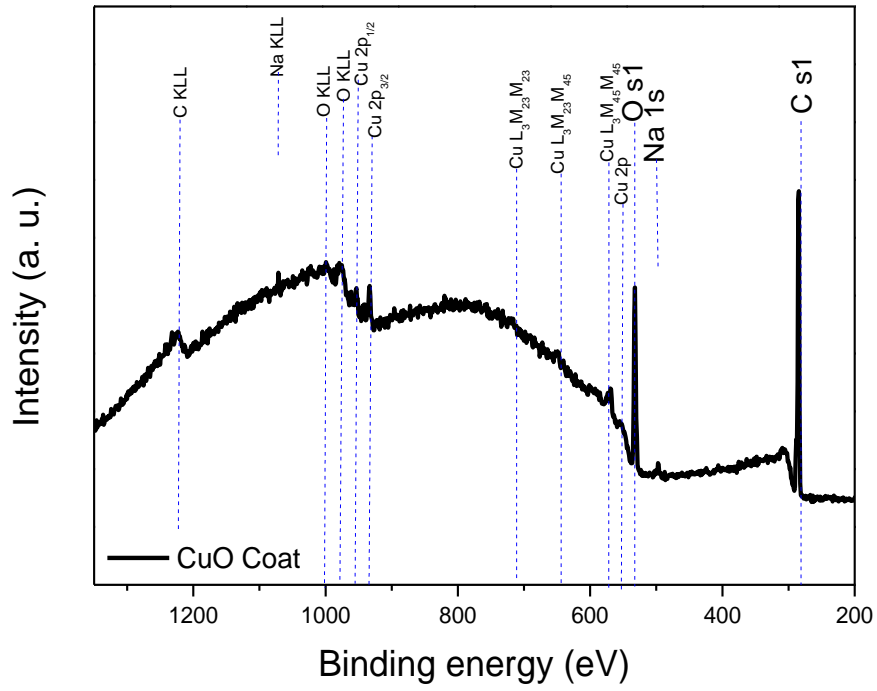Figure B.S.1 - Raman pattern of a) CuO TF, b) CuO coat and c) blank mesh.

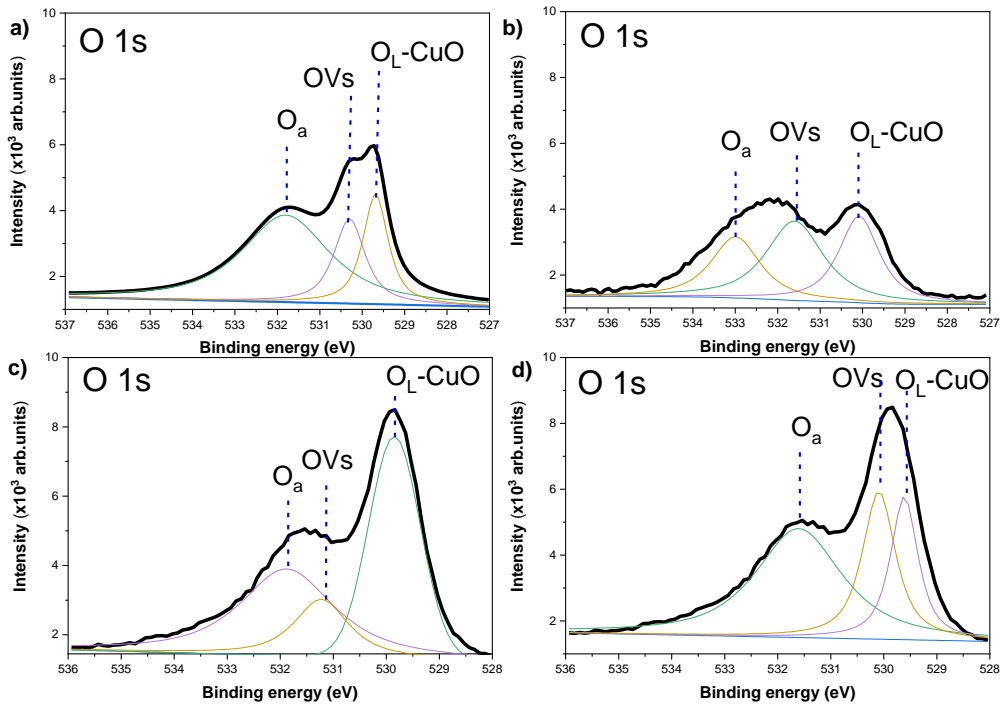Figure B.S.2 **-** XPS survey scan of sample CuO Coat.

Figure B.S.3 - High resolution O 1s spectra of a) CuO P, b) CuO US, c) CuO MW and d) CuO Coat.
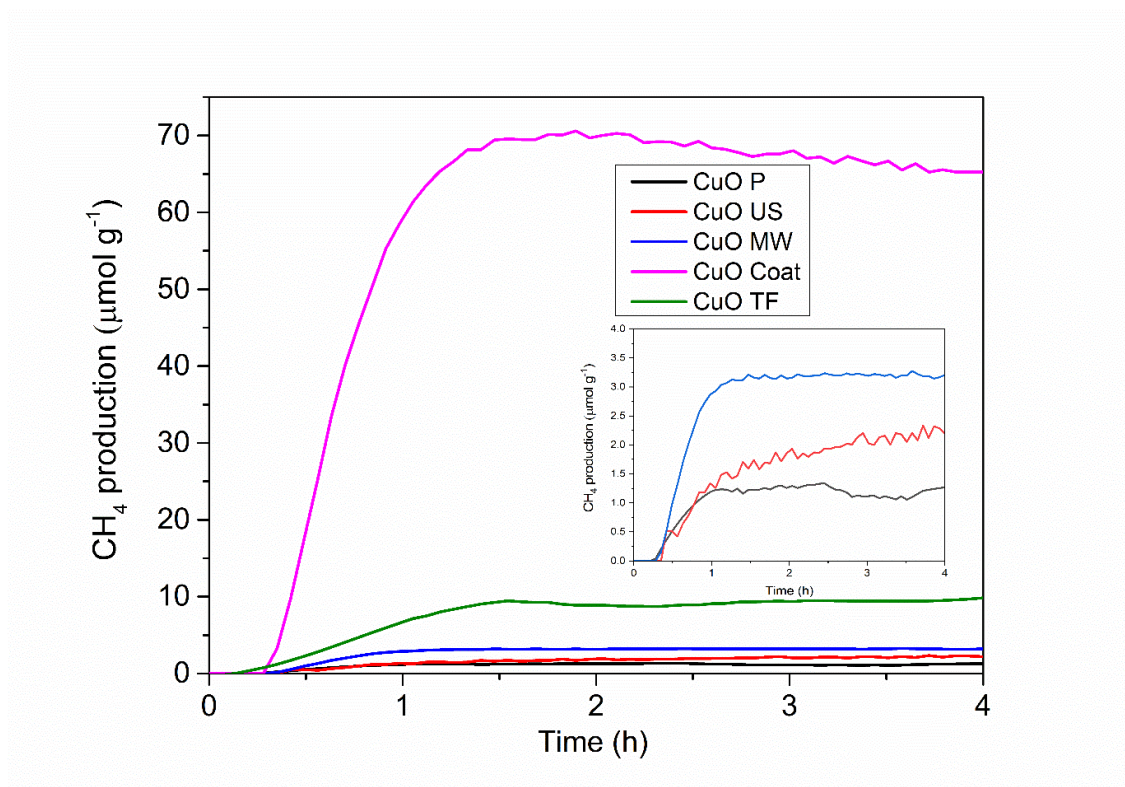

Figure B.S.4 - Action spectra of CH$_4$ production using different configurations of CuO under the irradiation of 300-600 nm. Inset: Zoom-in spectra of CuO P (black), CuO US (red) and CuO MW (blue).
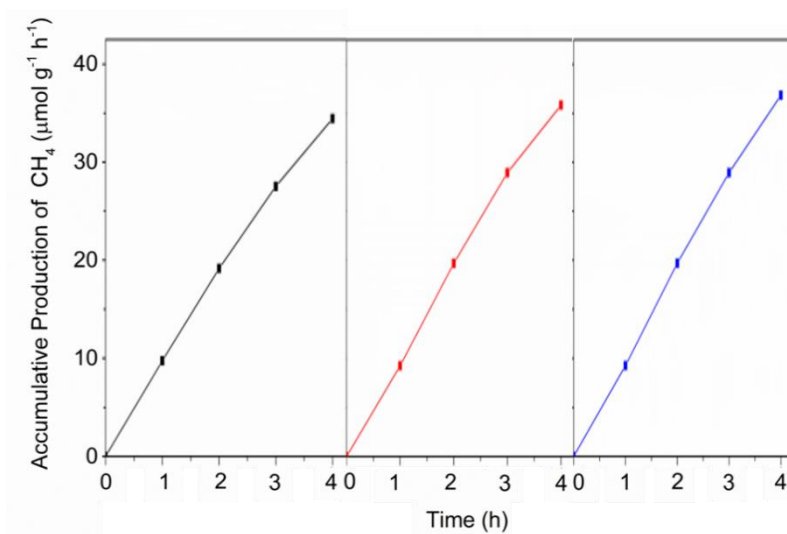

Figure B.S.5 - Accumulative production of CH$_4$ under UV-visible light irradiation.
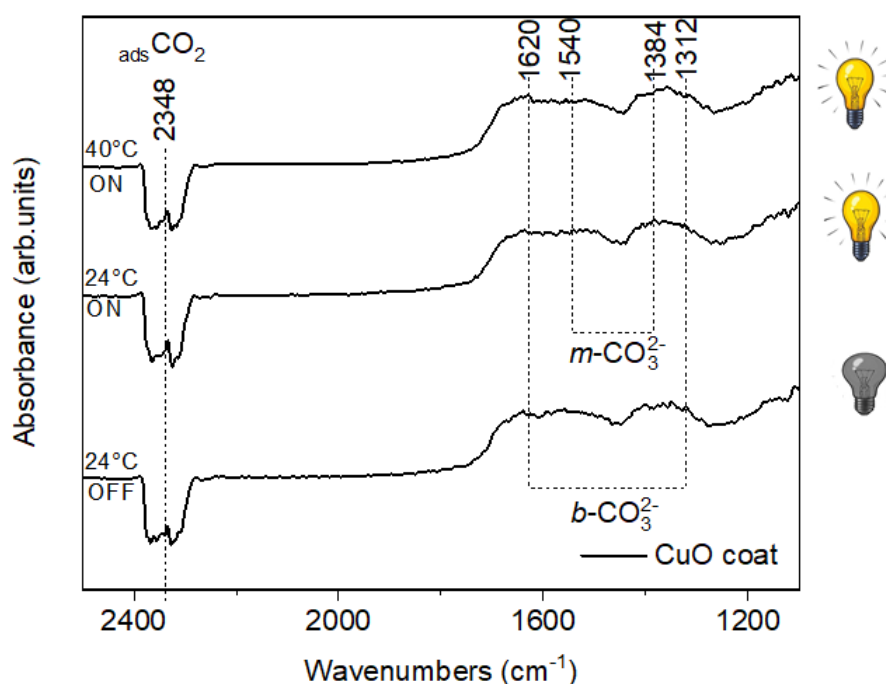
Figure B.S.6 - Operando DRIFTS spectra for CO_2-H_2O adsorption of the CuO coat
(Dark conditions at 24°C and Light at 40°C).

References

[1]   Y. Wang, L. Zhao, A. Otto, M. Robinius, and D. Stolten, "A review of post-combustion CO_2 capture technologies from coal-fired power plants," *Energy Procedia,* vol. 114, pp. 650-665, 2017.

[2]   D. Y. Leung, G. Caramanna, and M. M. Maroto-Valer, "An overview of current status of carbon dioxide capture and storage technologies," *Renewable and Sustainable Energy Reviews,* vol. 39, pp. 426-443, 2014.

[3]   L. Liu, C. Zhao, J. Xu, and Y. Li, "Integrated CO_2 capture and photocatalytic conversion by a hybrid adsorbent/photocatalyst material," *Appl. Catal., B,* vol. 179, pp. 489-499, 2015/12/01/ 2015, doi: https://doi.org/10.1016/j.apcatb.2015.06.006.

[4]   A. Crake, K. C. Christoforidis, A. Kafizas, S. Zafeiratos, and C. Petit, "CO_2 capture and photocatalytic reduction using bifunctional TiO_2/MOF nanocomposites under UV–vis irradiation," *Applied Catalysis B: Environmental,* vol. 210, pp. 131-140, 2017/08/05/ 2017, doi: https://doi.org/10.1016/j.apcatb.2017.03.039.

[5]   M. Flores-Flores, E. Luévano-Hipólito, L. M. T. Martínez, G. Morales-Mendoza, and R. Gómez, "Photocatalytic CO_2 conversion by MgAl layered

double hydroxides: Effect of Mg2+ precursor and microwave irradiation time," *Journal of Photochemistry and Photobiology A: Chemistry,* vol. 363, pp. 68-73, 2018.

[6]   A. Li *et al.*, "Tunable syngas production from photocatalytic CO_2 reduction with mitigated charge recombination driven by spatially separated cocatalysts," *Chemical science,* vol. 9, no. 24, pp. 5334-5340, 2018.

[7]   G. Qin *et al.*, "Photocatalytic reduction of carbon dioxide to formic acid, formaldehyde, and methanol using dye-sensitized TiO_2 film," *Applied Catalysis B: Environmental,* vol. 129, pp. 599-605, 2013.

[8]   J. Z. Tan, Y. Fernández, D. Liu, M. Maroto-Valer, J. Bian, and X. Zhang, "Photoreduction of CO2 using copper-decorated TiO_2 nanorod films with localized surface plasmon behavior," *Chem. Phys. Lett.,* vol. 531, pp. 149-154, 2012.

[9]   O. Ola and M. M. Maroto-Valer, "Copper based TiO_2 honeycomb monoliths for CO_2 photoreduction," *Catalysis Science & Technology,* vol. 4, no. 6, pp. 1631-1637, 2014 2014.

[10] W. A. Thompson, C. Perier, and M. M. Maroto-Valer, "Systematic study of sol-gel parameters on TiO_2 coating for CO_2 photoreduction," *Applied Catalysis B: Environmental,* vol. 238, pp. 136-146, 2018.

[11] D. Liu *et al.*, "On the impact of Cu dispersion on CO_2 photoreduction over Cu/TiO_2," *Catal. Commun.,* vol. 25, pp. 78-82, 2012.

[12] Y. Chiang and R. Juang, "Surface modifications of carbonaceous materials for carbon dioxide adsorption: a review. J Taiwan Inst Chem Eng 71: 214–234," ed, 2017.

[13] Q. Wang, J. Luo, Z. Zhong, and A. Borgna, "CO_2 capture by solid adsorbents and their applications: current status and new trends," *Energy Environ. Sci.,* vol. 4, no. 1, pp. 42-55, 2011.

[14] S. Sun, "Recent advances in hybrid Cu_2O-based heterogeneous nanostructures," *Nanoscale,* vol. 7, no. 25, pp. 10850-10882, 2015.

[15] M. Janczarek and E. Kowalska, "On the origin of enhanced photocatalytic activity of copper-modified titania in the oxidative reaction systems," *Catalysts,* vol. 7, no. 11, p. 317, 2017.

[16] W. N. R. W. Isahak *et al.*, "Adsorption–desorption of CO_2 on different type of copper oxides surfaces: Physical and chemical attractions studies," *Journal of CO_2 Utilization,* vol. 2, pp. 8-15, 2013.

[17] B.-J. Kim, K.-S. Cho, and S.-J. Park, "Copper oxide-decorated porous carbons for carbon dioxide adsorption behaviors," *J. Colloid Interface Sci.,* vol. 342, no. 2, pp. 575-578, 2010.

[18] J.-C. Wang *et al.*, "Enhanced photoreduction CO_2 activity over direct Z-scheme α-Fe_2O_3/Cu_2O heterostructures under visible light irradiation," *ACS applied materials & interfaces,* vol. 7, no. 16, pp. 8631-8639, 2015.

[19] S. I. In, D. D. Vaughn, and R. E. Schaak, "Hybrid CuO-TiO_2- xNx hollow nanocubes for photocatalytic conversion of CO2 into methane under solar irradiation," *Angew. Chem. Int. Ed.,* vol. 51, no. 16, pp. 3915-3918, 2012.

[20] N. Jantarasorn, O. Mekasuwandumrong, P. Kelly, and P. Praserthdam, "Reactive Magnetron Sputter Deposition of Copper on TiO_2 Support for Photoreduction of CO_2 to CH_4," *IOP Conference Series: Materials Science and Engineering,* vol. 559, no. 1, p. 012017, 2019/06/01 2019, doi: 10.1088/1757-899x/559/1/012017.

[21] Z. Xiong *et al.*, "Selective photocatalytic reduction of CO_2 into CH_4 over Pt-Cu_2O TiO_2 nanocrystals: The interaction between Pt and Cu_2O cocatalysts," *Applied Catalysis B: Environmental,* vol. 202, pp. 695-703, 2017.

[22]   A. E. Nogueira, J. A. Oliveira, G. T. da Silva, and C. Ribeiro, "Insights into the role of CuO in the CO_2 photoreduction process," *Sci. Rep.,* vol. 9, no. 1, pp. 1-11, 2019.

[23]   M. L. Ovcharov, A. M. Mishura, N. D. Shcherban, S. M. Filonenko, and V. M. Granchak, "Photocatalytic reduction of CO_2 using nanostructured Cu_2O with foam-like structure," *Solar Energy,* vol. 139, pp. 452-457, 2016/12/01/ 2016, doi: https://doi.org/10.1016/j.solener.2016.10.010.

[24]   T. Arai, S. Sato, and T. Morikawa, "A monolithic device for CO_2 photoreduction to generate liquid organic substances in a single-compartment reactor," *Energy Environ. Sci.,* 10.1039/C5EE01314C vol. 8, no. 7, pp. 1998-2002, 2015, doi: 10.1039/C5EE01314C.

[25]   M. Tahir and N. S. Amin, "Photocatalytic CO_2 reduction and kinetic study over In/TiO_2 nanoparticles supported microchannel monolith photoreactor," *Applied Catalysis A: General,* vol. 467, pp. 483-496, 2013 2013.

[26]   M. A. Ávila-López, E. Luévano-Hipólito, and L. M. Torres-Martínez, "CO_2 adsorption and its visible-light-driven reduction using CuO synthesized by an eco-friendly sonochemical method," *Journal of Photochemistry and Photobiology A: Chemistry,* vol. 382, p. 111933, 2019/09/01/ 2019, doi: https://doi.org/10.1016/j.jphotochem.2019.111933.

[27]   W. A. Thompson *et al.*, "Systematic study of TiO_2/ZnO mixed metal oxides for CO_2 photoreduction," *RSC Adv.,* 10.1039/C9RA03435H vol. 9, no. 38, pp. 21660-21666, 2019, doi: 10.1039/C9RA03435H.

[28]   I. R. Lewis and H. Edwards, *Handbook of Raman spectroscopy: from the research laboratory to the process line*. CRC press, 2001.

[29]   S. Guha, D. Peebles, and J. Terence Wieting, "Raman and infrared studies of cupric oxide," *Bull. Mater. Sci.,* vol. 14, no. 3, pp. 539-543, 1991/06/01 1991, doi: 10.1007/BF02744682.

[30]   M. Rashad, M. Rüsing, G. Berth, K. Lischka, and A. Pawlis, "CuO and Co_3O_4 nanoparticles: synthesis, characterizations, and Raman spectroscopy," *Journal of Nanomaterials,* vol. 2013, 2013.

[31]   H. Goldstein, D.-s. Kim, Y. Y. Peter, L. Bourne, J. Chaminade, and L. Nganga, "Raman study of CuO single crystals," *Physical Review B,* vol. 41, no. 10, p. 7192, 1990.

[32]   S. Chakraborty, A. Das, M. R. Begum, S. Dhara, and A. Tyagi, "Vibrational properties of CuO nanoparticles synthesized by hydrothermal technique," in *AIP Conference Proceedings*, 2011, vol. 1349, no. 1: American Institute of Physics, pp. 841-842.

[33]   P. Timchenko, E. Timchenko, L. Volova, and O. Frolov, "Chemometric analysis of the Raman spectra for determination of the composition of bones with different porosity," in *Journal of Physics: Conference Series*, 2018, vol. 1135, no. 1: IOP Publishing, p. 012054.

[34]   D. A. Long, "Infrared and Raman characteristic group frequencies. Tables and charts George Socrates John Wiley and Sons, Ltd, Chichester, Third Edition, 2001. " *Journal of Raman Spectroscopy,* vol. 35, no. 10, pp. 905-905, 2004, doi: https://doi.org/10.1002/jrs.1238.

[35]   D. He, S. Xing, B. Sun, H. Cai, H. Suo, and C. Zhao, "Design and construction of three-dimensional flower-like CuO hierarchical nanostructures on copper foam for high performance supercapacitor," *Electrochim. Acta,* vol. 210, pp. 639-645, 2016.

[36] L. Zhu, H. Li, Z. Liu, P. Xia, Y. Xie, and D. Xiong, "Synthesis of the 0D/3D CuO/ZnO heterojunction with enhanced photocatalytic activity," *The Journal of Physical Chemistry C,* vol. 122, no. 17, pp. 9531-9539, 2018.

[37] J.-Y. Park, K.-A. Lim, R. D. Ramsier, and Y.-C. Kang, "Spectroscopic and morphological investigation of copper oxide thin films prepared by magnetron sputtering at various oxygen ratios," *Bull. Korean Chem. Soc.,* vol. 32, no. 9, pp. 3395-3399, 2011.

[38] Q. Yang, P. Yan, J. Chang, J. Feng, and G. Yue, "Growth of bicrystal CuO microsheets from aqueous solution," *Phys. Lett. A,* vol. 361, no. 6, pp. 493-496, 2007.

[39] Y. Min, T. Wang, and Y. Chen, "Microwave-assistant synthesis of ordered CuO micro-structures on Cu substrate," *Appl. Surf. Sci.,* vol. 257, no. 1, pp. 132-137, 2010.

[40] W. Li, R. Liang, A. Hu, Z. Huang, and Y. N. Zhou, "Generation of oxygen vacancies in visible light activated one-dimensional iodine TiO_2 photocatalysts," *RSC Adv.,* vol. 4, no. 70, pp. 36959-36966, 2014.

[41] H. Yu *et al.*, "Three-in-one oxygen vacancies: whole visible-spectrum absorption, efficient charge separation, and surface site activation for robust CO_2 photoreduction," *Angew. Chem. Int. Ed.,* vol. 58, no. 12, pp. 3880-3884, 2019.

[42] Z.-P. Nie, D.-K. Ma, G.-Y. Fang, W. Chen, and S.-M. Huang, "Concave Bi_2WO_6 nanoplates with oxygen vacancies achieving enhanced electrocatalytic oxygen evolution in near-neutral water," *Journal of Materials Chemistry A,* vol. 4, no. 7, pp. 2438-2444, 2016.

[43] E. Desimoni and B. Brunetti, "X-ray photoelectron spectroscopic characterization of chemically modified electrodes used as chemical sensors and biosensors: a review," *Chemosensors,* vol. 3, no. 2, pp. 70-117, 2015.

[44] S. Jaiswar and K. Mandal, "Evidence of enhanced oxygen vacancy defects inducing ferromagnetism in multiferroic $CaMn_7O_{12}$ manganite with sintering time," *The Journal of Physical Chemistry C,* vol. 121, no. 36, pp. 19586-19601, 2017.

[45] S. Gavrielides, J. Z. Y. Tan, E. S. Fernandez, and M. M. Maroto-Valer, "Photo-generation of cyclic carbonates using hyper-branched Ru–TiO_2," *Faraday Discuss.,* 10.1039/C8FD00181B vol. 215, no. 0, pp. 407-421, 2019, doi: 10.1039/C8FD00181B.

[46] L. Proaño, E. Tello, M. A. Arellano-Trevino, S. Wang, R. J. Farrauto, and M. Cobo, "In-situ DRIFTS study of two-step CO2 capture and catalytic methanation over Ru,"Na_2O"/Al_2O_3 Dual Functional Material," *Appl. Surf. Sci.,* vol. 479, pp. 25-30, 2019.

[47] M. A. Ávila-López, E. Luévano-Hipólito, and L. M. Torres-Martínez, "CuO coatings on glass fibers: a hybrid material for CO_2 adsorption and photocatalytic reduction to solar fuels," *Journal of Materials Science: Materials in Electronics,* vol. 31, no. 16, pp. 13957-13969, 2020/08/01 2020, doi: 10.1007/s10854-020-03955-x.

[48] H. Du, C. T. Williams, A. D. Ebner, and J. A. Ritter, "In Situ FTIR Spectroscopic Analysis of Carbonate Transformations during Adsorption and Desorption of CO_2 in K-Promoted HTlc," *Chem. Mater.,* vol. 22, no. 11, pp. 3519-3526, 2010/06/08 2010, doi: 10.1021/cm100703e.

[49] Y. Liu *et al.*, "Chemical Adsorption Enhanced CO_2 Capture and Photoreduction over a Copper Porphyrin Based Metal Organic Framework," *ACS Applied Materials & Interfaces,* vol. 5, no. 15, pp. 7654-7658, 2013/08/14 2013, doi: 10.1021/am4019675.

[50]   A. Hakim *et al.*, "Studies on CO_2 adsorption and desorption properties from various types of iron oxides (FeO, Fe_2O_3, and Fe_3O_4)," *Industrial & Engineering Chemistry Research,* vol. 55, no. 29, pp. 7888-7897, 2016.

[51]   Y. Kato *et al.*, "Study on carbon dioxide reduction with water over metal oxide photocatalysts," *Surf. Interface Anal.,* vol. 51, no. 1, pp. 40-45, 2019, doi: https://doi.org/10.1002/sia.6542.

[52]   S. N. Habisreutinger, L. Schmidt-Mende, and J. K. Stolarczyk, "Photocatalytic Reduction of CO_2 on TiO_2 and Other Semiconductors," *Angew. Chem. Int. Ed.,* vol. 52, no. 29, pp. 7372-7408, 2013, doi: https://doi.org/10.1002/anie.201207199.

[53]   A. Dey and A. Aroonwilas, "CO_2 absorption into MEA-AMP blend: Mass transfer and absorber height index," *Energy Procedia,* vol. 1, no. 1, pp. 211-215, 2009.